TLR/RES/DE/REB-2021-08

Appendices to the Assessment of Graphite Properties and Degradation, Including Source Dependence

August 2021

PREPARED FOR:

U.S. NUCLEAR REGULATORY COMMISSION
CONTRACT NO. NRC-HQ-25-14-E-0004
TASK ORDER NO. 31310018F019

PREPARED BY:

NUMARK Associates Inc.
M. Srinivasan, B. Marsden, W. von Lensa, L. Cronise, R. Turk in conjunction with the U.S. Nuclear Regulatory Commission

PROGRAM MANAGERS:

Office of Nuclear Regulatory Research, U.S. Nuclear Regulatory Commission
M. Gordon, R. Iyengar

This report does not contain or imply legally binding requirements, nor does it establish or modify any regulatory guidance or positions of the U.S. Nuclear Regulatory Commission, and it is not binding on the Commission.

Appendix A

Compilation and Analysis of the Properties of IG-110, NBG-17, NBG-18, and PCEA Nuclear-Grade Graphites

Contents

List of Tables

List of Figures

List of Abbreviations

AG	against-grain orientation (in graphite)
AGC	Advanced Graphite Capsule
AGR	advanced gas-cooled reactor
ARI	activation-relevant impurity
ASME	American Society of Mechanical Engineers
ASTM	ASTM International (formerly, American Society for Testing and Materials)
BPVC	Boiler and Pressure Vessel Code
C	Celsius
cm	centimeter
COV	coefficient of variation
CTE	coefficient of thermal expansion
dpa	displacements per atom
DYM	dynamic Young's modulus (ultrasonic velocity determination)
ENHP	extruded, near-isotropic, high-purity (class of nuclear graphite)
ETV	electrothermal vaporization
F	Fahrenheit
FL-AAS	flameless atomic absorption spectrometry
FPY	full-power year
GA	General Atomics
GCC	graphite core component
GDMS	glow discharge mass spectrometry
GPa	gigapascal
GT-MHTGR	gas turbine modular high-temperature gas-cooled reactor
HTGR	high-temperature gas-cooled reactor
HTR	high-temperature reactor
HTR-PM	high-temperature gas-cooled reactor pebble-bed module
HTTR	High-Temperature Engineering Test Reactor
ICP-MS	inductively coupled plasma mass spectrometry
IIHP	isomolded, isotropic, high-purity (class of nuclear graphite)
INHP	isomolded, near-isotropic, high-purity (class of nuclear graphite)
INL	Idaho National Laboratory
JAEA	Japan Atomic Energy Agency
JAERI	Japan Atomic Energy Research Institute
K	Kelvin

kPa	kilopascal
L/min	liters per minute
m	meter
MDS	material data sheet
MeV	megaelectronvolt
Mg	megagram
MHTGR	modular high-temperature gas-cooled reactor
MIHP	molded, isotropic, high-purity (class of nuclear graphite)
MNHP	molded, near-isotropic, high-purity (class of nuclear graphite)
mm	millimeter
MPa	megapascal
MSR	molten salt reactor
MTR	material test reactor
n	neutron
NAI	neutron-absorbing impurity
NGNP	Next Generation Nuclear Plant
NQA	Nuclear Quality Assurance
NRC	U.S. Nuclear Regulatory Commission
OECD	Organisation for Economic Cooperation and Development
OPC	oxidation-promoting catalyst
OR	oxidation rate
ORNL	Oak Ridge National Laboratory
Pa	pascal
PBMR	pebble-bed modular reactor
PGA	Pile Grade A
ppm	parts per million
SENB	single-edge notched beam
SGL	Sigri Great Lakes
VHTR	very high temperature reactor
W	watt
WG	with-grain orientation (in graphite)
wppm	weight parts per million
μm	micrometer

1. Introduction

From a structural integrity viewpoint, near-isotropic high-density graphites are preferable for modern nuclear reactor designs. For this reason, international deliberation has led to the development of two ASTM International (ASTM) nuclear graphite material specifications, ASTM D7219-08, "Standard Specification for Isotropic and Near-Isotropic Nuclear Graphites," and ASTM D7301-08, "Standard Specification for Nuclear Graphite Suitable for Components Subjected to Low Neutron Irradiation Dose," which have been incorporated into the 2017 edition of the American Society of Mechanical Engineers (ASME) Boiler and Pressure Vessel Code (BPVC), Section III, "Rules for Construction of Nuclear Facility Components," Division 5, "High Temperature Reactors" (ASME BPVC-III-5), Subsection HH, "Class A Nonmetallic Core Support Structures," Subpart A, "Graphite Materials." It is generally recognized that complete isotropy in graphite properties is not possible because of the inherent anisotropy in the properties of individual graphitized crystal grains.

Nuclear-grade graphites used for previous reactors—including commercially operated reactors in the United States (Sigri Great Lakes (SGL) Carbon's H-451, anisotropic), commercial reactors in the United Kingdom (Pile Grade A (PGA) anisotropic graphite (Magnox reactors) and Gilsocarbon semi-isotropic graphite (advanced gas-cooled reactors (AGRs))), the Organisation for Economic Cooperation and Development's Dragon prototype high-temperature reactor (HTR), and experimental reactors in Germany (ATR-2E)—are no longer produced and are not commercially available (Idaho National Engineering and Environmental Laboratory, 2005). However, newer experimental graphite grades are manufactured using prototype facilities to provide properties that are as isotropic as possible. Some are in a relatively advanced stage of commercial manufacturing and may be currently available. Of these, this appendix concentrates on Toyo Tanso's IG-110, SGL Carbon's NBG-17 and NBG-18, and GrafTech International's PCEA graphites, for the following reasons:

- For the analysis of IG-110, a large amount of data on technical properties, including irradiated properties, generated by various international laboratories, is available.
- IG-110 is the material of construction for the core components of China's commercial high-temperature gas-cooled reactor pebble-bed module (HTR-PM).
- The European Union's Euratom Programme, the U.S. Next Generation Nuclear Plant (NGNP) program, and the AREVA NGNP Alliance high-temperature gas-cooled reactor (HTGR) planned to use NBG-17, NBG-18, and PCEA graphites (prismatic core design).
- The most recent data generated from the European Union's Petten irradiation facilities and the Oak Ridge National Laboratory (ORNL) and Idaho National Laboratory (INL) NGNP irradiation programs pertain to NBG-17, NBG-18, and PCEA graphites.
- These grades meet the material specifications ASTM D7219-08 and ASTM D7301-08.

Table 1-1 contains general information on these graphites (adapted from Burchell et al., 2007). Because interest in HTGRs has been intermittent, both in the United States and internationally, and because adequate and continued financial support has been lacking, the graphite

manufacturers listed in Table 1-1, other than Toyo Tanso, have not maintained their production facilities as necessary to produce an uninterrupted supply of graphite for building commercial nuclear reactors. Thus, to the best of the authors' awareness, none of the present suppliers has the infrastructure needed for Nuclear Quality Assurance (NQA)-1 certification, which would be required under several articles in ASME BPVC-III-5, Subsection HA, "General Requirements," Subpart B, "Graphite Materials." GrafTech produced the original PCEA at its facilities in Notre Dame, France; however, before its dissolution as a company (it was bought by a holding company (Brookfield) in 2015), GrafTech had planned to transfer production to its plant in Clarksburg, WV. GrafTech's current status and plans to participate in nuclear graphite development are unknown.

Currently, SGL Carbon does not produce NBG-17 graphite (Burchell et al., 2007). For about 18 months during the early 2000s, SGL Carbon produced limited quantities of NBG-18, in semiproduction mode, for South Africa's pebble-bed modular reactor (PBMR). However, since the PBMR's demise, the production of NBG-18 has been halted.

Table 1-1 Nuclear Graphite Compiled and Analyzed in This Assessment

Graphite Designation, Grain Size	Manufacturer	Type of Coke	Maximum Grain Size, mm	Reactor Designer	Graphite Core Component	Remarks
IG-110, fine grain	Toyo Tanso	Petroleum	0.02	JAEA HTTR/China	Prismatic fuel element, replaceable reflector, and core support pedestals. Pebble-bed reflector in HTR-PM.	Significant amount of properties data and HTTR (Japan) operational data; material of construction for HTR-PM.
PCEA, medium grain (preproduction)	GrafTech International	Petroleum	0.8	AREVA	Prismatic fuel and replaceable block. Pebble-bed reflector and insulation blocks.	AREVA's currently preferred material (AREVA NP Inc., 2008). AREVA plans to use this graphite for all of its core.
NBG-18, medium grain (preproduction)	SGL Carbon	Pitch	1.6	AREVA	Prismatic replaceable reflector.	
NBG-17, medium grain (preproduction)	SGL Carbon	Pitch	0.8	AREVA	Prismatic fuel element and replaceable reflector.	AREVA has indicated it could use a combination of NBG-17 and NBG-18 (AREVA NP Inc., 2007). NBG-17 is not commercially available at this time.

Unless there are guaranteed orders and a specific market for nuclear-grade graphite lasting for decades, graphite manufacturers are unlikely to keep their manufacturing facilities and necessary institutional knowledge. Despite potential deficiencies in the supply chain, research on nuclear graphites has generated sufficient data to be of value in assessing the ASME BPVC requirements for the structural integrity of graphite core components (GCCs).

This appendix examines data compiled by the authors to support a review of the source dependence of graphite properties. It provides properties data and discusses the applicability of

Subsection HH, Subpart A, for four graphites individually. This is in contrast to many technical publications, which present properties data for all graphites together. This report avoids such a presentation for the following reasons:

- Presenting properties data for all graphites in a single plot or table would lead to data comparison and potentially to judgments of the merit of one graphite over another, with an associated bias toward grade selection.
- This report aims to assess the sufficiency of the available properties data as required for the design of specific HTR components, as specified in the ASME BPVC's material data sheet (MDS).
- This research was sponsored by the U.S. Nuclear Regulatory Commission (NRC), which is typically design neutral and neutral with respect to the materials of construction used for reactors. As a regulator, the NRC assesses a design and the materials used in the design solely from the perspective of reactor safety and the regulatory requirements in Title 10 of the *Code of Federal Regulations* Part 50, "Domestic licensing of production and utilization facilities." The regulator is not a proponent of any particular design or construction type, nor does it require the use of a certain material or combination of materials. Rather, designers are responsible for choosing appropriate materials for the design and construction of nuclear reactors for which they seek certification. Therefore, this report presents properties data individually for each graphite, rather than presenting a single chart or table for each property, to prevent comparison between different grades and avoid influencing assessments of their sufficiency and of ASME BPVC applicability.
- Subsection HH, Subpart A, Article HHA-2200(a), "Materials Properties for Design," states the following:

> Graphite properties used for design shall be determined by the Designer and published in the Material Data Sheet. The Material Data Sheet contains the data required for design in accordance with this Subpart. Additional property data may be generated by the Designer as required. One Material Data Sheet is to be generated for each graphite grade used in the design.

This report contains data from publicly available sources in the MDS format for IG-110, NBG-17, NBG-18, and PCEA graphites. These data may not be used for design purposes. The designer is responsible for the generation and validation of data pertinent to the design and operational variables for the graphites used.

The authors of this report do not want to unduly influence a potential designer's choice of graphites. It is understood that a designer may have set material selection criteria. In addition to shape, size, and property specifications, the designer may need to consider manufacturability; the requirements of ASME BPVC-III-5, Subsection HA, Subpart B (including NQA-1 requirements); replacement longevity; technical and other support; and cost. Some of these considerations are outside the scope of the research presented here.

Additionally, the data in this report were extracted from publicly available information. Some of the data may have been obtained by test methods other than those cited in ASTM specifications and practices, and the authors have not attempted to normalize the data to conform to ASTM methods. Designers may not use the extracted data in this report for their designs; rather, they should examine the original data sources for applicability.

Section 5.2 of the report by Burchell et al. (2007) provides more information on graphite selection tradeoffs.

Notes on Irradiated Properties and Comparisons

The authors recognize the importance of and the need for verifiable data on irradiated properties of graphite for the design of GCCs in HTRs. Obtaining such data is difficult, time consuming, and costly; only a few laboratories around the world have sufficient qualified equipment and personnel. The cost and time arise from the complexities of procuring samples, machining to the particular size and shape that the irradiation capsule can accommodate, determining the irradiation time for the temperature and dose required, and finally determining the properties after irradiation. Because of these factors, it is almost always very difficult to examine an adequate test population. These concerns were the subject of a special ASTM meeting on nuclear graphite (Tzelepi and Carroll, 2014).

Although material test reactors (MTRs) provide valuable information on material behavior, before and during the materials' use in reactors designed based on properties obtained from the MTRs, the behaviors need to be verified from real-time irradiation of the materials in prototypical HTGR and molten salt reactor (MSR) environments. Typically, MTR samples involve accelerated testing to achieve the planned cumulative dose. Confirmation may be needed that such accelerated test data are valid. In AGRs, such confirmation has been obtained from trepanned samples (Eason et al., 2007; McEnaney, 2005).

In discussing the various properties, this report follows the format of the MDS form in ASME BPVC-III-5, Article HHA-II-2000. For illustration, the authors have entered some of these properties, extracted from various publications, in the MDS format.

Following the MDS format, this report first provides information on data and sources. Where possible, the authors have digitally extracted, reanalyzed, and recast the data for this report. Several graphs show either trend lines generated by Microsoft Excel from the data in the original publication, lines generated by the relational equations from the original publications, or simply reproductions of the lines from the original publications; thus, the graphs do not contain the actual data points. However, if the data were observed to have much scatter, this report includes both a trend line and the data points.

In many instances, the published literature does not include potentially important information, such as the number of specimens used for the test, the test standard used, and the conditions of testing. Thus, data comparisons should be made cautiously. The objective of this report is simply to inform the reader that data may vary depending on when the material was produced, and that material variability may contribute to dispersion in data on the same property in various

publications. The data in this report should not be used for design; rather, the designer should independently generate the required data on graphites available at the time of the design.

The dose range for HTGR designs varies considerably. Gallego and Burchell (2011) have stated that the dose may vary by up to about 5.75 displacements per atom (dpa) for prismatic designs and by up to about 25 dpa for pebble-bed designs. Such variations are due to the design and the flux rate imposed on graphite during service. Researchers at INL (2010) have calculated the expected dose ranges for reactor operating conditions as shown in Table 1-2.

Table 1-2 Estimation of Graphite Dose Ranges for HTGR Designs (INL, 2010)

Parameter	Prismatic Reactor	Pebble-Bed Reactor
Temperature (normal operations)		
Reflector blocks	1,000 °C (1,832 °F)	600–1,000 °C (1,112–1,832 °F)
Fuel blocks	1,000–1,100 °C (1,832–2,012 °F)	<1,000 °C (<1,832 °F)
Peak fast fluence (> 0.1 MeV); dose (0.78×10^{21} n/cm^2 = 1 dpa)		
Reflector	$1.7–12.2\times10^{20}$ n/cm^2 0.19–0.85 dpa/FPY	$1.6–12.2\times10^{20}$ n/cm^2 0.18–0.85 dpa/FPY

The INL researchers note the tradeoffs in design as follows:

> If the reflector walls only receive a dose of 0.2 dpa/full-power year (FPY), then it will take more than 20 years before the graphite blocks will obtain a dose approaching turnaround at 1,000 °C. However, if the reflectors received a dose of 0.85 dpa/FPY, the blocks will reach turnaround levels in approximately 5 to 6 years. Higher dose data experiments are, therefore, necessary for 0.85 dpa/FPY but not for 0.2 dpa/FPY.

In the above, the term “turnaround” refers to the dose at temperature at which the graphite shrinkage, as demonstrated by the increasingly negative linear dimensional change in the MTR data, begins to stop increasing.

Unlike materials in graphite-moderated HTRs, materials in MSRs are expected to operate at temperatures in the range of about 500–800 degrees Celsius (C) (932–1,472 degrees Fahrenheit (F)) and to experience lifetime doses of up to 100–150 dpa while also being exposed to molten salt (Yvon and Carré, 2009). The MSR designer may also need to limit irradiation changes in the graphite porosity, which may change the ability of components to reduce coolant ingress, and yet allow fission products such as xenon gas to escape. Thus, when examining the irradiated properties data available for various graphite grades, the designer must consider the needs of the design and the data limitations.

For general challenges in materials selection and performance demand for a variety of newer reactor types, it is pertinent to understand the temperature and irradiation dose ranges. Table 1-3 shows these parameters, as presently estimated.

Table 1-3 Estimated Operating Temperature and Irradiation Dose Ranges of Reactors of Newer Designs (Adapted from Carré et al., 2008; Fazio et al., 2009)

Reactor Type†	Temp, degrees C (degrees F)	Dose, dpa
SFR	390–700 (734–1,292)	Cladding ~200
GFR	600–1,200 (1,112–2,192)	60–90
LFR/ADS	350–480 (662–896)	Cladding ~100
VHTR	600–1,600 (1,112–2,912)	7–25
SCWR	350–620 (662–1,148)	~20
MSR	500–800 (932–1,472)	100–150
Fusion	500–700 (932–1,292)	~100

† SFR = sodium fast reactor; GFR = gas fast reactor; LFR/ADS = lead fast reactor, subcritical accelerator-driven system; VHTR = very-high-temperature reactor; SCWR = supercritical water reactor; MSR = molten salt reactor.

The rest of this report examines the properties for each grade of graphite in the order in which they appear in the MDS form of ASME BPVC-III-5, Article HHA-II-2000.

2. Toyo Tanso IG-110 Graphite

2.1. Information Pertaining to ASME Material Data Sheet for IG-110 Graphite

Table 2-1 provides properties information for IG-110 graphite, following the ASME graphite code MDS format. For each property, the table cites the corresponding section of this report, which contains further information extracted from publicly available data.

2.2. Material Grade

The material grade is IG-110.

2.3. Material Specification ID

This identifies the construction specification for the graphite grade applicable to this MDS. The designer enters this value.

2.4. ASTM Specification

This is the material specification (ASTM) number from Mandatory Appendix HHA-I, “Graphite Material Specifications,” that applies to the manufacture of the material. The designer enters this number.

Table 2-1 Example ASME MDS for IG-110 Graphite

ASME BPVC-III-5-2017, FORM MDS-1 MATERIAL DATA SHEET (SI UNITS)		
Grade Designation		
Material grade	**IG-110**	(1) Material grade: The manufacturer's grade designation that complies with the requirements of the Mandatory Appendix HHA-I material specification.
Material spec. ID	Not applicable	(2) Material spec. ID: The construction specification for the graphite grade applicable to this MDS.
ASTM spec.	ASTM D7219-08 (view of authors, not confirmed by manufacturer).	(3) ASTM spec.: The Mandatory Appendix HHA-I material specification (ASTM) number that applies to the manufacture of the material.
Max. grain size (mm) (Section 2.5)	0.02 (Burchell et al., 2007). This is also the mean grain size (Ubic, 2015).	(4) Maximum grain size: The maximum filler particle grain size that is used in the mix formulation. (For isostatically pressed graphite, report mean grain size.)
Designation (Section 2.6)	IIHP*	(5) Designation: Material designation as defined in the Mandatory Appendix HHA-I material specification.

* Isomolded isotropic high-purity graphite (authors' estimate; also estimated by Yu and Sun (2010)).

ASME BPVC-III-5-2017, FORM MDS-1 MATERIAL DATA SHEET (SI UNITS)				
Temperature-Dependent Parameters				
Property	Units			
Bulk density (Section 2.7)	kg/m^3	Mean		(6) Bulk density: The material bulk density. Mean and standard deviation of material test specimen results.
		Std. Dev.		

ASME BPVC-III-5-2017, FORM MDS-1 MATERIAL DATA SHEET (SI UNITS)									
		1.83 (Homerin and Miller, 2002); 1.77±0.017 (Campbell and Katoh, 2018); 1.925 (Kane et al., 2011). (See Section 2.7.)							
Strength—tensile (Section 2.8)	MPa	WG	20 °C	200 °C	400 °C	600 °C	800 °C	1,000 °C (see Note 1 below)	(7) Strength, tensile: Mean and standard deviation of material test specimen results. Note that the temperature dependence of only one strength parameter need be determined; the others can be assumed to change by the same relative amount.
		Mean	20 (Homerin and Miller, 2002)	See Figure 2-2 for temperature dependence of tensile strength.					
		Std. Dev.							
	MPa	AG	20 °C	200 °C	400 °C	600 °C	800 °C	1,000 °C	
		Mean	16 (Homerin and Miller, 2002)						
		Std. Dev.							
Strength—flexural (four-point) (Section 2.10)	MPa	WG	20 °C	200 °C	400 °C	600 °C	800 °C	1,000 °C	(8) Strength, flexural (four-point): Mean and standard deviation of material test specimen results. Note that the temperature dependence of only one strength parameter need be determined; the others can be assumed to change by the same relative amount.

ASME BPVC-III-5-2017, FORM MDS-1 MATERIAL DATA SHEET (SI UNITS)									
		Mean	26 (Homerin and Miller, 2002); 36±1.3 (Campbell and Katoh, 2018)						
		Std. Dev.							
	MPa	AG	20 °C	200 °C	400 °C	600 °C	800 °C	1000 °C	
		Mean	23 (Homerin and Miller, 2002); 34±1.8 (Campbell and Katoh, 2018)						
		Std. Dev.							
Strength—compressive (Section 2.12)	MPa	WG	20 °C	See Figure 2-3 for temperature dependence of the compressive strength of IG-110.					(9) Strength, compressive: Mean and standard deviation of material test specimen results. Note that the temperature dependence of only one strength parameter need be determined; the others can be assumed to change by the same relative amount.

ASME BPVC-III-5-2017, FORM MDS-1 MATERIAL DATA SHEET (SI UNITS)									
		Mean	67 (Homerin and Miller, 2002) (only one value available; not known if it is WG or AG); 77 ± 2.1 (AG) and 77 ± 3.3 (WG) (Campbell and Katoh, 2018)						
		Std. Dev.							
	MPa	AG	20 °C	200 °C	400 °C	600 °C	800 °C	1,000 °C	
		Mean	75 ± 2.7 (Campbell and Katoh, 2018)						
		Std. Dev.							
Elastic modulus (dynamic) (Section 2.14)	GPa	WG	20 °C	200 °C	400 °C	600 °C	800 °C	1,000 °C	(10) Elastic modulus (dynamic): Mean and standard deviation of material test specimen results.
		Mean	11 (Homerin and Miller, 2002); 9.7±0.22 (Campbell and Katoh, 2018)						
		Std. Dev.							
		AG	20 °C	200 °C	400 °C	600 °C	800 °C	1,000 °C	

ASME BPVC-III-5-2017, FORM MDS-1 MATERIAL DATA SHEET (SI UNITS)									
		Mean	10 (Homerin and Miller, 2002); 9.1 ± 0.23 (Campbell and Katoh, 2018)						
		Std. Dev.							
Elastic modulus (static) (obtained by the initial slope of the stress-strain curve) (Section 2.15)	GPa	WG	20 °C	200 °C	400 °C	600 °C	800 °C	1,000 °C	(10) Elastic modulus (dynamic): Mean and standard deviation of material test specimen results. (11) Elastic modulus (static): Mean and standard deviation. Use a measured value of the dynamic elastic modulus (10) scaled by the ratio between static and dynamic. Note that the dynamic and static modulus are related. Only one need be measured; the other can be computed from these measurements and the ratio between the two values.
		Mean	7.9–9.9 (Shibata et al., 2010)						
		Std. Dev.							
		AG	20 °C	200 °C	400 °C	600 °C	800 °C	1,000 °C	
		Mean							
		Std. Dev.							
Coefficient of thermal expansion (CTE), β (Section 2.17)	/°C	WG	20 °C	200 °C	400 °C	600 °C	800 °C	1,000 °C	(12) Coefficient of thermal expansion: Mean and standard deviation of material test specimen results. This property's temperature dependence shall be determined.

ASME BPVC-III-5-2017, FORM MDS-1 MATERIAL DATA SHEET (SI UNITS)									
		Mean	5.1 (Homerin and Miller, 2002); 4.2 ± 0.11 (Campbell and Katoh, 2018); ⩽4.5 (Yu and Sun, 2010)	3.8 (Homerin and Miller, 2002); 4.2 ± 0.11 (Campbell and Katoh, (2018); ⩽4.5 (Yu and Sun, 2010)	3.8 (Hom-erin and Miller, 2002); 4.2 ± 0.11 (up to 500 °C) (Camp-bell and Katoh, 2018); ⩽4.5 (Yu and Sun, 2010)	3.8 (Hom-erin and Miller, 2002)	3.8 (Hom-erin and Miller, 2002)	3.8 (Homerin and Miller, 2002)	
		Std. Dev.							
		AG	20 ºC	200 ºC	400 ºC	600 ºC	800 ºC	1,000 ºC	
		Mean	5.6 (Homerin and Miller, 2002); 4.5 ± 0.04 (Campbell and Katoh, 2018)	4.3 (Homerin and Miller, 2002); 4.5 ± 0.04 (Campbell, and Katoh, 2018)	4.3 (Hom-erin and Miller, 2002); 4.5 ± 0.04 (up to 500 °C) (Camp-bell and Katoh, 2018)	4.3 (Hom-erin and Miller, 2002)	4.3 (Hom-erin and Miller, 2002)	4.3 (Homerin and Miller, 2002)	
		Std. Dev.							
Thermal conductivity (Section 2.19)	W/m° K	WG	20 °C	200 °C	400 °C	600 °C	800 °C	1,000 °C	(13) Thermal conductivity: Mean and standard deviation of material test specimen results.

ASME BPVC-III-5-2017, FORM MDS-1 MATERIAL DATA SHEET (SI UNITS)									
		Mean	165 (Homerin and Miller, 2002); 130 ± 3.7 (Campbell and Katoh, 2018)		165 (Hom-erin and Miller, 2002); 77 ± 1.4 (at 500 °C) (Camp-bell and Katoh, 2018)				
		Std. Dev.							
		AG	20 °C	200 °C	400 °C	600 °C	800 °C	1,000 °C	
		Mean	129 ± 7.2 (Campbell and Katoh, 2018)		77 ± 1.4 (at 500 °C) (Camp-bell and Katoh, 2018)				
		Std. Dev.							
Temperature-Independent Parameters									
Poisson's ratio (Section 2.21)			0.138–0.21						(14) Poisson's ratio: Mean and standard deviation of material test specimen results. As an alternative, a published historical value may be used.
Anisotropy factor (Section 2.22)			1.13 (Homerin and Miller, 2002); 1.057 (Campbell and Katoh, 2018); ⩽1.08 (Yu and Sun, 2010)						(15) Anisotropy factor: Mean and standard deviation for the charges as described in the graphite specification (Mandatory Appendix HHA-I). The average of the charges is then given in the MDS.

ASME BPVC-III-5-2017, FORM MDS-1 MATERIAL DATA SHEET (SI UNITS)									
Critical stress intensity factor (K_{Ic}) (Section 2.24)	MPa · √m	0.97 (AG) (Burchell et al., 2017); 1.33 ± 0.06 (WG) and 1.48 ± 0.06 (Burchell et al., 2017)							(16) Critical stress intensity factor (K_{Ic}): The average and standard deviation of the material test specimen results.
Design Strength and Material Reliability Curve Values									
Ratio of compressive to tensile strength (R_{tc})	Designer to provide this information.								(17) Ratio of compressive to tensile strength (R_{tc}): Computed from the mean tensile and mean compressive strengths as published in (7) and (9) above. R_{tc} = compressive strength (9) ÷ tensile strength (7). This quantity is defined as positive.
Ratio of flexural to tensile strength (R_{tf})	Designer to provide this information.								(18) Ratio of flexural to tensile strength (R_{tf}): Computed from the mean tensile and mean flexural strengths as published in (7) and (8) above. R_{tf} = flexural strength (8) ÷ tensile strength (7). This quantity is defined as positive.
$S_{c95\%}$	MPa	Designer to provide this information.							(19) $S_{c95\%}$: The computed single-sided 95% confidence interval value for the Weibull characteristic strength that defines the material reliability curve. This is calculated in accordance with HHA-II-3100, based on the tensile strength measurements.
$m_{95\%}$		Designer to provide this information.							(20) $m_{95\%}$: The computed single-sided 95% confidence interval value for the Weibull modulus that defines the material reliability curve. This is calculated in accordance with HHA-II-3100, based on the tensile strength measurements.

ASME BPVC-III-5-2017, FORM MDS-1 MATERIAL DATA SHEET (SI UNITS)			
S_0	MPa	Designer to provide this information.	(21) S_0: The computed value for the threshold stress based on the three-parameter distribution that defines the material reliability curve. This is calculated in accordance with HHA-II-3200, based on the tensile strength measurements.
$S_{c095\%}$		Designer to provide this information.	(22) $S_{c095\%}$: The computed single-sided 95% confidence interval value for the characteristic stress based on the three-parameter distribution that defines the material reliability curve. This is calculated in accordance with HHA-II-3200, based on the tensile strength measurements.
$m_{095\%}$		Designer to provide this information.	(23) $m_{095\%}$: The computed single-sided 95% confidence interval value for the Weibull modulus based on the three-parameter distribution that defines the material reliability curve. This is calculated in accordance with HHA-II-3200, based on the tensile strength measurements.
S_g (10^{-4})	MPa	Designer to provide this information.	(24) S_g (10^{-4}): The design allowable stress value corresponding to the probability of failure of 10^{-4}, computed in accordance with HHA-II-3300 based on $S_{c95\%}$ and $m_{95\%}$ ((19) and (20) above).
S_g (10^{-3})	MPa	Designer to provide this information.	(25) S_g (10^{-3}): The design allowable stress value corresponding to the probability of failure of 10^{-3}, computed in accordance with HHA-II-3300 based on $S_{c95\%}$ and $m_{95\%}$ ((19) and (20) above).

ASME BPVC-III-5-2017, FORM MDS-1 MATERIAL DATA SHEET (SI UNITS)									
S_g (10^{-2})	MPa	Designer to provide this information.							(26) S_g (10^{-2}): The design allowable stress value corresponding to the probability of failure of 10^{-2}, computed in accordance with HHA-II-3300 based on $S_{c95\%}$ and $m_{95\%}$ ((19) and (20) above).
S_g (5×10^{-2})	MPa	Designer to provide this information.							(27) S_g(5×10^{-2}): The design allowable stress value corresponding to the probability of failure of 5×10^{-2}, computed in accordance with HHA-II-3300 based on $S_{c95\%}$ and $m_{95\%}$ ((19) and (20) above).
Graphite Oxidation Effects									
Property	Units	2%	4%	6%	8%	10%			
Strength [.] (Section 2.30)									(28) Oxidation change in strength: As either a chart or a curve that describes the mean behavior of the relative property change as a function of weight loss. This is expressed as a value normalized to the as-manufactured value and may be based on a strength parameter selected by the designer. The strength parameter used shall be recorded in an attachment to the MDS. The figures in HHA-3141 may be used as an alternative to measurements.
Elastic modulus (dynamic) [.] (Section 2.31)									(29) Oxidation change in elastic modulus (dynamic): As either a chart or a curve that describes the mean behavior of the relative property change as a function of weight loss. This is expressed as a value normalized to the as-manufactured value.

ASME BPVC-III-5-2017, FORM MDS-1 MATERIAL DATA SHEET (SI UNITS)									
Thermal conductivity [.] (Section 2.32)									(30) Oxidation change in thermal conductivity: As either a chart or a curve that describes the mean behavior of the relative property change as a function of weight loss. This is expressed as a value normalized to the as-manufactured value.
Irradiated Graphite									
Property									
Dimensional change [.] (Section 2.34)									(31) Irradiation-induced dimensional change: This is the change in length, normalized to the initial length expressed as a percentage. The data shall be expressed as either a table of data or a mathematical fit, appended to the MDS. Range of applicability to be identified and checked as part of the design assessment.
Creep coefficient [.] (Section 2.35)									(32) Irradiation-induced creep coefficient: Shall be expressed as either a table of data or a mathematical fit, appended to the MDS. Range of applicability to be identified and checked as part of the design assessment. The creep coefficient to be used is the coefficient (or set of coefficients) required for the irradiation creep model proposed for use by the designer. The model shall be recorded in an attachment to the MDS.

ASME BPVC-III-5-2017, FORM MDS-1 MATERIAL DATA SHEET (SI UNITS)									
Coefficient of thermal expansion [.] (Section 2.36)									(33) Irradiation-induced change in coefficient of thermal expansion: Shall be expressed as either a table of data or a mathematical fit, appended to the MDS. Range of applicability to be identified and checked as part of the design assessment. This is expressed as a value normalized to the as-manufactured value. The temperature dependence of this property shall be determined.
Strength [.] (Section 2.37)									(34) Irradiation-induced change in strength: Shall be expressed as either a table of data or a mathematical fit, appended to the MDS. Range of applicability to be identified and checked as part of the design assessment. This is expressed as a value normalized to the as-manufactured value and shall be based on a strength parameter selected by the designer. The strength parameter used shall be recorded in an attachment to the MDS. Note that irradiation-induced change in strength need only be measured should the designer desire to take account of the strength increase at low or intermediate damage doses.
Elastic modulus [.] (Section 2.38)									(35) Irradiation-induced change in elastic modulus: This is expressed as a value normalized to the as-manufactured value.

ASME BPVC-III-5-2017, FORM MDS-1 MATERIAL DATA SHEET (SI UNITS)									
Thermal conductivity [.] (Section 2.39)									(36) Irradiation-induced change in thermal conductivity: This is expressed as a value normalized to the as-manufactured value. The temperature dependence of this property shall be determined.
GENERAL NOTES:									
(a) WG and AG refer to the with- and against-grain orientations of the material.									
(b) [.] indicates a dimensionless quantity.									
NOTE:									
(1) If the maximum intended use temperature exceeds 1,000 degrees C, then the temperature-dependent data shall be extended to cover the property values at the maximum intended use temperature.									

2.5. Maximum Grain Size

For isotropic graphite, the MDS guidance requests the mean particle size used in the mix formulation. The particle size distribution used in the manufacture of IG-110 is not publicly available. However, the manufacturer has indicated that the maximum coke particle size is 0.02 millimeters (mm) (20 micrometers (μm)). Kane et al. (2011), by using optical microscopy and digital analysis, found the mean graphite grain particle size to be 27 ± 2 μm. Also using optical microscopy and digital analysis, Huang et al. (2014) found the mean graphite grain particle size to be 43 μm. Assuming the manufacturer used a narrow particle size distribution, this variation is acceptable. Kane et al. (2011) also determined the aspect ratio of the graphitized coke grains to be 3.9 ± 0.2, while Huang et al. reported an aspect ratio of 3.4. Thus, it appears that the pulverizing and grinding techniques used on the coke grains before mixing and green compaction did not yield near-spherical coke particles. Some shrinkage occurs in the coke grains when transformed into graphite by the graphitization process, which may explain part of the discrepancy between the raw material data and the graphitized grain data. The amount of shrinkage depends on the characteristics of the coke, determined by its origin and calcination, and the graphitization temperature. However, such process details are generally proprietary and are not publicly available.

Ubic, 2009 showed the microstructure of IG-110 at different magnifications (Figure 2-1). In this figure, Panel (a) depicts a region showing graphitized filler, graphitized binder, and porosity. Panel (b) gives a magnified view of the highlighted region in Panel (a). Panel (c) depicts a graphite grain, with regions of shallow shrinkage cracks running along the grain. Panel (d) provides a dark-field micrograph of elongated filler particle.

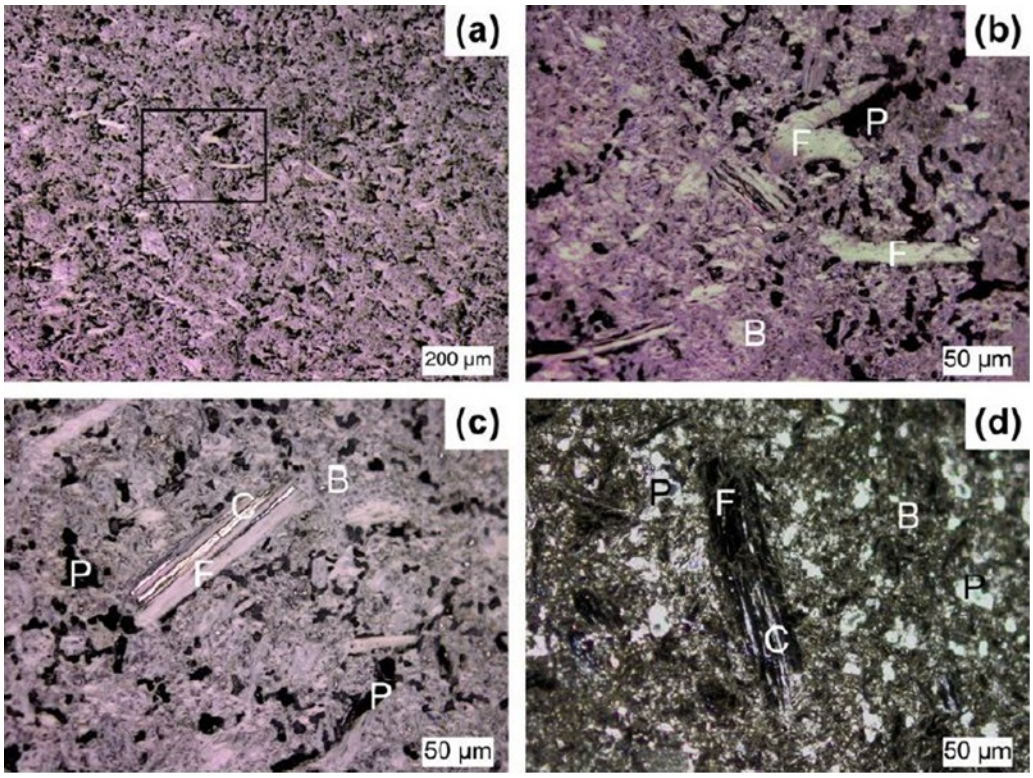

Figure 2-1 Optical micrographs of IG-110 graphite, P = Porosity, F = Filler, B = Binder, C = Shrinkage crack (Ubic, 2009)

The occurrence of the long “needle-type” graphite grain, F, is abnormal for this grade and could be due to contamination during mixing or inadequate sieving to obtain the desirable particle size distribution for optimum compaction. Such disparate flaws can affect the extreme values in properties; however, from the point of view of structural integrity, these anomalies would be captured by the statistical strength distribution, which is used in the ASME BPVC.

It is notable that the final graphitized product has a preferred orientation, even though the raw material filler coke is finely ground to as near a spherical shape as possible and equal pressure is applied along all directions during cold isostatic pressing. This preferred orientation of the graphite grains and pores causes the properties to vary in the two orthogonal directions.

2.6. Designation

The Mandatory Appendix HHA-I material specification defines “material designation.” As stated in Article HHA-I-1110, “Material Specifications,” the designation can be either ASTM D7219-08, “Standard Specification for Isotropic and Near-Isotropic Nuclear Graphites,” or ASTM D7301-08, “Standard Specification for Nuclear Graphite Suitable for Components Subjected to Low Neutron Irradiation Dose.” The designer enters the designation. Since most of the data available for this report pertain to ASTM D7219-08, that is the designation entered in Table 2-1.

Temperature-Dependent Parameters

2.7. Bulk Density

Although bulk density is designated as a temperature-dependent parameter in the MDS, its variation with temperature, if any, should be negligible. Typically, bulk density is measured by mensuration. ASTM Standard C559-90, "Standard Test Method for Bulk Density by Physical Measurements of Manufactured Carbon and Graphite Articles" (reapproved 2010), describes the ASTM method for measuring bulk density. Measured densities for IG-110 have varied between 1.77 and 1.93 megagrams per cubic meter (Mg/m^3). Carroll (2014) measured the density of 194 specimens and obtained a (Weibull) mean of 1.774 ± 0.015 Mg/m^3. The theoretical density of graphite is 2.266 Mg/m^3. However, Kane et al. (2011) calculated the theoretical density of IG-110, from lattice parameter determinations using x-ray diffraction, to be 2.257 Mg/m^3. Thus, about 16 percent of the volume of a bulk piece of graphite is open or closed pores. As stated in ASTM D7219-08, IG-110 belongs to the isomolded, isotropic, high-purity (IIHP) class. The ASTM standard requires a minimum bulk density of 1.7 Mg/m^3 for graphites in this class. IG-110 graphite meets this requirement.

2.8. Tensile Strength

ASTM Test Standard C749-08, "Standard Test Method for Tensile Stress-Strain of Carbon and Graphite," presents the ASTM method for determining the tensile strength of graphites. However, it is likely that many of the data currently available were not obtained by following this test standard. Both Toyo Tanso and the Japan Atomic Energy Research Institute (JAERI) have conducted considerable room-temperature testing to support the design and construction of the High-Temperature Engineering Test Reactor (HTTR). Data extraction for this report involved mining these data and data recently collected at Petten, the Netherlands, and at ORNL and INL in the United States.

Typically, room-temperature tests have been conducted at ambient conditions in oxygen-containing atmospheres and not in the helium environment expected under normal HTGR conditions. The majority of strength data under abnormal HTGR operating conditions of a steam oxidation environment have been measured closer to ambient temperatures than to expected HTGR operating temperatures. That said, high-temperature strength data are also available.

Table 2-2 contains some information on the room-temperature tensile strength from various tests. ASTM D7219-08 requires a minimum strength of 22 megapascals (MPa) for IIHP graphites and 20 MPa for isomolded, near-isotropic, high-purity (INHP) graphites. However, the specification does not state whether this is the minimum strength in a (designated) test population or a minimum average strength. In Table 2-2, the tests conducted at various times, with a statistically significant test population, provide an average strength that exceeds the ASTM specification requirement, except for the value of 16.7 MPa reported by Heijna et al. (2017), which was obtained using a diametric compression test and has not been corrected for tensile stress profile.

Table 2-2 Summary of Selected Room-Temperature Tensile Strength Data on IG-110 Graphite

No. of Tests	Room-Temperature Mean Tensile Strength (MPa)	Coefficient of Variation (COV, %)	Reference	Remarks
640	29.6	19.8	Sumita et al. (2006)	Conducted in cooperation with Toyo Tanso
640	29.6	5	Shibata et al. (2008)	
40	24.8 (A, AG)*	7.3	Arai et al. (1991a)	1981 test
40	24.0 (R, WG)*	15		
20	26.5 (A, AG)	9.4	Arai et al. (1991a)	1981 test
53	25.5 (A, AG)	7.1	Arai et al. (1991a)	1982 test
70	26.1 (A, AG)	7.3	Arai et al. (1991a)	1983 test
70	24.4 (R, WG)	10		
34	26.1 (A, AG)	7.3	Arai et al. (1991a)	1984 test
35	25.7 (R, WG)	8.6		
64	25.8 (A)	7.0	Arai et al. (1991a)	1986 test
65	25.6 (R, WG)	9.4		
25	27.8 (A, AG)	5.4	Arai et al. (1991a)	1989 test
64	25.8 (A, AG)	7.1	Arai et al. (1991b)	Mean obtained from tests from various locations in the billet
65	25.6 (R, WG)	9.6		
165	25.27 (R, WG)	12.9	Ishihara et al. (1987)	
80	24.4	11.9	Ishiyama et al. (1987)	
2	26	-	Kikuchi and Futakawa (1987)	
-	26.5	-	Eto et al. (1991)	
Unknown	25.3	-	Ishihara et al. (2004)	Used in HTTR design
362	25.3	9.6	Shibata et al. (2010)	JAEA HTGR draft code
Unknown	16.7	-	Heijna et al. (2017)	Tensile strength reported from diametral compression testing of

No. of Tests	Room-Temperature Mean Tensile Strength (MPa)	Coefficient of Variation (COV, %)	Reference	Remarks
				cylindrical specimens of circular cross section
Unknown	20	-	Homerin and Miller (2000)	
Unknown	25	-	Shibata (2013)	
-	24.9 (WG)	-	Eto et al. (1990)	
-	24.0 (AG)	-		
48	24.81*	9.3	Carroll (2014)	

*Weibull mean, obtained from two-parameter Weibull distribution data and parameters (ASTM C749-08 standard tensile test).

2.9. Temperature Dependence of Tensile Strength

The strength of graphite increases with test temperature, which is generally attributed to the increased density due to microcrack and pore closure resulting from thermal expansion of graphite crystallites. However, greater strength increase occurs in nonoxidizing atmospheres than in atmospheres containing oxygen or oxygen-steam.

Figure 2-2 shows the temperature dependence of tensile strength, as reported by the Japan Atomic Energy Agency (JAEA) draft code (Shibata et al., 2010). This behavior is typical for graphite of all grades, including those used in electric arc furnaces for melting of steel as electrodes (by far the largest commercial use of synthetic graphite). Shibata et al. (2010) have not provided any information on the test atmosphere; however, since there is no strength reduction at elevated temperatures, this report presumes that the testing was conducted in an inert gas atmosphere. The same figure shows data obtained by Eto et al. (1991) for tests conducted in a vacuum for up to 1,200 degrees C (2,192 degrees F) and the results obtained in room-temperature testing for both air and water atmospheres.

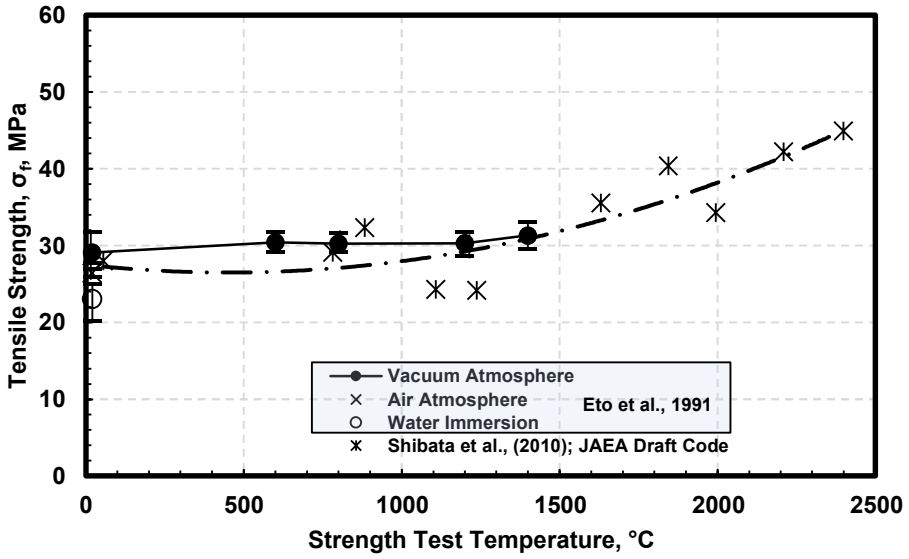

Figure 2-2 Temperature dependence of tensile strength of IG-110

Note that the test conducted in air shows that the room-temperature strength decreases by about 15 percent after immersion in water. The residence time in water before testing for strength was not reported. However, this observation is akin to the slow crack growth effect, which has been termed "static fatigue" in glass and high-performance oxide and nonoxide ceramics. Considering that fracture has occurred in graphite at substantially lower than the typical strength distribution, the potential for such static fatigue effects may need to be considered, especially in impure helium and moisture-containing atmospheres, even for reactor operation under normal conditions.

2.10. Flexural Strength (Four-Point)

ASTM Test Standard C651-11, "Standard Test Method for Flexural Strength of Manufactured Carbon and Graphite Articles Using Four-Point Loading at Room Temperature," presents the ASTM method for determining the tensile strength of graphites. However, it is likely that many of the data currently available were not obtained by following this test standard. Both Toyo Tanso and JAERI have conducted considerable room-temperature testing to support the design and construction of the HTTR.

Table 2-3 contains some information on the room-temperature flexural strength from various tests. ASTM D7219-08 requires a minimum strength of 35 MPa for IIHP graphites and 30 MPa for INHP graphites. However, the specification does not state whether this is the minimum strength in a (designated) test population or a minimum average strength. In Table 2-3, the tests conducted with statistically significant test populations show average strengths both lower and higher than the required ASTM D7219-08 value.

Table 2-3 Summary of Selected Room-Temperature Four-Point Flexural Strength for IG-110 Graphite

No. of Tests	Room-Temperature Mean Bend Strength (MPa)	Coefficient of Variation (COV, %)	Reference	Remarks
59	34.7 (A,† AG)	7.2	Arai et al. (1991a)	1981 test
80	32.8 (R,†† WG)	11		
40	39.0 (A, AG)	6.4	Arai et al. (1991a)	1981 test
70	39.7 (A, AG)	7.8	Arai et al. (1991a)	1983 test
70	39.3 (R, WG)	8.4		
30	33.6 (A, AG)	7.1	Arai et al. (1991a)	1986 test
30	34.4 (R, WG)	7.0		
30	33.6	7.3	Arai et al. (1991b)	Mean obtained from tests from various locations in the billet.
30	34.4	6.7		
-	39.2	-	Maruyama et al. (1995)	Bend test type not reported. Maximum grain size 30 μm; average grain size 10 μm.
Unknown	34 (A, AG)	5.3	Campbell and Katoh (2018)	
Unknown	36 (R, WG)	3.6		
Unknown	39	-	Shibata (2011)	
Unknown	37.5 (AG)	-	Matsuo et al. (1987)	Bend test type not reported.
	37 (WG)			

No. of Tests	Room-Temperature Mean Bend Strength (MPa)	Coefficient of Variation (COV, %)	Reference	Remarks
5	45.5	-	Kukuchi and Futakawa (1987)	Bend test type not reported.
-	39.6		Eto et al. (1991)	Bend test type not reported.
-	34.3 (WG)	-	Eto et al. (1990)	
-	32.8 (AG)			
90	35.60*	8.5	Carroll (2014)	*Weibull mean, obtained from two-parameter Weibull distribution data and parameters (ASTM C651-10 standard four-point bend test).

†A = axial direction. ††R = radial direction.

2.11. Temperature Dependence of Bend Strength

Thus far, the literature search conducted for this report has uncovered no data on the temperature dependence of the bend strength of IG-110. Such data could be important in determining the buckling strength of core support components and columns. Traditionally, it has been the practice to assume that the temperature-dependence factor is the same for both tensile strength and bend strength.

2.12. Compressive Strength

ASTM Test Standard C695-91, “Standard Test Method for Compressive Strength of Carbon and Graphite,” presents the ASTM method for determining the tensile strength of graphites. However, it is likely that many of the data currently available were not obtained by following this test standard. Both Toyo Tanso and JAERI have conducted considerable room-temperature testing to support the design and construction of the HTTR.

Table 2-4 contains information on the room-temperature compressive strength from various tests. ASTM D7219-08 requires a minimum strength of 65 MPa for IIHP graphites and 60 MPa for INHP graphites. However, the specification does not state whether this is the minimum strength in a (designated) test population or a minimum average strength. In Table 2-4, the tests conducted at various times, with statistically significant test populations, demonstrate that the average strength exceeds the ASTM specification requirement.

Table 2-4 Summary of Selected Room-Temperature Compressive Strength Data on IG-110 Graphite

No. of Tests	Room-Temperature Mean Compressive Strength (MPa)	Coefficient of Variation (COV, %)	Reference	Remarks
Unknown	80.1 (AG)	-	Matsuo et al. (1987)	Type of bend test not reported.
	76.1 (WG)			
80	69.6 (R, WG)	6.5	Arai et al. (1991a)	1981 test
40	83.8 (A, AG)	5.7		
54	80.9 (A, AG)	3.9	Arai et al. (1991a)	1982 test
70	79.0 (A, AG)	4.8	Arai et al. (1991a)	1983 test
70	78.9 (R, WG)	6.3		
31	78.5 (A, AG)	4.5	Arai et al. (1991a)	1986 test
31	76.3 (R, WG)	3.9		
31	77.9 (A, AG)	4.1	Arai et al. (1991b)	Mean obtained from tests from various locations in the billet.
31	76.4 (R, WG)	4.4		
-	83.8	-	Eto et al. (1991)	
Unknown	76.8	-	Ishihara et al. (2004)	Value used for HTTR design.
Unknown	77 (A, AG)	4.3	Campbell and Katoh (2018)	
Unknown	77 (R, WG)	2.7		
3[†]	76.8	-	Kim et al. (2010)	ASTM C695-91 [†]Even though the sample population is small, this datum was added because the testing followed ASTM methods and included high-temperature tests (Figure 2-3).
Unknown	78	-	Shibata (2011)	
5	86.4	-	Kukuchi and Futakawa (1987)	
Unknown	82.6	2.9	Shibata et al. (2008)	
373	76.9	8.3	Shibata et al. (2010)	JAEA HTGR draft code
5	86.4	-	Kukuchi and Futakawa (1987)	
-	76.8	-	Shibata (2013)	
-	69.6 (AG)	-	Oku et al. (1990)	

-	73.4 (WG)	-		
89	74.02*	5	Carroll (2014)	* Weibull mean, obtained from two-parameter Weibull distribution data and parameters (ASTM C695-91 standard compression test).

2.13. Temperature Dependence of Compressive Strength

Figure 2-3 (Kim et al., 2010) shows the temperature dependence of compressive strength. Kim et al. (2010) did not specify the atmosphere used for testing; however, from the information provided on the test apparatus and the significant decrease observed in the strength, this report concludes that the testing was conducted in ambient air, and that the strength reduction is due to the oxidation of graphite at elevated temperatures. Even though the sample population was small, these data are included because the testing followed the ASTM C695-91 method.

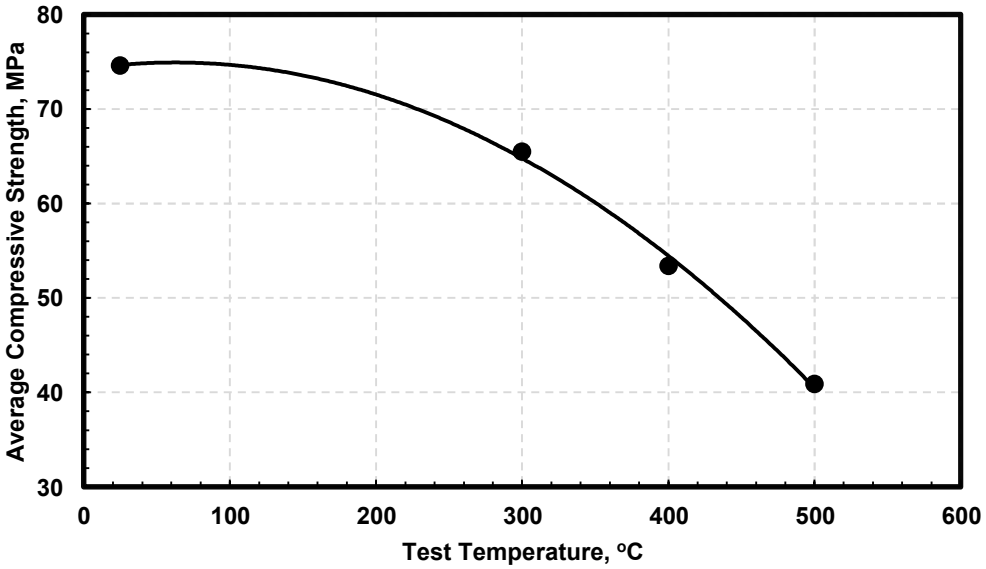

Figure 2-3 Temperature dependence of compressive strength of IG-110 in ambient air atmosphere (Kim et al., 2010)

Ishihara et al. (2004) provided data on the effect of oxidation on the room-temperature tensile and compressive strength of IG-110 graphite. The oxidation conditions were not published in Ishihara et al. (2004). Interestingly, when the data are analyzed in terms of the ratio of oxidized strength to nonoxidized strength as a function of temperature, the strength behavior is identical for tensile strength and compressive strength. Figure 2-4 shows this behavior.

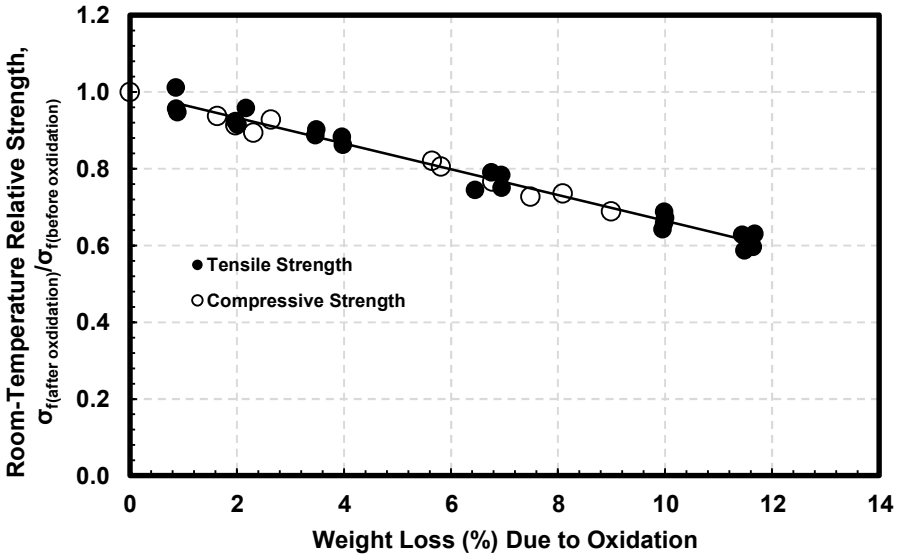

Figure 2-4 Effect of oxidation on the room-temperature strength of IG-110 (Ishihara et al., 2004)

2.14. Elastic Modulus (Dynamic)

ASTM Test Standard C769-09, "Standard Test Method for Sonic Velocity in Manufactured Carbon and Graphite Materials for Use in Obtaining Young's Modulus," presents the ASTM method for determining the dynamic elastic modulus (DYM) of graphites. However, it is likely that many of the data currently available were not obtained by following this test standard. Both Toyo Tanso and JAERI have conducted considerable room-temperature testing to support the design and construction of the HTTR. As stated in the ASTM standard, for both IIHP and INHP graphite classes, the DYM should be less than 15 gigapascals (GPa) in the with-grain (WG) direction and greater than 8 GPa in the against-grain (AG) direction. Table 2-5 lists the DYM values reported by several researchers.

2.15. Elastic Modulus (Static)

The JAEA draft code uses a room-temperature static modulus value of 9.9, which is obtained from the slope of the initial ("linear") portion of the nonlinear stress-strain curve of IG-110.

The intrinsic and fundamental properties that govern the elastic moduli, strength, thermal diffusivity (thermal conductivity), and coefficient of thermal expansion (CTE) of graphite are its porosity (or, more specifically, the fraction of porosity and the pore size distribution) and the pore morphology, which includes the size, shape, and orientation of the major axis. Generally, experimentally determined properties are reported as a function of porosity. For example, Maruyama et al. (1995) reported the porosity dependence of Young's modulus, as shown in Figure 2-5. Here, the factor 1.9 depends on pore morphology; the factor would exceed 1.9 for anisotropic graphites. Maruyama et al. believe that because IG-110 consists of relatively fine

grains, pore size is relatively small and, perhaps, the pores are more spherical in shape; thus the value is closer to 2.

Table 2-5 Summary of Selected Room-Temperature Dynamic Young's Modulus Data on IG-110 Graphite

No. of Tests	Room-Temperature Mean DYM (GPa)	Coefficient of Variation (COV, %)	Reference	Remarks
Unknown	10.1 (AG)	-	Matsuo et al. (1987)	
	10.5 (WG)	-		
14	9.32 (A, AG)	5.8	Arai et al. (1991b)	Mean obtained from tests from various locations in the billet.
14	9.65 (R, WG)	4.8		
-	11.4	-	Maruyama et al. (1995)	
Unknown	9.1	2.5	Campbell and Katoh (2018)	
	9.7	2.2		
>50	10.89 (AG)	2.15	Windes et al. (2013a)	
>50	10.17 (WG)	3.52		
-	19.5 (AG)	3.85	Windes et al. (2017b)	DYM values are unusually high.
-	18.23 (WG)	4.06		
-	11.2 (AG)	3.97	Windes et al. (2013b)	
-	10.81 (WG)	3.08		
-	10.3	-	Kikuchi and Futakawa (1987)	
-	9.53	-	Eto et al. (1991)	HTTR IG-110
90	9.26*	5.7	Carroll (2014)	Sonic resonance technique ASTM C747-93; *Weibull mean, obtained from two-parameter Weibull distribution data and parameters.

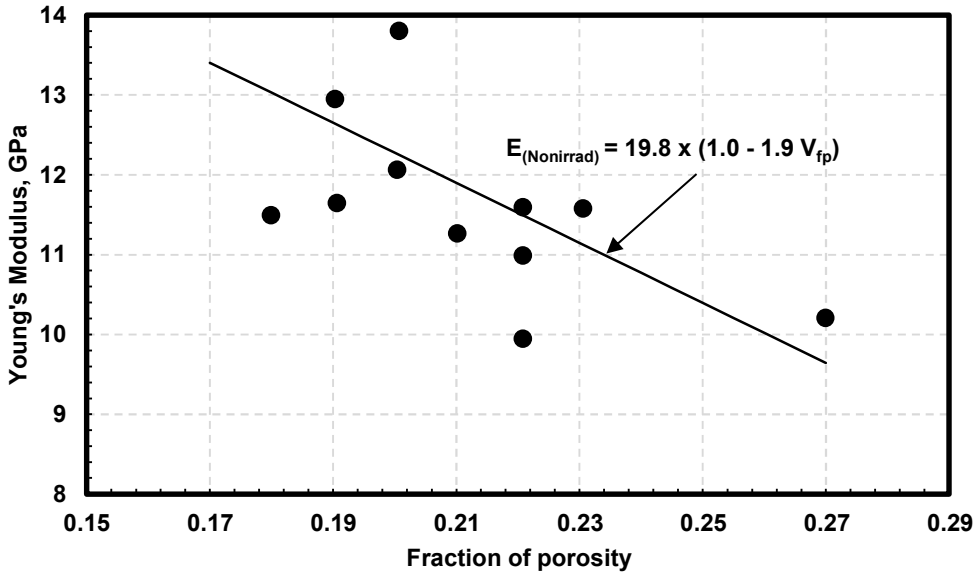

Figure 2-5 Density dependence of Young's modulus for IG-110 (Maruyama et al., 1995)

2.16. Temperature Dependence of Young's Modulus

Figure 2-6 shows the design data used for the HTTR in Japan; however, the draft code (Shibata et al., 2010) does not provide information on the method used to determine Young's modulus. The original data were also plotted in a normalized form, as E/E_o versus temperature, where E_o was the elastic modulus at room temperature and E the longitudinal elastic modulus at high temperatures. This report uses an average of 10 MPa (for both directions) for the room-temperature value, since the code does not mention whether the data represented WG or AG orientation. As the pores close because of thermal expansion at higher temperatures, the density increases and thus the Young's modulus also increases. The curve fit line falls on the same data, as published by Eto et al. (1991), who determined the modulus at high temperatures using the dynamic Young's modulus (time of transit, DYM) in a vacuum atmosphere.

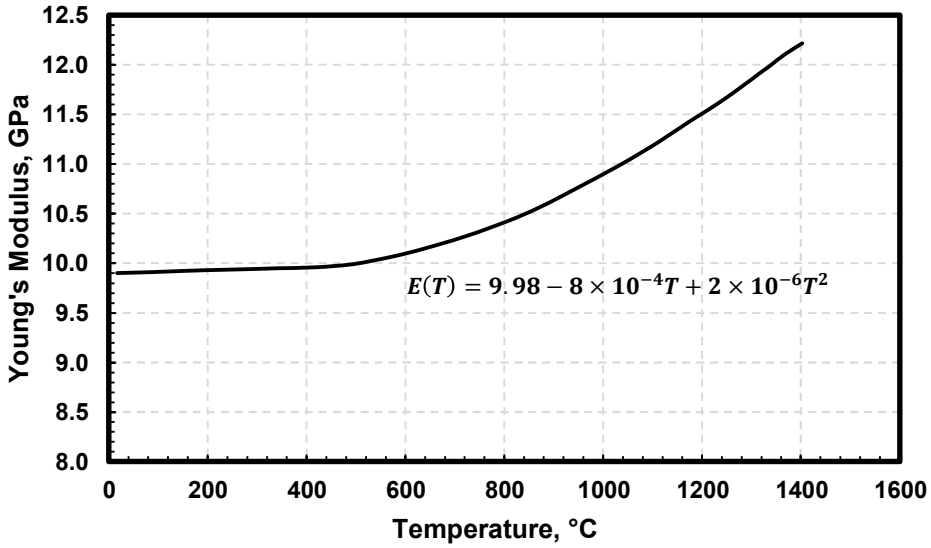

Figure 2-6 Temperature dependence of Young's modulus for IG-110 (Shibata et al., 2010)

2.17. Coefficient of Thermal Expansion

ASTM E228-06, "Standard Test Method for Linear Thermal Expansion of Solid Materials with a Push-Rod Dilatometer," presents the ASTM method for determining the CTE,[1] β, of graphites. However, it is likely that many of the data currently available were not obtained by following this test standard. Both Toyo Tanso and JAERI have conducted considerable room-temperature and high-temperature CTE testing to support the design and construction of the HTTR. Various other researchers have measured the CTE over the last 30 years. As stated in the ASTM standard, for IIHP and INHP graphite classes, the CTE value in the WG direction should range from 3.5×10^{-6}/degree C to 6.0×10^{-6}/degree C for the temperature range of 25–500 degrees C (77–932 degrees F). The values in Table 2-6 indicate that this requirement is easily satisfied for IG-110.

[1] This report uses the symbol β for CTE, rather than α as found in most literature, to be consistent with the notation typical in the heat transfer literature. See Favre-Marinet and Tardu (2009).

Table 2-6 Summary of Selected CTE Data for IG-110 Graphite

No. of Tests	Mean CTE, x 10^{-6}/°C	Coefficient of Variation (COV, %)	Reference	Remarks
-	5.1	-	Homerin and Miller (2002)	
-	4.06	-	Shibata (2013), Shibata et al. (2010)	25–400 °C; value used in the JAEA draft code.
-	4.50 (AG)	0.9	Campbell and Katoh (2018)	Measured at 500 °C.
-	4.2 (WG)	2.6		
-	⩽4.5	-	Yu and Sun (2010)	
10	4.16 (AG)	4.3	Arai et al. (1991b)	Mean obtained from tests from various locations in the billet.
10	4.03 (WG)	4.5		
-	4.61 (AG)	-	Matsuo et al. (1987)	
	4.42 (WG)			
-	4.06	-	Ishihara et al. (2004)	25–400 °C
-	3.82	1.6	Windes et al. (2013b)	Measured at 100 °C.
-	3.88	2.5		
-	3.75–4.1	-	Swank et al. (2010)	
-	4.41	-	Heijna et al. (2017)	

2.18. Temperature Dependence of the Coefficient of Thermal Expansion for Nonirradiated IG-110

Figure 2-7 shows the CTE of nonirradiated IG-110 graphite obtained by three different organizations. The original data of these authors have been extracted and fitted to the relationships shown, from which the lines have been drawn. The values appear to be reasonably consistent across all three investigations.

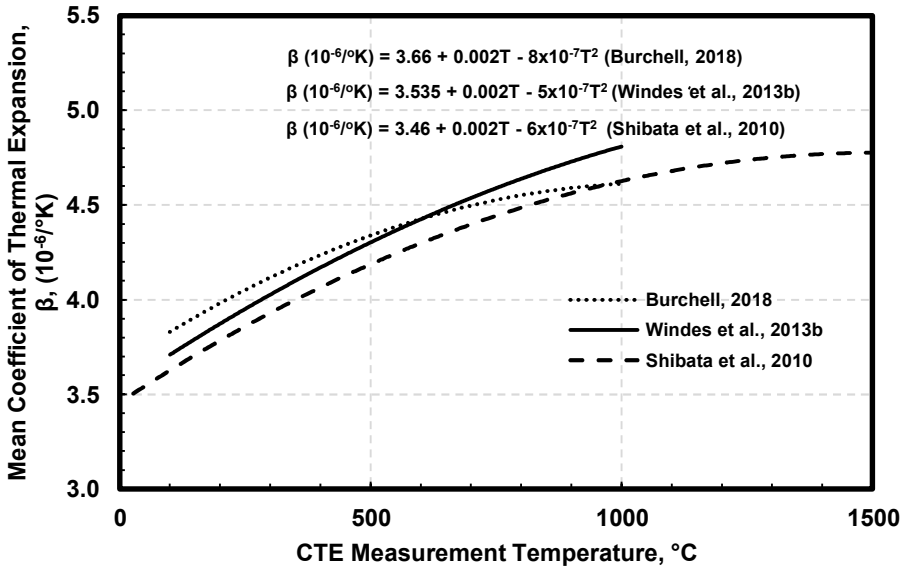

Figure 2-7 The temperature dependence of CTE for nonirradiated IG-110 graphite

Zhou et al. (2011) made some interesting observations about changes in CTE resulting from an applied stress. As shown in Figure 2-8, they cut vertical (V) and radial (R) cylindrical specimens from an IG-110 block installed in the HTR-10 reactor in China.

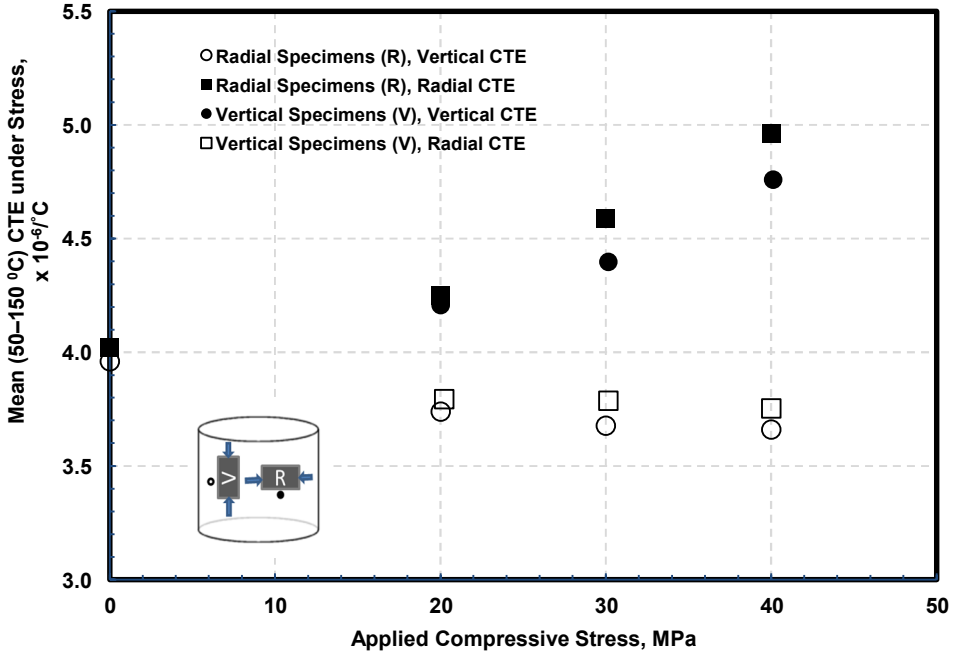

Figure 2-8 CTE anisotropy in IG-110 graphite installed per HTR-10 reactor configuration (based on Zhou et al., 2011)

Zhou et al. (2011) did not provide any information on the compacting direction in graphite processing or subsequent microscopy analysis to delineate the WG and AG orientations. Applying strain gauges in the two orthogonal directions of the sample, they measured the thermal expansion between 50 degrees C (122 degrees F) and 150 degrees C (302 degrees F), under varying loads at 20, 30, and 40 MPa. Figure 2-9 shows their CTE results. Because there are no microscopy data, it is difficult to understand the significance of these results. When they are analyzed in terms of maintaining the CTE anisotropy under load, it appears that the CTE isotropy change with load varies with the orientation of the sample corresponding to the direction of installation in the reactor.

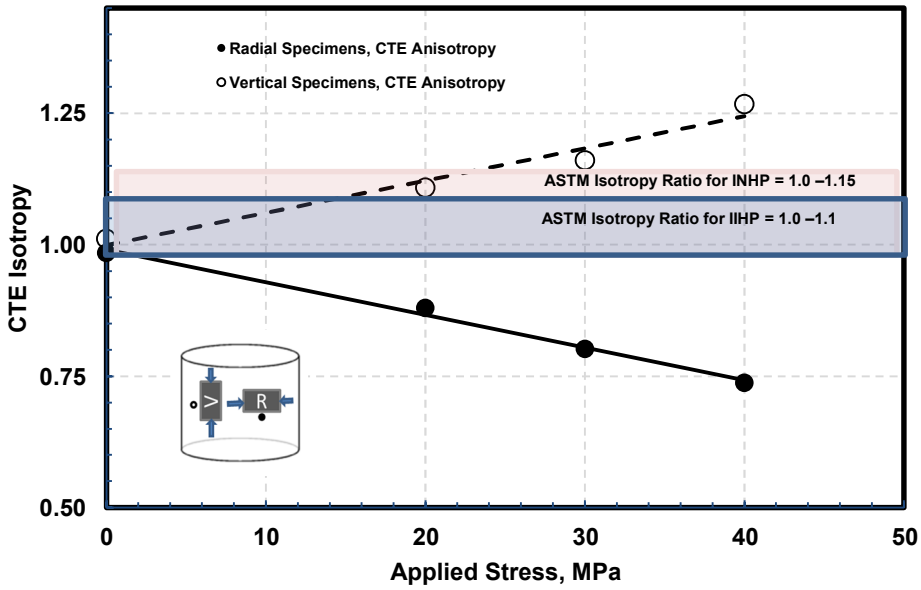

Figure 2-9 Change in CTE anisotropy with load for vertically and radially oriented specimens within an installed block (based on Zhou et al., 2011)

The deviations from the nonstressed anisotropy are rather immediate: positive deviation occurs for the vertically oriented specimens, and negative deviation occurs for the radially oriented specimens. Although these phenomena are yet to be understood with respect to the grain (and porosity) orientation, the results indicate that differential CTE in the two directions is possible under stress, which could have design implications. Since these results are only for temperatures up to 150 degrees C (302 degrees F), it may be important to conduct experiments at higher temperatures to establish the CTE behavior under load.

2.19. Thermal Conductivity

The thermal conductivity of graphite is an important factor in the safe operation of HTRs, under both normal and accident conditions (International Atomic Energy Agency, 2003). For reactors with annular core designs, the peak fuel temperature in depressurized accident scenarios (for a given total core power and vessel size) is lower than it is for a cylindrical active core. Peak fuel temperatures can be reduced by increasing the core graphite conductivity. Irradiation significantly decreases graphite thermal conductivity, but at high temperatures, the core graphite

anneals, so that its conductivity effectively increases with increasing temperature. In an accident scenario, at very high temperatures, radiation (T^4) effects tend to become the dominating heat transfer mechanism and overtake the conduction mechanism for both prismatic and pebble cores.

Lessons learned from Arbeitsgemeinschaft Versuchsreaktor operation have resulted in better fuel management in modern PBMR designs (Boer, 2008). For example, the designs of the HTR-PM and the South African PBMR include inner and outer graphite reflectors. The inner reflector prevents a power peak at the center of the pebble-bed. It also adds to the thermal capacity of the core, which is beneficial during accidents.

Thermal conductivity (k) is usually a derived property for nuclear graphites. It is typically calculated from the density of the sample and the thermal diffusivity, which is measured using a laser flash technique. Thermal conductivity is crucial to the passive removal of decay heat. It influences the heat-removal rate and peak temperature of the core, which, in turn, influence the fuel temperature during off-normal events.

ASTM E1461-07, "Standard Test Method for Thermal Diffusivity by the Flash Method," presents the ASTM method for determining thermal diffusivity. The thermal conductivity is calculated using the following expression:

$$k = \alpha\, C_p\, \rho,$$

where α is the thermal diffusivity, C_p is the specific heat, and ρ is the density of the specimen.

It is likely that many of the data currently available were not obtained by following the ASTM test standard. Both Toyo Tanso and JAERI have conducted considerable room-temperature and high-temperature laser diffusivity measurements to support the design and construction of the HTTR. Various other researchers have also measured the thermal conductivity of IG-110 over the last 30 years. As stated in the ASTM standard, the room-temperature thermal conductivity in the WG direction should have a minimum value of 90 watts per meter-Kelvin (W/m-°K) for the IIHP graphite class, and 80 W/m-°K for the INHP graphite classes. The values in Table 2-7 indicate that some investigators found that IG-110 did not satisfy this requirement.

Table 2-7 Summary of Selected Room-Temperature Thermal Conductivity Data on IG-110 Graphite

No. of Tests	Mean Room-Temperature Thermal Conductivity, k, W/m°K	Coefficient of Variation (COV, %)	Reference	Remarks
-	129 (AG)	5.6	Campbell and Katoh (2018)	
-	130 (WG)	2.8		
-	80	-	Ishihara et al. (2004); Shibata (2013)	Value at 325 °C.
	81.4	-	Shibata et al. (2010)	Value at 400 °C.
	68.1	-	Heijna et al. (2017)	This value is considerably lower than the ASTM requirement.
	123 (AG)	-	Matsuo et al. (1987)	
	131 (WG)	-		
14	77.5 (AG)	5.9	Arai et al. (1991b)	Mean obtained from tests from various locations in the billet.
14	79.1 (WG)	4.9		

2.20. Temperature Dependence of Thermal Conductivity

Figure 2-10 shows the dependence of the thermal conductivity, *k*, of nonirradiated IG-110 graphite on temperature. The data represented by closed circles are from Windes et al. (2013b). The data shown in open circles are calculations made for this work, using the Windes et al. data, assuming that the density remains constant and using temperature-dependent specific heat data from ASTM Standard Procedure C-781-08, "Standard Practice for Testing Graphite and Boronated Graphite Materials for High-Temperature Gas-Cooled Nuclear Reactor Components," and in accordance with McEligot et al. (2016). Although the diffusivity data can be adequately represented using a power-law relationship with temperature, the thermal conductivity data seem to be better represented by a polynomial fit with the temperature.

For calculating thermal conductivity, this report assumes that the density remains invariant with temperature. For the temperature dependence of specific heat, the following equation was derived from the representation in McEligot et al. (2016):

$$C_p(J/kgK) = 642.72 + 2.8674T - 2.3x10^{-3}T^2 + 7x10^{-7}T^3.$$

El-Genk et al. (2012) and Travis and El-Genk (2013) have used thermal conductivity data that are significantly different from these measurements in their analytical work to understand heat transfer in coolant channels in a very-high-temperature reactor (VHTR). Their thermal

conductivity data seem to differ substantially from those of others, as shown in Figure 2-11, and appear to be far too high for a polycrystalline graphite.

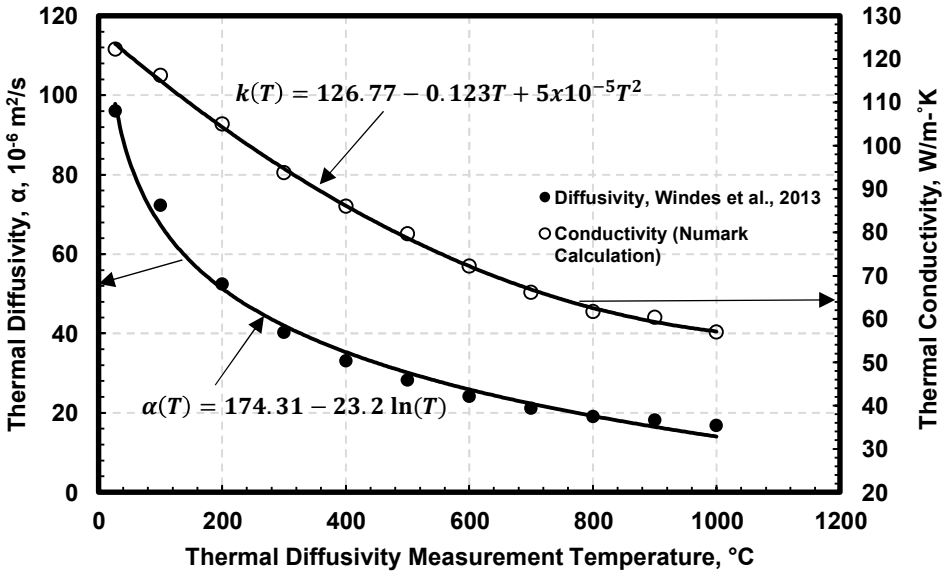

Figure 2-10 Temperature dependence of thermal diffusivity and thermal conductivity for IG-110 graphite (Windes et al., 2013b)

However, below about 1,000 degrees C (1,832 degrees F), thermal conductivity values vary considerably between laboratories. Differences in the test material due to billet-to-billet and within-billet variations, as well as measurement practices, could explain this variation. However, above 1,000 degrees C (1,832 degrees F), the values essentially converge.

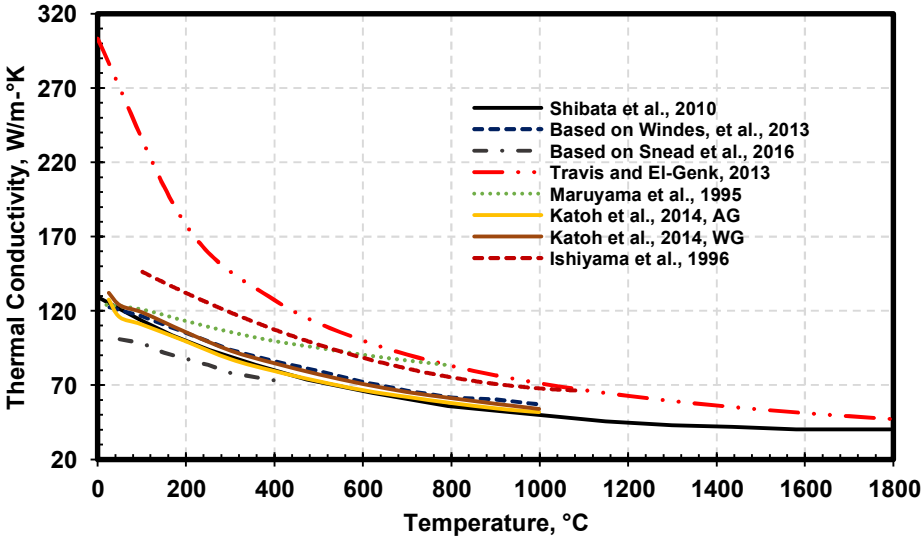

Figure 2-11 Temperature dependence of thermal conductivity of nonirradiated IG-110

Temperature-Independent Parameters

2.21. Poisson's Ratio

The ASTM materials specification standards do not specify any requirements for Poisson's ratio for nuclear-grade graphite for either low- or high-dose applications in an HTR.

Poisson's ratio can be measured statically during a tensile test using strain gauges placed in orthogonal directions. Poisson's ratio can also be determined from sonic resonance measurements using longitudinal vibrations for Young's modulus, E, and torsional vibrations for shear modulus, G, through the relationship $\nu = (E/2G) - 1$. For the NGNP materials characterization research, Carroll (2014) measured fundamental resonant frequency, specimen dimensions, and mass and calculated the dynamic Young's modulus, shear modulus, and Poisson's ratio in accordance with ASTM C747-93, "Standard Test Method for Moduli of Elasticity and Fundamental Frequencies of Carbon and Graphite Materials by Sonic Resonance" (reapproved 2010), in combination with apparatus and calculations described in ASTM C1259-08, "Standard Test Method for Dynamic Young's Modulus, Shear Modulus, and Poisson's Ratio for Advanced Ceramics by Impulse Excitation of Vibration." Table 2-8 lists the values of Poisson's ratio determined by several investigators.

2.22. Anisotropy Factor

Section 3.2.11 of the ASTM Nuclear Graphite Materials Specification defines this factor. For isotropic and near-isotropic nuclear graphite, as stated in ASTM D7219-08 the isotropy ratio is based on the CTE, which should be between 1.00 and 1.10. This ratio is the numerical value of the CTE determined in the AG orientation divided by the value determined in the WG orientation. The ASME BPVC refers to this ratio as the anisotropy factor. The anisotropy factor for IG-110, as reported by various researchers and shown in Table 2-9, generally meets the requirements of the ASME BPVC, including the ASME specifications for nuclear-grade graphites.

Although the ASME BPVC MDS lists the anisotropy factor as a temperature-independent parameter, it is in fact temperature dependent.

2.23. Temperature Dependence of Anisotropy Factor

Because of potential partial or complete closure of micropores, the density of graphite increases with temperature, with slightly more contraction in the AG direction. This leads to a slight change in the CTE anisotropy factor, as shown in Figure 2-12.

Table 2-8 Summary of Selected Room-Temperature Poisson's Ratio Data on IG-110 Graphite

No. of Tests	Room-Temperature Poisson's Ratio	Coefficient of Variation (COV, %)	Reference	Remarks
-	0.138	-	Carroll (2014)	Above the mean value, represented by 63.2% probability of occurrence, in a Weibull statistical plot of data obtained using sonic method.
-	0.3	-	Gao et al. (2016)	This value is rather high for graphite.
-	0.14	-	Munk (2013)	
-	0.14	-	Shibata et al. (2010)	JAEA draft code; irradiation creep Poisson's ratio = 0.30.
-	0.209	-	Carroll (2014)	Calculated from the Weibull scale parameters from ASTM C747-93 modulus measurements in flexural and torsional modes.

Table 2-9 Summary of Selected Room-Temperature CTE Anisotropy Factors for IG-110 Graphite

No. of Tests	Room-Temperature Anisotropy Factor	Coefficient of Variation (COV, %)	Reference	Remarks
-	1.057	-	Campbell and Katoh (2018)	
-	1.009	-	Windes et al. (2013b)	
-	<1.10	-	Shibata et al. (2010)	Used for design.
-	⩽1.15	-		Lot average.
10	1.04	-	Arai et al. (1991b)	Obtained from tests from various locations in the billet.

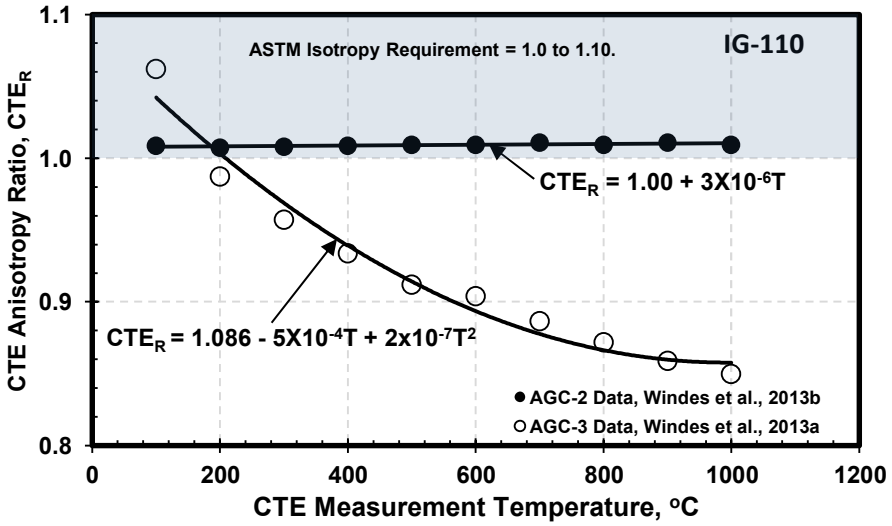

Figure 2-12 Temperature dependence of the anisotropy factor for near-isotropic IG-110 graphite

Windes et al. did not offer a reason for the discrepancy between the two sets of data shown in Figure 2-12. These results appear to contradict expected microstructural behavior. As temperature increases, Mrozowski cracks close, and the influence of the crystal CTE in the c-direction (AG) on the bulk CTE increases. Thus, if there were any changes at all, the CTE would be expected to rise, probably more in the AG direction, leading to an increase in the anisotropy factor with temperature. The data obtained from Advanced Graphite Capsule (AGC)-3 experiments indicate that at higher temperatures, IG-110 graphite is unlikely to meet the ASTM isotropy requirement. For this report, the authors have performed their own analysis of the data and identified the best-fit equation providing the lowest R^2 value.

2.24. Critical Stress Intensity Factor, K_{Ic}

In ceramics and graphite, the room-temperature critical stress intensity factor, K_{Ic}, also known as fracture toughness, is usually determined using rectangular beam specimens containing a center notch of precise geometry and depth and tested under either three-point or four-point bending. ASTM D7779-11, "Standard Test Method for Determination of Fracture Toughness at Ambient Temperature," presents the ASTM method for determining fracture toughness.

Several researchers have determined the fracture toughness of IG-110 graphite to be between 0.82 and 1.27 megapascal square root meters (MPa $\sqrt{m}$) (Oku et al., 1988; Takahashi et al., 2001; Burchell et al., 2017; Kim et al., 2008; Burchell et al., 1990; Romanoski and Burchell, 1991 and 1999; Ishiyama et al., 1991). Chi (2016) obtained an average value of 0.77 at room temperature for IG-110 with two different specimen depths in three-point single-edge notched beam (SENB) tests. Burchell et al. (2017) noted the absence of fracture toughness requirements in the current ASTM material specification for nuclear graphite and proposed a minimum value of 0.98 MPa $\sqrt{m}$, which they derived by subtracting three standard deviations from the mean value obtained from measurements of several nuclear-grade graphites.

ASME BPVC-III-5, Article HHA-3100, "General Design," states, "The Designer is required to evaluate the effects of cracking of individual Graphite Core Components in the course of the design of the Graphite Core Assembly and ensure that the assembly is damage tolerant." The fracture toughness formulations have largely used linear elastic fracture mechanics theory and modeling. Numark Associates Inc., in its assessment of Subsection HH, Subpart A, recommended the topic of damage tolerance, as described in HHA-3100, for further review by the NRC staff. Srinivasan (2017, 2018a, 2018b) had previously developed a nonlinearly elastic model, particularly applicable to graphites, which also takes into account the effect of fracture surface roughness on the behavior of the strain energy release rate as the crack propagates. This model more clearly differentiates the crack propagation behavior according to the graphite grain size. The total energy spent for fracture comprises the energy required to initiate a crack and the energy required to propagate the crack through the structure. For fine-grained graphites, such as IG-110, the crack initiation energy is the larger component; once a crack initiates, it may propagate catastrophically with relative ease. As grain size increases, the crack initiation energy becomes a smaller part of the total energy. This implies that "crack management" or management of degradation may be more feasible. Further study of such considerations would be useful in developing quantitative information on damage tolerance.

At present, it is a top priority in the United Kingdom to establish a better understanding of crack growth and arrest, in order to safely extend the operational life of several AGRs. The application of such low values of K_{Ic} (~1 MPa $\sqrt{m}$) for analysis is problematic. Tomographic analysis of graphite (Hodgkins et al., 2006) certainly shows microcracks forming and coalescing into macrocracks before failure, as well as crack bridging and crack arresting in pores. Tortuosity caused by the microstructure is also evident. Srinivasan (2018c) also observed these crack propagation mechanisms.

Although the ASME BPVC MDS lists fracture toughness as a temperature-independent parameter, it is in fact temperature dependent.

2.25. Temperature Dependence of Fracture Toughness of IG-110

The fracture toughness of graphite generally increases with temperature, which is consistent with the increase in density and the concomitant increase in strength. The reason is that increasing temperature may result in partial or complete closure of micropores and microcracks within graphite grains. Figure 2-13 shows an example, based on the research of Kim et al. (2008). Samples were preoxidized and tested in flowing nitrogen.

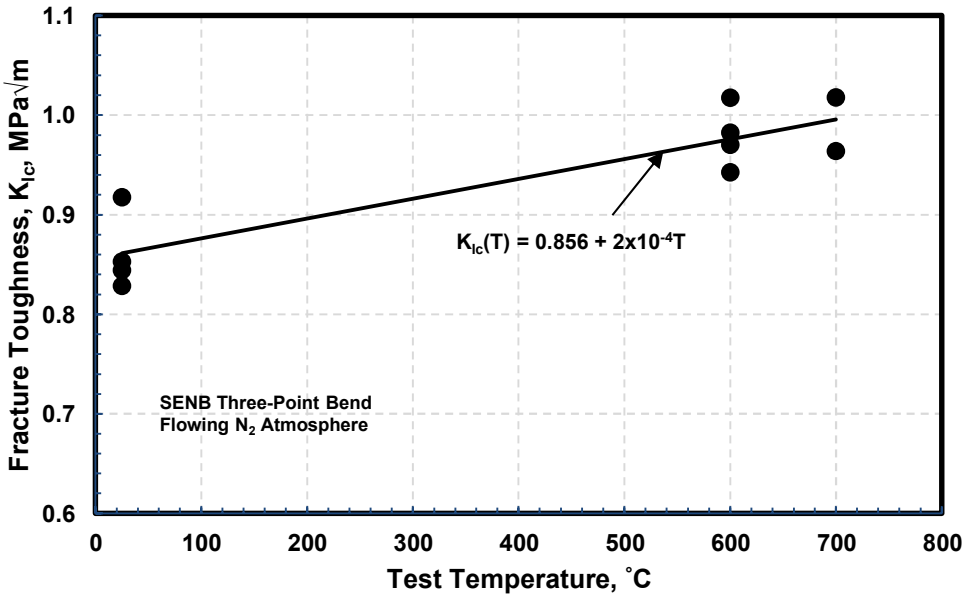

Figure 2-13 Temperature dependence of fracture toughness for IG-110 graphite (Kim et al., 2008)

2.26. Graphite Oxidation Effects

Oxidation of graphite is a well-known and well-understood phenomenon. In addition, because of the absence of zirconium alloy cladding, there is no zirconium-water reaction producing hydrogen to exacerbate accident consequences. Perhaps the main concern about oxidation in a graphite-moderated HTR arises from the “chronic” mechanism, which will be discussed below.

As stated in ASME BPVC-III-5, HHA-3141, “Oxidation,” the designer needs to conduct detailed oxidation analyses to estimate the weight loss profiles of graphite structures, since reaction rates depend on the temperature, reactants, and graphite grade. Oxidation modifies the pore structure because of the loss of graphitic carbon as it is oxidized away, increasing porosity. Thus, the density of the graphite decreases, with a concomitant decrease in both strength and fracture toughness.

Figure 2-14 shows the decrease in compressive strength for IG-110 graphite. Here, σ_ρ represents the compressive strength for samples having bulk density ρ, and σ_0 is the initial compressive strength of the unoxidized IG-110. The decrease in density due to oxidation is represented by a change in bulk density ($\Delta\rho$). The original data of Chi (2009) showed an exponential relationship with the density change. Figure 2-14 also shows the results of Ishihara et al. (2004) on the effects of oxidation on the compressive strength. The trendline fit of the data from Ishihara et al. (2004) in Figure 2-14 was calculated by Oh et al. (2011). As can be seen, Chi's work shows a more rapid drop in strength. Oxidation conditions were not reported. Park and No (2010) conducted compression tests after oxidation at 500 degrees C (932 degrees F) and 600 degrees C (1,112 degrees F) in dry air and found a similar decrease in strength, as shown.

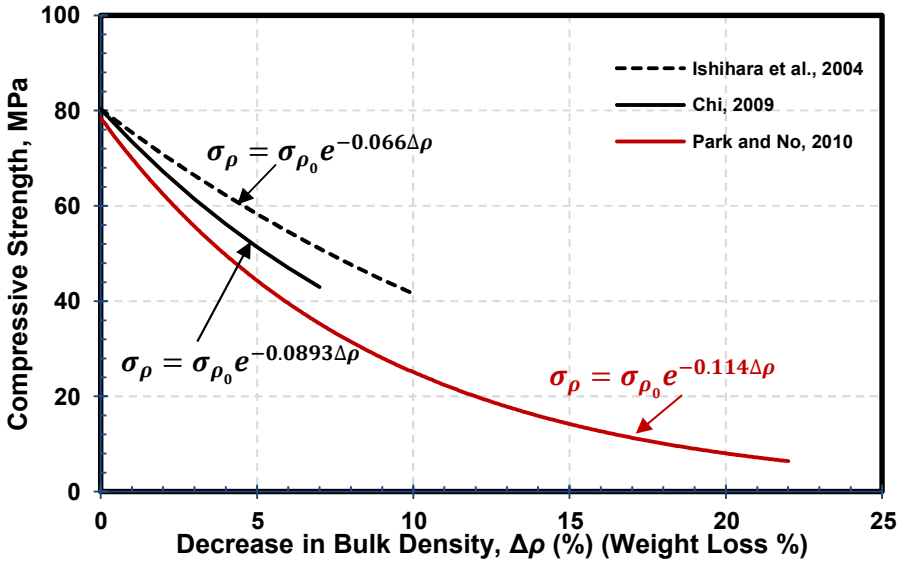

Figure 2-14 Loss in compressive strength for IG-110 graphite due to decrease in density (weight loss) as a result of oxidation

Figure 2-15 shows the loss in tensile strength due to oxidation, based on the results of Ishihara et al. (2004).

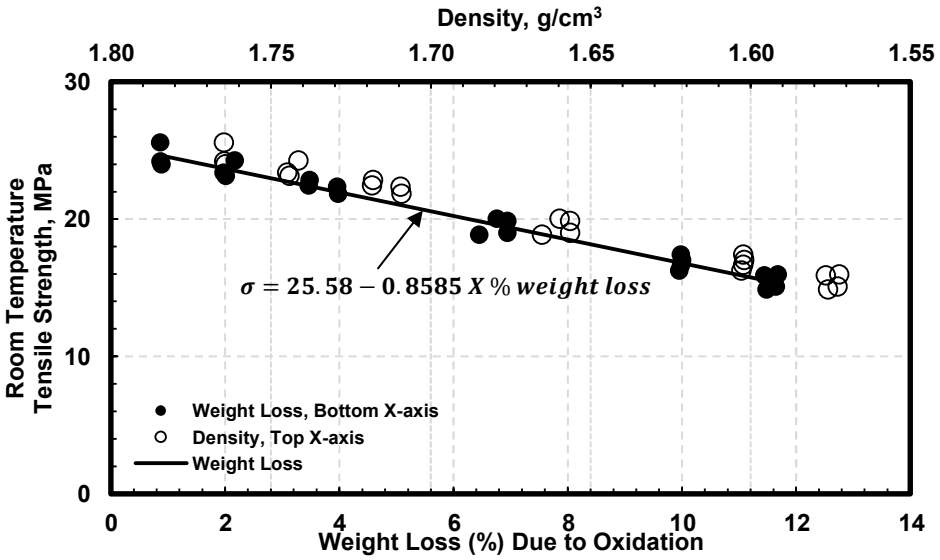

Figure 2-15 Oxidative loss of room-temperature tensile strength for IG-110 (based on Ishihara et al., 2004)

Figure 2-16 shows the effect of oxidation on the fracture toughness of IG-110. Samples were preoxidized and tested in flowing nitrogen.

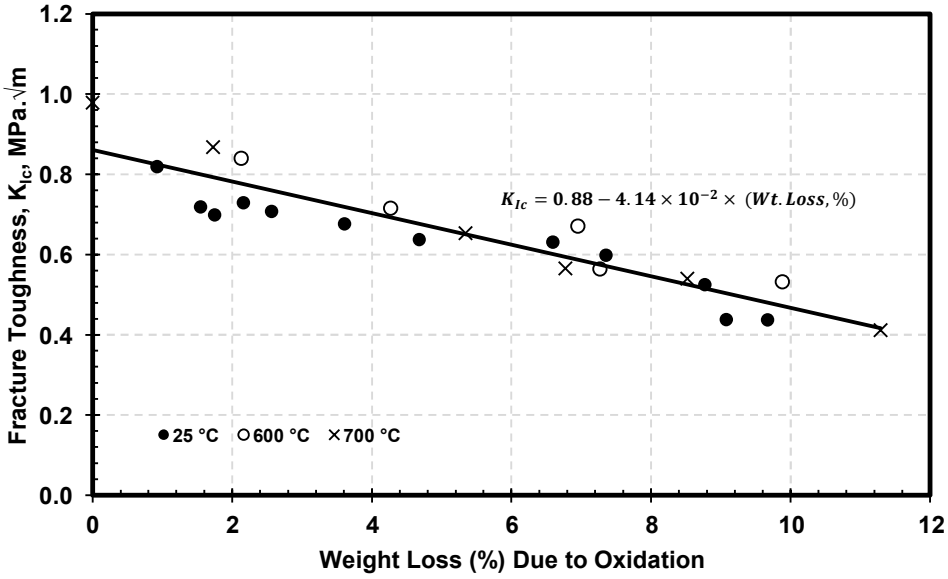

Figure 2-16 Effect of oxidative weight loss on the fracture toughness of IG-110 (Kim et al., 2008)

The specimens were oxidized at 600 degrees C (1,112 degrees F) and 700 degrees C (1,292 degrees F) for the respective weight losses shown as data points. Within the limited test population and the expected data scatter caused by variability in pore structure due to oxidation, the combined data indicate a linear pattern of decrease with weight loss due to oxidation, regardless of how that weight loss was achieved (that is, independent of oxidation temperature).

ASME BPVC-III-5, HHA-3141(d), requires consideration of large-scale oxidation resulting from accidental air or water ingress occurring over a short time scale. Eto et al. (1987) conducted substantial testing of IG-110 graphite for oxidative weight loss by exposure to 0.65-volume-percent water vapor in helium (sometimes referred to as water gas) at 900 degrees C (1,652 degrees F) and 1,200 degrees C (2,192 degrees F). Such experiments can provide useful data on moisture intrusion, showing how oxidative weight loss during accidents can affect component strength, particularly for columns and posts. Figure 2-17 shows a portion of the results from Eto et al. (1987). The shaded area at the top right in Figure 2-17 represents substantial degradation that occurs within about 0.2 centimeters (cm) from the surface; thus, the reaction cannot be considered a “skin effect.” In fact, it proceeds deeper into the specimen, although the majority of material loss occurs within about 0.2 cm from the surface, where the chemical reaction (kinetics) is most severe.

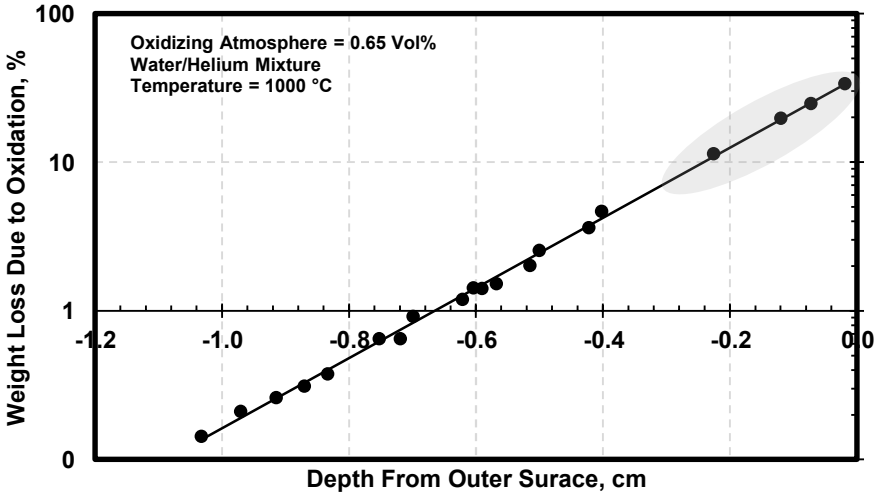

Figure 2-17 Oxidation weight loss in steam-coolant gas mixture for IG-110 (Eto et al., 1987)

Chi and Kim (2008) have conducted a detailed oxidation study on several nuclear-grade graphites, using the method of ASTM D7542-09, “Standard Test Method for Oxidation Rate and Threshold Oxidation Temperature for Manufactured Carbon and Graphite in Air,” with a minimum gas flow rate of 10 liters per minute (L/min) of dry air at temperatures ranging from about 600 degrees C (1,112 degrees F) to about 900 degrees C (1,652 degrees F). Figure 2-18 shows their results.

It is evident that the oxidation starts rather slowly at lower temperatures, and at 603 degrees C (1,117 degrees F), it takes about 26 hours to lose about 5 percent of the sample weight. The time to lose this percentage of the weight decreases very rapidly (to minutes) at temperatures greater than 800 degrees C (1,472 degrees F). At 911 degrees C (1,672 degrees F), it takes about 15 minutes to lose about 10 percent of the weight. Thus, as expected, the oxidation rate (OR) starts off low, increases rapidly, and then tails off as the oxygen penetration depth increases. Figure 2-18 illustrates this behavior.

Thus, as can be expected, the OR increases as the temperature increases, which is typical of Arrhenius behavior. However, results of Chi et al. (2008), Huang et al. (2014), and Lee et al. (2018) show that the increase in OR decreases at a temperature of approximately 850 degrees C (1,562 degrees F), as shown in Figure 2-19. These results were obtained on relatively small cylindrical samples, as specified in ASTM oxidation test standards. All of the experiments used dry air as the oxidizing environment. Chi et al. (2008) used 25.4 mm x 25.4 mm cylindrical specimens; Huang et al. (2014) used cylinders 15 mm high with a 10-mm diameter; and Lee et al. (2018) used 12.5-mm cubical specimen.

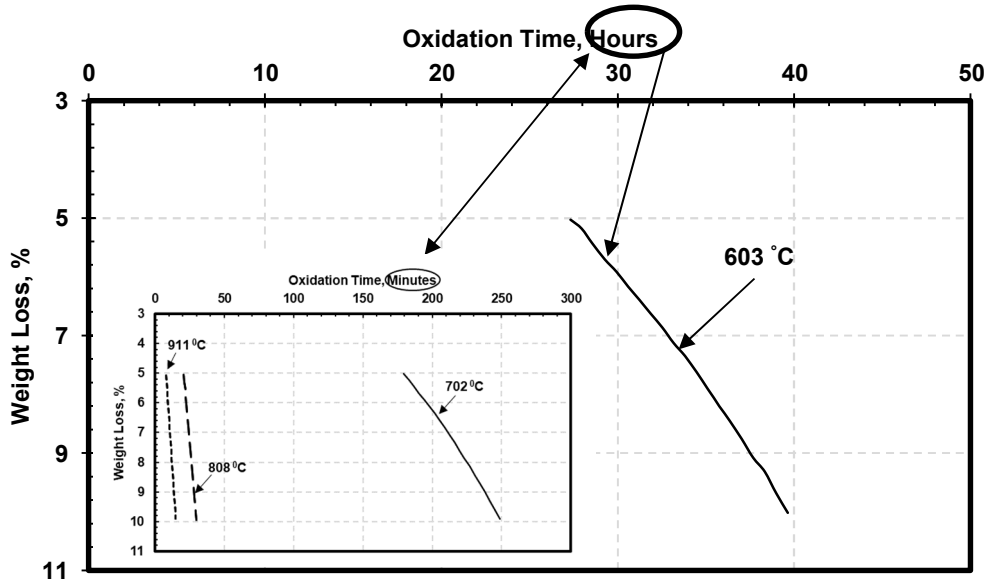

Figure 2-18 Oxidation weight loss dependence on oxidation temperature (note the relatively short time to achieve the same weight loss at very high temperatures) (Chi and Kim, 2008)

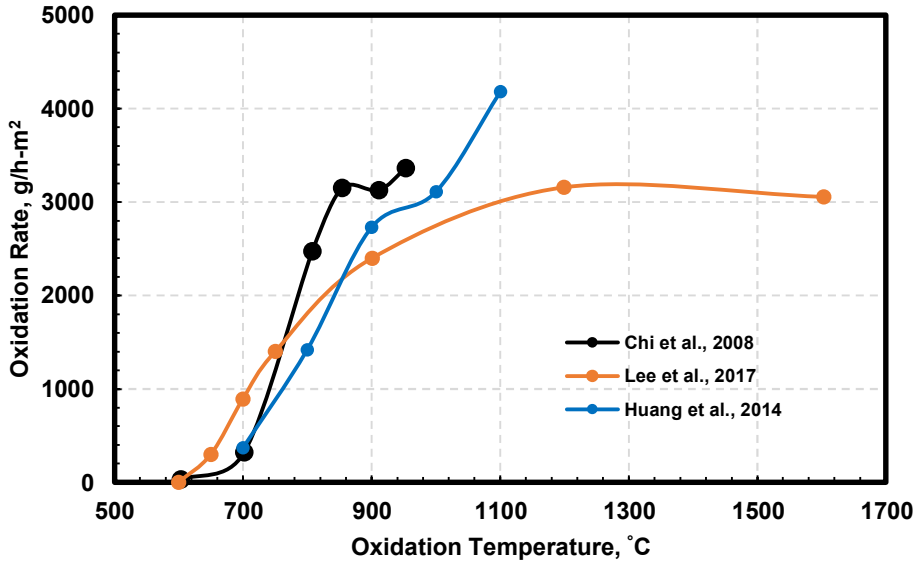

Figure 2-19 Effect of oxidation temperature on OR for IG-110 graphite

Huang et al. (2014) also studied the effect of oxidation on larger specimens, especially under accident conditions at temperatures of 1,000 degrees C (1,832 degrees F) or higher. They machined sleeves of diameter 34 mm and length 580 mm and conducted oxidation experiments with a dry air flow rate of 2 L/min, measuring thickness losses at various times. Figure 2-20 shows the resulting data.

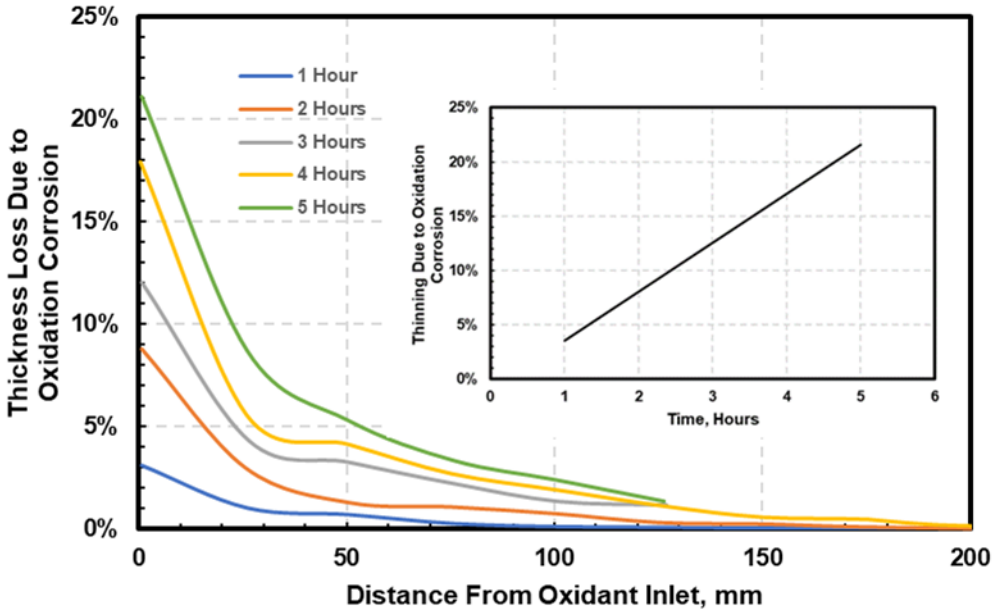

Figure 2-20 Thinning due to oxidation of a large IG-110 graphite sleeve (based on Huang et al., 2014)

Huang et al. (2014) concluded that oxidation occurred only at the front of the sleeve (near the air inlet), indicating that oxygen concentration was high at the front. In other words, oxygen did not diffuse to the back of the sleeve; all the oxygen reacted with the graphite at the front. Nevertheless, it is notable that oxidation can cause rapid thinning of about 20 percent in 5 hours at 1,000 degrees C (1,832 degrees F).

Kim et al. (2007) analyzed practical aspects of graphite oxidation in core components. Gleaning from the literature, they observed that graphite can be completely oxidized into carbon monoxide (CO) and carbon dioxide (CO_2) gases in less than 8 days at 700 degrees C (1,292 degrees F), and in 2 to 3 days at temperatures over 800 degrees C (1,472 degrees F). In an accident scenario, temperatures may increase to 1,500 degrees C (2,732 degrees F); massive and rapid oxidation under these conditions could weaken graphite seriously enough to cause core collapse.

For their study, Kim et al. (2007) used a newly developed graphite oxidation model in the VHTR system analysis code, the gas multi-component mixture analysis code (GAMMA), developed by the Korea Advanced Institute of Science and Technology and INL for analyzing VHTR air-ingress accidents. Their study relied on oxidation data obtained in dry air. They selected the 600-megawatt Gas Turbine Modular Helium Reactor (GT-MHR) as a reference reactor. From the results of the model, they calculated the change in mechanical strength due to oxidation using the following equation (Eto and Growcock, 1983), which applies to IG-110 graphite:

$$\frac{(\sigma_f)}{(\sigma_f)_0} = \left(\frac{\rho}{\rho_0}\right)^{6.08}.$$

Figure 2-21 shows the calculation results.

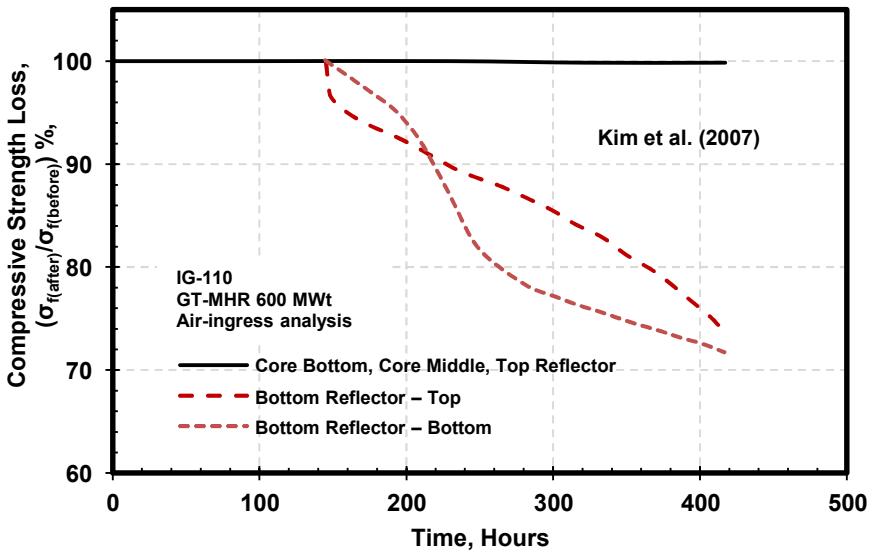

Figure 2-21 Impact of air-ingress on the reduction in compressive strength of IG-110 core components (Kim et al., 2007)

According to the calculation of Kim et al. (2007), most oxidation occurs in the bottom reflector; thus, the exothermic heat generated by oxidation does not significantly heat up the core. However, the oxidation process significantly decreases the density of the bottom reflector, making it vulnerable to mechanical stress failure. The bottom reflector supports the reactor core, and the stress is highly concentrated on this part. Kim et al. estimated a 4.5-percent density decrease, resulting in a 30-percent mechanical strength reduction, 11 days after the accident. Thus, as noted in ASME BPVC-III-5, HHA-3141(d), the maximum allowable probability of failure during design needs to account for the likelihood of such reductions in the compressive strength of components.

Ishihara et al. (1997) also studied the oxidation of graphite. Their study concerned the effects of oxidation on the fracture of IG-110 posts with curved ends resting on a seat with a mating curvature of the post, the design of which was based on a 1/6 model of the actual HTTR design. Graphite was oxidized in ambient air at 500 degrees C (932 degrees F) and 650 degrees C (1,202 degrees F) with forced convection and 800 degrees C (1,472 degrees F) with natural convection. Their paper states that the basic design concept for the post and seat components was the same as that of the Fort St. Vrain Nuclear Generating Station reactor. During compression testing of the post, the spherical contacts at both ends of the seats allowed relative horizontal displacement at the angle of their inclination. Figure 2-22 shows the experimental setup.

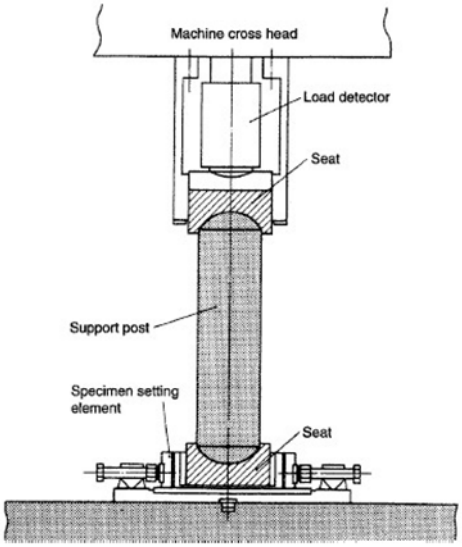

Figure 2-22 A schematic of the compression test setup for IG-110 support post cylinder (Ishihara et al., 1997)

The relative horizontal displacement in the reactor could be caused by the temperature difference and the seismic loading displacement between the keyed and the lower plenum blocks. Before the compression test, the specimens were oxidized isothermally at 550 degrees C (1,032 degrees F), 650 degrees C (1,202 degrees F), and 800 degrees C

(1,562 degrees F). Figure 2-23 shows the fracture loads at various oxidative weight loss stages.

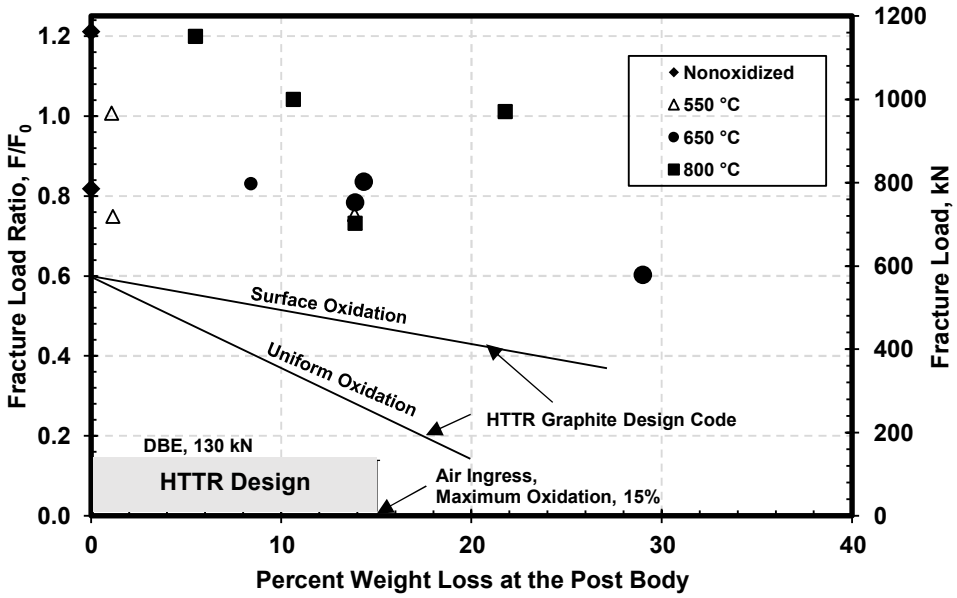

Figure 2-23 Fracture load ratio (F = oxidized; F_0 = nonoxidized) as a function of weight loss of the post body (Ishihara et al., 1997)

Generally, two types of failure modes can be expected in such tests. When the length-to-diameter ratio of the post is too large, the buckling fracture mode of the post is dominant; when the ratio is too small, the stress concentration fracture mode prevails. In the experiments of Ishihara et al. (1997), where fracture occurs mostly in the spherical contact region, stress concentration fracture is more significant than buckling fracture, for oxidation weight loss levels below about 30 percent.

Ishihara et al. argue that at higher temperatures, the availability of the oxidant between the post and the seat component is reduced, presumably because of the earlier oxidation of the moderators and reflectors. Thus, more damage occurs at the mating surfaces at lower temperatures. For this reason, the fracture load depicted in the results is lower at 550 degrees C (1,032 degrees F) and 650 degrees C (1,202 degrees F) than at 800 degrees C (1,472 degrees F). Ishihara et al. further argue that the HTTR design-basis earthquake load, which is about 130 kilonewtons, as shown in Figure 2-23, is conservative and is far less than the fracture loads, with a safety factor of approximately 4, using a hypothetical air-ingress accident weight loss of 15 percent.

Ishihara et al. (1997) also studied the dual effects of surface oxidation and uniform oxidation separately and recalculated fracture loads in their compression test. Their model of uniform oxidation, which can be seen as equivalent to the phenomenon of chronic oxidation discussed in Section 2.26, considers only compressive strength, assuming no loss in the cross section of the post. This assumption is valid only for relatively low-temperature oxidation, around 550 degrees C (1,022 degrees F). For higher temperatures, where surface oxidation results in

loss of material at the surface, the calculation of the buckling strength, which involves the diameter-to-length ratio, needs to consider reductions in cross section and changes in geometry. The design of the HTTR incorporates such considerations.

Numark recommends that such experiments be carried out for other candidate HTGR graphites, and that the overarching results be considered in establishing ASME design code requirements for allowable stress concentration factor, given the effects of oxidation on the strength of GCCs. The design code requirements should include conservative estimates, based on expected normal, off-normal, and accident temperatures for the HTGR design.

2.27. Chronic Oxidation

Chronic oxidation of graphite in HTGRs refers to the gradual penetration of oxygen over long periods of time. It can arise, for example, if humidity and moisture leak during shutdown operations and are retained within graphite components. While such moisture may be driven off by subsequent heatup, slight oxidation over time may be of concern. Trace moisture may also be present in coolant helium. Contescu and Mee (2016) at ORNL studied the chronic oxidation problem for IG-110 and found a parametric phenomenological model that may be used to better understand the OR—for example, to establish how the corroding gas mixtures diffuse into the porous structure of the graphite. Figure 2-24 shows the experimental results (points), along with the trendlines predicted by an enhanced model developed by Contescu and Mee.

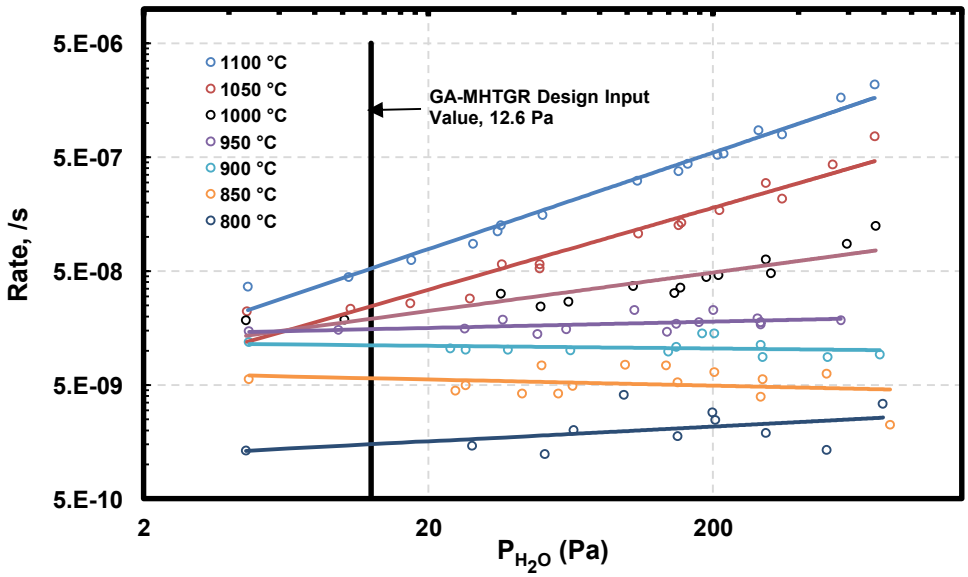

Figure 2-24 Oxidation rates measured for graphite IG-110: trend prediction lines from enhanced model (Contescu and Mee, 2016); rate = (1/original mass)×(Δmass/Δtime); vertical line, design input for General Atomics MHTGR (General Atomics, 1988b)

These experiments used ultra-high-purity helium containing less than 0.1 part per million (ppm) water and less than 0.5 ppm oxygen, with the balance helium (over 99.999 percent). The source of hydrogen added in some experiments was a certified H_2/He mixture with 1 percent H_2 by volume.

The ORNL results were further evaluated using an earlier study by General Atomics (GA) (1988b). During normal operation, the GA analysis predicted the maximum temperatures to be 1,080 degrees C (1,976 degrees F) and 1,180 degrees C (2,156 degrees F) for the graphite core support structure and core components respectively. However, the graphite core support structure and permanent side reflectors were expected to be made from Stackpole 2020 graphite; fuel elements and central reflectors were expected to be made from H-451 graphite. These graphites are no longer produced.

Table 2-10 shows the long-term expected and design operating limits on primary coolant impurity for the modular high-temperature gas-cooled reactor (MHTGR). Figure 2-24 shows the design input for P_{H2O} as a vertical line. The effect of chronic moisture needs to be analyzed in light of the designed life of the components. For the gas turbine modular high-temperature gas-cooled reactor (GT-MHTGR), typical fuel elements were designed for replacement after 964 days of full-power operation, while the bottom reflectors adjacent to the core were designed to be replaced every 2,892 days.

Table 2-10 Long-Term Design Limits of Primary Coolant Impurities

Chemical Impurities	Expected Concentration, ppm	Chemical Impurities	Expected Concentration, ppm
H_2O	0.01 to 0.1	H_2	0.1 to 1
CO_2	0.01 to 0.1	CH_4	0.1 to 0.2
CO	0.1 to 1	N_2	0.01 to 0.1
		Particulates	< 45 g/year

As stated in ASME BPVC-III-5, HHA-3141, “Oxidation,” a GCC may be oxidized by oxygen or carbon dioxide in the coolant. This makes it pertinent to understand the coolant chemistry and its potential for change over the reactor lifetime. The weight loss within the GCC can be expected to vary depending on the conditions at which the oxidation occurs and the distance from the surface exposed to the gas flow.

It is also important to consider the effect of chronic oxidation on slow crack growth in graphite, which could be initiated in areas of geometrical discontinuity, such as keyways. Possible oxidation at a crack front provides a driving factor for the crack, even under conditions of relatively low stress, with the global stress in the component remaining constant and well below the acceptable and designed S_g levels required in Subsection HH, Subpart A. Section 2.24 of this report also mentions this point.

2.28. Design Strength and Material Reliability Curve Values

Designers must enter the items under this category in the MDS, based on the results of their own testing and analyses and the requirements in ASME BPVC-III-5, Article HHA-2200,

“Materials Properties for Design.” The authors of this report made no attempt to derive these values from the literature and are not providing information on MDS Items 17–27.

2.29. Graphite Oxidation Effects

Recognizing the complexity of the phenomenon of oxidation in graphite, ASME BPVC-III-5, HHA-3141, “Oxidation,” states, “The corroding gas mixtures diffuse into the porous structure of the graphite. The weight loss in the Graphite Core Component varies depending on the conditions at which the oxidation occurs and the distance from the surface exposed to the gas flow.”

Weight loss due to oxidation depends on several other factors as well. The graphite OR depends on temperature, availability and concentration of reactant (O_2), and gas flow rate (Zhou et al., 2018). The geometry of the article and the microstructure of the graphite impose restrictions on oxidation reaction (activation energy). The effects of these factors on OR are nonlinear, interactive, and varied, and a detailed consideration of them is beyond the scope of this work. This report considers only the results obtained in recent experiments with IG-110 graphite. Figure 2-25 shows an example. The material was oxidized at 700 degrees C (1,292 degrees F), using thermogravimetric analysis equipment. For this graphite, most of the mass loss is within 1.5 mm of the oxidizing surface, with a maximum grain size of 0.02 mm. An exposure time of about 5 hours in air at 700 degrees C (1,292 degrees F) was reported to result in about a 10-percent weight loss (Lee, 2016).

Chi and Kim (2008) performed similar oxidation experiments in dry air. Figure 2-26 shows a sample of their results for IG-110. Here, under the experimental conditions, the surface penetration of oxygen occurs at relatively short times, on the order of minutes. As established before, a reduction in density is directly related to the weight loss; thus, strength loss can be expected within short periods at temperatures over 1,000 degrees C (1,832 degrees F), if IG-110 is exposed to environmental air that has entered the graphite core.

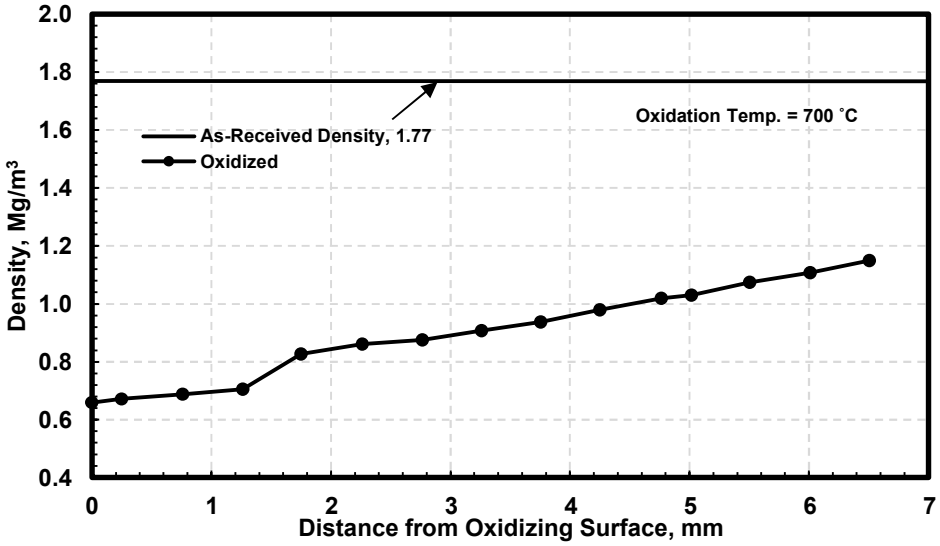

Figure 2-25 Average density profile of IG-110 oxidized specimens (Lee et al., 2018)

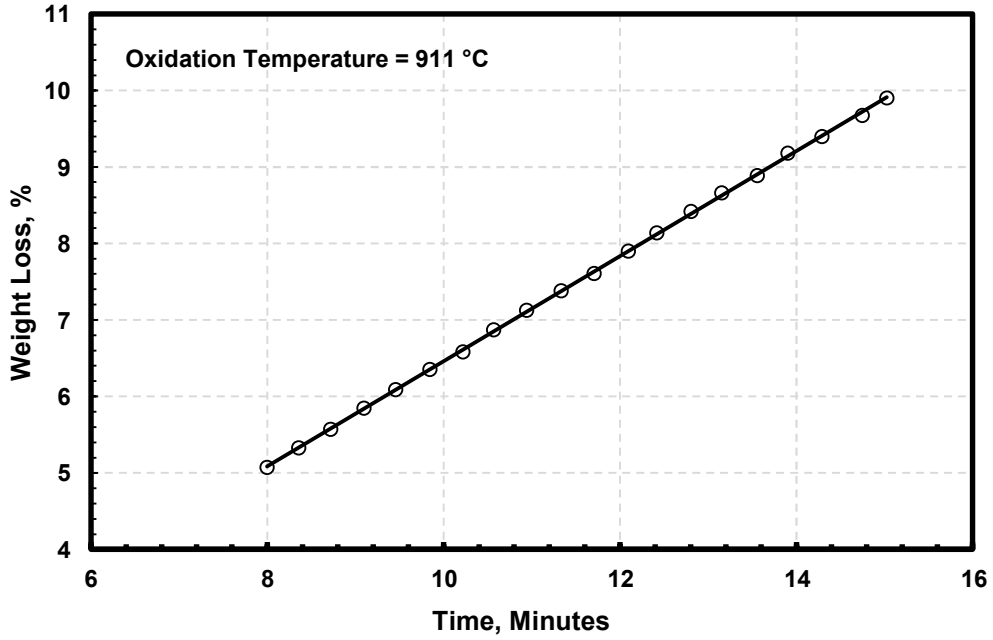

Figure 2-26 Weight loss versus time for IG-110 (Chi and Kim, 2008)

Tournier and El-Genk (2011) modeled the oxidation of nuclear graphite considering the various intermediate reactions involved in carbon oxidation. Their model includes the reaction kinetics involved in (1) the adsorption of oxygen molecules to form undissociated $C(O_2)$ surface complexes, (2) the breakup of undissociated $C(O_2)$ oxygen radicals to form stable (CO) complexes, (3) desorption of stable (CO) surface complexes to produce CO gas, and

(4) desorption of CO_2 gas. Their multiparameter algorithm also includes other variables, such as the test sample temperature, the total gas pressure and flow rate in the test tube, the concentration of the gaseous oxygen in the bulk gas mixture, and the dimensions and initial mass of the graphite test specimen. Figure 2-27 shows their model verification.

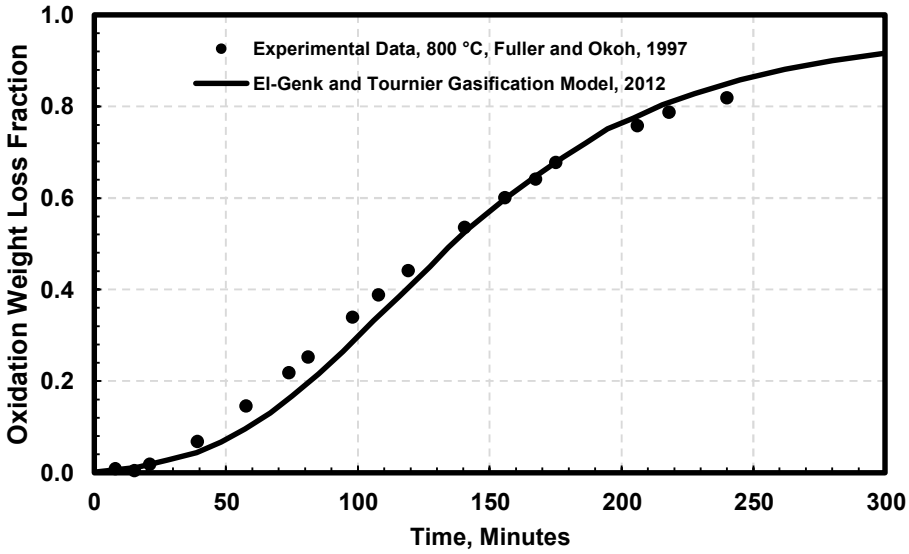

Figure 2-27 Results of a gasification prediction model, based on experiments and carbon-oxygen chemical reaction kinetics analysis

2.30. Strength

As stated previously, oxidation reduces the strength of graphites. Weight loss obviously decreases the density, which influences the retention of strength. Although empirical power-law correlations between strength and density are common, changes in pore morphology, represented by aspect ratio, orientation, and distribution, govern the strength, which depends on the orientation of the load applied in the strength test. The following section discusses the effects of oxidation on room-temperature strength. It seems that the authors of the publications reviewed below assumed anisotropy in the postoxidation strength response, as none of them reported postoxidation strength experiments in the two orthogonal specimen directions.

Eto et al. (1987) conducted oxidation tests on IG-110 in an atmosphere of steam-helium mixture. Figure 2-28 shows their results, in which a density decrease of about 11 percent due to oxidation reduces the bending strength by about 50 percent. Coincidentally, the analytical results of Kim et al. (2007) showed a 6.4-percent density reduction causing an approximately 30-percent reduction in mechanical strength (the point marked by the arrows in Figure 2-28). This matches the predicted line shown in Figure 2-29, despite the scatter in the data and the differences between the oxidation conditions of Kim et al. (2007) and those of Eto et al. (1987). On the other hand, the oxidation times corresponding to the same weight loss differ substantially between the analytical study of Kim et al. (2007) and the experimental study of Chi and Kim (2008), although both studies used oxidation data gathered in dry air.

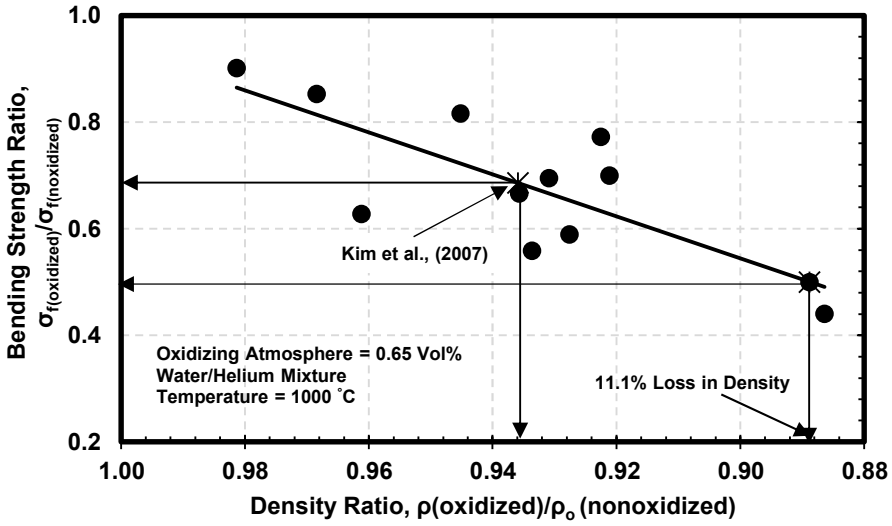

Figure 2-28 Effect of steam oxidation on bending strength as related to density decrease (Eto et al., 1987)

Figure 2-29 shows the loss in compressive strength due to oxidation, with data extracted from Ishihara et al. (2004). The JAEA draft code (Shibata et al., 2010) used these data, although it seems to claim no strength loss for up to about 1-percent oxidative weight loss. Regrettably, neither authors state the oxidation conditions. Here a strength loss of about 29.5 percent is seen at a weight loss of 4.5 percent, as compared to the analytical estimate of 30 percent by Kim et al. (2007) mentioned above. Also, according to this work, a 10-percent weight loss can reduce compressive strength by about 50 percent.

Figure 2-30 shows the loss in tensile strength due to oxidation, normalized with respect to nonoxidized strength, with data extracted from Ishihara et al. (2004), which were used in the JAEA draft code (Shibata et al., 2010). According to Ishihara et al. (2004), a 10-percent weight loss can reduce tensile strength by about 33.6 percent. In terms of the reliability targets for the various loading conditions for graphite components for the three structural reliability classes, it is highly likely that a 50-percent strength loss can result from anywhere between 10 and 12 percent of oxidative weight loss. Thus, these results seem to support ASME BPVC-III-5, HHA-3141(b), which states that “the region where strength decreases to less than 50% shall not be credited in the stress evaluation.”

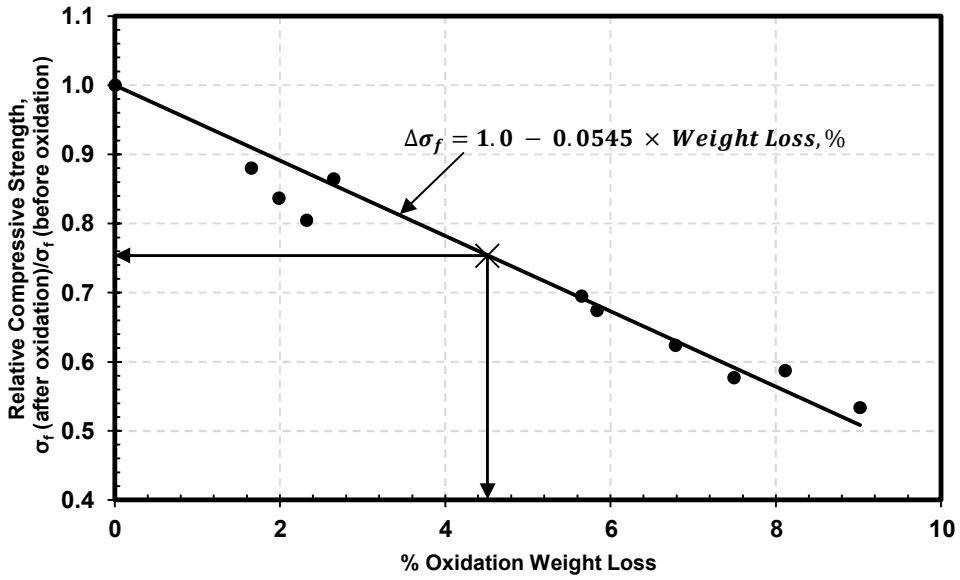

Figure 2-29 Dependence of compressive strength on weight loss in uniformly oxidized IG-110 graphite (Ishihara et al., 2004)

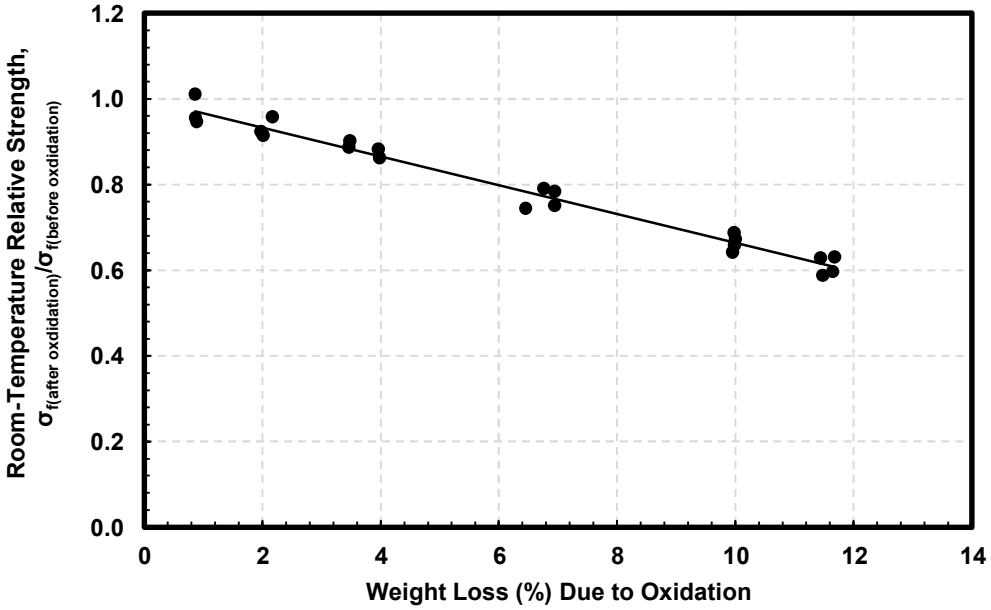

Figure 2-30 Dependence of tensile strength on weight loss in uniformly oxidized IG-110 graphite (Ishihara et al., 2004)

2.31. Elastic Modulus

The elastic modulus of graphite is closely related to its density, or, more accurately, to its pore structure, which includes the shape, size, and orientation distribution of the pores. Thus, the elastic modulus may be anisotropic, and changes to the pore morphology due to oxidation can be expected to alter its value as well. The "Graphite Design Handbook," issued by General Atomics (1988a), assumes that the elastic modulus change will follow the strength change. For Stackpole 2020 graphite, the following relationship is given:

$$\frac{S}{S_0} = \frac{E}{E_0} = 1 - e^{-10x},$$

where *S* is the graphite strength, *E* is the Young's modulus, the subscript 0 indicates the nonoxidized state, and *x* is the fractional weight loss due to oxidation.

In the studies of IG-110 conducted by Eto et al. (1991), Numark related the change ratios directly to density. Figure 2-31 shows their results.

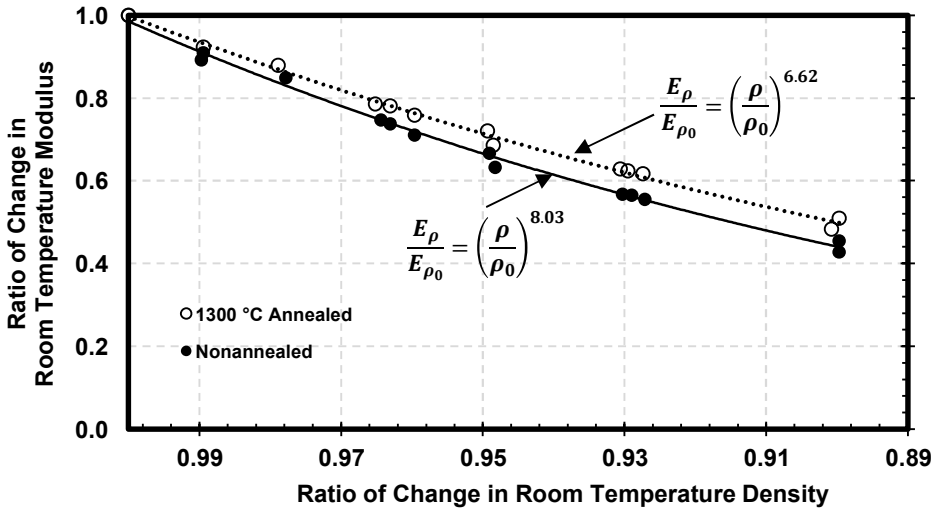

Figure 2-31 Room-temperature Young's modulus change ratio as a function of density change ratio for IG-110 graphite, after oxidation (Eto et al., 1991)

The oxidation was performed in static air at 500 degrees C (932 degrees F). Annealing at 1,300 degrees C (2,372 degrees F) resulted in the partial recovery of the Young's modulus. The authors attributed these changes to the morphology and the distribution of microcracks and micropores during oxidation heatup and annealing thereafter. They believed the recovery to correspond to the reduction in the size of micropores and microcracks.

Eto et al. (1991) studied the modulus recovery of oxidized specimens after annealing from 200 degrees C (392 degrees F) to 1,800 degrees C (3,272 degrees F) in a vacuum at 1 degree per hour. Figure 2-32 shows their results. The recovery in modulus begins at about

400 degrees C (752 degrees F), with increased recovery up to about 1,300 degrees C (2,372 degrees F), above which the recovery slows and, perhaps, eventually ceases.

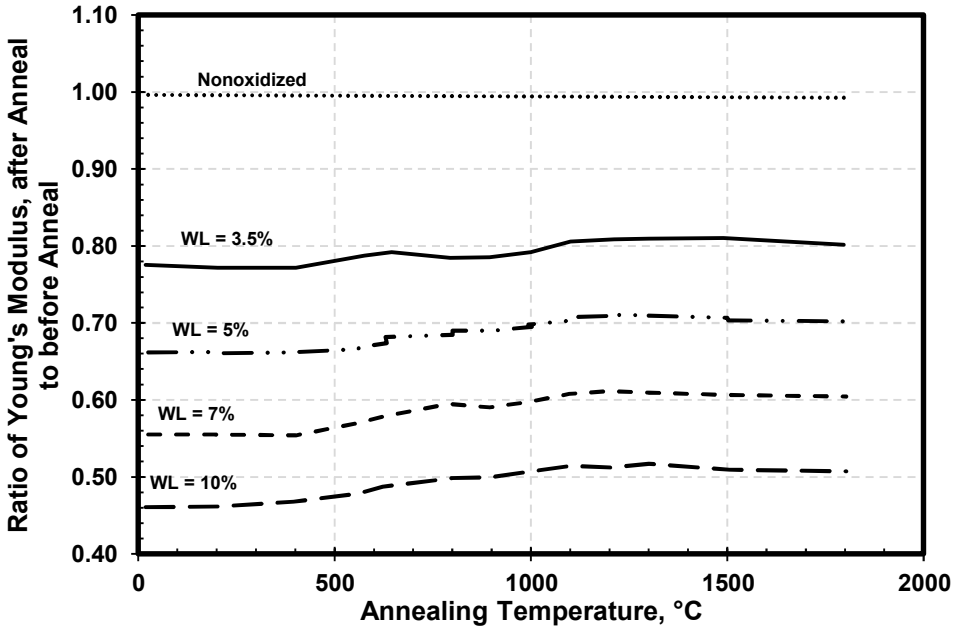

Figure 2-32 Effect of annealing in the recovery of Young's modulus for IG-110 graphite (Eto et al., 1991)

The dependence of room-temperature Young's modulus on weight loss was calculated from the data of Eto et al. (1991) on weight loss due to oxidation, as shown in Figure 2-33.

Overall, the governing factor for the loss in strength and elastic modulus due to oxidation is the change in pore density. In addition, the pore size, shape, and orientation distribution within the microstructure dictate the direction-dependent properties. The study reported in Ishihara et al. (2004) assumed IG-110 was isotropic and did not provide direction-dependent changes in properties due to oxidation.

In addition to decreasing the structural integrity of graphite through loss of strength, oxidation may also lead to radiological consequences due to material loss, since radionuclides trapped or absorbed during reactor operation could be carried away with the reactants of oxidation. Analysis of this phenomenon is beyond the scope of this work.

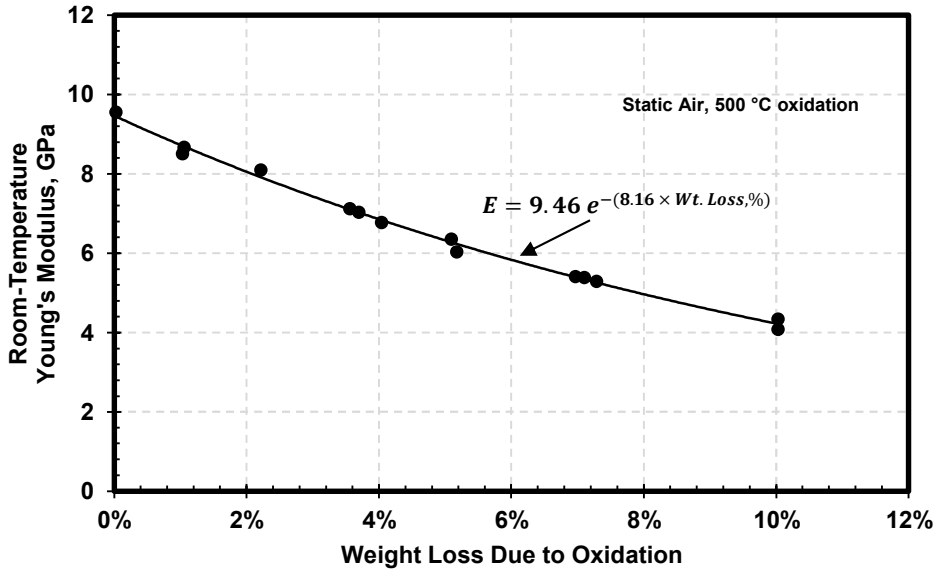

Figure 2-33 Effect of weight loss due to oxidation on Young's modulus for IG-110 graphite (Eto et al., 1991)

2.32. Thermal Conductivity

Thus far, the literature search conducted for this report has uncovered no experimental data on the effects of oxidation on the thermal conductivity of IG-110 graphite. However, it is known that thermal conductivity is proportional to density and thus directly related to it. Specific heat, C_p, is independent of density; however, thermal diffusivity, α, decreases as density decreases. Therefore, thermal conductivity, which scales with thermal diffusivity, decreases with increased porosity due to oxidation.

Thermal conductivity can be estimated as a function of porosity, as shown in Figure 2-35 based on the data in Figure 2-34. Independently, this report also invokes the two-phase model for cellular materials, which was developed by Collishaw and Evans (1994). The simplest approach treats the solid and pore phases as thermal resistors in parallel with the following relation:

$$\boldsymbol{k = k_s\left(1 - \nu_p\right) + \nu_p k_p,}$$

where k_s is the effective thermal conductivity of the solid phase (graphite), $\boldsymbol{\nu_p}$ is the pore volume fraction, and k_p is the pore thermal conductivity. The above equation is also the rule of mixtures; it provides an upper limit to the combination of the two phases, on the basis that they do not interact with each other and can be attributed with the same response at all length scales.

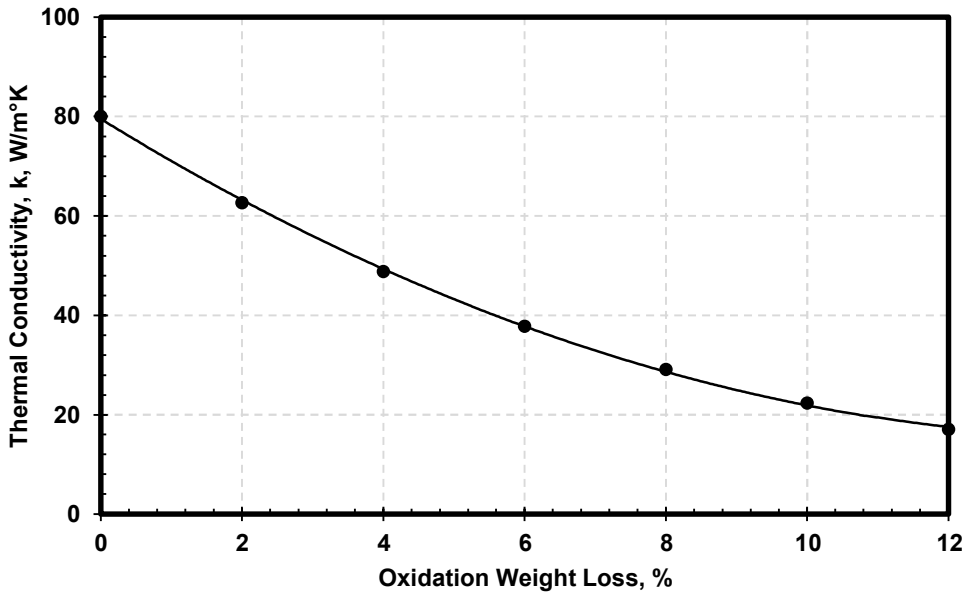

Figure 2-34 The effect of weight loss on room-temperature thermal conductivity for IG-110 graphite (calculated from data in Ishihara et al., 2004)

Considering $k_p << k_s$, the simplification $k_p = 0$ yields Loeb's relation:

$$k = k_s(1 - \nu_p).$$

Collishaw and Evans (1994) have posited that the above is a useful approximation.

Using this simplification, the authors of the present report recalculated the data of Figure 2-34 in terms of the effect of increased the fraction of porosity due to oxidation. Figure 2-35 shows the results. The oxidation conditions were not published in Ishihara et al. (2004).

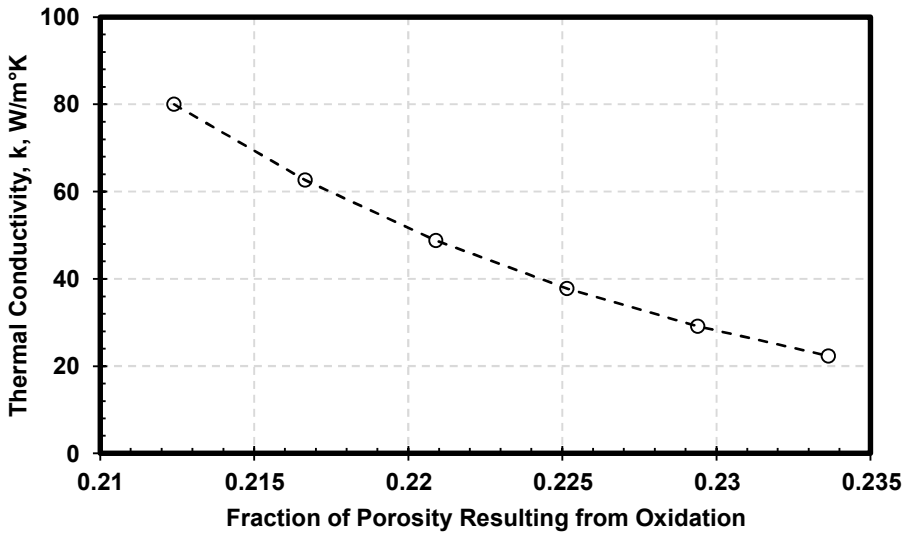

Figure 2-35 The effect of fractional increase in porosity due to oxidation on room-temperature thermal conductivity (calculated from data in Ishihara et al., 2004)

The results are not surprising, since the mathematical relationship between density and porosity is the same, and the oxidation weight loss decreases the density.

During air-ingress accidents, where rapid oxidation and thus rapid weight loss are possible, the substantial reduction of thermal conductivity by about 10-percent oxidation could affect the designed capability to remove heat from the core.

2.33. Irradiated Graphite

Graphitized coke grains, graphitized binder grains, micro- and macro-porosity, and graphitization shrinkage Mrozowski microcracks are intrinsic microstructural features of manufactured graphite. Thus, these individual items can be considered intrinsic properties of graphite. Density is one measure describing these intrinsic properties; it depends primarily on the porosity. In other words, density is a derived property resulting from the assemblage of the intrinsic features of graphite. Likewise, all other physical, thermal, mechanical, and chemical (resistance) properties are derived properties resulting from the microstructure existing at the time they are measured (using established consensus testing standards and practices).

When graphite is irradiated, its density changes, because irradiation causes structural changes to the binder-graphitized and coke-graphitized graphite grains and to the porosity arising from manufacturing practices. These structural changes are functions of irradiation temperature and the accumulated irradiation dose; they affect the density and all subsequent irradiated properties. Generally, at a given temperature, the density increases with irradiation dose, but after a certain dose, which depends on the grade of graphite, the density increase slows down, and then the density decreases. Figure 2-36 provides an example.

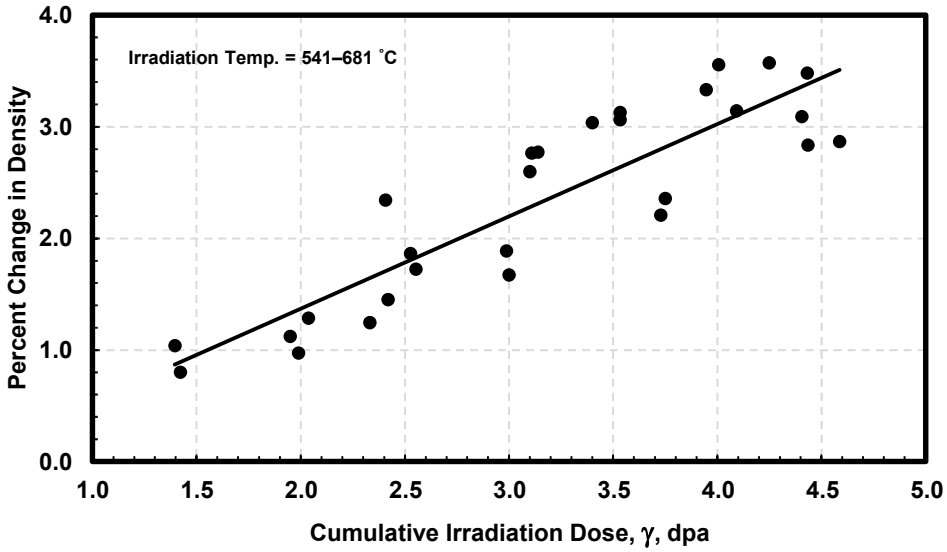

Figure 2-36 Density change with irradiation for IG-110 (Windes et al., 2017a)

As mentioned previously, the data scatter may be due to several factors, including the inherent variation in graphite homogeneity and individual sample temperature and dose. The fundamental changes in pore fraction and pore morphology after irradiation affect all other properties that are functions of density, such as Young's modulus, strength, and creep.

It is also pertinent to recast the data to show how the irradiation dose affects (global) porosity and thus other properties. The authors of this report performed such an analysis to reveal how increased the fraction of porosity due to oxidation may affect thermal conductivity. The results appear in Figure 2-37, which shows that one of the effects of increased irradiation dose is to close microcracks and pores, decreasing the fraction of porosity.

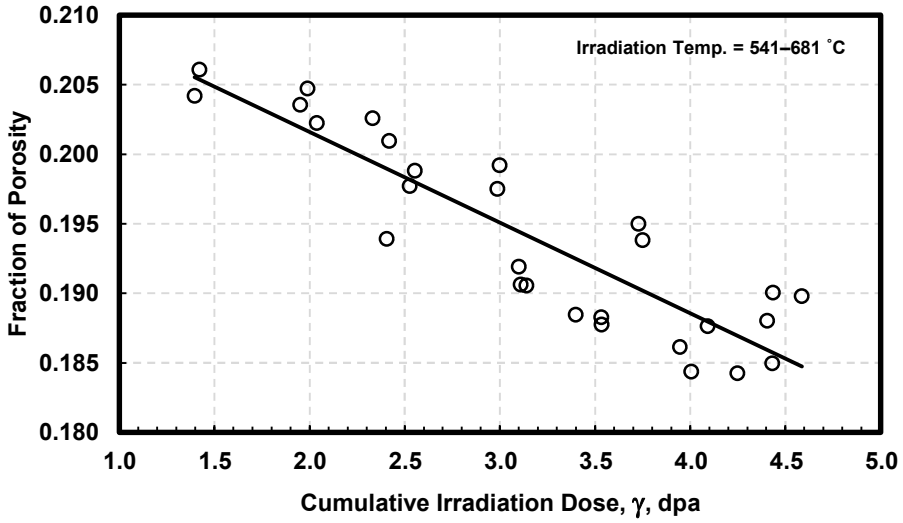

Figure 2-37 Effect of irradiation on the fraction of porosity on irradiated IG-110 graphite (Windes et al., 2017a)

2.34. Dimensional Change

Dimensional change caused by irradiation is a major concern. Dimensional change is an interactive phenomenon, depending on both temperature and dose.[2] Because of anisotropy, and because the flux and temperature distribution are not homogeneous, not only may shrinkage and expansion occur, but lengthwise and radial changes may be uneven, leading to distortion of the graphite component. This, in turn, may affect the geometry of the reactor coolant, fuel, and control rod channels, compromising the top-tier safety requirements of unimpeded coolant flow and unimpeded fuel rod and control rod movement.

As an experimental test reactor, the HTTR was designed for a relatively small cumulative operational dose. The JAEA is currently conducting preliminary investigations on extending the experience of the HTTR to building and operating a VHTR with a prismatic core design; however, as indicated in Figure 2-38, graphite components in this reactor are also expected to be subjected to less than 1 dpa in their lifetime. A low-dose exposure may be applicable for experimental HTGRs, but graphite components in new commercial reactors are expected to experience substantially higher irradiation doses during their lifetime, as indicated in Table 1-2.

Shibata et al. (2010) extended experiments on IG-110 to high dose levels and developed models to interpolate and extrapolate the experimental data to dose regions where experimental

[2] The United Kingdom's operational experience is that dimensional change is weight-loss dependent as well. However, any weight loss in an HTR is expected to be small compared to that in an AGR; thus, the effect will be minimal. Also, the experiments of the United Kingdom Atomic Energy Authority indicate that thermal creep reduces strength, modulus, and thermal conductivity faster than radiolytic oxidation does.

data were unavailable for the draft JAEA standard. Figure 2-38 shows their interpolated and extrapolated data.

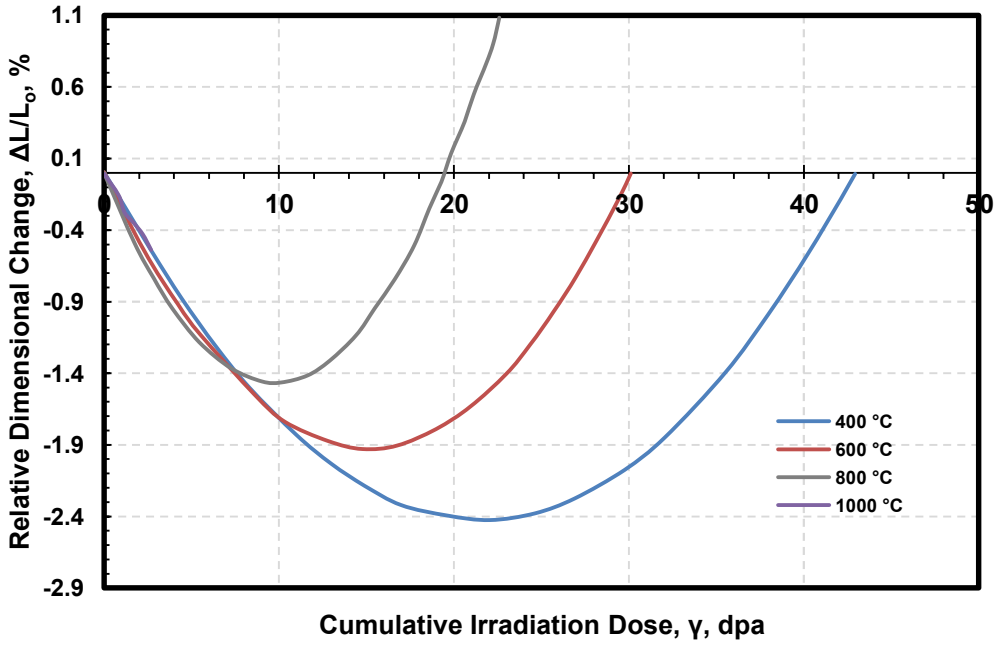

Figure 2-38 Dependence of irradiation dimensional change with temperature and dose interpolated and extrapolated from experimental data for the JAEA design code (Shibata et al., 2010)

Campbell and Katoh (2018) performed experiments with samples cut in the WG (termed axial) and AG (termed transverse) directions to distinguish the possible effects of grain orientation on the dimensional change due to irradiation. Their results have been included as data points in Figure 2-39, with the grain orientations and irradiation temperature ranges indicated. In addition, as a Euratom Petten irradiation data, reported by Heijna et al. (2017) at approximately 750 degrees C (1382 degrees F) are also presented in Figure 2-39 comparison.

Several items are to be noted from these experimental results. There are significant differences between the dimensional change due to irradiation and dose published in the JAEA HTGR code and the dimensional change due to irradiation temperature obtained by Campbell and Katoh (2018) above 10 dpa in Figure 2-39. Considerable differences also exist between measurements made in the two orthogonal directions of the test specimens, which represent the two grain orientations in IG-110 graphite. From the data shown, the JAEA HTGR draft code may not provide conservative estimates of dimensional change at higher dpa.

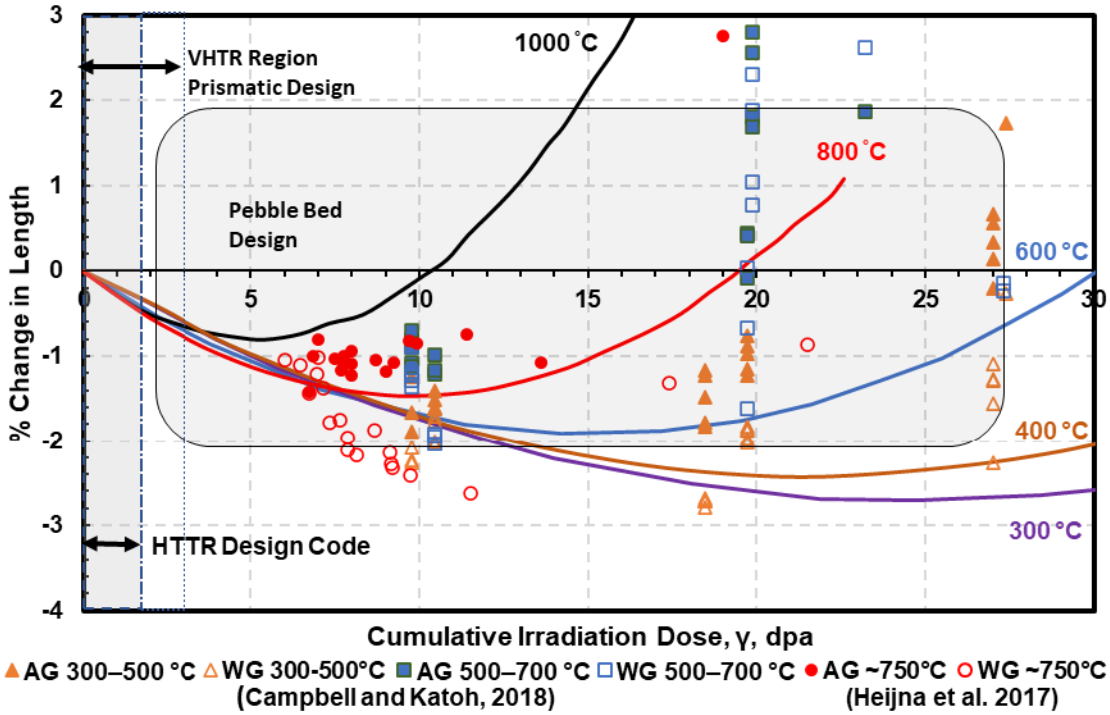

Figure 2-39 Relative change in specimen length after irradiation for IG-110 (Campbell and Katoh, 2018 and Heijna et al. 2017), with recommended trendline curves based on Kunimoto et al., 2014 and Shibata et al., 2010, and with dimensional change in the plot limited to a maximum of 3 percent for clarity

Additional data generated are also available for IG-110 graphite in Figure 2-40. The Japanese irradiated code data for very early dose range matches well with the Euratom Petten irradiation data, reported by Heijna et al. (2017). The shrinkage in the WG direction reported by Heijna et al. (2017) is higher than that in the AG direction. The data obtained by Snead et al. (2016) and Windes et al. (2012) are included for comparison, even though their irradiation temperature range is lower than that of the JAEA HTGR draft code data and the Petten irradiation data.

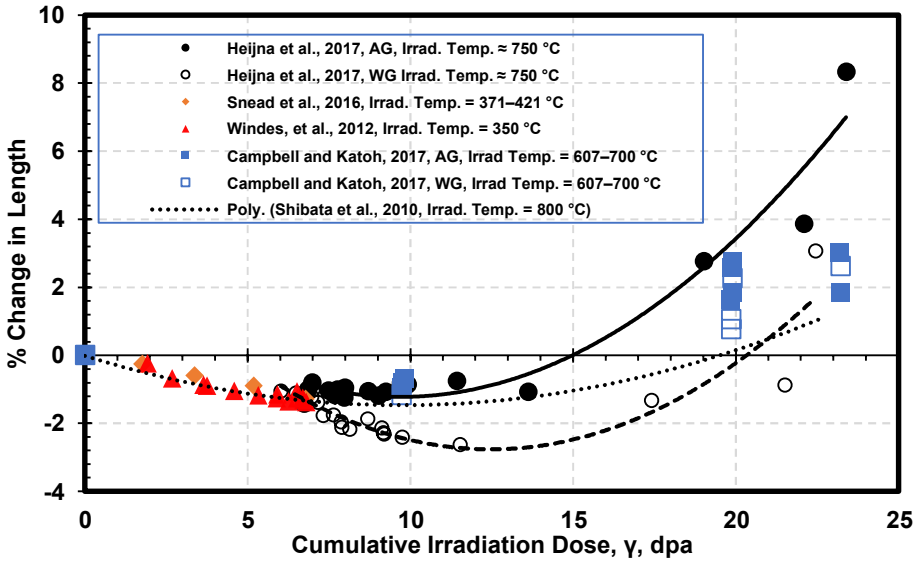

Figure 2-40 Irradiation-induced dimensional change for IG-110

The results of the dimensional changes of irradiated IG-110 reported by Campbell and Katoh (2017) over the complete range of temperatures studied is provided in Figure 2-41.

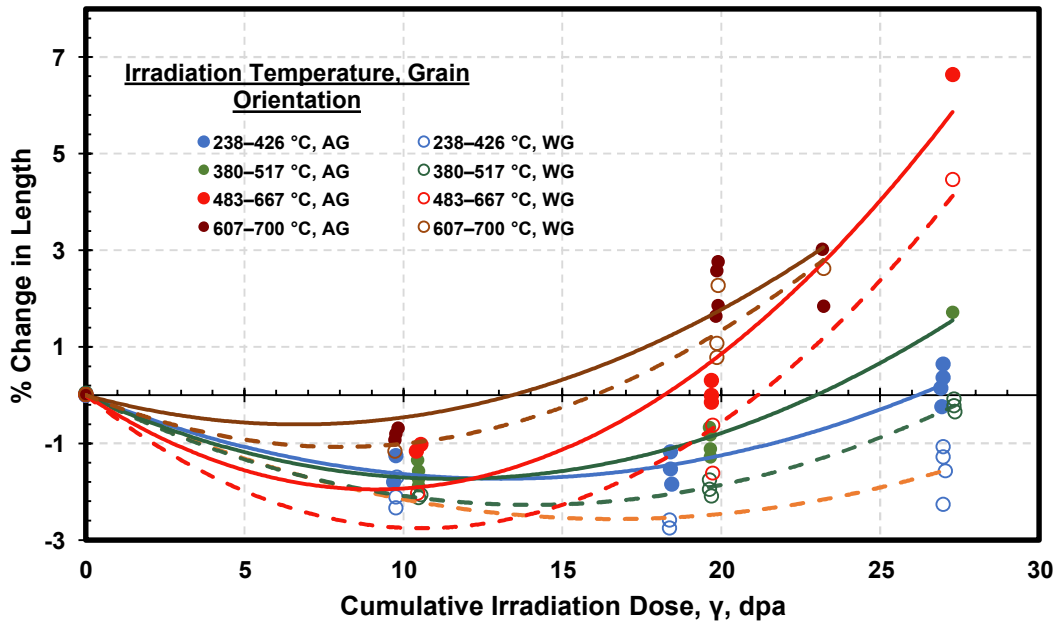

Figure 2-41 Irradiation-induced dimensional change for IG-110 for various temperatures and each grain orientation (Campbell and Katoh, 2017)

The data scatter and overlap make coherent interpretation difficult; also, there were significant deviations from the target irradiation temperatures. However, at the irradiation temperatures

studied, the AG change of length is less than the WG change of length, as a function of irradiation dose.

ASME BPVC-III-5, Article HHA-3142.4, defines the graphite cohesive life limit as the fluence at which the material experiences a +10-percent linear dimensional change in the WG direction. Material that exceeds this limit is considered to provide no contribution to the structural performance (stiffness and strength) of the GCC. According to the data shown here, it appears that IG-110 graphite does not exceed this limit at an irradiation temperature of 750 degrees C (1,382 degrees F) for up to about 27 dpa, or a fluence of about 1.9×10^{26} neutrons per square meter (n/m^2).

Figure 2-42 depicts the overall volume change, considering the dimensional changes in the two orthogonal directions, as a function of irradiation dose for various irradiation temperatures. As expected, the volume turnaround (the dose at which shrinkage stops increasing) shifts to lower doses as the irradiation temperature increases. In addition, as irradiation temperature increases, the point at which volume expansion begins (corresponding to the destruction of the cohesion of graphite grains) shifts to lower doses.

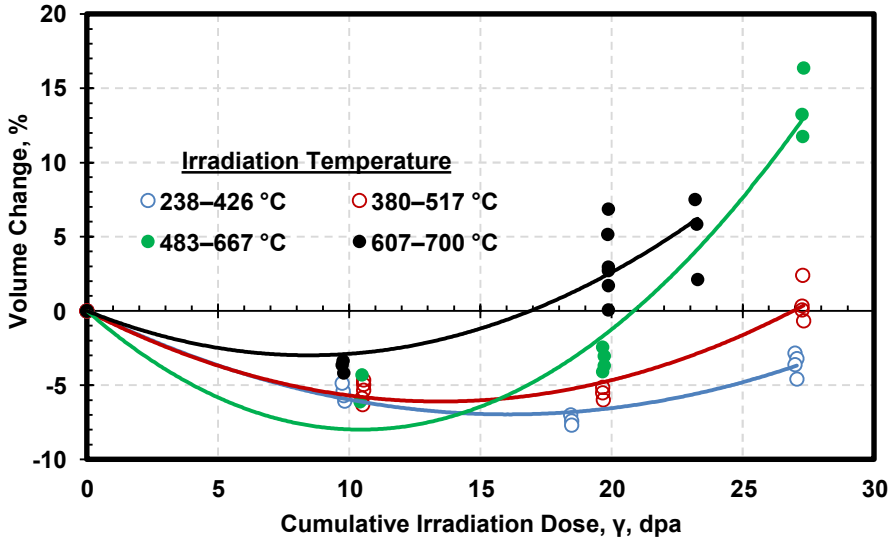

Figure 2-42 Volume change for IG-110 due to irradiation, as a function of dose, for irradiation temperatures shown (Campbell and Katoh, 2017)

2.35. Creep Coefficient

Irradiation creep experiments for graphite are very difficult to carry out successfully and reliably. In metals and alloys, creep deformation (deformation because of plastic flow) is dependent on applied stress and the temperature. Creep experiments for metallic materials are conducted either at isothermal temperature for different applied stresses or at a constant applied stress for varying temperatures. The deformation is measured at the temperature of the experiments.

Irradiation creep is essentially the difference between the dimensional change in a loaded sample and the dimensional change in an unloaded sample. Creep measurements for graphite, unlike those for metals and metal alloys, are taken at room temperature after irradiation.

The deformation behavior of alloys can be analyzed using an Arrhenius-type mathematical formulation, and deformation mechanisms can be determined by correlating with the diffusion coefficients for various alloying elements, which influence the dislocation motion and thus the plastic flow. In contrast, for graphite in a reactor, the irradiation creep deformation is a function of applied dose and temperature. The nature of irradiation experiments in MTRs makes it very difficult to maintain a constant temperature for the test, especially for samples located at various positions along the length of the irradiation capsule in which the specimens are loaded and the compressive stress is applied. Additionally, after the experiment ends, when the test specimens are cooling, the stress relaxes, which means the final length can be expected to differ from the length at the end of the experiment while the specimen is in the capsule.[3]

Irradiation-induced dimensional changes result in differential strains. Burchell (2011) briefly summarizes irradiation creep in graphite as follows. In weaker graphites, cracking occurs because of the generation of new pores. Stronger graphites resist pore generation, resulting in strain manifested as irradiation creep strain. Irradiation creep occurs in two stages. In the first stage, primary creep, the creep strain is inversely proportional to Young's modulus, and the phenomenon is reversible. In the second stage, secondary creep, the creep strain is influenced by applied stress, irradiation dose, irradiation temperature, and Young's modulus. Secondary creep is generally considered essentially permanent; however, there is also clear evidence that secondary creep is not permanent but recovers far more than 1 elastic strain unit[4] (Kelly and Brocklehurst, 1977; Davies and Bradford, 2008). Many disagreements exist about the operating mechanisms for irradiation creep in graphite. The mechanisms need to address (1) deformation within the graphite crystal, (2) pore generation and reorientation of pores, and (3) structural changes that occur at high irradiation doses.

Figure 2-43 presents the results of some recent creep deformation experiments on IG-110 graphite. There is quite a large variation between the two sets of dimensional shrinkage data, which were obtained at different laboratories. In the data of Snead et al. (2016), the difference between the unstressed and stressed specimens is rather small, and the creep contribution, while significant, is not as large as for the data of Windes (2012). These differences may be attributed partly to variations in the specific amount of compressive stress applied and the manner of stressing the samples; however, they are mainly expected to be due to differences in

---

[3] At the start of irradiation, the sample has modulus E1 and CTE1; at the end of the irradiation, the sample has modulus E2 and CTE2. These changes in E and CTE will affect the final length of the sample, as well as the temperature of the sample if determined by the clearances in the sample holder. During irradiation, the sample changes dimensions and the clearances change, as does the temperature. In addition, if the load is exerted by a spring or bellows, as the sample changes dimensions, the load also changes. If the bellows leak, as has occurred in several irradiation creep experiments, the load can change significantly.

[4] The elastic strain unit for creep is defined as

$$esu = \frac{E_0}{\sigma}\varepsilon_{cr},$$

where E_0 is the static Young's modulus, σ is the creep stress, and ε_{cr} is the creep strain.

the individual specimen temperatures and doses. In general, the creep deformation contribution increases with increasing cumulative dose. This is because, during secondary creep, the creep strain increases with dose at a more or less constant rate.

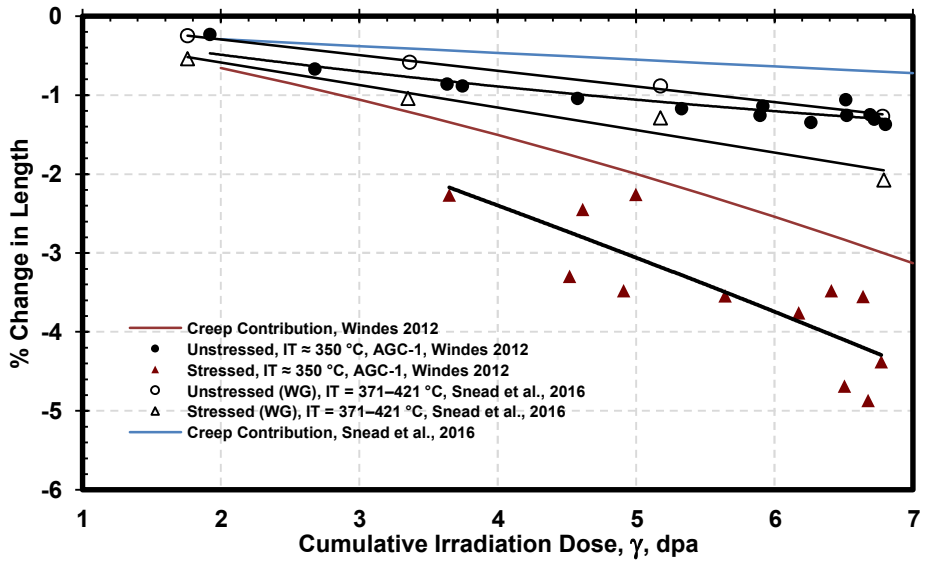

Figure 2-43 Creep deformation contribution to irradiation dimensional change for IG-110

Reliable data on the creep coefficients of IG-110 are not as abundant; most such data come from investigations conducted decades ago. Figure 2-44 shows the limited data available. For the tensile creep experiments conducted by Arai et al. (1990), the scatter in creep coefficients plotted against temperature appears to be rather large; however, this is mainly due to the variation in dose, irradiation temperature, and applied stress, as shown in Table 2-11. Additionally, the inevitable gradients in both neutron flux and temperature (exacerbated by a decrease in thermal conductivity with irradiation) produce internal stresses, which need to be accounted for in the actual available creep stress.

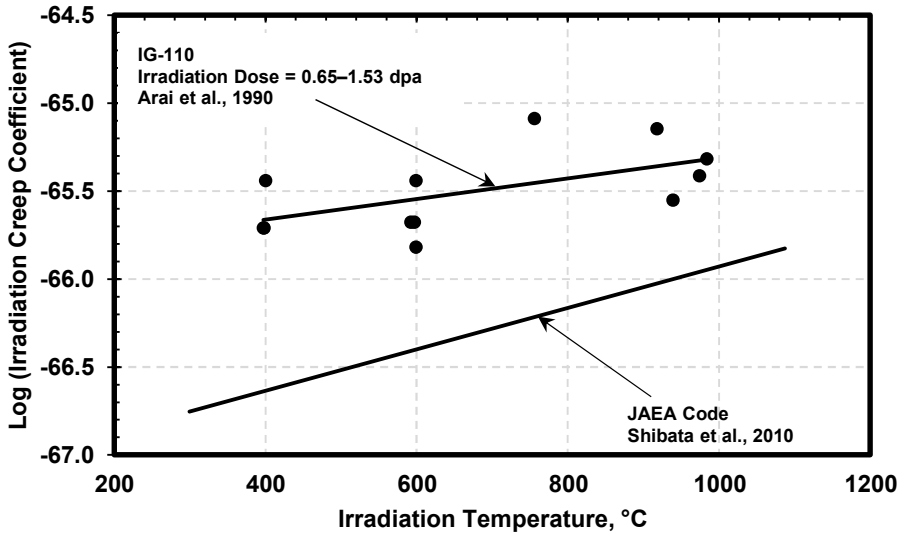

Figure 2-44 Temperature dependence of irradiation creep coefficient for IG-110 graphite

Table 2-11 Tensile Creep Coefficients for IG-110 (Arai et al., 1990)

Irradiation Temp, °C	Dose, dpa	Stress, MPa	Creep Coeff. (10^{-29} m^2/MPa)
397	0.876	7.50	2.9
398	1.241	9.17	2.9
400	1.241	7.50	3.8
592	1.533	11.00	3.0
597	1.022	9.17	3.0
599	0.730	9.12	3.8
599	1.314	11.40	2.6
756	0.650	9.05	5.4
918	0.876	9.03	5.1
939	1.095	13.50	3.4
974	1.314	11.00	3.9
984	1.314	13.50	4.3

The irradiation secondary creep coefficient for IG-110 has been reported for three temperatures normalized to a stress of 20.7 MPa, as shown in Table 2-12 (Windes et al., 2019).

Table 2-12 Irradiation Secondary Creep Coefficient for IG-110 Normalized to a Stress of 20.7 MPa (Windes et al., 2019)

Irradiation Temperature, °C (°F)	Creep Coefficient K, (%/MPa-dpa)
600 (1,112)	0.020
625 (1,157)	0.018
820 (1,508)	0.028

Considering the difficulties in attaining and maintaining constant temperature in any materials irradiation program, it may be appropriate to interpret this information as effectively giving the same creep coefficient for an average temperature of about 600 degrees C (1,112 degrees F). Because the data are so limited, not much can be concluded from these values in relation to the overall phenomenon of irradiation creep in IG-110 graphite other than the creep coefficient increases at 820 degrees C (1,508 degrees F), which is expected.

2.36. Coefficient of Thermal Expansion

Irradiation affects the CTE because shrinkage causes porosity to decrease with dose, until the turnaround.

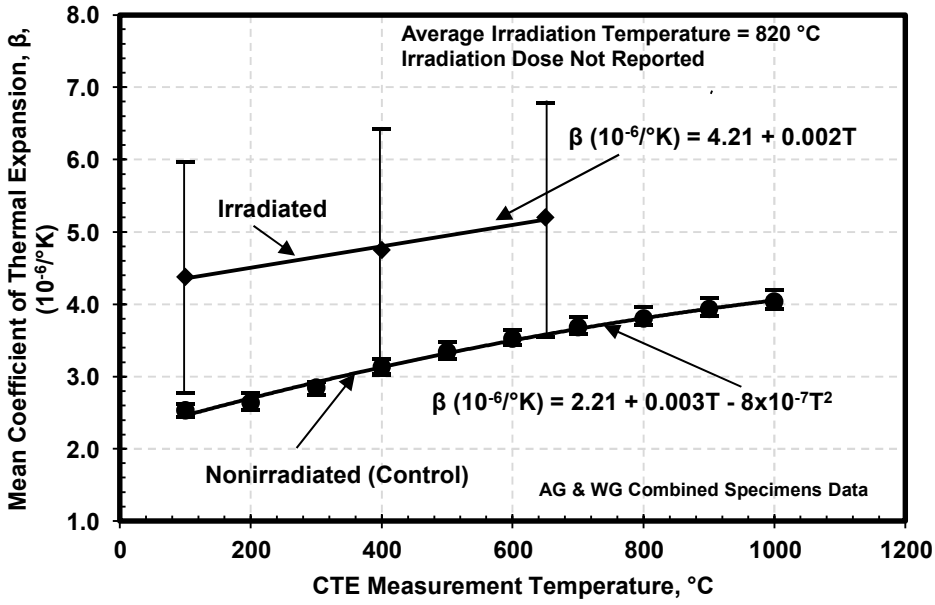

Figure 2-45 Nonirradiated and irradiated CTE for IG-110 (Windes et al., 2017b)

Figure 2-45 shows a comparison of CTE between nonirradiated and irradiated IG-110 as a function of temperature, derived from the investigations by Windes et al. (2017b). Windes et al. measured CTE in both WG and AG orientations, before and after irradiation. Wider data scatter was observed for irradiated specimens than for baseline nonirradiated specimens. The doses

varied for the individual irradiated specimens; this, together with the microstructural variations within a CTE test population, could explain the observed scatter. Also, the CTE data were not corrected for the effect of creep stress resulting from internal (shrinkage) stress. Measurements were made after irradiation, with potential relaxation of stresses, which may have varied across specimens in the CTE test population or dataset.

The effect of creep stress, which varies with irradiation dose, is to increase the room-temperature CTE after irradiation, as shown in Figure 2-46 (Snead et al., 2016). The data show that, after irradiation at 400 degrees C (752 degrees F) with an applied compressive stress of 5.4 MPa, the relative increase in mean CTE increases with cumulative irradiation dose for the range indicated. Here, the experiments address CTE in the WG orientation of the sample.

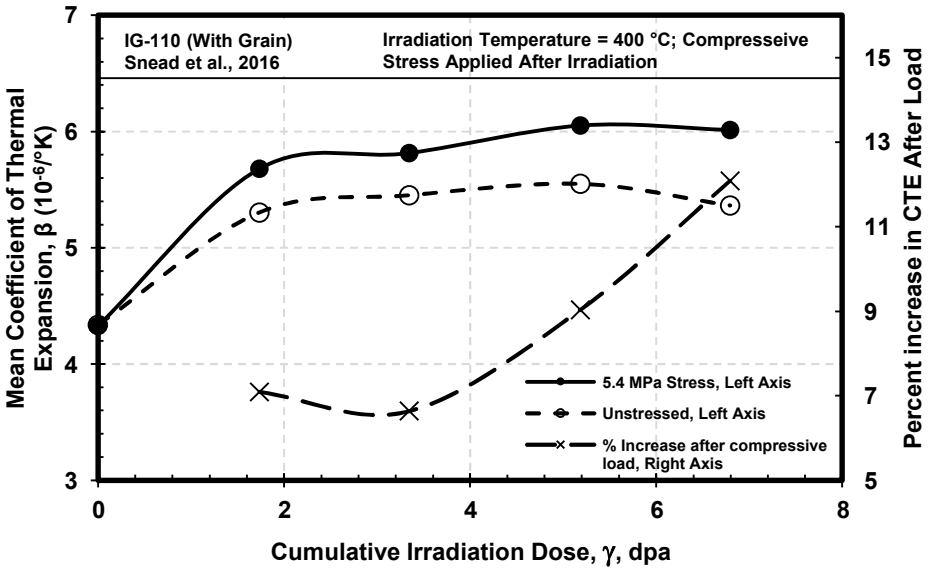

Figure 2-46 Effect of creep stress on CTE of irradiated IG-110, with CTE measured at 400 degrees C (averaged from 20 degrees C to 400 degrees C) (Snead et al., 2016)

On the other hand, the results of Windes et al. (2015) suggest that the percent change in CTE may not vary with irradiation temperature, as indicated for various compressive applied stresses during irradiation (Figure 2-47). Here, the mean CTE was measured at 500 degrees C (932 degrees F) for samples irradiated at various temperatures; however, the doses for the samples were not the same. The trend seems to be that CTE change increases with increased applied stress but with a tendency to reach saturation. Also, relaxation in CTE is possible after 500 degrees C (932 degrees F).

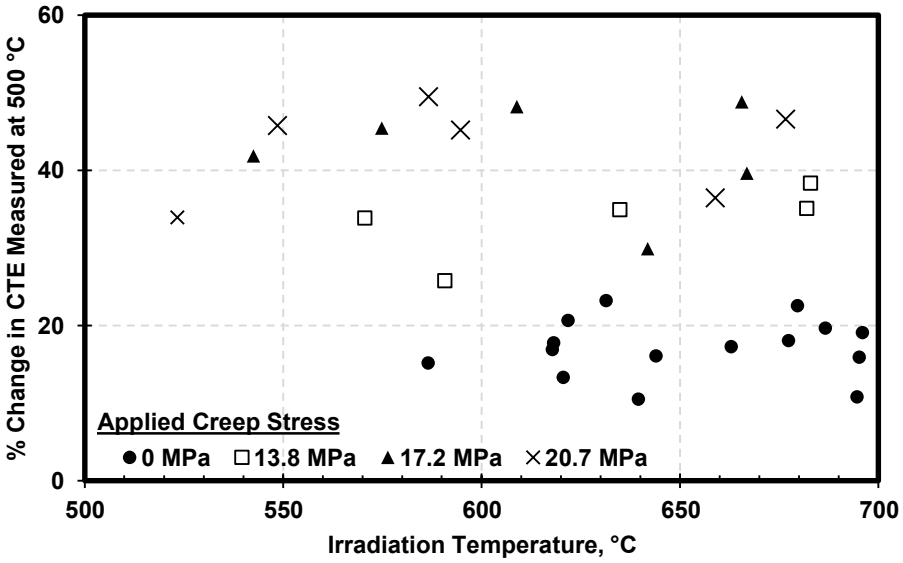

Figure 2-47 Effect of creep stress on mean CTE change as a function of irradiation temperature (CTE dependence on irradiation dose is not presented) (Windes et al., 2015)

Interestingly, the mean CTE change after irradiation seems to depend on grain orientation, irradiation temperature, and dose, as shown in Figure 2-48 (Campbell and Katoh, 2017). Because of the limited number of test observations, it is not possible to observe the trend for grain orientation from these data; however, such details can be further analyzed if data on x-ray diffraction pole figures become available. In their work, Campbell and Katoh observed that CTE decreases, rather than increasing, for doses above 10 dpa for all irradiation temperatures.

To add to the complexity of CTE behavior under irradiation, creep also plays a significant role, as shown in Figure 2-46 and Figure 2-47. Generally, the CTE increases with irradiation dose for a given measurement temperature, as shown in Figure 2-49. Furthermore, the CTE increases with the measurement temperature for both nonirradiated and irradiated IG-110 graphite; however, the incremental rate of increase is higher for irradiated graphite.

Figure 2-50 and Figure 2-51 depict the change in mean CTE with irradiation dose for IG-110. The Petten data (Figure 2-50) indicate that the CTE generally increases up to an approximate dose of 2 dpa, after which it decreases. The irradiation temperature here is 750 degrees C (1,382 degrees F). The JAEA draft code data (Figure 2-51) show a similar trend, with peaking at different values depending on the irradiation temperature. Generally, the observed peak CTE value tends to decrease with the irradiation temperature.

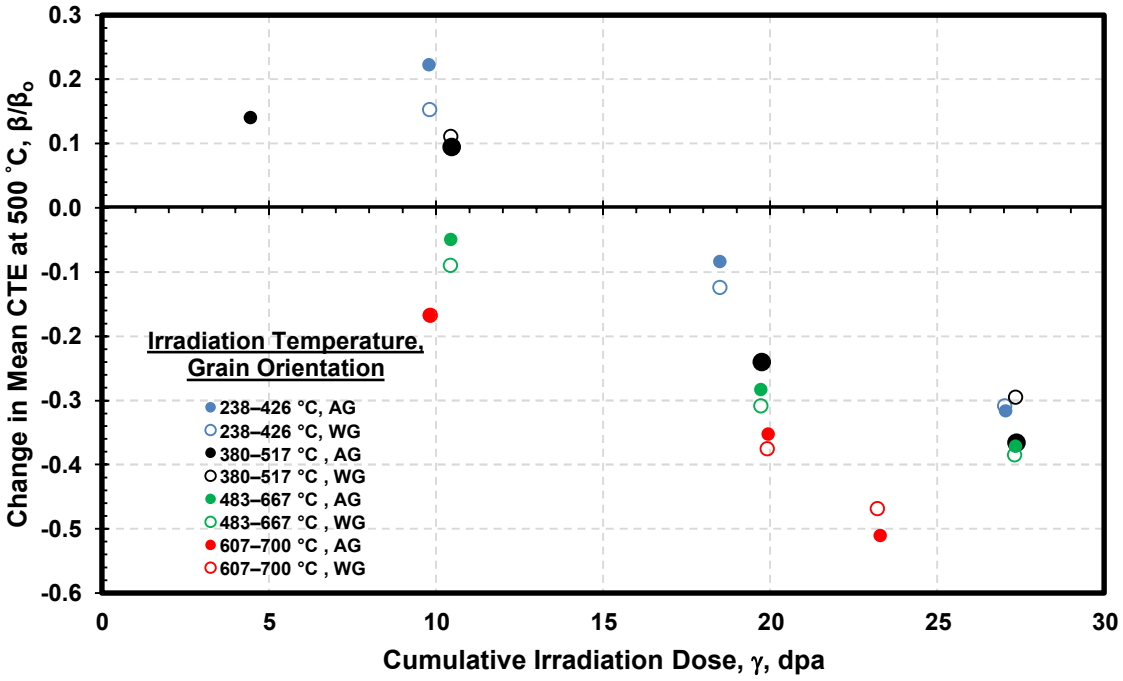

Figure 2-48 Mean CTE change with irradiation dose for various irradiation temperatures, for AG and WG orientations (Campbell and Katoh, 2017)

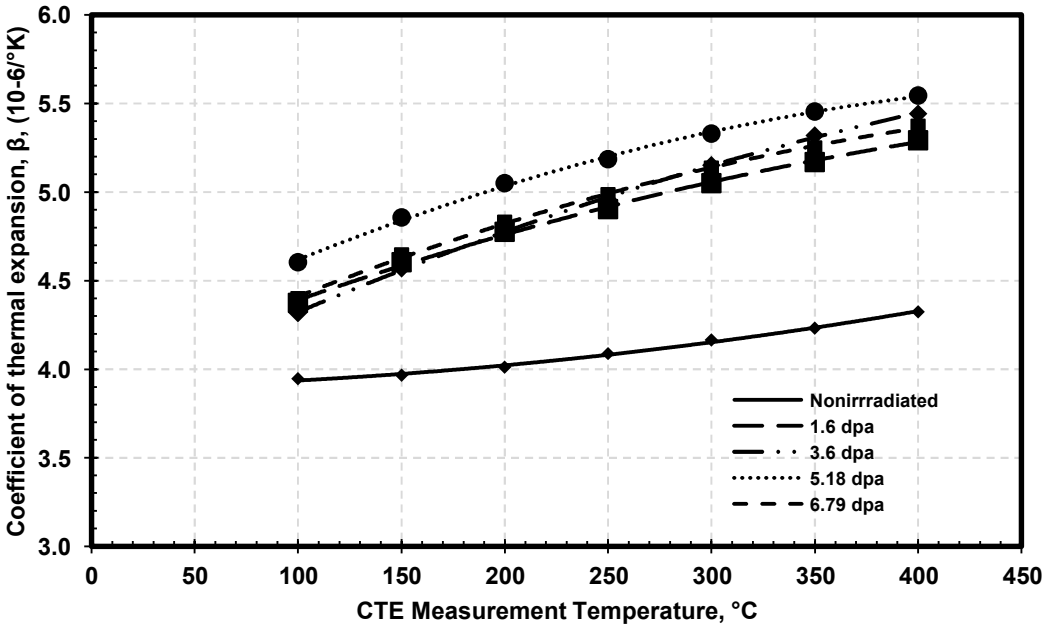

Figure 2-49 Effects of irradiation on CTE variation with temperature (irradiation temperature is about 425 degrees C (797 degrees F)) (Snead et al., 2016)

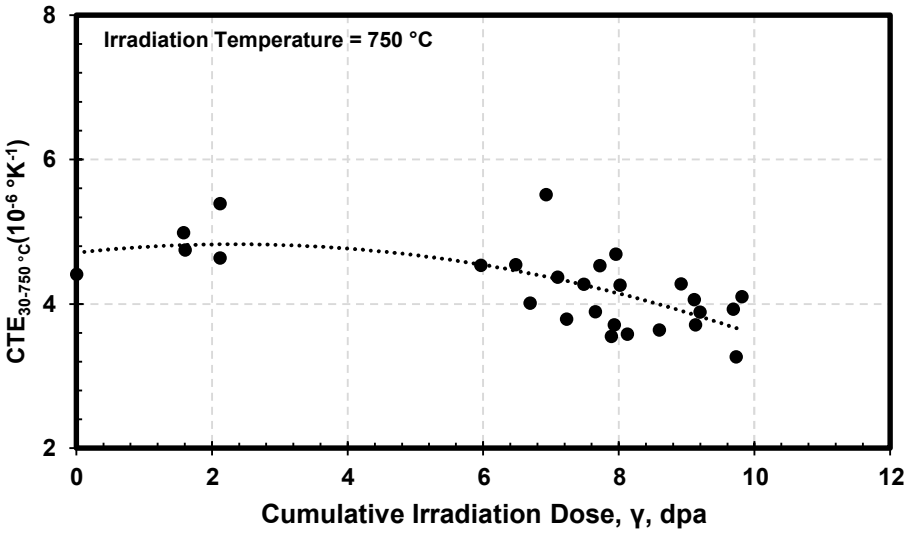

Figure 2-50 Effect of irradiation on CTE (Heijna et al., 2017)

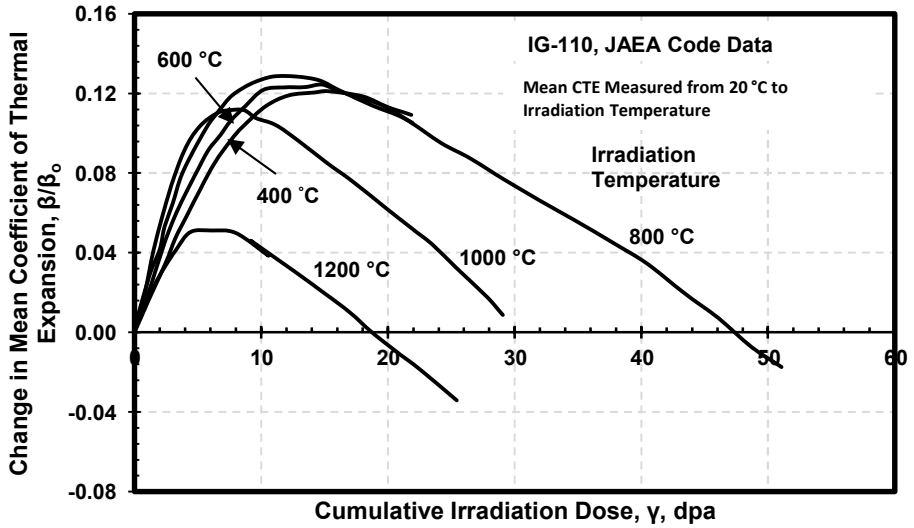

Figure 2-51 Change in CTE with dose at various irradiation temperatures (Shibata et al., 2010)

Kunimoto et al. (2009) also extended their irradiation experiments to higher doses at lower temperatures, interpolating and extrapolating the data using specific models that they had developed both for HTTR design and to expand the database for future VHTR design. Figure 2-52 shows these interpolated and extrapolated data.

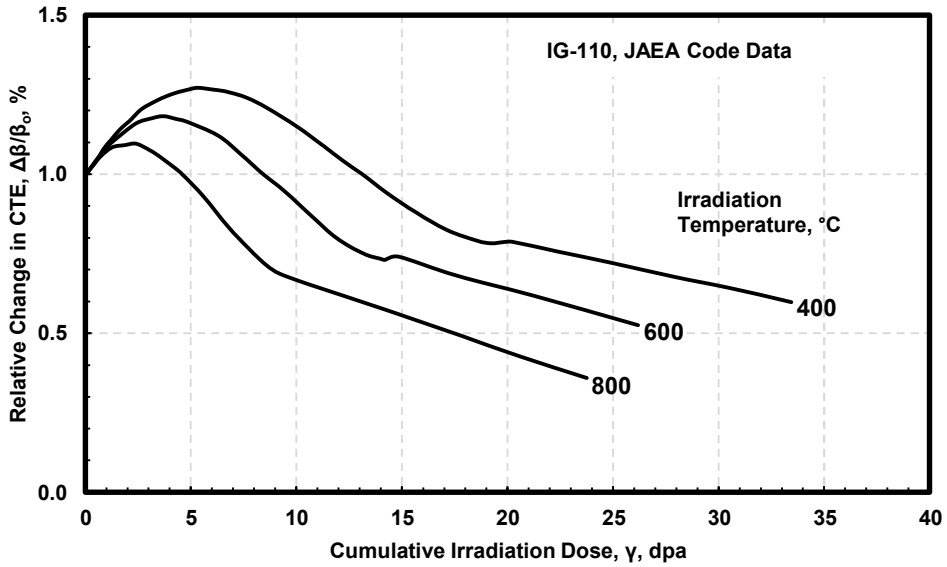

Figure 2-52 Change in CTE with dose at the temperatures shown (Shibata et al., 2010, based on Kunimoto et al., 2009)

2.37. Strength

The strength of graphite tends to increase with irradiation. The data shown in Figure 2-53 indicate a slight increase in the bend strength with irradiation of IG-110 graphite.

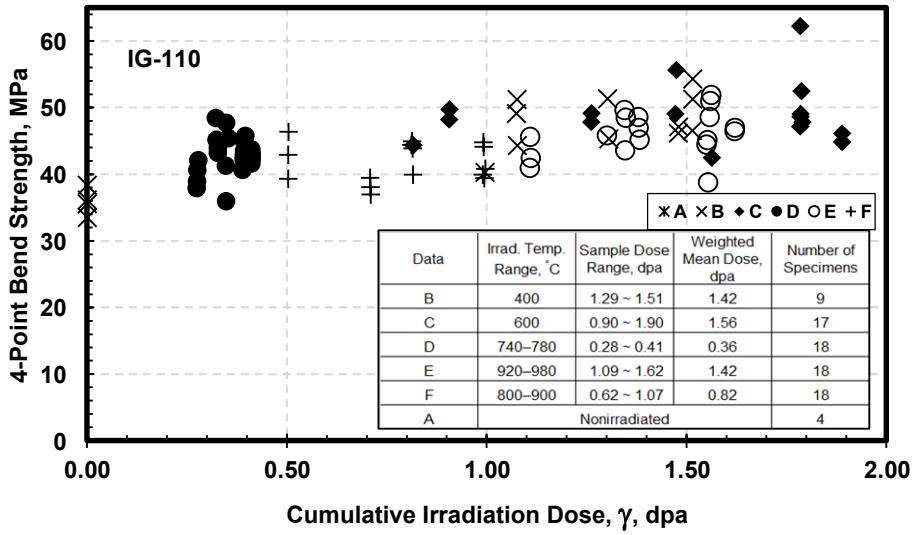

Data	Irrad. Temp. Range, °C	Sample Dose Range, dpa	Weighted Mean Dose, dpa	Number of Specimens
B	400	1.29 ~ 1.51	1.42	9
C	600	0.90 ~ 1.90	1.56	17
D	740–780	0.28 ~ 0.41	0.36	18
E	920–980	1.09 ~ 1.62	1.42	18
F	800–900	0.62 ~ 1.07	0.82	18
A	Nonirradiated			4

Figure 2-53 Dose dependence of four-point bend strength of IG-110 graphite, irradiated at temperatures shown (Ugachi et al., 1990)

As is typical, the scatter in the data is due to multiple factors, including the natural specimen-to-specimen variation in the microstructure of irradiated graphite, especially variation in pore density and pore morphology.

The JAEA draft code (Shibata et al., 2010) also refers to the dependence of tensile strength on irradiation dose, based on interpolation and extrapolation of data from Kunimoto et al. (2009). This is shown in Figure 2-54. It is seen that the irradiated strength behavior mirrors the irradiated elastic modulus behavior, which is shown in Figure 2-58.

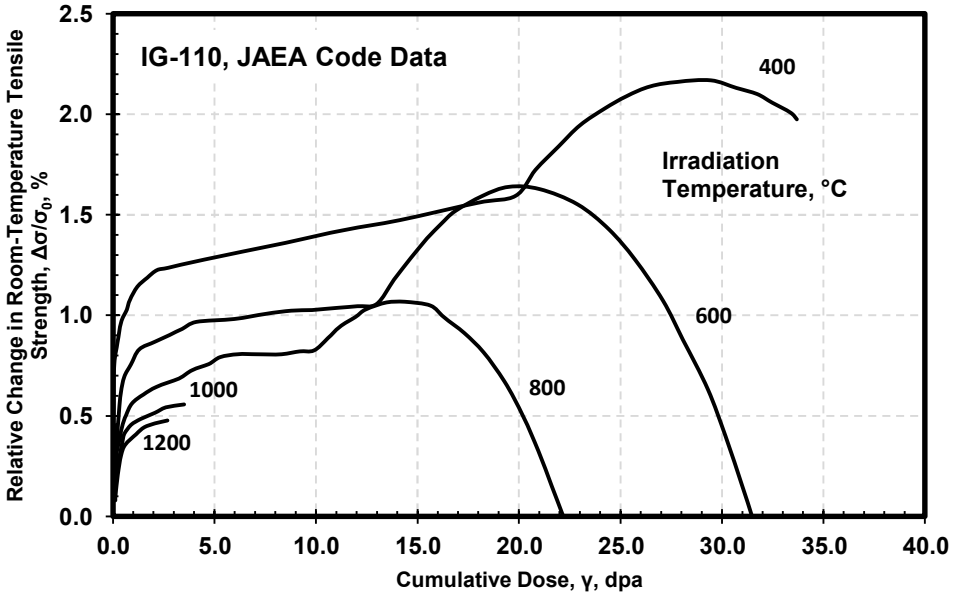

Figure 2-54 Change in tensile strength after irradiation for IG-110 graphite (Shibata et al., 2010)

2.38. Elastic Modulus

As mentioned previously, the fundamental change in microstructure due to irradiation is the closure of micropores and microcracks, which increases the density. Thus, Young's modulus increases with density, as shown in Figure 2-5, which includes the data on nonirradiated IG-110 shown in Figure 2-55. The increase in modulus due to irradiation has also been attributed to the pinning of the crystallite basal planes resulting from atomic displacements.

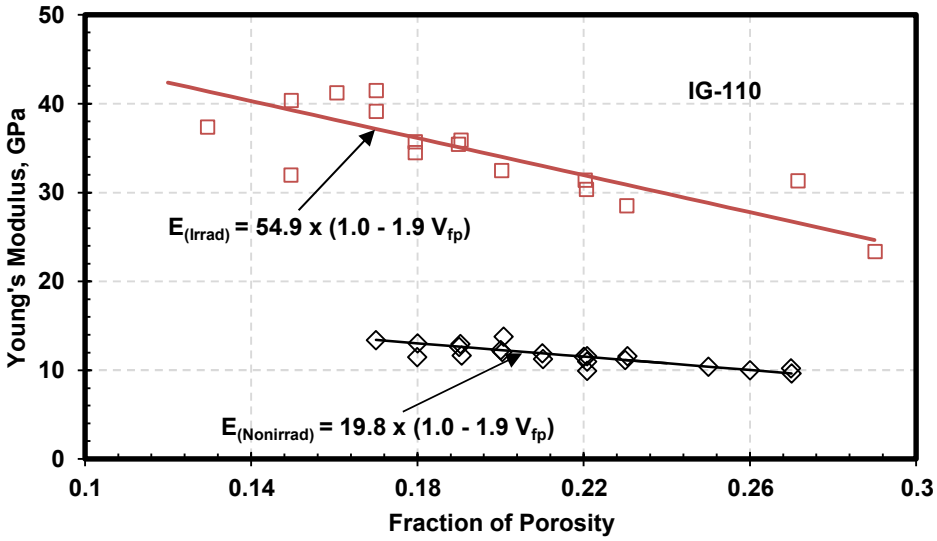

Figure 2-55 Irradiated and nonirradiated Young's modulus dependence of IG-110 graphite on the fraction of porosity (Maruyama et al., 1995)

At all irradiation temperatures, the graphite lattice contraction occurs very early in the irradiation process, leading to a decrease in the overall volume. Elastic modulus, which depends on density and the pinning of crystallite basal planes, increases with increasing cumulative irradiation dose (see Figure 2-56 to Figure 2-58).

The initial rapid increase in Young's modulus is seen at all irradiation temperatures, as shown in Figure 2-56. However, the degree of change decreases as a function of dose, primarily because of decreasing shrinkage and the inability to fully close the microvoids and microcracks. At higher temperatures, although the irradiated modulus is higher than the nonirradiated modulus, saturation sets in, primarily because of "annealing" of the internal stresses caused by irradiation shrinkage.

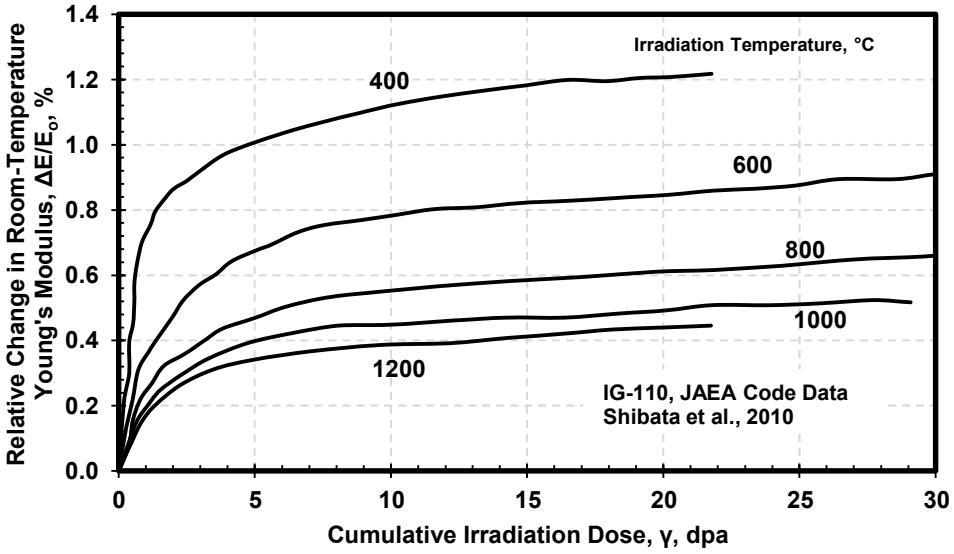

Figure 2-56 Irradiation dose effect on room-temperature Young's modulus as a function of irradiation temperature (data from Shibata et al., 2010)

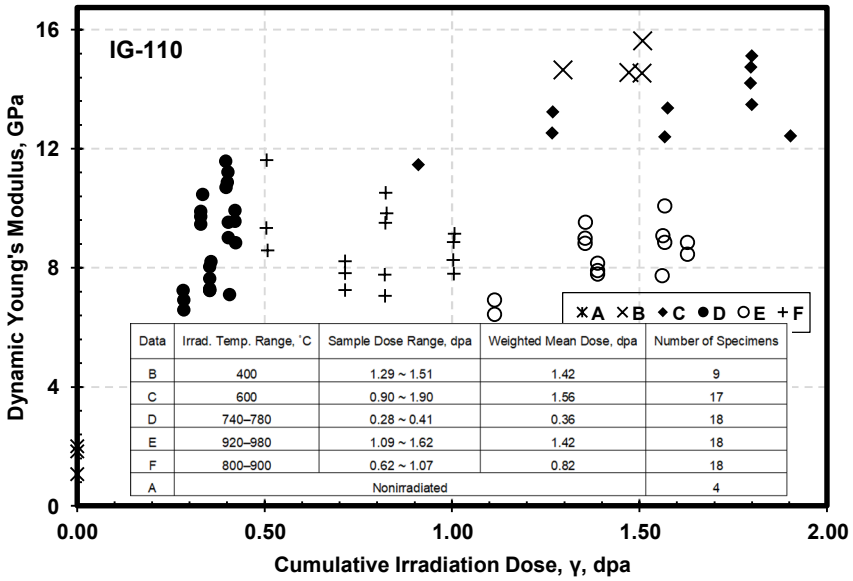

Data	Irrad. Temp. Range, °C	Sample Dose Range, dpa	Weighted Mean Dose, dpa	Number of Specimens
B	400	1.29 ~ 1.51	1.42	9
C	600	0.90 ~ 1.90	1.56	17
D	740–780	0.28 ~ 0.41	0.36	18
E	920–980	1.09 ~ 1.62	1.42	18
F	800–900	0.62 ~ 1.07	0.82	18
A	Nonirradiated			4

Figure 2-57 Dose dependence of dynamic Young's modulus of IG-110 graphite, irradiated at temperatures shown (data from Ugachi et al., 1990)

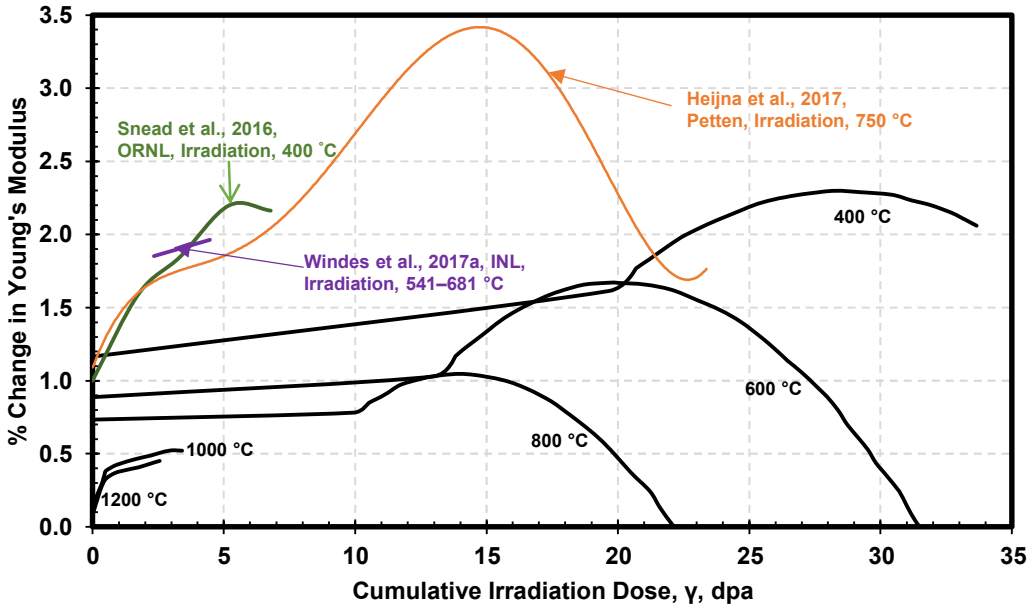

Figure 2-58 Change in Young's modulus with irradiation dose and irradiation temperature for IG-110

The Petten irradiation data, from Heijna et al. (2017), extend to higher irradiation doses at an irradiation temperature of 750 degrees C (1,382 degrees F). However, in the irradiation data from other laboratories, most of the increase in Young's modulus seems to occur within the first 5-dpa dose. The Petten data represent a regression analysis fit of the original data using the following fifth-order polynomial:

$$\Delta E(\%) = 1.0898 + 0.479\gamma - 0.1351\gamma^2 + 0.0185\gamma^3 - 0.001\gamma^4 + 2 \times 10^{-5}\gamma^5.$$

The data of Snead et al. (2016) represent measurements made in the WG direction. These data reflect variations in irradiation temperature and dose for the samples tested; the reader should be aware of this in attempting to interpret any irradiated properties data for graphites. The HTTR operated at a relatively low dose of less than 2 dpa.

Care is needed in interpreting the above data, because applied load (creep) may affect Young's modulus. The creep modulus, however, is separate from this; it is related to relative change in strain versus change in dose.

Windes et al. (2017a) reported the change in shear modulus as a function of irradiation dose, as shown in Figure 2-59. Within the observed data scatter, shear modulus appears to increase moderately with temperature, after irradiation to a dose of approximately 4 dpa.

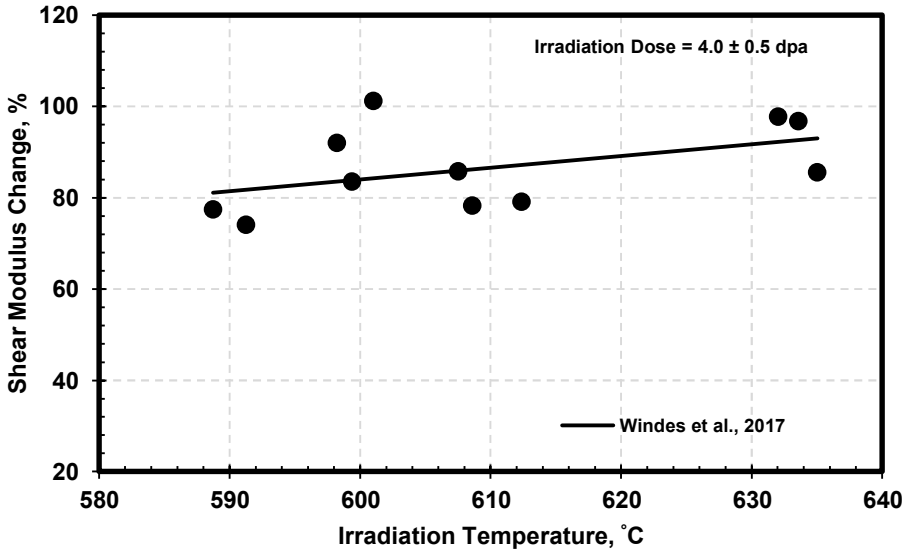

Figure 2-59 Effect of irradiation on change in shear modulus as a function of temperature (Windes et al., 2017a)

2.39. Thermal Conductivity

The specific heat of irradiated IG-110 has been found to vary with temperature in a manner almost identical to that of the specific heat of nonirradiated IG-110, as shown in Figure 2-60 (Maruyama et al., 1995). This reaffirms that the specific heat of graphite does not depend on its porosity or density. Thus, the dependence of thermal conductivity on irradiation should be proportional to the changes in thermal diffusivity caused by changes in pore morphology due to irradiation-induced changes in the graphite crystal structure.

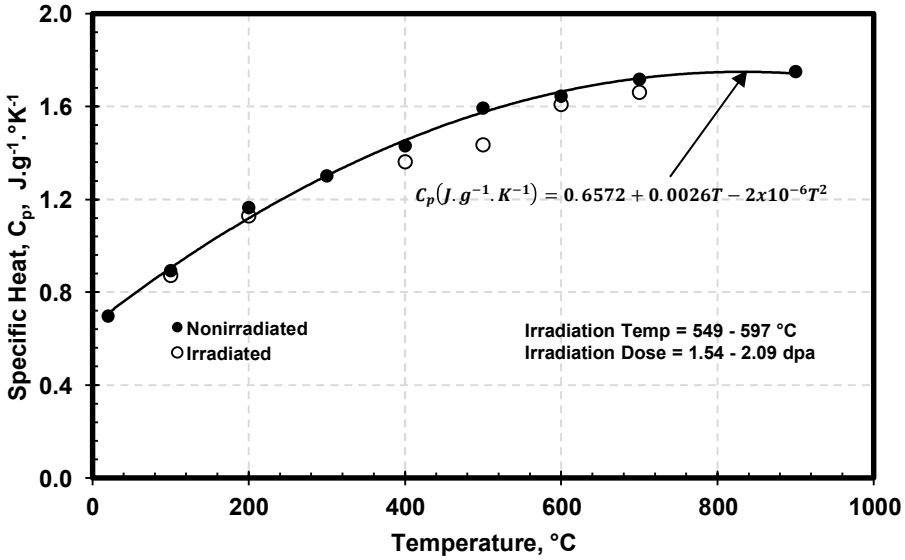

Figure 2-60 Temperature dependence of specific heat for IG-110 graphite (data from Maruyama et al., 1995)

Irradiation affects thermal conductivity, with the change in thermal conductivity depending on the irradiation dose and temperature. This is shown in Figure 2-61 (Shibata et al., 2010), where the relative change in thermal conductivity is plotted against irradiation dose for various irradiation temperatures. Rapid decrease occurs at lower irradiation doses and temperatures. Major closure of microporosity and microcracks occurs because of graphite crystal lattice shrinkage during early stages of irradiation and at lower temperatures, typically less than 500–600 degrees C (932–1,112 degrees F). At temperatures over 600 degrees C (1,112 degrees F), annealing of the residual (shrinkage) stresses occurs, leading to the partial restoration of the graphite microstructure. Thus, recovery in thermal conductivity occurs to some extent. The specimens irradiated at Petten (Heijna et al., 2017) at an irradiation temperature of 750 degrees C (1,382 degrees F) show a more rapid decrease in relative change to thermal conductivity. The data of Campbell and Katoh (2017), obtained at the same temperature, complement the data of Heijna et al. (2017), but the decrease is continuous, with no plateau observed, in contrast to the Shibata et al. (2010) data.

Figure 2-62 shows the temperature dependence of thermal conductivity, with data cited from various investigations. The lines represent a best-fit polynomial for the data. The upper part of Figure 2-62, shaded light blue, provides the data for nonirradiated IG-110 graphite. Much of the wide variation observed may be due to variability in the graphite used by different investigations. Notably, however, the variations are minimal for irradiated data, which are shown at the bottom of Figure 2-62, shaded light red. The irradiated data represent a dose range of 1.54–24.8 dpa and temperatures of 375–650 degrees C (707–1,202 degrees F). It is further observed that after irradiation, thermal conductivity does not vary significantly with temperature. For accident conditions, modeling would likely use the most conservative data; however, this is not specified in the ASME BPVC which mainly concerns structural integrity and does not address minimum requirements for heat dissipation during accidents.

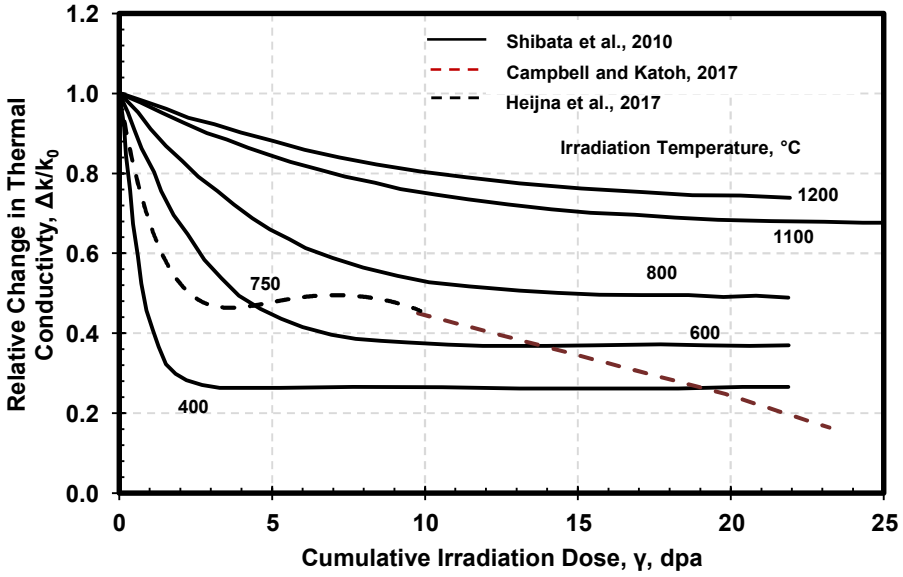

Figure 2-61 Dependence of thermal conductivity on irradiation dose for IG-110 graphite

Thermal conductivity is attributed to lattice vibrations. Defects due to irradiation defects in the graphite crystallite will lead to phonon/phonon scattering, reducing thermal conductivity. This effect eventually plateaus. However, at high fluence (over 10 dpa), as the graphite microstructure cracks because of high dimensional change, there is a secondary decrease in thermal conductivity.

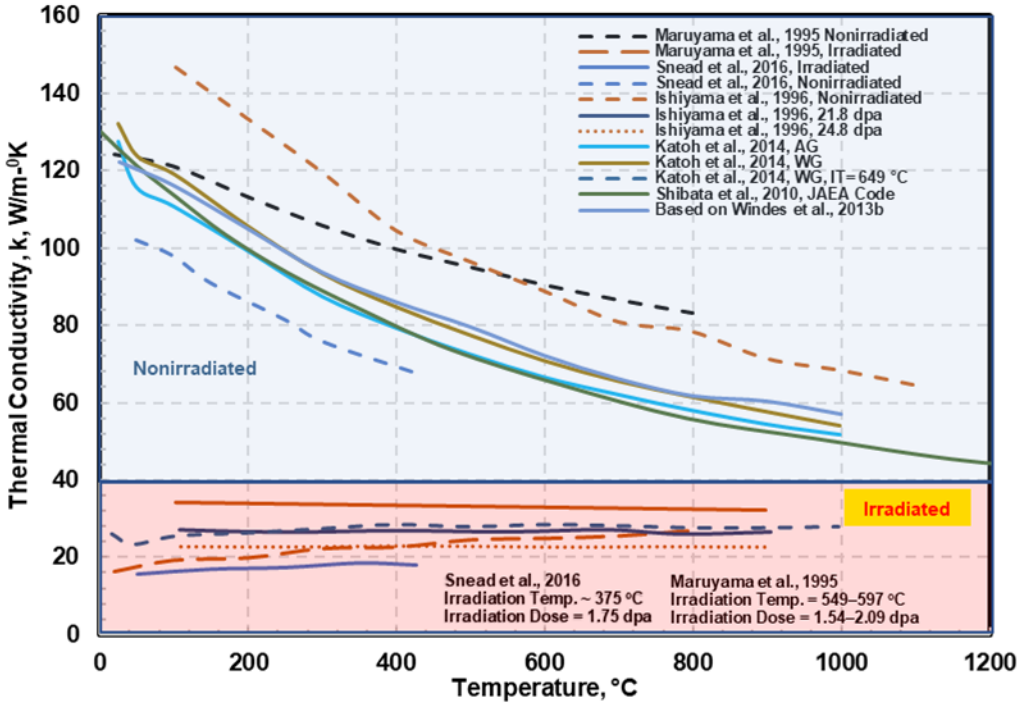

Figure 2-62 Temperature dependence of thermal conductivity for nonirradiated and irradiated IG-110 graphite

After irradiation, thermal conductivity increases slightly with temperature, as shown in Figure 2-62, which also shows the dependence of nonirradiated thermal conductivity on temperature. Irradiated thermal conductivity is substantially lower than the nonirradiated thermal conductivity at all measurement temperatures.

Irradiation creep also influences thermal conductivity because of the microstructural changes it causes. Figure 2-63 shows this effect (Snead et al., 2016). In these experiments, the measurements were made after samples were irradiated at 375 degrees C (707 degrees F) up to a dose of 1.75 dpa, with an applied creep stress of 5 MPa. Here again, after irradiation, thermal conductivity increases slightly with temperature. The change is small; the irradiation temperatures of the control and irradiated samples may have been different.

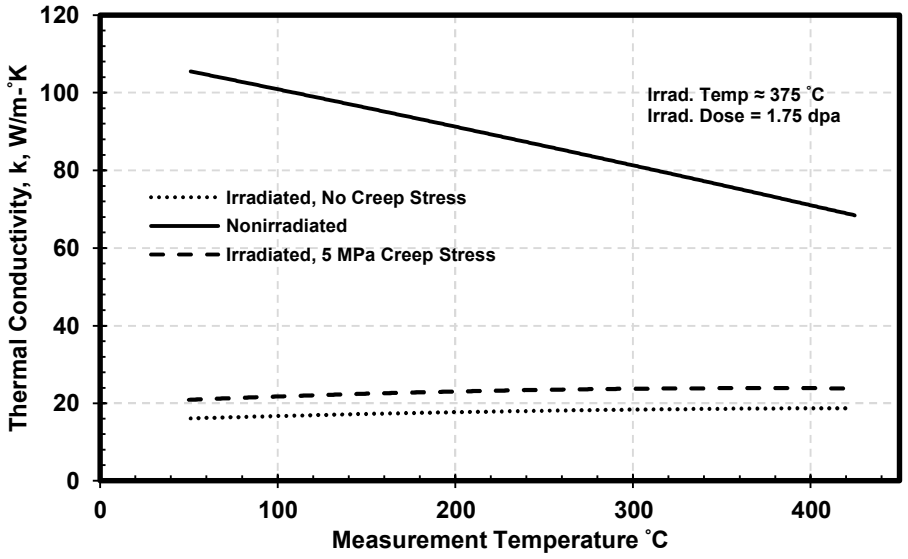

Figure 2-63 The effect of creep stress on thermal conductivity for IG-110 in the WG direction (Snead et al., 2016)

Figure 2-64 shows the effect of applied creep stress on the relative change in thermal conductivity of nonirradiated and irradiated IG-110 graphite (Snead et al., 2016); these values are derived from the data in Figure 2-63.

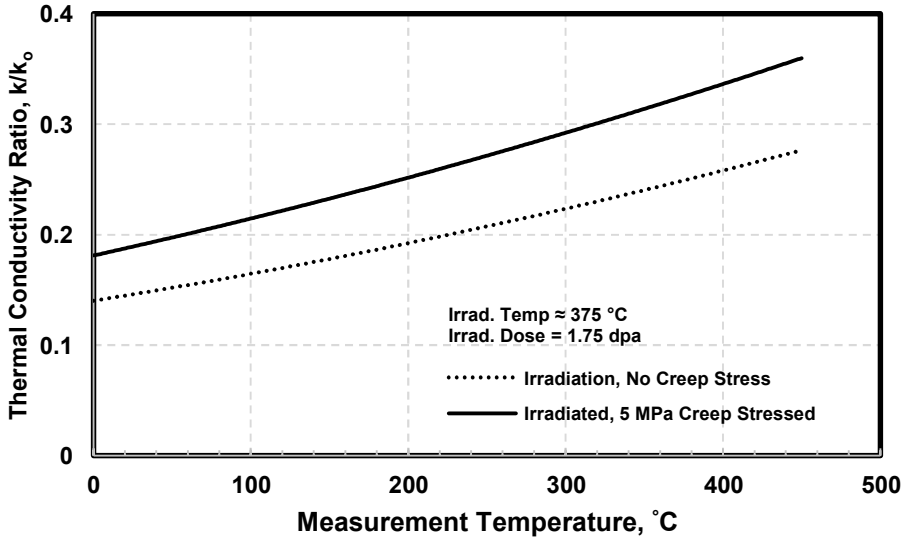

Figure 2-64 Effect of creep stress on normalized thermal conductivity for IG-110 (Snead et al., 2016)

2.40. Chemical Analysis of IG-110

Table 2-13 reports the chemical analyses of IG-110 graphite from several investigations, in weight parts per million (wppm), while Table 2-14 provides the manufacturer's stated analysis.

Table 2-13 Chemical Elemental Analysis (wppm) of IG-110 Graphite

Element	Lee et al., 2014	Lee et al., 2018	Wu et al., 2018, GDMS
Ash		<10	
B	0.15	0.03	
Si	0.15	1.6	18
Ca	0.08	<0.05	4.5
Fe	0.06	<0.01	0.55
Al	0.012	<0.05	6.9
Na		<0.05	
K	0.04	<0.1	7.1
V	0.018	<0.01	3.2
Cd		<0.1	
Ni		<0.1	1.1
Cr		<0.5	1.1
Co		<0.05	
Gd		<0.05	
Sm		<0.05	
Li		<0.01	14
Mg		<0.5	1.4
Be			0.08
F			16
As			2.4
O			12
S			29
Cl			4.1

In the above table, the analysis of Wu et al. (2018) using glow discharge mass spectrometry (GDMS) seems to identify an unusually high level of impurities for IG-110 nuclear graphite, which is purified at least twice, using halogen and chemical purification steps (Toyo Tanso, 2013).

Table 2-14 lists the purity levels given in the Toyo Tanso product brochure for high-purity graphite, which the company states is purified by a halogen treatment.

Table 2-14 Typical Elemental Analysis of Toyo Tanso High-Purity Graphite

Element	[wppm]	Measurement Method†	Element	[wppm]	Measurement Method†
Li	<0.001	ICP-MS	V	0.018	ICP-MS
B	0.15	ICP-MS	Cr	0.006	ICP-MS
Na	<0.002	ICP-MS	Mn	<0.001	ICP-MS
Mg	0.004	ICP-MS	Fe	0.06	ICP-MS
Al	0.012	ICP-MS	Co	<0.001	ICP-MS
Si	<0.1	UV	Ni	0.006	ICP-MS
K	0.04	FL-AAS	Cu	<0.002	ICP-MS
Ca	0.08	FL-AAS	Zn	<0.003	ICP-MS
Ti	<0.001	ICP-MS	Pb	<0.004	ICP-MS

† ICP-MS = inductively coupled plasma mass spectrometry; UV = absorption spectrophotometry; FL-AAS = flameless atomic absorption spectrometry.

3. Sigri Great Lakes Carbon NBG-17 Graphite

3.1. Information Pertaining to ASME Material Data Sheet for NBG-17 Graphite

Table 3-1 provides properties information for NBG-17 graphite, following the ASME graphite code MDS format. For each property, the table cites the corresponding section of this report, which contains further information extracted from publicly available data.

3.2. Material Grade

The material grade is NBG-17.

3.3. Material Specification ID

This identifies the construction specification for the graphite grade applicable to this MDS. The designer enters this value.

3.4. ASTM Specification

This is the Mandatory Appendix HHA-I material specification (ASTM) number that applies to the manufacture of the material. The designer enters this number.

Table 3-1 Example ASME MDS for NBG-17 Graphite

ASME BPVC-III-5-2017, FORM MDS-1 MATERIAL DATA SHEET (SI UNITS)															
Grade Designation															
Material grade	NBG-17			(1) Material grade: The manufacturer's grade designation that complies with the requirements of the Mandatory Appendix HHA-I material specification.											
Material spec. ID	Not applicable			(2) Material spec. ID: The construction specification for the graphite grade applicable to this MDS.											
ASTM spec.	ASTM D7219-08			(3) ASTM spec: The Mandatory Appendix HHA-I material specification (ASTM) number that applies to the manufacture of the material.											
Max. grain size (mm) (Section 3.5)	0.8 (Lee et al., 2018)			(4) Maximum grain size: The maximum filler particle grain size that is used in the mix formulation. (For isostatically pressed graphite, report mean grain size.)											
Designation				(5) Designation: Material designation as defined in the Mandatory Appendix HHA-I material specification.											
Temperature-Dependent Parameters															
Property	Units														
Bulk density (Section 3.7)	kg/m^3	Mean	Std. Dev						(6) Bulk density: The material bulk density. Mean and standard deviation of material test specimen results.						
		1.883 (Windes et al., 2015)	0.017												
Strength—tensile (Section 3.8)	MPa	WG	20 °C	200 °C	400 °C	600 °C	800 °C	1,000 °C (see Note 1 below)							
		Mean							(7) Strength, tensile: Mean and standard deviation of material test specimen results. Note that the temperature dependence of only one strength parameter need be determined; the others can be assumed to change by the same relative amount.						
		Std. Dev.													
	MPa	AG	20 °C	200 °C	400 °C	600 °C	800 °C	1,000 °C							
		Mean													

ASME BPVC-III-5-2017, FORM MDS-1 MATERIAL DATA SHEET (SI UNITS)															
		Std. Dev.													
Strength—flexural (four-point) (Section 3.9)	MPa	WG	20 °C	200 °C	400 °C	600 °C	800 °C	1,000 °C	(8) Strength, flexural (four-point): Mean and standard deviation of material test specimen results. Note that the temperature dependence of only one strength parameter need be determined; the others can be assumed to change by the same relative amount.						
		Mean													
		Std. Dev.													
	MPa	AG	20 °C	200 °C	400 °C	600 °C	800 °C	1,000 °C							
		Mean													
		Std. Dev.													
Strength—compressive (Section 3.10)	MPa	WG	20 °C	200 °C	400 °C	600 °C	800 °C	1,000 °C	(9) Strength, compressive: Mean and standard deviation of material test specimen results. Note that the temperature dependence of only one strength parameter need be determined; the others can be assumed to change by the same relative amount.						
		Mean													
		Std. Dev.													
	MPa	AG	20 °C	200 °C	400 °C	600 °C	800 °C	1,000 °C							
		Mean													
		Std. Dev.													
Elastic modulus (dynamic) (Section 3.11)	GPa	WG	20 °C	200 °C	400 °C	600 °C	800 °C	1,000 °C	(10) Elastic modulus (dynamic): Mean and standard deviation of material test specimen results.						
		Mean													
		Std. Dev.													
		AG	20 °C	200 °C	400 °C	600 °C	800 °C	1,000 °C							
		Mean													

ASME BPVC-III-5-2017, FORM MDS-1 MATERIAL DATA SHEET (SI UNITS)															
		Std. Dev.													
Elastic modulus (static) (Section 3.12)	GPa	WG	20 °C	200 °C	400 °C	600 °C	800 °C	1,000 °C	(11) Elastic modulus (static): Mean and standard deviation. Use a measured value of the dynamic elastic modulus (10) scaled by the ratio between static and dynamic. Note that the dynamic and static modulus are related. Only one need be measured; the other can be computed from these measurements and the ratio between the two values.						
		Mean													
		Std. Dev.													
		AG	20 °C	200 °C	400 °C	600 °C	800 °C	1,000 °C							
		Mean													
		Std. Dev.													
Coefficient of thermal expansion (CTE), β (Section 3.13)	/°C	WG	20 °C	200 °C	400 °C	600 °C	800 °C	1,000 °C	(12) Coefficient of thermal expansion: Mean and standard deviation of material test specimen results. This property's temperature dependence shall be determined.						
		Mean													
		Std. Dev.													
		AG	20 °C	200 °C	400 °C	600 °C	800 °C	1,000 °C							
		Mean													
		Std. Dev.													
Thermal conductivity (Section 3.14)	W/m°K	WG	20 °C	200 °C	400 °C	600 °C	800 °C	1,000 °C	(13) Thermal conductivity: Mean and standard deviation of material test specimen results.						
		Mean													
		Std. Dev.													
		AG	20 °C	200 °C	400 °C	600 °C	800 °C	1,000 °C							
		Mean													

ASME BPVC-III-5-2017, FORM MDS-1 MATERIAL DATA SHEET (SI UNITS)															
		Std. Dev.													
Temperature-Independent Parameters															
Poisson's ratio (Section 3.15)									(14) Poisson's ratio: Mean and standard deviation of material test specimen results. As an alternative, a published historical value may be used.						
Anisotropy factor (Section 3.16)									(15) Anisotropy factor: Mean and standard deviation for the charges as described in the graphite specification (Mandatory Appendix HHA-I). The average of the charges is then given in the MDS.						
Critical stress intensity factor, K_{Ic} (Section 3.17)	MPa √ m								(16) Critical stress intensity factor (K_{Ic}): Mean and standard deviation of material test specimen results.						
Design Strength and Material Reliability Curve Values															
Ratio of compressive to tensile strength (R_{tc})	Data to be provided by the designer.								(17) Ratio of compressive to tensile strength (R_{tc}): Computed from the mean tensile and mean compressive strengths as published in (7) and (9) above. R_{tc} = Compressive Strength (9) ÷ Tensile Strength (7). This quantity is defined as positive.						
Ratio of flexural to tensile strength (R_{tf})	Data to be provided by the designer.								(18) Ratio of flexural to tensile strength (R_{tf}): Computed from the mean tensile and mean flexural strengths as published in (7) and (8) above. R_{tf} = Flexural Strength (8) ÷ Tensile Strength (7). This quantity is defined as positive.						
$S_{c95\%}$	MPa	Data to be provided by the designer.							(19) $S_{c95\%}$: The computed single-sided 95% confidence interval value for the Weibull characteristic strength that defines the material reliability curve. This is calculated in accordance with HHA-II-3100, based on the tensile strength measurements.						
$m_{95\%}$		Data to be provided by the designer.							(20) $m_{95\%}$: The computed single-sided 95% confidence interval value for the Weibull modulus that defines the material reliability curve. This is calculated in accordance with HHA-II-3100, based on the tensile strength measurements.						

ASME BPVC-III-5-2017, FORM MDS-1 MATERIAL DATA SHEET (SI UNITS)			
S_0	MPa	Data to be provided by the designer.	(21) S_0: The computed value for the threshold stress based on the three-parameter distribution that defines the material reliability curve. This is calculated in accordance with HHA-II-3200, based on the tensile strength measurements.
$S_{c095\%}$		Data to be provided by the designer.	(22) $S_{c095\%}$: The computed single-sided 95% confidence interval value for the characteristic stress based on the three-parameter distribution that defines the material reliability curve. This is calculated in accordance with HHA-II-3200, based on the tensile strength measurements.
$m_{095\%}$		Data to be provided by the designer.	(23) $m_{095\%}$: The computed single-sided 95% confidence interval value for the Weibull modulus based on the three-parameter distribution that defines the material reliability curve. This is calculated in accordance with HHA-II-3200, based on the tensile strength measurements.
S_g (10^{-4})	MPa	Data to be provided by the designer.	(24) S_g (10^{-4}): The design allowable stress value corresponding to the probability of failure of 10^{-4}, computed in accordance with HHA-II-3300 based on $S_{c95\%}$ and $m_{95\%}$ [(19) and (20) above].
S_g (10^{-3})	MPa	Data to be provided by the designer.	(25) S_g (10^{-3}): The design allowable stress value corresponding to the probability of failure of 10^{-3}, computed in accordance with HHA-II-3300 based on $S_{c95\%}$ and $m_{95\%}$ [(19) and (20) above].
S_g (10^{-2})	MPa	Data to be provided by the designer.	(26) S_g (10^{-2}): The design allowable stress value corresponding to the probability of failure of 10^{-2}, computed in accordance with HHA-II-3300 based on $S_{c95\%}$ and $m_{95\%}$ [(19) and (20) above].
S_g (5×10^{-2})	MPa	Data to be provided by the designer.	(27) $S_g(5\times10^{-2})$: The design allowable stress value corresponding to the probability of failure of 5×10^{-2}, computed in accordance with HHA-II-3300 based on $S_{c95\%}$ and $m_{95\%}$ [(19) and (20) above].

ASME BPVC-III-5-2017, FORM MDS-1 MATERIAL DATA SHEET (SI UNITS)									
Graphite Oxidation Effects									
Property	Units	2%	4%	6%	8%	10%			
Strength [.] (Section 3.21									(28) Oxidation change in strength: As either a chart or a curve that describes the mean behavior of the relative property change as a function of weight loss. This is expressed as a value normalized to the as-manufactured value and may be based on a strength parameter selected by the designer. The strength parameter used shall be recorded in an attachment to the MDS. The figures in HHA-3141 may be used as an alternative to measurements.
Elastic modulus (dynamic) [.] (Section 3.22)									(29) Oxidation change in elastic modulus (dynamic): As either a chart or a curve that describes the mean behavior of the relative property change as a function of weight loss. This is expressed as a value normalized to the as-manufactured value.
Thermal conductivity [.] (Section 3.23)									(30) Oxidation change in thermal conductivity: As either a chart or a curve that describes the mean behavior of the relative property change as a function of weight loss. This is expressed as a value normalized to the as-manufactured value.
Irradiated Graphite									
Property									
Dimensional change [.] (Section 3.24)									(31) Irradiation-induced dimensional change: This is the change in length, normalized to the initial length expressed as a percentage. The data shall be expressed as either a table of data or a mathematical fit, appended to the MDS. Range of applicability to be identified and checked as part of the design assessment.
Creep coefficient [.] (Section 3.25)									(32) Irradiation-induced creep coefficient: Shall be expressed as either a table of data or a mathematical fit, appended to the MDS. Range of applicability to be identified and checked as part of the design assessment. The creep coefficient to be used is the coefficient (or set of coefficients) required for the irradiation creep model proposed for use by the designer. The

ASME BPVC-III-5-2017, FORM MDS-1 MATERIAL DATA SHEET (SI UNITS)									
									model shall be recorded in an attachment to the MDS.
Coefficient of thermal expansion [.] (Section 3.26)									(33) Irradiation-induced change in coefficient of thermal expansion: Shall be expressed as either a table of data or a mathematical fit, appended to the MDS. Range of applicability to be identified and checked as part of the design assessment. This is expressed as a value normalized to the as-manufactured value. The temperature dependence of this property shall be determined.
Strength [.] (Section 3.27)									(34) Irradiation-induced change in strength: Shall be expressed as either a table of data or a mathematical fit, appended to the MDS. Range of applicability to be identified and checked as part of the design assessment. This is expressed as a value normalized to the as-manufactured value and shall be based on a strength parameter selected by the designer. The strength parameter used shall be recorded in an attachment to the MDS. Note that irradiation-induced change in strength need only be measured should the designer desire to take account of the strength increase at low or intermediate damage doses.
Elastic modulus [.] (Section 3.28)									(35) Irradiation-induced change in elastic modulus: This is expressed as a value normalized to the as-manufactured value.
Thermal conductivity [.] (Section 3.29)									(36) Irradiation-induced change in thermal conductivity: This is expressed as a value normalized to the as-manufactured value. The temperature dependence of this property shall be determined.
GENERAL NOTES:									
(a) WG and AG refer to the with- and against-grain orientations of the material.									
(b) [.] indicates a dimensionless quantity.									
NOTE:									
(1) If the maximum intended use temperature exceeds 1,000°C, then the temperature-dependent data shall be extended to cover the property values at the maximum intended use temperature.									

3.5. Maximum Grain Size

For near-isotropic graphite, the MDS guidance states that this value should be the mean particle size used in the mix formulation. The coke particle size distribution used in the manufacture of NBG-17 graphite is not publicly available and may be proprietary. The manufacturer has indicated that the maximum coke particle size is 0.8 mm (800 μm). However, Kim et al. (2013) have reported the maximum coke size to be 900 μm, while Huang et al. (2014) have reported a mean graphite particle size of 669 μm (observed in optical microscopy) and a maximum graphite grain size of 984 μm.

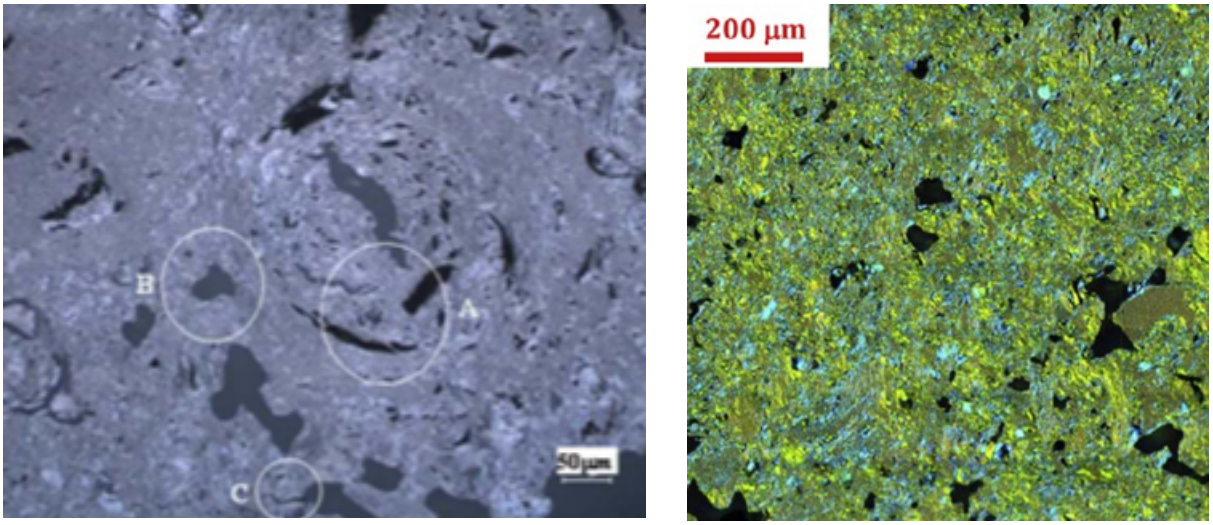

Figure 3-1 Optical microstructure of NBG-17 graphite (left, Kim et al., 2013; right, Contescu et al., 2018)

Some confusion arises from using the grain size to define whether a graphite is isotropic. It is the structure within the grain that is important. If that structure is both fine and isotropic, the coke can be defined as an isotropic coke. For example, Gilsocarbon has 0.5-mm grains, and magnification of a grain shows a microstructure consisting of very fine wavy and twisted graphite layers, which can be described as isotropic. On the other hand, PGA has needles about 1 mm long, and the grain microstructure is coarse and very anisotropic.

In the images above, NBG-17 graphite appears to have a fine, isotropic structure inside the grains.

3.6. Designation

As stated in Article HHA-I-1110, this can be either ASTM D7219-08 or ASTM D7301-08. The designer enters the designation. Since most of the data available for this report pertain to ASTM D7219-08, that is the designation entered in Table 3-1.

Temperature-Dependent Parameters

3.7. Bulk Density

As stated in ASTM D7219-08, NBG-17 graphite belongs to the molded, near-isotropic, high-purity (MNHP) class. Béghein et al. (2012) reported a density of 1.89 Mg/m^3 for this

material, while Kim et al. (2013) reported a density of 1.84 Mg/m^3. Research at INL has determined the variation in density, as shown in Table 3-2 (Windes et al., 2015 and 2017). From this work, the overall average can be calculated to be 1.883 Mg/m^3. The ASTM standard requires a minimum bulk density of 1.7 Mg/m^3 for graphites in the MNHP class. NBG-17 graphite meets this requirement.

Table 3-2 NBG-17 Graphite Density (Mg/m^3) from INL NGNP Research (Windes et al., 2015 and 2017)

Specimen Designation	Mean Value	Std. Dev.	COV††	Median Value	Upper Limit	Lower Limit
Piggyback (Combined)†	1.9028	0.0139	0.73	1.8998	1.9254	1.8783
Piggyback (AG)	1.9063	0.0094	0.49	1.9011	1.9167	1.8977
Piggyback (WG)	1.901	0.0159	0.83	1.898	1.9254	1.8783
Creep (Combined)	1.8621	0.0193	1.04	1.8631	1.9005	1.8227
Creep (AG)	1.8613	0.0251	1.35	1.8597	1.9363	1.7999
Creep (WG)	1.8629	0.0117	0.63	1.8655	1.8939	1.8291
All Specimens in Mechanical Properties Program	1.814*	0.0076	0.004	* Weibull mean of density measured in accordance with ASTM C559-90, obtained from two-parameter Weibull distribution data and parameters (Carroll, 2014)		

† Piggyback specimens are small ("button-sized") specimens 6 mm (0.25 inches) long, designed to permit measurements of changes in dimensions, density, and thermal diffusivity due to irradiation.

†† Coefficient of variation.

3.8. Tensile Strength

Béghein et al. (2012) reported the room-temperature tensile strength of NBG-17 graphite as 22 MPa; however, they did not report the number of samples tested or the standard deviation for the data. From Carroll's (2014) Weibull distribution data and parameters obtained in room-temperature tensile testing (ASTM C749-08) of 24 NBG-17 graphite specimens, the authors of this report have calculated a (Weibull) mean strength of 19.41 ± 1.89 MPa.

3.9. Flexural Strength (Four-Point)

Béghein et al. (2012) reported the flexural strength of NBG-17 graphite as 32 MPa; however, they did not report the test type (three-point bend or four-point bend), number of samples tested, or standard deviation. From Carroll's (2014) Weibull distribution data and parameters obtained in room-temperature four-point bend testing of 200 NBG-17 graphite specimens, conducted according to ASTM C651-11, the authors of this report have calculated a (Weibull) mean strength of 30.08 ± 1.99 MPa.

3.10. Compressive Strength

Béghein et al. (2012) reported the compressive strength of NBG-17 graphite as 90 MPa; however, they did not report the number of samples tested or the standard deviation. Chi (2009) reported a room-temperature compressive strength of 74.7 MPa but did not report the number of samples tested or the standard deviation. From Carroll's (2014) Weibull distribution data and parameters obtained in room-temperature compressive strength testing (ASTM C695-91) of 128 NBG-17 graphite specimens, conducted according to ASTM C651-10, the authors of this report have calculated a (Weibull) mean strength of 77.35 ± 5.59 MPa.

3.11. Elastic Modulus (Dynamic)

Béghein et al. (2012) reported Young's modulus of NBG-17 graphite as 11.9 GPa; however, they did not report the method of measurement. INL investigators doing NGNP research (Windes et al., 2013b) measured the elastic modulus of NBG-17 graphite through both dynamic (ultrasonic, ASTM C769-09) and sonic resonance (ASTM C747-93) methods on baseline samples used for irradiation creep. Table 3-3 shows their results.

Table 3-3 Room-Temperature Young's Modulus Data from NGNP Research (Windes et al., 2013b)

Room-Temperature Young's Modulus Measurement Method	Against-Grain, GPa	With-Grain, GPa	Anisotropy Ratio (AG/WG)
DYM	14.23 ± 0.10	14.31 ± 0.70	0.99
Resonance	11.16 ± 0.03	11.28 ± 0.53	0.99

3.12. Elastic Modulus (Static)

Carroll (2014) reported the static elastic modulus of NBG-17 graphite, obtained from tensile tests, in the form of Weibull statistics. From those data, a (Weibull) mean static elastic modulus of 9.49 ± 0.51 GPa can be calculated. It is not clear from the report which grain direction these data represent.

3.13. Coefficient of Thermal Expansion

Béghein et al. (2012) reported the mean CTE (20–200 degrees C (68–392 degrees F)) of NBG-17 graphite as 4.6 in the WG direction and 4.8 in the AG direction.

3.14. Thermal Conductivity

The room-temperature thermal conductivity of NBG-17 graphite has been reported as 72.5 W/m-°K by Heijna et al. (2017), and as 142 W/m-°K by Béghein et al. (2012). The literature search conducted for the present report found no information on the temperature dependence of the thermal conductivity of nonirradiated NBG-17 graphite. However, the authors of this report were able to extract limited data from the thermal diffusivity information presented for irradiated NBG-17 graphite specimens, which they compared with data for nonirradiated baseline specimens. The calculations for nonirradiated specimens included a

density correction, accounting for irradiation shrinkage. Figure 3-2 shows these results. In view of the steep decrease in thermal conductivity as a function of initial lower temperatures, which is common, the data of Windes et al. (2015) are not comparable with the room-temperature values found by Heijna et al. (2017).

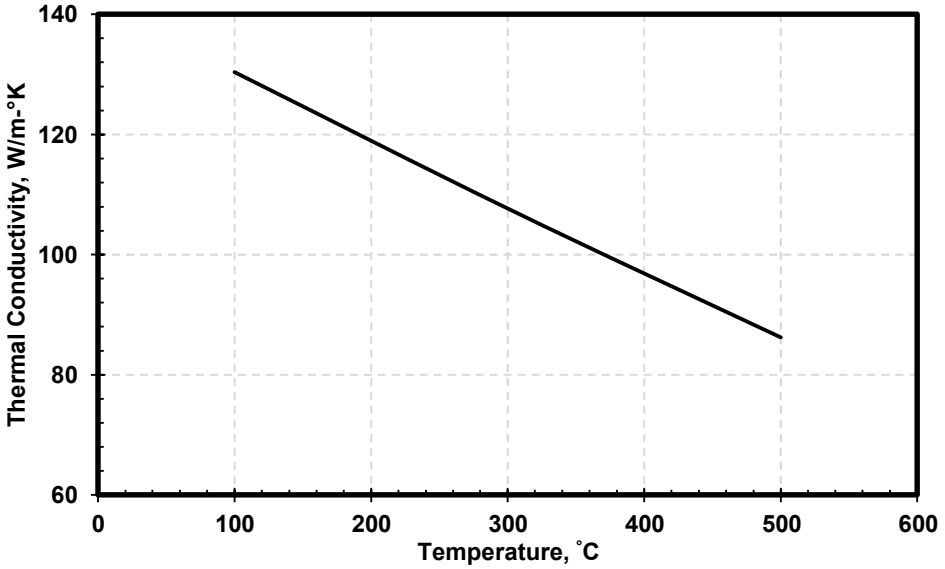

Figure 3-2 Thermal conductivity of NBG-17 graphite as a function of temperature (derived from the data of Windes et al., 2015)

Temperature-Independent Parameters

3.15. Poisson's Ratio

Using the (Weibull) mean values of 11.195 GPa for the resonance Young's modulus and 4.153 GPa for the torsional shear modulus, a Poisson's ratio of 0.348 can be calculated for NBG-17 graphite from the data of Carroll (2014). However, Windes et al. (2013) published a value of 0.1667 for NBG-17 graphite.

3.16. Anisotropy Factor

Based on the data of Béghein et al. (2012), the CTE anisotropy factor is 1.043. The ASTM D7219-08 standard requires a CTE isotropy ratio for molded, isotropic, high-purity (MIHP) graphite is 1.0–1.1, and for MNHP graphite is 1.1–1.15.

3.17. Critical Stress Intensity Factor, K_{Ic}

For NBG-17 graphite, Béghein et al. (2012) reported a room-temperature K_{Ic} of 1.4 MPa $\sqrt{}$ m. Chi (2016) obtained a value of 0.85 ± 0.07; however, this value depends on the specimen thickness. These fracture toughness values were determined using SENB specimens in three-point bending.

3.18. Graphite Oxidation Effects

Béghein et al. (2012) stated that NBG-17 graphite can undergo about 1.4-percent mass loss through oxidation at 600 degrees C (1,112 degrees F) in air. Lee et al. (2018) studied the oxidation of NBG-17 graphite in dry air using thermogravimetry; Figure 3-3 shows their results. The typical S-curve behavior is seen, with a combination of several operating mechanisms, as generally discussed in the graphite oxidation literature.

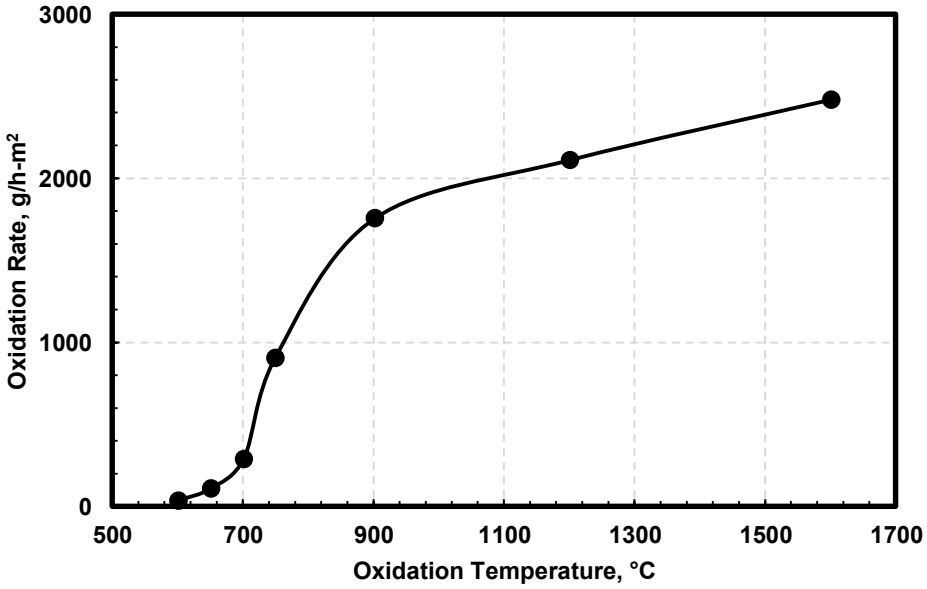

Figure 3-3 Oxidation rates of NBG-17 graphite at different oxidation temperatures (Lee et al., 2018)

3.19. Chronic Oxidation

The oxidation of graphite under HTGR operating conditions involves several potential reactions. As the coolant gas composition is controlled, the accumulation of CO and H_2 in the reactor is expected to be small. The real concern is that chronic oxidation of graphite may slowly corrode the fuel elements and other structural components in the core, weakening their mechanical strength and jeopardizing reactor integrity. Over the HTGR lifetime of several decades, it is inevitable that extremely slow, but continuous (chronic), oxidation of graphite by traces of water will occur at these high temperatures.

Contescu and Mee (2016) studied the effects of chronic oxidation in the presence of moisture. They conducted accelerated oxidation kinetics experiments in a controlled manner for several nuclear graphites at temperatures from 800 degrees C (1,472 degrees F) to 1,100 degrees C (2,012 degrees F). They used ultra-high-purity helium at a flow rate of 1.5 L/min, corresponding to a linear velocity of 7.5 centimeters per second in the reaction tube. The gas composition was adjusted to contain partial pressures of water vapor between 3 and 1,000 pascals (Pa), occasionally with added partial pressures of hydrogen between 10 and 300 Pa. The final weight

loss of individual specimens was in general less than 0.5 percent, only occasionally reaching 1.5 percent in the most aggressive oxidation conditions. At these low oxidation levels, Contescu and Mee concluded that the correction for the material loss that accounts for the variation of ORs with the degree of oxidation was not necessary.

Contescu and Mee analyzed their results using a classical Langmuir–Hinshelwood model, which was found to be insufficient to represent their data. They therefore included the temperature activation of the graphite surface, modeled as a Boltzmann activation function. The Boltzmann-enhanced Langmuir–Hinshelwood model, with 10 parameters, was tested successfully on three grades of graphite and found to be robust. The use of a comprehensive mathematical function allowed better fitting of experimental results spanning a wide range of temperatures and partial pressures of water vapor and hydrogen.

Figure 3-4 depicts the mathematically fitted oxidation kinetics data ("predicted" rate) for NBG-17 for various temperatures. As expected, these data show an increase in OR with increasing temperature for a given partial pressure of moisture. At low water vapor pressures (P_{H_2O}), the effect of temperature on OR is very small. The isothermal plots of curve fit rates separate well at high P_{H_2O} and are closer together at low P_{H_2O}.

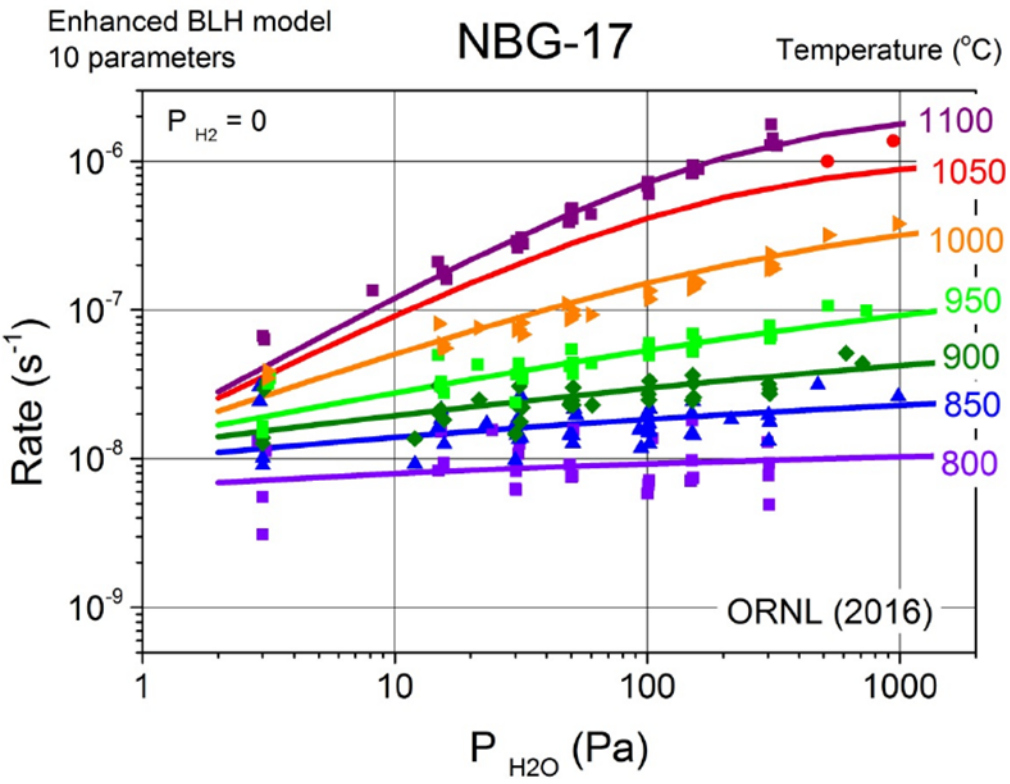

Figure 3-4 NBG-17 graphite OR versus partial pressure of water vapor, with no hydrogen injection (Contescu and Mee, 2016); rate = (1/original mass) × (Δmass/Δtime)

Adding 26 Pa of hydrogen to the oxidation gas causes strong inhibition of the ORs, as seen in Figure 3-5, which represents a mathematical fit of the experimental data with six parameters using the Langmuir–Hinshelwood model. The rates predicted in the presence of H_2 show

almost parallel trends, spread over several orders of magnitude. The trend is more noticeable when $P_{H_2} \geq P_{H_2O}$.

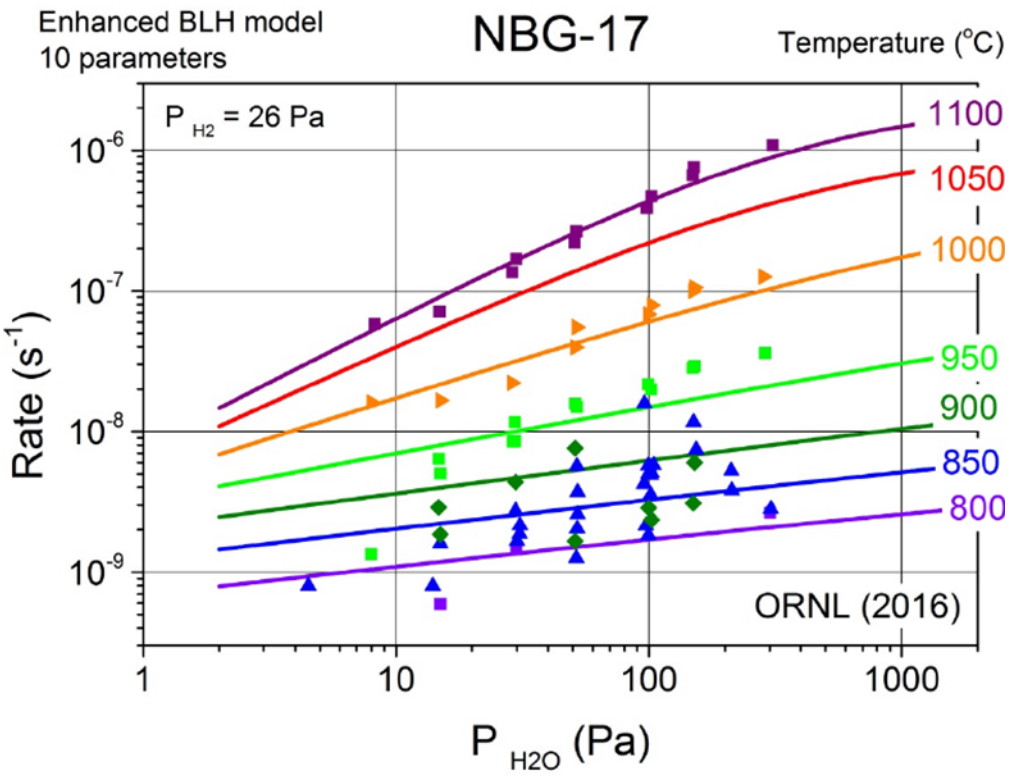

Figure 3-5 Addition of hydrogen generally lowering the OR of NBG-17 (Contescu and Mee, 2016); rate = (1/original mass) × (Δmass/Δtime)

3.20. Design Strength and Material Reliability Curve Values

Designers must enter the items under this category in the MDS, based on the results of their own testing and analyses and following the requirements in ASME BPVC-III-5, Article HHA-2200. The authors of this report did not attempt to derive these values from the literature and are not providing information on MDS Items 17–27.

3.21. Strength

The strength of NBG-17 graphite decreases with oxidation, in correlation with the material loss (density). As an example, Figure 3-6 shows the decrease in room-temperature compressive strength after oxidation, using data from Chi (2009). (Chi (2009) does not specify the oxidation conditions under which these data were obtained.)

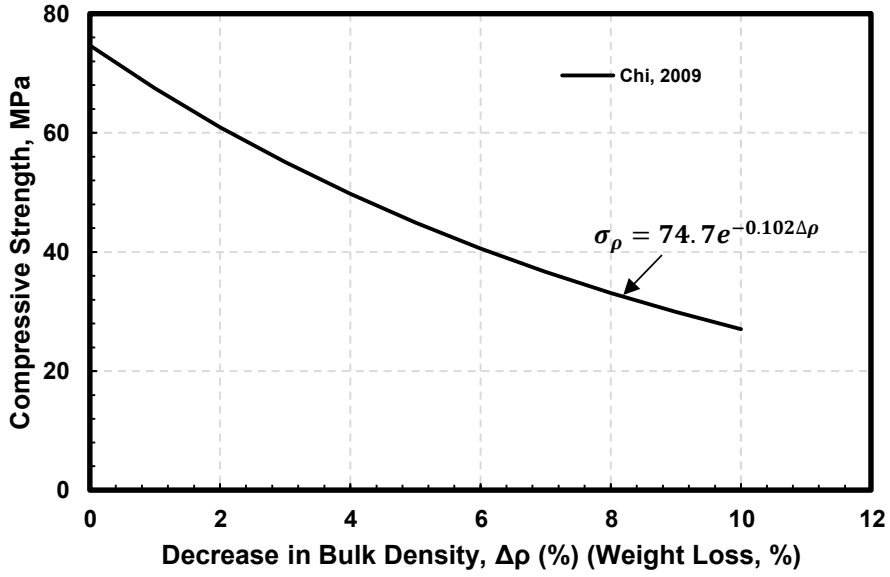

Figure 3-6 Degradation in compressive strength of NBG-17 graphite due to density decrease (expressed as percent of weight loss) resulting from oxidation (Chi, 2009)

3.22. Elastic Modulus

Data on the effect of oxidation on the elastic modulus of NBG-17 graphite have yet to be developed. However, inasmuch as oxidation affects graphite density, changes in the elastic modulus are expected to correspond to the density changes, which are largely influenced by the changes in the fraction of porosity and pore morphology.

3.23. Thermal Conductivity

Data on the effect of oxidation on thermal conductivity of NBG-17 graphite have yet to be developed. However, inasmuch as oxidation affects the density of NBG-17 graphite, the thermal conductivity changes likely follow the trend found in changes in elastic modulus due to oxidation. The density changes are largely influenced by the fractional changes in pore density and the morphology changes of the pores.

Irradiated Graphite

3.24. Dimensional Change

Heijna et al. (2017) and Windes (2012) have reported irradiation-induced dimensional change data for NBG-17 graphite. Figure 3-7 shows their results, expressed as volume change, which includes the potential effects of specimen orientation. Although Heijna et al. (2017) specified the irradiation temperature to be 750 degrees C (1,382 degrees F), it is expected that variations in specimen temperature are possible; this variation could be one of the reasons for the observed data scatter, another being the inherent microstructural variation (grain size and porosity morphology distributions) of the graphite. Windes (2012) conducted experiments at lower temperatures, as indicated in the figure, with a reported range of 541–681 degrees C (1,006–1,258 degrees F); this explains the lower shrinkage compared to the observations of Heijna et al.

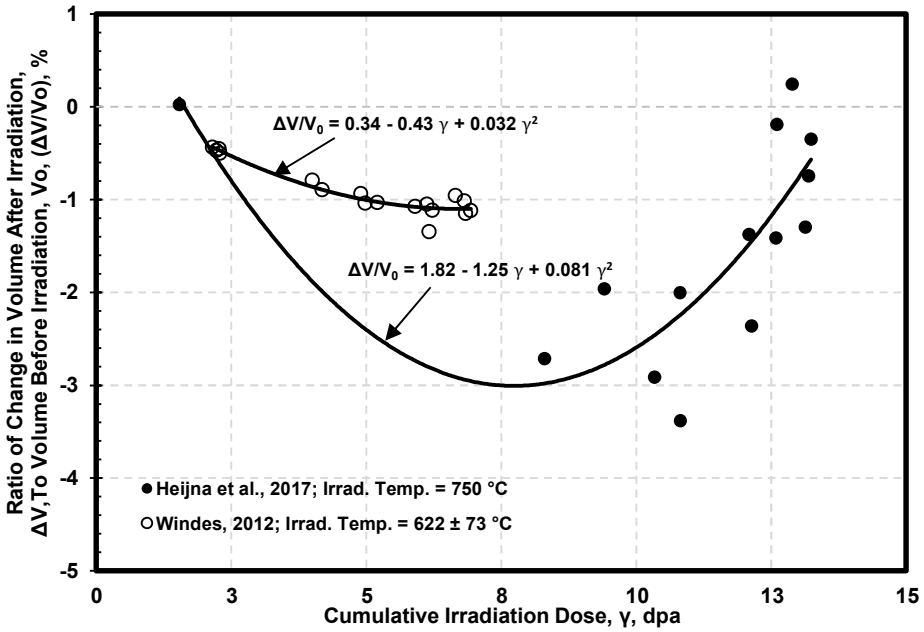

Figure 3-7 Irradiation-induced dimensional change for NBG-17 graphite

The individual irradiation samples in the AGC-1 irradiation program by Windes (2012) (shown in Figure 3-7) were generally subjected to a wide range of irradiation doses, as shown in Figure 3-8.

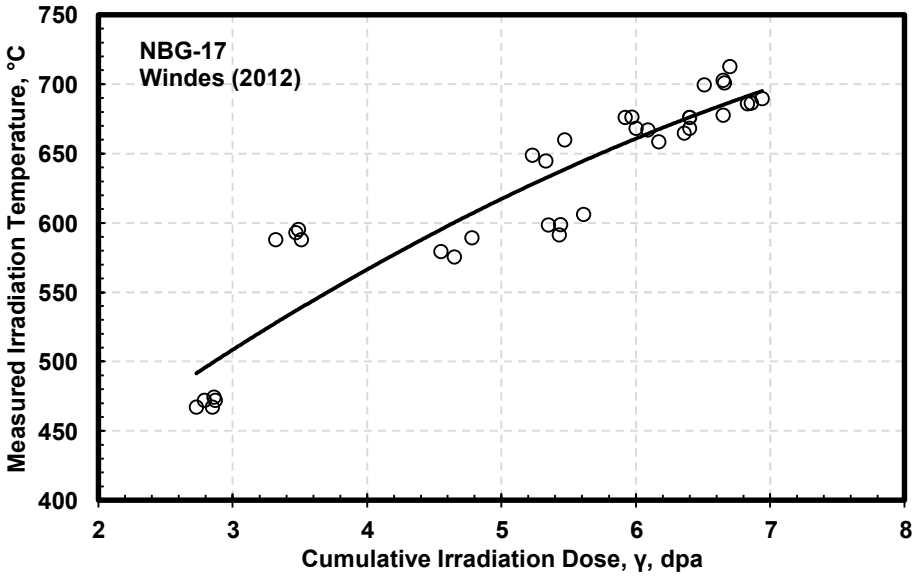

Figure 3-8 Temperature-dose distribution of the NBG-17 graphite specimens in the AGC-1 irradiation at INL (Windes, 2012)

The load imposed on the graphite in the reactor environment affects the overall dimensional change. Thus, the effect of creep strain on the total strain while under load is pertinent. Figure 3-9 shows the effect of applied load and the creep strain for NBG-17 graphite, as found in the investigations at INL (Windes, 2012).

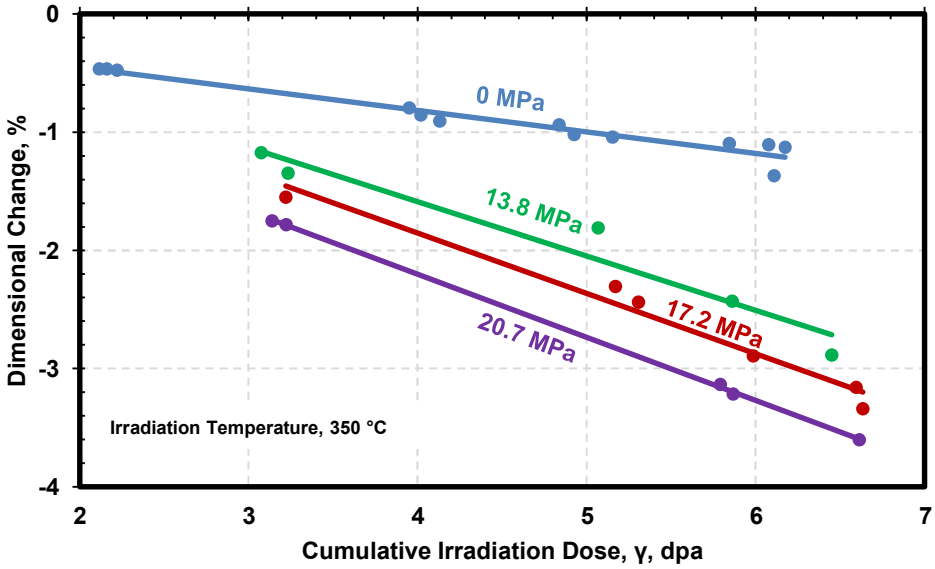

Figure 3-9 Effects of creep strain on dimensional change due to irradiation (Windes, 2012)

As the applied stress increases, the magnitude of irradiation-induced dimensional change increases. The increase in creep strain with increasing stress for a constant irradiation dose is consistent with the creep mechanism.

Windes et al. (2015) reported on the effect of applied creep stress on the overall volume change. Figure 3-10 presents their results. As expected, the volume decreases with externally applied creep stress. However, from these data alone, it is not possible to evaluate the effects of irradiation temperature and dose.

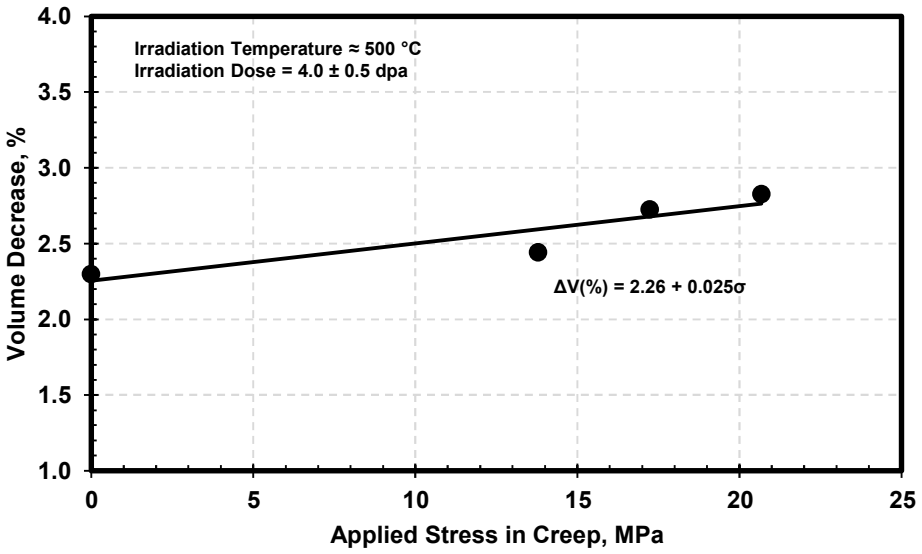

Figure 3-10 Effect of creep stress on volume change during irradiation at 500 degrees C and 4 dpa dose for NBG-17 graphite (Windes et al., 2015)

There are also some observable differences between WG and AG dimensional change of NBG-17 graphite, as shown in Figure 3-11. Windes et al. (2015) did not clearly state the grain orientation of the samples in their study. Assuming that the WG orientation is along the length of the sample, dimensional change along the diameter or in the radial direction would mean AG dimensional change. Accounting for the data scatter, it appears that the dimensional change is greater in the AG orientation than the WG orientation, for the dose levels and temperature range studied here. Heijna et al. (2017) also reported this trend. This is the inverse of the general trend for PGA graphite, as noted by Marsden et al. (2016) in Figure 27 of their paper.

Figure 3-12 shows the data of Heijna et al. (2017) on anisotropy in dimensional change. Heijna et al. (2017) define the anisotropy parameter as the length change in the AG direction minus the length change in the WG direction for a given dose.

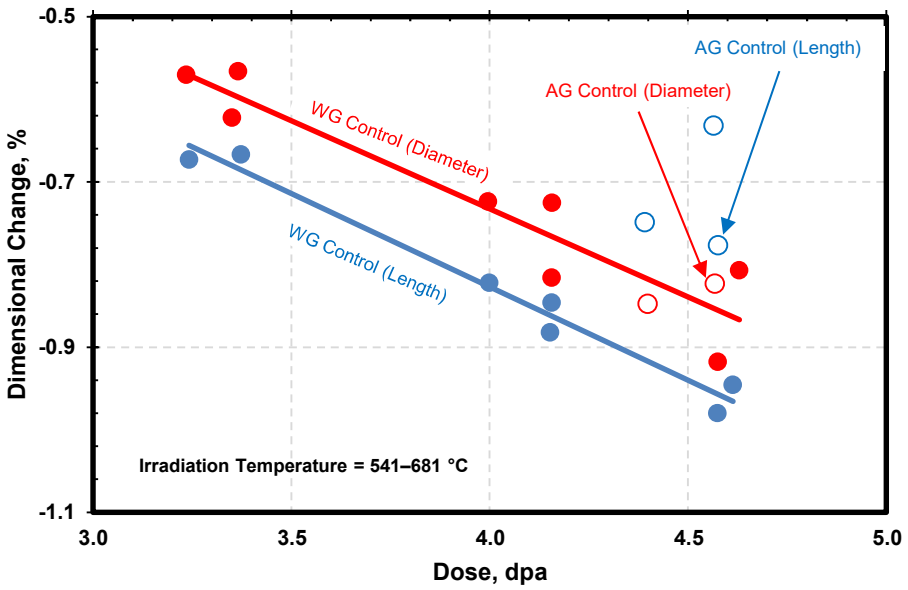

Figure 3-11 Orientation dependence of dimensional change due to irradiation for NBG-17 graphite (Windes et al., 2016)

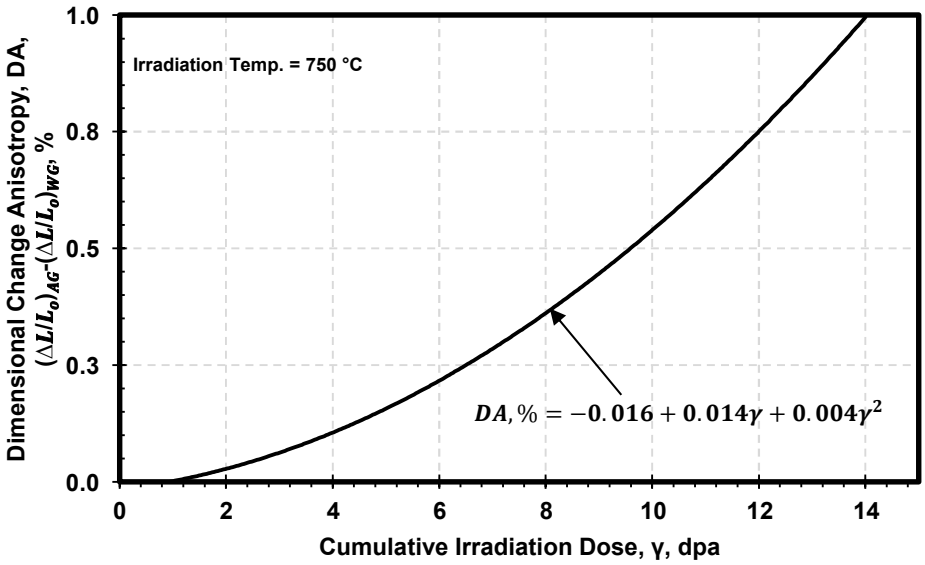

Figure 3-12 Dose dependence of anisotropy in dimensional change at an irradiation temperature of 750 degrees C for NBG-17 graphite (Heijna et al., 2017)

3.25. Creep Coefficient

The irradiation secondary creep coefficient for NBG-17 has been reported for three temperatures normalized to stress of 20.7 MPa, as shown in Table 3-4 (Windes et al., 2019).

Table 3-4 Irradiation Secondary Creep Coefficient Normalized to Stress of 20.7 MPa for NBG-17 Graphite (Windes et al., 2019)

Irradiation Temperature, °C (°F)	Creep Coefficient K, (%/MPa-dpa)
600 (1,112)	0.015
625 (1,157)	0.015
820 (1,508)	0.028

Considering the difficulties in attaining and maintaining constant temperature in any materials irradiation program, it may be appropriate to interpret this information as effectively giving the same creep coefficient for an average temperature of about 600 degrees C (1,112 degrees F). Because the data are so limited, not much can be concluded from these values in relation to the overall phenomenon of irradiation creep in NBG-17 graphite other than the creep coefficient increases at 820 degrees C (1,508 degrees F), which is expected.

3.26. Coefficient of Thermal Expansion

The CTE generally increases after the irradiation of NBG-17 graphite, as shown in Figure 3-13 for various irradiation temperatures (Windes et al., 2017a). In these experiments, the irradiation dose was 4.0 ± 0.5 dpa. The CTE was measured as the mean for 30–500 degrees C (86–932 degrees F). These results do not favor any particular trend; however, the sample size is rather small, and scatter arises because of imprecise temperature and dose estimates, as well as the inherent inhomogeneity in graphite microstructure and in its changes under irradiation.

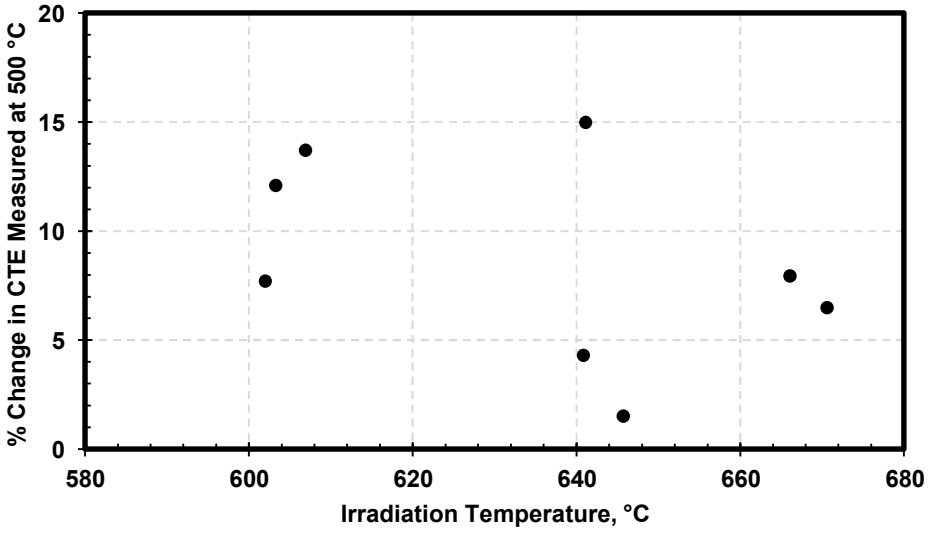

Figure 3-13 Relative change in CTE as a function of irradiation temperature for NBG-17 graphite (Windes et al., 2017a)

Figure 3-14 shows the CTE change for NBG-17 graphite as a function of irradiation dose. The range of irradiation temperatures for these data is 541–681 degrees C (1,006–1,258 degrees F). No particular trend is visible in the grain orientations, although the sample size is rather small.

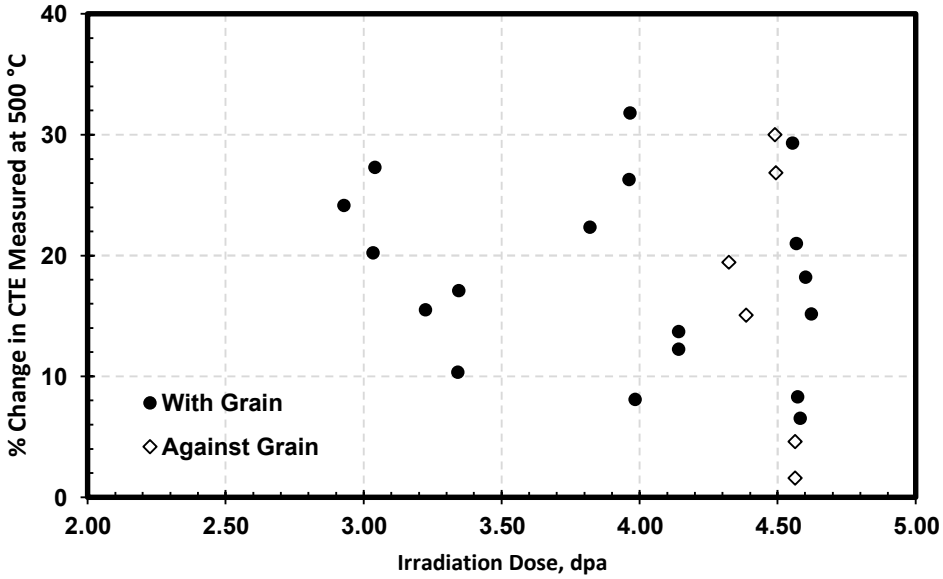

Figure 3-14 Relative change in mean CTE (30–500 degrees C) (86–932 degrees F) of irradiated NBG-17 graphite as a function of irradiation dose (Windes et al., 2017a)

3.27. Strength

As can be expected, irradiation-induced shrinkage causes narrow microcracks and small micropores to close and pores in general to shrink. This decreases porosity and conversely increases density, as shown in Figure 3-15, which is based on the work of Windes et al. (2017a). Here, the individual specimens experienced temperatures within the range of 627 ± 78 degrees C (1,161 ± 172 degrees F).

Positional temperature and dose variations within a graphite component lead to nonuniform shrinkage; thus, dimensional change is not uniform, and localized distortions may occur.

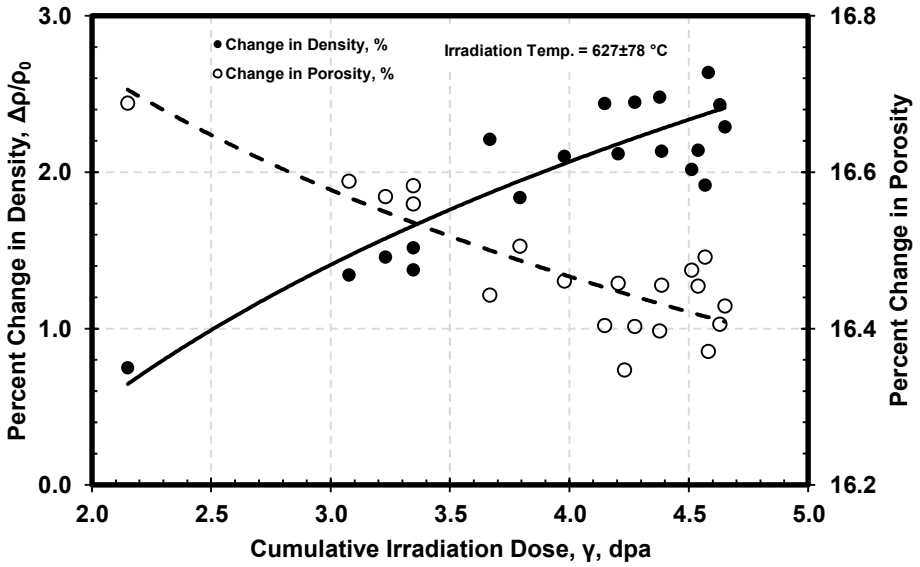

Figure 3-15 Shrinkage-assisted decrease in porosity due to irradiation of NBG-17 graphite (Windes et al., 2017a)

Since the strength of graphite is correlated with its density, with higher densities corresponding to greater strength, the strength of irradiated graphite can be expected to increase up to at least the maximum shrinkage obtained as a function of irradiation dose. This is indeed observed for NBG-17 graphite, as shown in Figure 3-16 (Heijna et al., 2017).

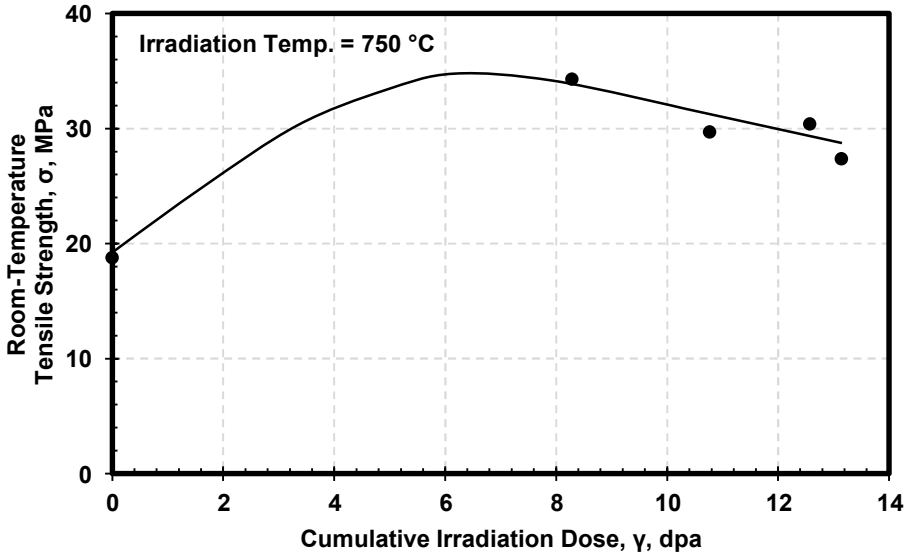

Figure 3-16 Dependence of tensile strength on irradiation dose for NBG-17 graphite (Heijna et al., 2017)

The decrease in strength shown in Figure 3-16 corresponds to the volumetric turnaround (shown in Figure 3-7) due to the breakup of the microstructure with large dimensional change.

Heijna et al. (2017) conducted irradiation testing with discs of NBG-17 graphite, irradiating to 750 degrees C (1,382 degrees F). After irradiation, they conducted diametral compression tests at room temperature and derived the tensile strength from the results. Because of the test specimen geometry and test method, the investigators did not provide information on strength for WG and AG orientations. However, the trend in the irradiated strength behavior is generally independent of the grain orientation.

3.28. Elastic Modulus

The Young's modulus changes with irradiation dose, as shown in Figure 3-17. Only a limited range in dose is indicated; the scatter is due to graphite's natural inhomogeneity and also to the variation in the irradiation temperature of individual specimens. The modulus increase generally tracks the density increase with dose, as shown earlier in Figure 3-15.

A similar irradiation effect has been observed for shear modulus, as shown in Figure 3-18.

The elastic modulus also changes with applied stress during irradiation, mainly because of changes in the structure of microcracks and micropores, in addition to the contribution from irradiation-induced dimensional change (shrinkage); Figure 3-19 shows this effect.

Figure 3-20 shows the effect of creep on the change in shear modulus due to irradiation. The data scatter is due to material, test environment, and temperature variations from sample to sample.

The elastic modulus changes both with irradiation temperature and with irradiation dose. Figure 3-21 shows an example of the modulus change, measured using the DYM technique for NBG-17 graphite. Here, the data shown are for individual specimens, which would have had varying irradiated doses, as indicated.

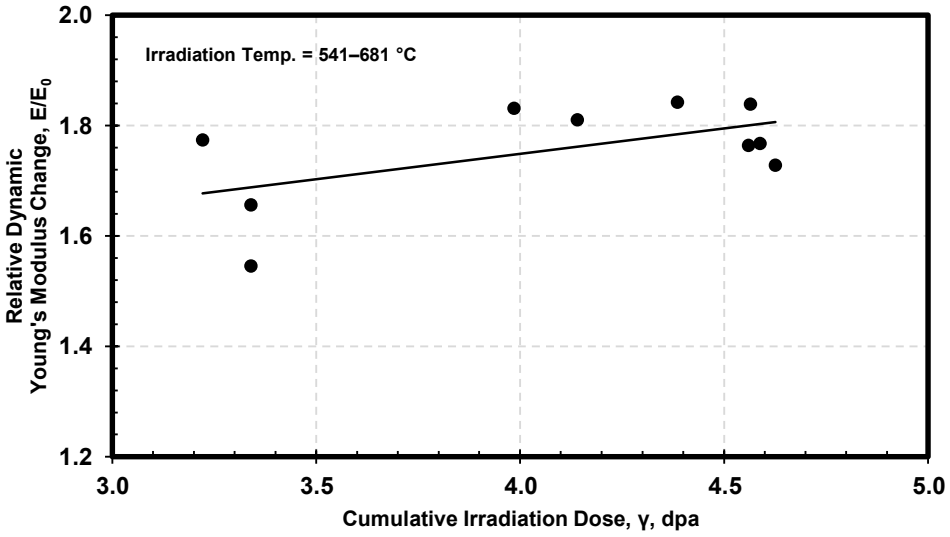

Figure 3-17 Relative change in modulus with irradiation dose for the range of irradiation temperatures indicated (Windes et al., 2017a)

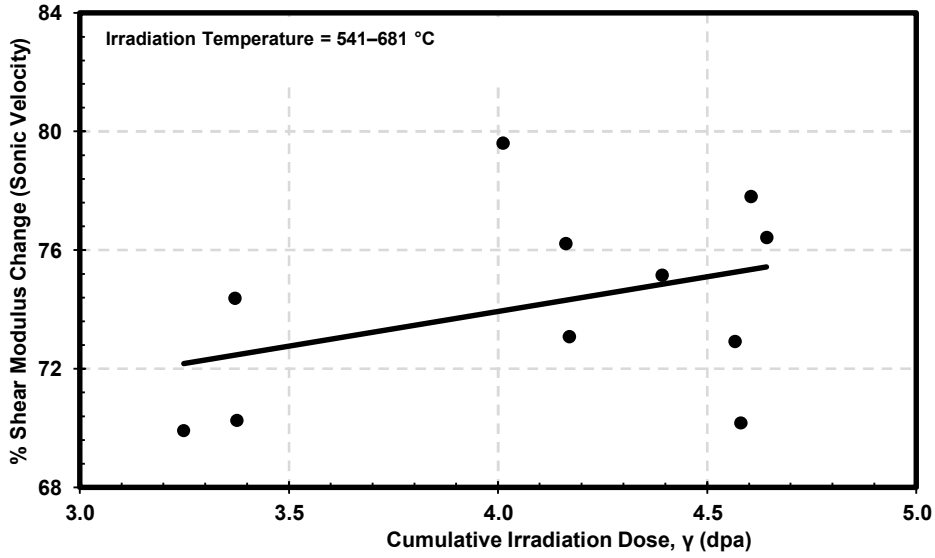

Figure 3-18 Effect of irradiation on the shear modulus (Windes et al., 2017a)

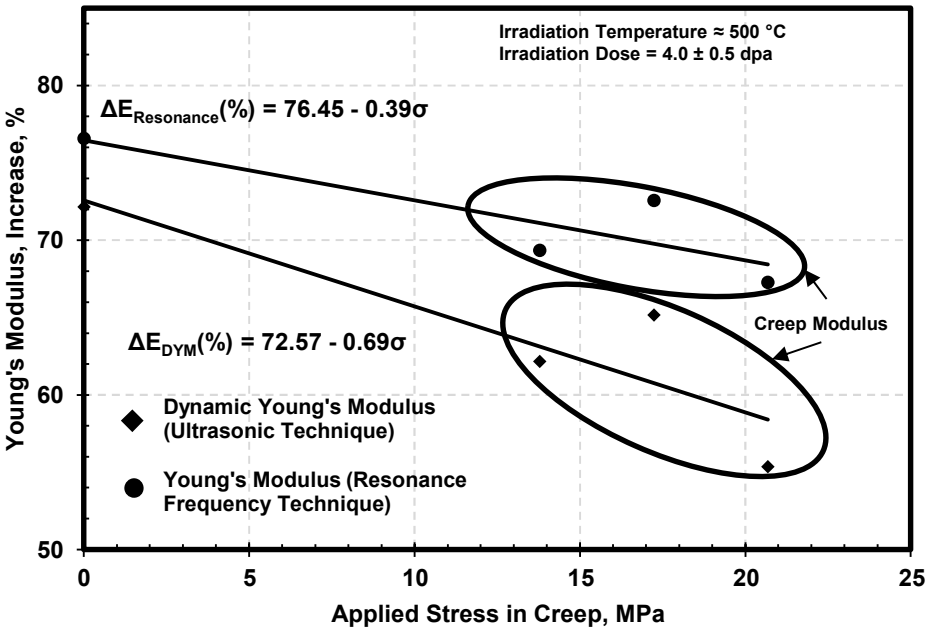

Figure 3-19 Effect of applied stress on the increase in Young's modulus due to irradiation for NBG-17 graphite (Windes et al., 2015)

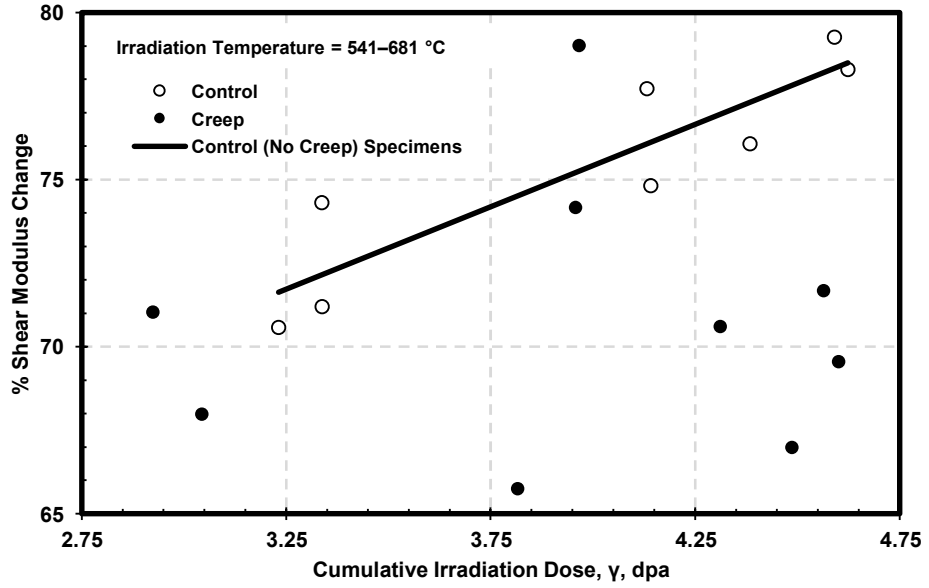

Figure 3-20 Effect of irradiation creep on the shear modulus as a function of dose for NBG-17 graphite (Windes et al., 2017a)

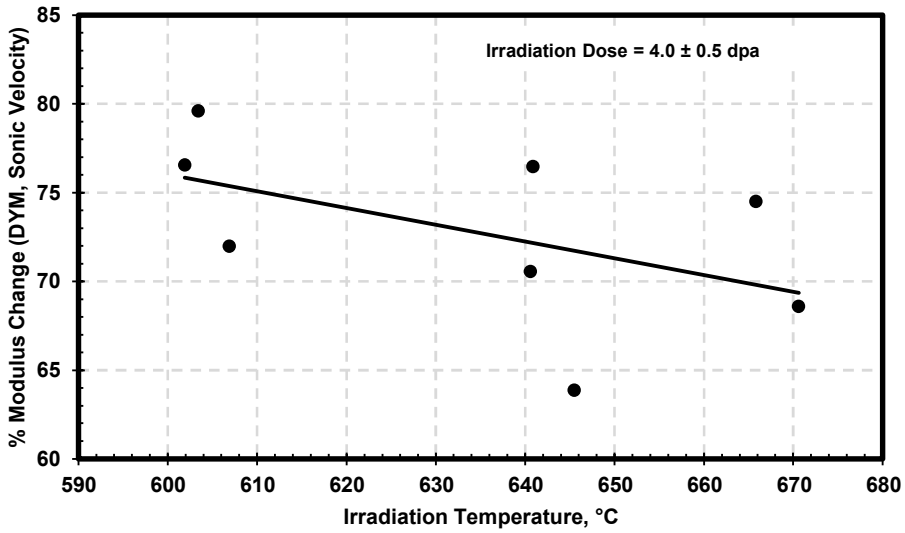

Figure 3-21 Change in elastic modulus with irradiation temperature for NBG-17 graphite (Windes et al., 2017a)

Interestingly, the change in shear modulus does not seem to vary much with irradiation temperature, as shown in Figure 3-22.

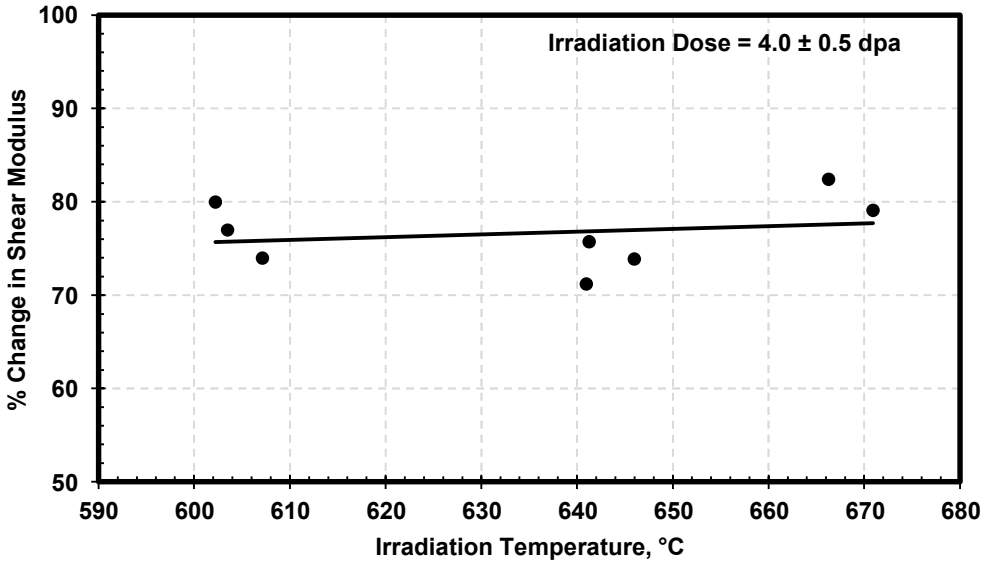

Figure 3-22 Change in shear modulus with irradiation temperature for NBG-17 graphite (Windes et al., 2017a)

Windes et al. (2017a) studied the effects of grain and pore orientation on the irradiated modulus behavior of NBG-17 graphite. Figure 3-23 shows the change in Young's modulus with irradiation dose for both WG and AG orientations. The large scatter in the observed values

precludes any inferences about the dependence of the change in Young's modulus on the orientation.

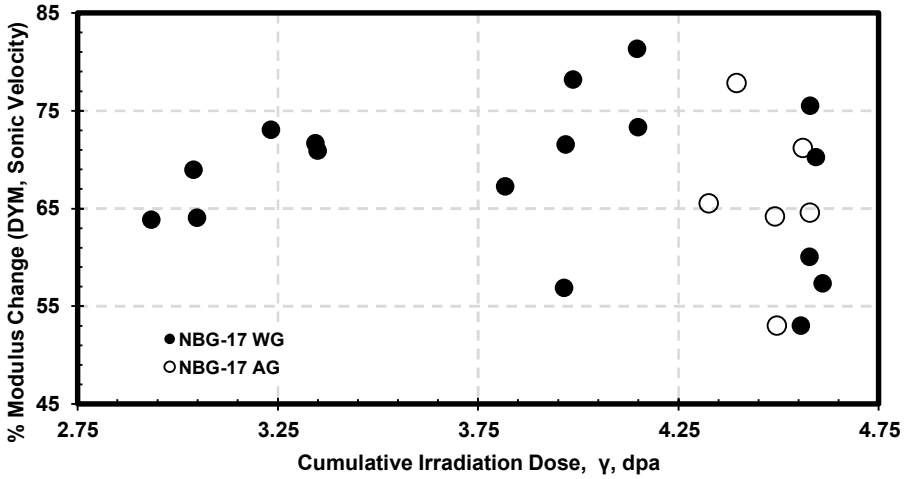

Figure 3-23 Relative change in Young's modulus with irradiation dose for WG and AG orientations as a function of irradiation dose (Windes et al., 2017a)

Figure 3-24 shows the change in shear modulus with irradiation dose for both WG and AG orientations. Again, the large scatter in the observed values precludes any inferences about the dependence of the change in shear modulus on the orientation.

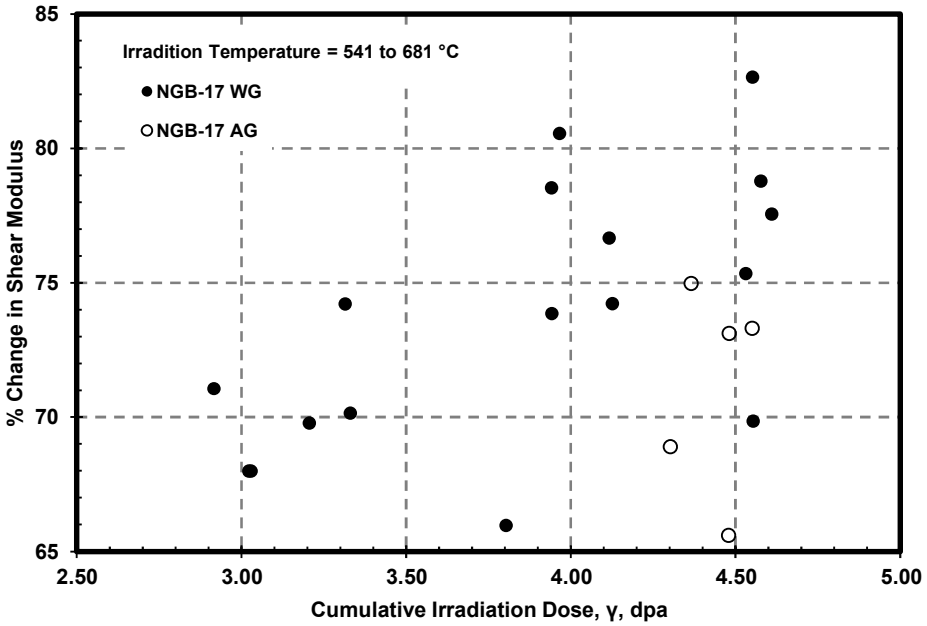

Figure 3-24 Relative change in shear modulus with irradiation dose for WG and AG orientations in the indicated irradiation temperature range (Windes et al., 2017a)

3.29. Thermal Conductivity

Limited data are available on the irradiation temperature and dose dependence of thermal conductivity. Figure 3-25 contains the information from the literature survey done for this report. The data of Windes et al. (2015) represent thermal conductivity calculated by the authors of this report using the room-temperature thermal diffusivity and specimen density, together with specific heat values as a function of temperature, determined using the equation mentioned previously in Section 2.19 for IG-110.

Figure 3-26 shows the thermal diffusivity data obtained by Windes et al. (2015) at INL for the NGNP program. The data show no differences between the diffusivity values in the two orthogonal directions. Here, the samples were irradiated to approximately 500 degrees C (932 degrees F) and to an irradiation dose of approximately 4 dpa.

The same research also determined the diffusivity change from a nonirradiated to an irradiated condition, as shown in Figure 3-27. These are average values, and the diffusivity change seems to be well characterized as a linear dependence on irradiation temperature.

From the data of Windes et al. (2015) in Figure 3-27, together with the data on density change, which show a 2.3-percent increase in density under irradiation at 500 degrees C (932 degrees F) at an irradiation dose of 4 dpa additional data were derived to compare the dependence of thermal conductivity on temperature for nonirradiated and irradiated NBG-17 graphite. Figure 3-28 shows this comparison. The data in Figure 3-28 show a substantial reduction in thermal conductivity due to irradiation, which is also commonly observed for other graphites.

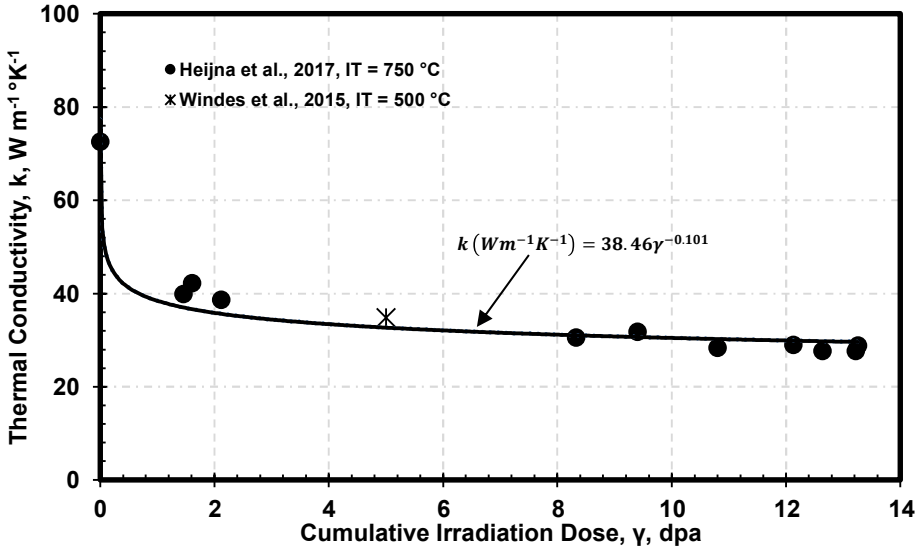

Figure 3-25 Thermal conductivity as a function of dose for NBG-17 graphite

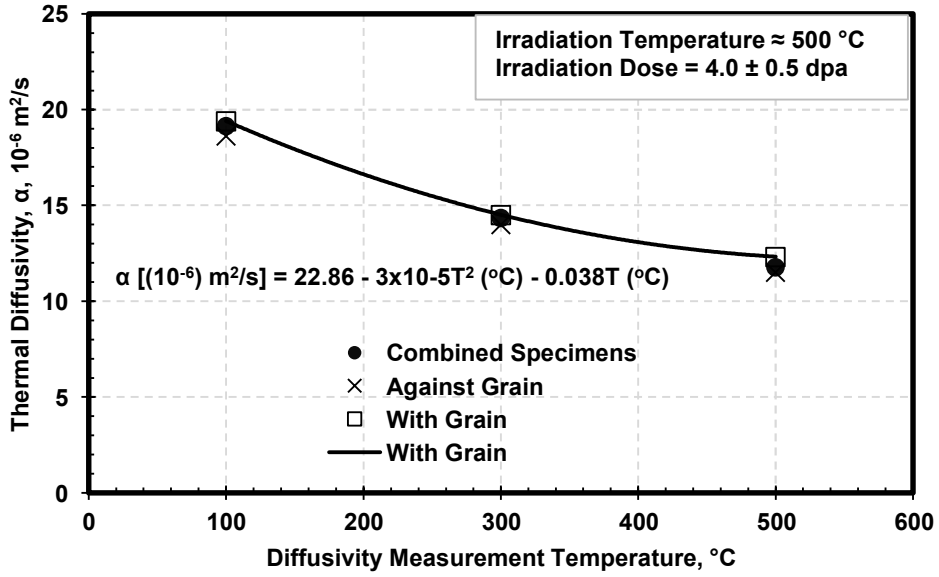

Figure 3-26 Thermal diffusivity as a function of temperature for NBG-17 graphite (Windes et al., 2015)

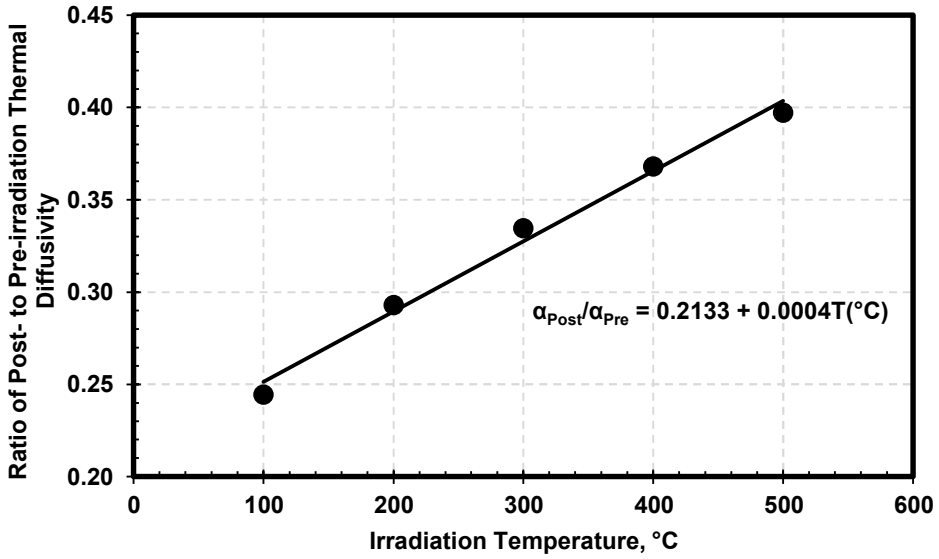

Figure 3-27 Relative change in thermal diffusivity after irradiation as a function of irradiation temperature for NBG-17 graphite (Windes et al., 2015)

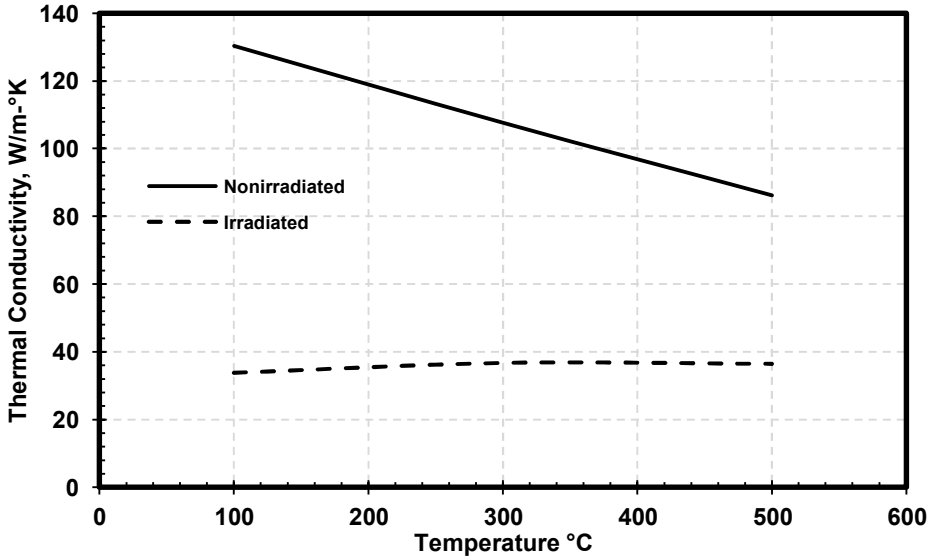

Figure 3-28 Comparison of thermal conductivity behavior as a function of temperature for nonirradiated and irradiated NBG-17 graphite (derived from Windes et al., 2015)

3.30. Chemical Analysis of NBG-17

Table 3-5 presents the chemical analysis data for NBG-17 graphite. All analysis was performed using GDMS.

Table 3-5 Chemical Analysis of NBG-17 Graphite (Strizak et al., 2006)

Element	ppm (wt%)	Element	ppm (wt%)	Element	ppm (wt%)	Element	ppm (wt%)
Li	0.21	Mn	<0.05	Ag	<0.1	Tm	<0.05
Be	<0.01	Fe	26	Cd	<0.1	Yb	<0.05
B	0.61	Co	0.11	In	<0.1	Lu	<0.05
C	Matrix	Ni	1.2	Sn	<0.5	Hf	<0.05
N	-	Cu	<0.1	Sb	<0.5	Ta	<5
O	-	Zn	<0.1	Te	<0.1	W	<0.05
F	<1	Ga	<0.1	I	<0.1	Re	<0.05
Na	0.28	Ge	<0.1	Cs	<0.1	Os	<0.05
Mg	<0.5	As	<0.1	Ba	<0.1	Ir	<0.05
Al	0.09	Se	<0.1	La	<0.5	Pt	<0.05
Si	100	Br	<0.1	Ce	<0.05	Au	<0.1
P	0.35	Rb	<0.05	Pr	<0.05	Hg	<0.5
S	12	Sr	<0.05	Nd	<0.05	Tl	<0.1
Cl	0.21	Y	<0.05	Sm	<0.05	Pb	<0.5
K	0.35	Zr	0.49	Eu	<0.05	Bi	<0.1
Ca	2.2	Nb	<0.1	Gd	<0.05	Th	<0.05
Sc	<0.05	Mo	0.08	Tb	<0.05	U	<0.05
Ti	5.5	Ru	<0.1	Dy	<0.05		
V	0.73	Rh	<0.1	Ho	<0.05		
Cr	<0.5	Pd	<0.1	Er	<0.05		

4. Sigri Great Lakes Carbon NBG-18 Graphite

Table 4-2 provides properties information for NBG-18 graphite, following the ASME graphite code MDS format. For each property, the table cites the corresponding section of this report, which contains further information extracted from publicly available data.

4.1. Material Grade

The material grade is NBG-18.

4.2. Material Specification ID

This identifies the construction specification for the graphite grade applicable to this MDS. The designer enters this value.

4.3. ASTM Specification

This is the Mandatory Appendix HHA-I material specification (ASTM) number that applies to the manufacture of the material. The designer enters this number.

Table 4-1 Example ASME MDS for NBG-18 Graphite

ASME BPVC-III-5-2017, FORM MDS-1 MATERIAL DATA SHEET (SI UNITS)															
Grade Designation															
Material grade	NBG-18			(1) Material grade: The manufacturer's grade designation that complies with the requirements of the Mandatory Appendix HHA-I material specification.											
Material spec. ID	Not appli-cable			(2) Material spec. ID: The construction specification for the graphite grade applicable to this MDS.											
ASTM spec.	ASTM D7219-08			(3) ASTM spec: The Mandatory Appendix HHA-I material specification (ASTM) number that applies to the manufacture of the material.											
Max. grain size (mm) (Section 4.4)	1.6 (Lee et al., 2018)			(4) Maximum grain size: The maximum filler particle grain size that is used in the mix formulation. (For isostatically pressed graphite, report mean grain size.)											
Designation				(5) Designation: Material designation as defined in the Mandatory Appendix HHA-I material specification.											
Temperature-Dependent Parameters															
Property	Units														
Bulk density (Section 4.6)	kg/m^3	Mean	Std. Dev						(6) Bulk density: The material bulk density. Mean and standard deviation of material test specimen results.						
		1.87 (300 specimens, Fechter and Fazluddin, 2008); 1.89 ± 0.014 (Windes et al., 2015, 2017); 1.852 ± 0.004 (Matthews et al., 2019)													
Strength—tensile (Section 4.7)	MPa	WG	20 °C	200 °C	400 °C	600 °C	800 °C	1,000 °C (see Note 1 below)							

ASME BPVC-III-5-2017, FORM MDS-1 MATERIAL DATA SHEET (SI UNITS)															
		Mean	20.8 (184 specimens, Fechter and Fazluddin, 2008); 20.49 (Hindley et al., 2012); 19.60 ± 1.65 (Carroll et al., 2010). Specific Note 1.						(7) Strength, tensile: Mean and standard deviation of material test specimen results. Note that the temperature dependence of only one strength parameter need be determined; the others can be assumed to change by the same relative amount.						
		Std. Dev.	2.64												
	MPa	AG	20 °C	200 °C	400 °C	600 °C	800 °C	1,000 °C							
		Mean	20.4 (118 specimens, Fechter and Fazluddin, 2008); 20.49 ± 2.64 (Hindley et al., 2012); Specific Note 1.												
		Std. Dev.	2.64												
Strength—flexural (four-point) (Section 4.8)	MPa	WG	20 °C	200 °C	400 °C	600 °C	800 °C	1,000 °C	(8) Strength, flexural (four-point): Mean and standard deviation of material test specimen results. Note that the temperature dependence of only one strength parameter need be determined; the others can be assumed to change by the same relative amount.						

ASME BPVC-III-5-2017, FORM MDS-1 MATERIAL DATA SHEET (SI UNITS)															
		Mean	31.1 (130 specimens, Fechter and Fazluddin, 2018); 30.31 ± 3.74 (Hindley et al., 2012); 27.77 ± 1.62 (Carroll et al., 2010); Specific Note 1.												
		Std. Dev.													
	MPa	AG	20 °C	200 °C	400 °C	600 °C	800 °C	1,000 °C							
		Mean	29.7 (130 specimens, Fechter and Fazluddin, 2018); 30.31 (Hindley et al., 2012); 27.77 ± 1.62 (Carroll et al., 2010); Specific Note 1.												
		Std. Dev.	3.74												
Strength—compressive (Section 4.9)	MPa	WG	20 °C	200 °C	400 °C	600 °C	800 °C	1,000 °C	(9) Strength, compressive: Mean and standard deviation of material test specimen results. Note that the temperature dependence of only one strength parameter need be determined; the others can be assumed to change by the same relative amount.						

ASME BPVC-III-5-2017, FORM MDS-1 MATERIAL DATA SHEET (SI UNITS)															
		Mean	77.4 (110 specimens, Fechter and Fazluddin, 2018); 77.62 ± 8.73 (Hindley et al., 2012); 81.4 ± 4.34 (Carroll et al., 2010); Specific Note 1.												
		Std. Dev.													
	MPa	AG	20 °C	200 °C	400 °C	600 °C	800 °C	1,000 °C							
		Mean	78.5 (110 specimens, Fechter and Fazluddin, 2018); 77.62 ± 8.73 (Hindley et al., 2012), Specific Note 1; 81.4 ± 4.34 (Carroll et al., 2010)												
		Std. Dev.	8.73												
Elastic modulus (dynamic) (Section 4.10)	GPa	WG	20 °C	200 °C	400 °C	600 °C	800 °C	1,000 °C	(10) Elastic modulus (dynamic): Mean and standard deviation of material test specimen results.						

ASME BPVC-III-5-2017, FORM MDS-1 MATERIAL DATA SHEET (SI UNITS)															
		Mean	11.7 (Fechter and Fazluddin, 2018); 10.1 ± 0.86 (ultrasonic) and 12.1 ± 2.65 (sonic resonance) (Carroll et al., 2010)												
		Std. Dev.													
		AG	20 °C	200 °C	400 °C	600 °C	800 °C	1,000 °C							
		Mean	11.6 (Fechter and Fazluddin, 2018)												
		Std. Dev.													
Elastic modulus (static) (Section 4.11)	GPa	WG	20 °C	200 °C	400 °C	600 °C	800 °C	1,000 °C	(11) Elastic modulus (static): Mean and standard deviation. Use a measured value of the dynamic elastic modulus (10) scaled by the ratio between static and dynamic. Note that the dynamic and static modulus are related. Only one need be measured; the other can be computed from these measurements and the ratio between the two values.						
		Mean	Bend test: 9.41 ± 2.34; tensile test: 10.1 ± 0.86) (Carroll et. al., 2010)												
		Std. Dev.													

ASME BPVC-III-5-2017, FORM MDS-1 MATERIAL DATA SHEET (SI UNITS)															
		AG	20 °C	200 °C	400 °C	600 °C	800 °C	1,000 °C							
		Mean													
		Std. Dev.													
Coefficient of thermal expansion, CTE, β (Section 4.12)	/°C	WG	20 °C	200 °C	400 °C	600 °C	800 °C	1,000°°C	(12) Coefficient of thermal expansion: Mean and standard deviation of material test specimen results. This property's temperature dependence shall be determined.						
		Mean													
		Std. Dev.													
		AG	20 °C	200 °C	400 °C	600 °C	800 °C	1,000 °C							
		Mean													
		Std. Dev.													
Thermal conductivity (Section 4.13)	W/m°K	WG	20 °C	200 °C	400 °C	600 °C	800 °C	1,000 °C	(13) Thermal conductivity: Mean and standard deviation of material test specimen results.						
		Mean													
		Std. Dev.													
		AG	20 °C	200 °C	400 °C	600 °C	800 °C	1,000 °C							
		Mean													
		Std. Dev.													
Temperature-Independent Parameters															
Poisson's ratio (Section 4.14)			0.2 (Fechter and Fazluddin, 2008)						(14) Poisson's ratio: Mean and standard deviation of material test specimen results. As an alternative, a published historical value may be used.						
Anisotropy factor (Section 4.15)		1.04 (Fechter and Fazluddin, 2008)							(15) Anisotropy factor: Mean and standard deviation for the charges as described in the graphite specification (Mandatory Appendix HHA-I). The average of the charges is then given in the MDS.						
Critical stress intensity factor, K_{Ic} (Section 4.16)	MPa √ m	1.36 ± 0.1 (WG), 1.41 ± 0.05 (AG) (Burchell et al., 2017)							(16) Critical stress intensity factor (K_{Ic}): Mean and standard deviation of material test specimen results.						

ASME BPVC-III-5-2017, FORM MDS-1 MATERIAL DATA SHEET (SI UNITS)									
Design Strength and Material Reliability Curve Values									
Ratio of compressive to tensile strength (R_{tc})			3.79						(17) Ratio of compressive to tensile strength (R_{tc}): Computed from the mean tensile and mean compressive strengths as published in (7) and (9) above. R_{tc} = Compressive Strength (9) ÷ Tensile Strength (7). This quantity is defined as positive.
Ratio of flexural to tensile strength (R_{tf})			1.48						(18) Ratio of flexural to tensile strength (R_{tf}): Computed from the mean tensile and mean flexural strengths as published in (7) and (8) above. R_{tf} = flexural strength (8) ÷ tensile strength (7). This quantity is defined as positive.
$S_{c95\%}$	MPa	Data to be provided by the designer.							(19) $S_{c95\%}$: The computed single-sided 95% confidence interval value for the Weibull characteristic strength that defines the material reliability curve. This is calculated in accordance with HHA-II-3100, based on the tensile strength measurements.
$m_{95\%}$		Data to be provided by the designer.							(20) $m_{95\%}$: The computed single-sided 95% confidence interval value for the Weibull modulus that defines the material reliability curve. This is calculated in accordance with HHA-II-3100, based on the tensile strength measurements.
S_0	MPa	Data to be provided by the designer.							(21) S_0: The computed value for the threshold stress based on the three-parameter distribution that defines the material reliability curve. This is calculated in accordance with HHA-II-3200, based on the tensile strength measurements.
$S_{c095\%}$		Data to be provided by the designer.							(22) $S_{c095\%}$: The computed single-sided 95% confidence interval value for the characteristic stress based on the three-parameter distribution that defines the material reliability curve. This is calculated in accordance with HHA-II-3200, based on the tensile strength measurements.

ASME BPVC-III-5-2017, FORM MDS-1 MATERIAL DATA SHEET (SI UNITS)																
$m_{095\%}$		Data to be provided by the designer.							(23) $m_{095\%}$: The computed single-sided 95% confidence interval value for the Weibull modulus based on the three-parameter distribution that defines the material reliability curve. This is calculated in accordance with HHA-II-3200, based on the tensile strength measurements.							
S_g (10^{-4})	MPa	Data to be provided by the designer.							(24) S_g (10^{-4}): The design allowable stress value corresponding to the probability of failure of 10^{-4}, computed in accordance with HHA-II-3300 based on $S_{c95\%}$ and $m_{95\%}$ [(19) and (20) above].							
S_g (10^{-3})	MPa	Data to be provided by the designer.							(25) S_g (10^{-3}): The design allowable stress value corresponding to the probability of failure of 10^{-3}, computed in accordance with HHA-II-3300 based on $S_{c95\%}$ and $m_{95\%}$ [(19) and (20) above].							
S_g (10^{-2})	MPa	Data to be provided by the designer.							(26) S_g (10^{-2}): The design allowable stress value corresponding to the probability of failure of 10^{-2}, computed in accordance with HHA-II-3300 based on $S_{c95\%}$ and $m_{95\%}$ [(19) and (20) above].							
S_g (5×10^{-2})	MPa	Data to be provided by the designer.							(27) $S_g(5\times10^{-2})$: The design allowable stress value corresponding to the probability of failure of 5×10^{-2}, computed in accordance with HHA-II-3300 based on $S_{c95\%}$ and $m_{95\%}$ [(19) and (20) above].							
Graphite Oxidation Effects																
Property	Units	2%	4%	6%	8%	10%										
Strength [.] (Section 4.19)									(28) Oxidation change in strength: As either a chart or a curve that describes the mean behavior of the relative property change as a function of weight loss. This is expressed as a value normalized to the as-manufactured value and may be based on a strength parameter selected by the designer. The strength parameter used shall be recorded in an attachment to the MDS. The figures in HHA-3141 may be used as an alternative to measurements.							

ASME BPVC-III-5-2017, FORM MDS-1 MATERIAL DATA SHEET (SI UNITS)									
Elastic modulus (dynamic) [.] (Section 4.20)									(29) Oxidation change in elastic modulus (dynamic): As either a chart or a curve that describes the mean behavior of the relative property change as a function of weight loss. This is expressed as a value normalized to the as-manufactured value.
Thermal conductivity [.] (Section 4.21)									(30) Oxidation change in thermal conductivity: As either a chart or a curve that describes the mean behavior of the relative property change as a function of weight loss. This is expressed as a value normalized to the as-manufactured value.
Irradiated Graphite									
Property									
Dimensional change [.] (Section 4.22)									(31) Irradiation-induced dimensional change: This is the change in length, normalized to the initial length expressed as a percentage. The data shall be expressed as either a table of data or a mathematical fit, appended to the MDS. Range of applicability to be identified and checked as part of the design assessment.
Creep coefficient [.] (Section 4.23)									(32) Irradiation-induced creep coefficient: Shall be expressed as either a table of data or a mathematical fit, appended to the MDS. Range of applicability to be identified and checked as part of the design assessment. The creep coefficient to be used is the coefficient (or set of coefficients) required for the irradiation creep model proposed for use by the designer. The model shall be recorded in an attachment to the MDS.
Coefficient of thermal expansion [.] (Section 4.24)									(33) Irradiation-induced change in coefficient of thermal expansion: Shall be expressed as either a table of data or a mathematical fit, appended to the MDS. Range of applicability to be identified and checked as part of the design assessment. This is expressed as a value normalized to the as-manufactured value. The temperature dependence of this property shall be determined.

ASME BPVC-III-5-2017, FORM MDS-1 MATERIAL DATA SHEET (SI UNITS)									
Strength [.] (Section 4.25)									(34) Irradiation-induced change in strength: Shall be expressed as either a table of data or a mathematical fit, appended to the MDS. Range of applicability to be identified and checked as part of the design assessment. This is expressed as a value normalized to the as-manufactured value and shall be based on a strength parameter selected by the designer. The strength parameter used shall be recorded in an attachment to the MDS. Note that irradiation-induced change in strength need only be measured should the designer desire to take account of the strength increase at low or intermediate damage doses.
Elastic modulus [.] (Section 4.26)									(35) Irradiation-induced change in elastic modulus: This is expressed as a value normalized to the as-manufactured value.
Thermal conductivity [.] (Section 4.27)									(36) Irradiation-induced change in thermal conductivity: This is expressed as a value normalized to the as-manufactured value. The temperature dependence of this property shall be determined.
GENERAL NOTES:									
(a) WG and AG refer to the with- and against-grain orientations of the material.									
(b) [.] indicates a dimensionless quantity.									
NOTE:									
(1) If the maximum intended use temperature exceeds 1,000°C, then the temperature-dependent data shall be extended to cover the property values at the maximum intended use temperature.									
SPECIFIC NOTES:									
1. The analysis of statistical properties was performed ignoring the orientation and position of the test sample. This approach contradicts the recommendations of Price (1976) but was judged acceptable as the sampling and specimen extraction plans ensured that approximately equal numbers of specimens were removed in each direction and from all locations within the billet. Furthermore, this ensured that no single portion of the data set dominated the results.									

4.4. Maximum Grain Size

The maximum grain size of the raw coke used in the green mix for NBG-18 graphite is 1,600 μm. The maximum grain size of the graphitized coke is expected to be lower than this value, because the coke particles shrink during graphitization. Huang et al. (2014) confirm this, reporting the maximum grain size of the graphitized coke as 1,100 μm.

In Figure 4-1, Panel (a) depicts a region showing graphitized filler, graphitized binder, and porosity. Panel (b) shows a filler particle surrounded by the binder. Panel (c) is a magnification of the inner region of the filler particle in Panel (a). Panel (d) shows a dark-field micrograph of the perimeter of the filler particle.

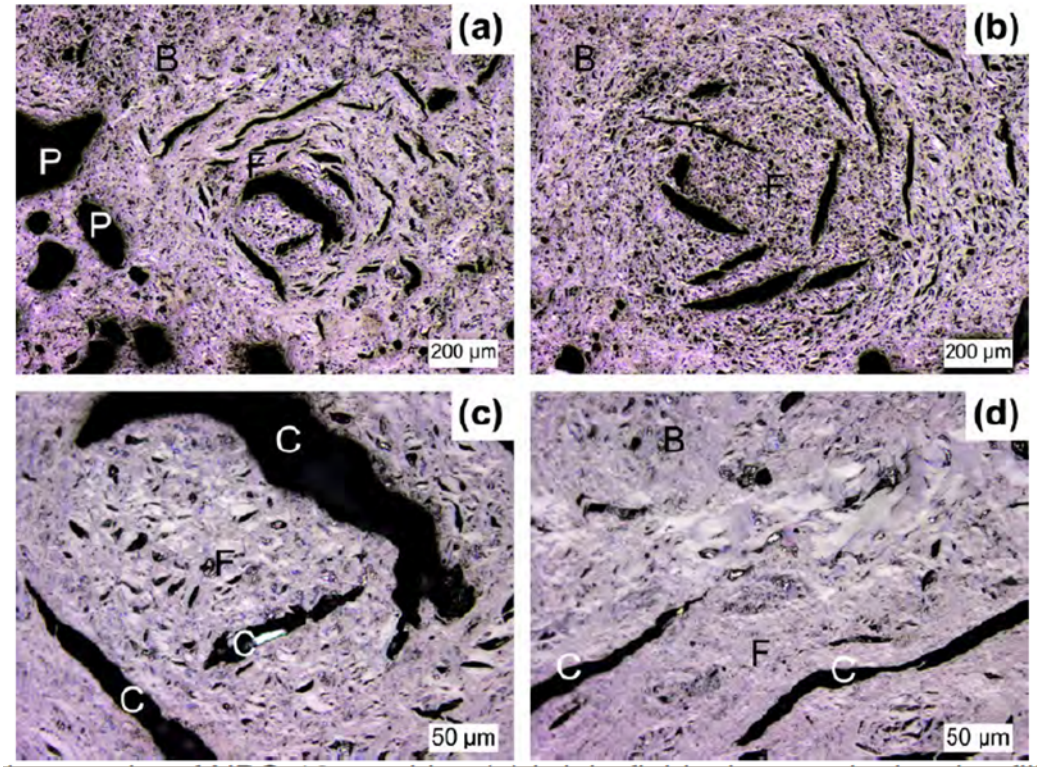

Figure 4-1 Optical micrographs of NBG-18 graphite, P = Porosity, F = Filler, B = Binder, C = Shrinkage crack (Ubic, 2009)

4.5. Designation

As stated in Article HHA-I-1110, this can be either ASTM D7219-08 or ASTM D7301-08. The designer enters the designation. Since most of the data available for this report pertain to ASTM D7219-08, that is the designation entered in Table 4-1.

Temperature-Dependent Parameters

4.6. Bulk Density

As stated in ASTM D7219-08, NBG-18 belongs to the molded, near-isotropic, high-purity (MNHP) class. Huang et al. (2014) and Zheng et al. (2014) reported a density of 1.85 Mg/m^3, based on information from Béghein et al. (2012). Calculations using the Weibull statistics data of the densities measured for 1,093 NBG-18 test specimens, reported by Carroll and Rohrbaugh (2013), yield a (Weibull) mean density of 1.847 ± 0.013 Mg/m^3. Table 4-2 provides more density information for NBG-18, obtained from the INL NGNP research.

Table 4-2 Bulk Density of NBG-18 Graphite

Sample Designation	Density, Mg/m^3	Reference
Piggyback Combined Specimens	1.898 ± 0.009	Windes et al. (2015)
Piggyback AG Specimens	1.891 ± 0.007	
Piggyback WG Specimens	1.901 ± 0.008	
Creep Combined Specimens	1.883 ± 0.020	Windes et al. (2017b)
Creep AG Specimens	1.889 ± 0.017	
Creep WG Specimens	1.877 ± 0.021	
Oxidation Specimens	1.852 ± 0.004	Matthews et al. (2019)

The ASTM standard requires a minimum bulk density of 1.7 Mg/m^3 for graphites in the MNHP class. NBG-18 graphite meets this requirement.

4.7. Tensile Strength

Béghein et al. (2012) reported the room-temperature tensile strength for NBG-18 graphite as 30 MPa; however, they did not report the test type (three-point bend or four-point bend), number of samples tested, or standard deviation for the data. Using the ASTM C749-08 test standard, Carroll et al. (2010) determined a mean tensile strength of 19.61 ± 1.65 MPa on 255 test specimens. Carroll and Rohrbaugh (2013) also measured the room-temperature tensile strength of NBG-18 graphite, again using ASTM C749-08. However, they did not report the mean strength or the standard deviation for their results, providing only information on the Weibull statistical analysis of the strength data obtained on a sample population of 698. An evaluation of their data yields a (Weibull) mean tensile strength of 19.76 ± 2.00 MPa.

Figure 4-2 shows the temperature dependence of the tensile strength of NBG-18 (Fechter, 2010). The strength increases monotonically with temperature.

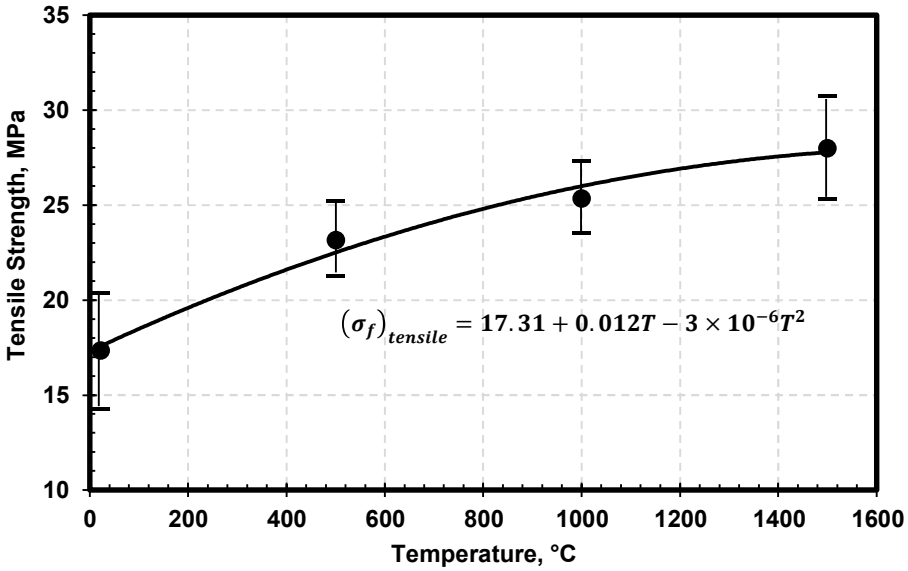

Figure 4-2 Tensile strength of NBG-18 graphite as a function of temperature (Fechter, 2010)

4.8. Flexural Strength (Four-Point)

Béghein et al. (2012) reported the room-temperature flexural strength for NBG-18 graphite as 30 MPa; however, they did not report the test type (three-point bend or four-point bend), number of samples tested, or standard deviation for the data. Using the ASTM C651-11 test standard, Carroll et al. (2010) determined a mean flexural strength of 27.77 ± 1.62 MPa on 255 test specimens. Carroll and Rohrbaugh (2013) also measured the room-temperature flexural strength of NBG-18 graphite, using the ASTM C651-10 four-point bend test standard. However, they did not report the mean strength or the standard deviation for their results, providing only information on the Weibull statistical analysis of the strength data obtained on a sample population of 515. An evaluation of their data yields a (Weibull) mean flexural strength of 27.75 ± 2.05 MPa.

4.9. Compressive Strength

Béghein et al. (2012) reported the room-temperature compressive strength for NBG-18 graphite as 80 MPa; however, they did not report the number of samples tested or the standard deviation for the data. Using the ASTM C695-91 test standard, Carroll et al. (2010) determined a mean compressive strength of 81.28 ± 4.34 MPa on 260 test specimens. Using the same test standard, Carroll and Rohrbaugh (2013) measured the room-temperature compressive strength of NBG-18 graphite on yet another batch of NBG-18 specimens. However, they did not report the mean strength or the standard deviation for their results, providing only information on the Weibull statistical analysis of the strength data obtained on a sample population of 516. An evaluation of their data yields a (Weibull) mean flexural strength of 81.31 ± 4.96 MPa.

4.10. Elastic Modulus (Dynamic)

Béghein et al. (2012) reported Young's modulus of NBG-18 graphite as 11.5 GPa. However, they did not report the method of measurement or the direction of measurement (WG, AG, or combined). INL researchers engaged in NGNP investigations measured the elastic modulus of NBG-18 graphite (Windes et al., 2013b) using both dynamic (ultrasonic, ASTM Standard C769-09) and sonic resonance (ASTM Standard C747-93) methods, on baseline samples used for irradiation creep. Table 4-3 shows their results.

Table 4-3 Room-Temperature Young's Modulus Data from NGNP Research

Measurement Method	Against-Grain, GPa	With-Grain, GPa	Anisotropy Ratio (AG/WG)
DYM	16.11 ± 0.08	12.42 ± 0.07	1.04
Resonance	15.46 ± 0.11	11.99 ± 0.13	1.04

4.11. Elastic Modulus (Static)

Carroll and Rohrbaugh (2013) reported the static elastic modulus of NBG-18 graphite, obtained from tensile tests, in the form of Weibull statistics. From their data, a (Weibull) mean static elastic modulus of 10.44 ± 0.95 GPa can be calculated. It is not clear from the report which grain direction these data represent.

4.12. Coefficient of Thermal Expansion

Béghein et al. (2012) reported the mean CTE of NBG-18 graphite as 4.5×10^{-6}/°K in the WG direction and 4.6×10^{-6}/°K in the AG direction, for temperatures of 20–200 degrees C (68–932 degrees F).

Vasudevamurthy et al. (2015) studied the effect of temperature on the mean CTE of NBG-18 graphite in the WG direction. Figure 4-3 shows their results.

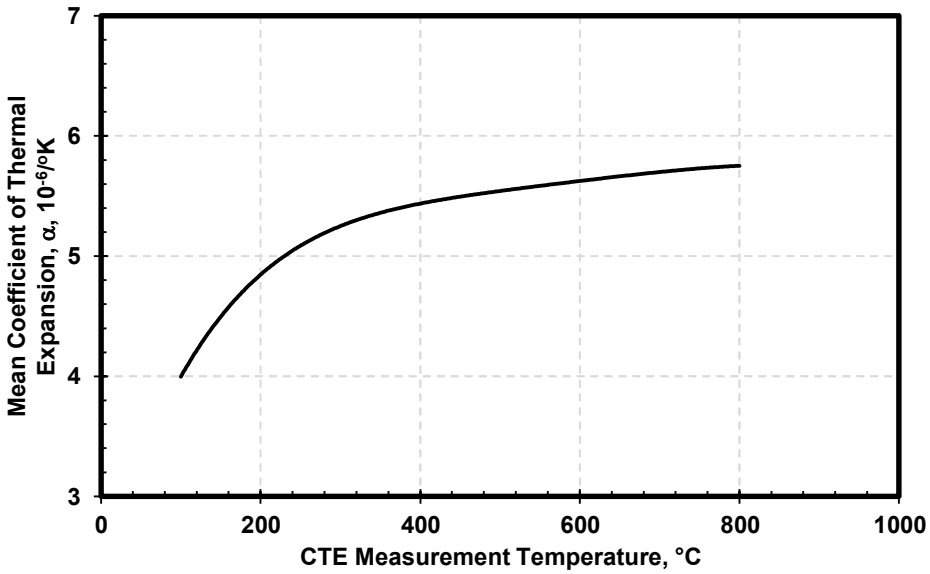

Figure 4-3 Effect of temperature on WG CTE of NBG-18 graphite (Vasudevamurthy et al., 2015)

Zhou et al. (2011) obtained data on the effect of applied stress on the CTE of NBG-18, measured with reference to the orientation of the samples relative to the installed direction of the blocks in the HTR-10 reactor. The results are ambiguous. Unfortunately, the authors did not provide any information on the graphite grain orientation within the sample. They provided information only on specimens cut in the axial (vertical) and circumambient directions of a block as it would be constructed in a reactor. The anisotropy ratios have been calculated based on these data, which are shown in Figure 4-4.

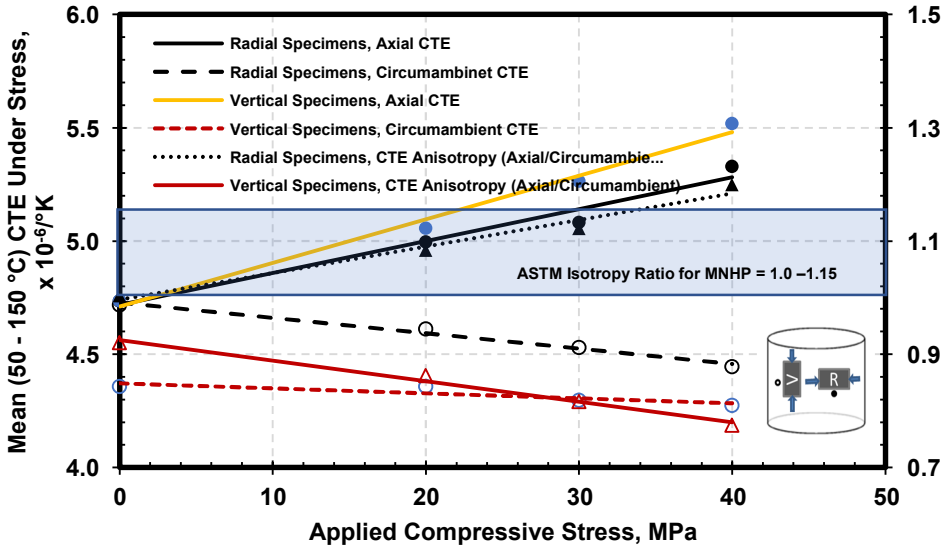

Figure 4-4 CTE behavior under stress for NBG-18 in specimens cut in the radial and vertical directions (Zhou et al., 2011)

4.13. Thermal Conductivity

Figure 4-5 shows the temperature dependence of thermal conductivity of nonirradiated NBG-18 graphite. The typical trend for graphites, of decrease in thermal conductivity with temperature, is evident.

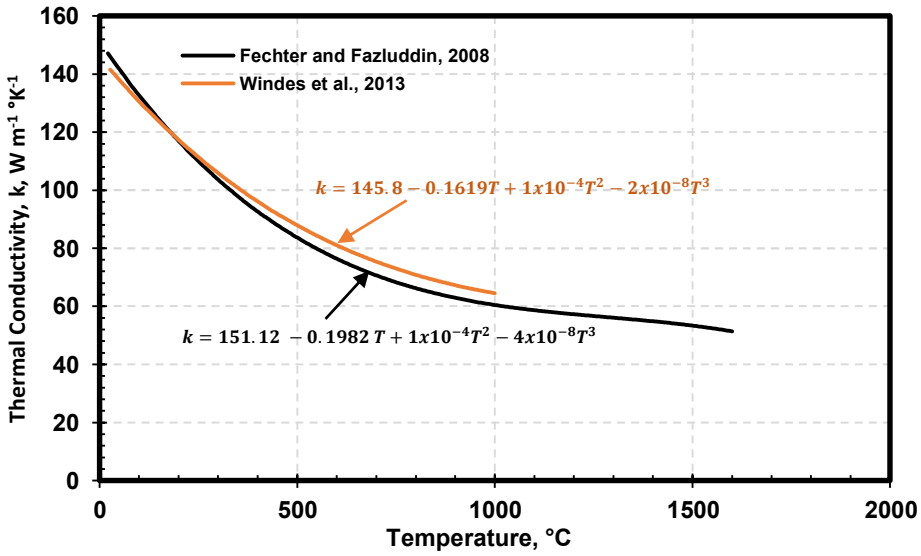

Figure 4-5 Temperature dependence of thermal conductivity of nonirradiated NBG-18 graphite

Temperature-Independent Parameters

4.14. Poisson's Ratio

Carroll (2014) calculated a room-temperature Poisson's ratio (μ) value of 0.230 for NBG-18 graphite from the Weibull scale parameters for the modulus measurements in flexural and torsional modes.

4.15. Anisotropy Factor

Although the ASME BPVC MDS lists the anisotropy factor as a temperature-independent parameter, it is in fact mildly dependent on temperature, as shown in Figure 4-6.

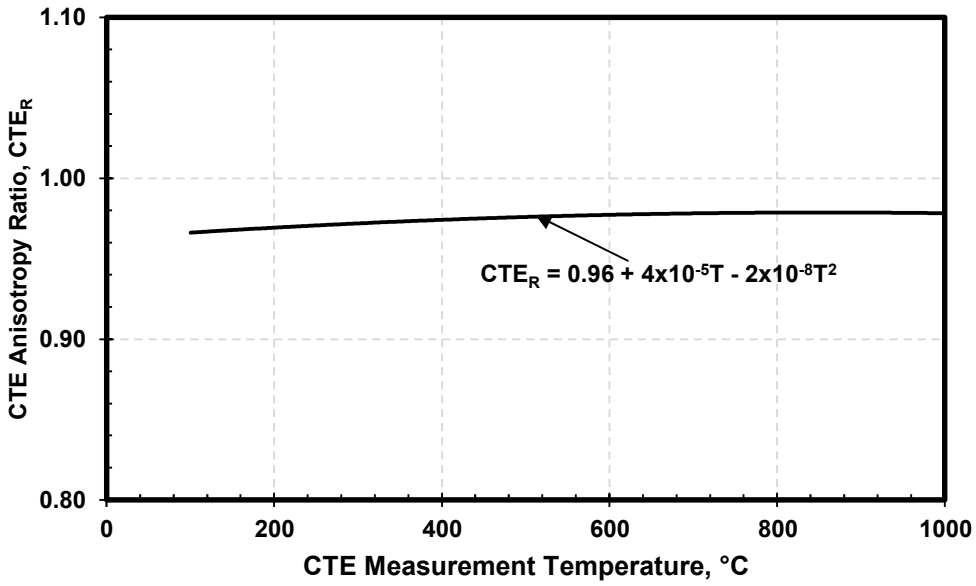

Figure 4-6 Temperature dependence of CTE anisotropy for NBG-18 graphite (Windes et al., 2013)

4.16. Critical Stress Intensity Factor, K_{Ic}

For NBG-18 graphite, Chi (2016) obtained an average fracture toughness value of 1.02–1.11 MPa √m for two specimen thicknesses at room temperature. These values were determined using SENB specimens in three-point bending. Burchell et al. (2017) reported a value of 1.36 ± 0.1 MPa √m in the WG specimen orientation and 1.41 ± 0.05 MPa √m in the AG specimen orientation. They used three-point bend specimens in tests conducted at room temperature.

Graphite Oxidation Effects

Several investigators have studied the weight loss of NBG-18 graphite due to oxidation. Figure 4-7 shows one example of such work, plotting weight loss as a function of residence time in dry air for various oxidation temperatures.

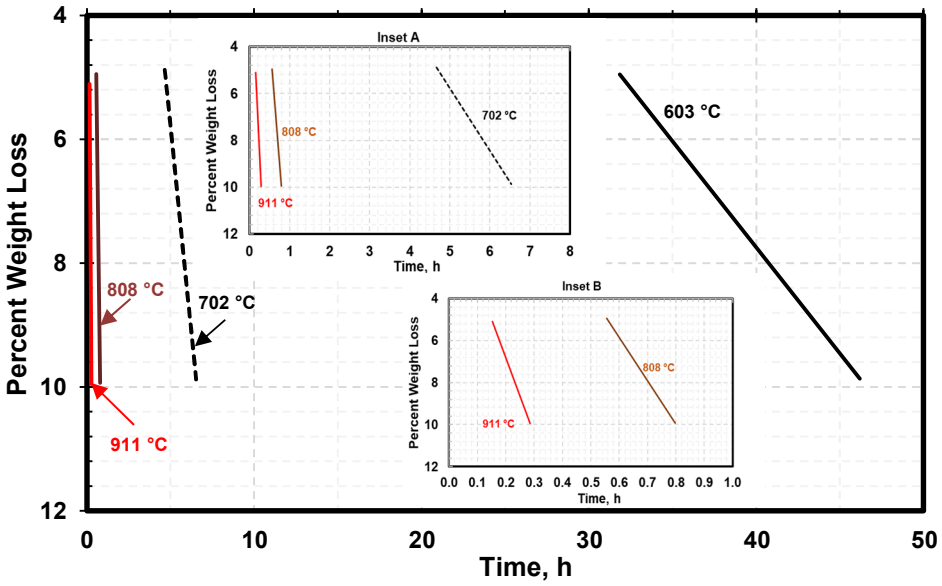

Figure 4-7 Weight loss behavior of NBG-18 graphite (Chi and Kim, 2008)

In this research, Chi and Kim (2008) determined ORs in dry air at six temperatures between 600 and 960 degrees C (1,112 and 1,760 degrees F), using a three-zone vertical tube furnace at an air flow rate of 10 L/min. The specimens were cylinders of 25.4-mm diameter and 25.4-mm length. The system conformed to the ASTM standard test method (ASTM 7542-15) for determining OR in graphite. As can be expected, weight loss increases with oxidation time, and the time scale for a given level of weight loss decreases markedly with the oxidation temperature, as seen in Figure 4-7 Weight loss behavior of NBG-18 graphite (Chi and Kim, 2008) The insets A and B have expanded time scales in the *x*-axes to emphasize the effect of oxidation temperature on the rapidity of oxidation.

These weight loss measurements can be used to estimate the OR of NBG-18 graphite. Figure 4-8 provides two examples of this, showing the OR as a function of oxidation temperature. The results from the two separate investigations coincide for oxidation temperatures up to approximately 800 degrees C (1,472 degrees F). At higher oxidation temperatures, the results of Chi and Kim (2008) indicate much more rapid oxidation in dry air than those of Lee et al. (2018).

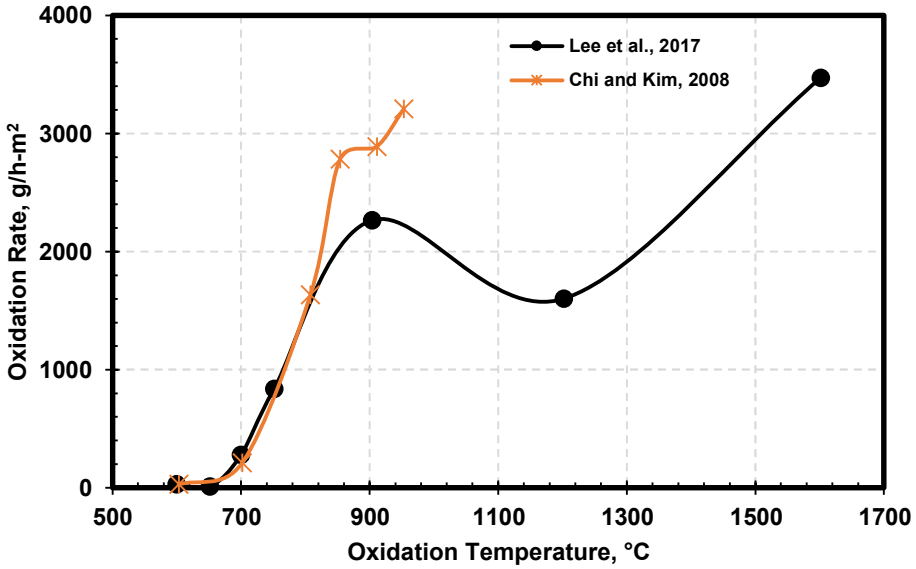

Figure 4-8 Rate of oxidation as a function of oxidation temperature for NBG-18 graphite

The OR also depends on the flow rate of oxygen. Figure 4-9 shows the results of an experimental study of this effect by Chi and Kim (2017) using dry air. Here, temperature seems to play a significant role, especially above 700 degrees C (1,292 degrees F).

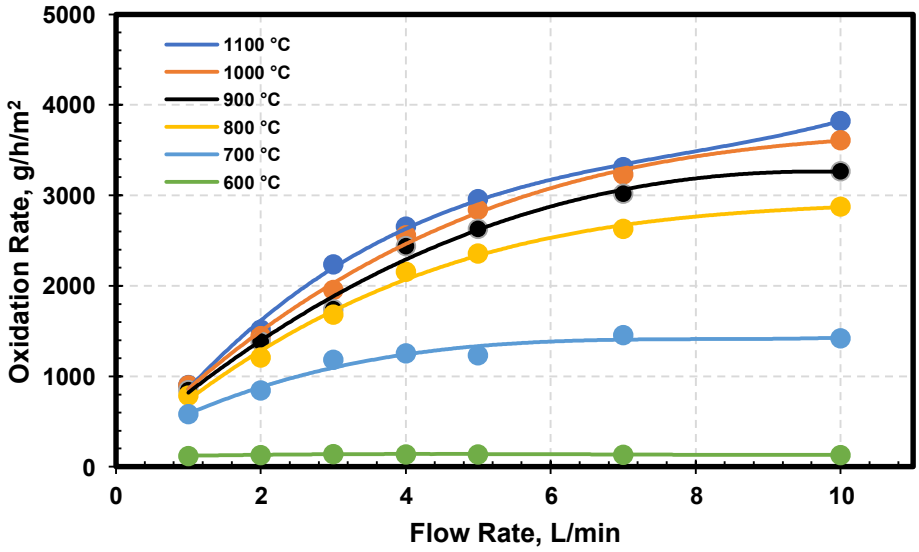

Figure 4-9 Dependence of OR on the rate of flow of oxygen for NBG-18 graphite (Chi and Kim, 2017)

At 600 degrees C (1,112 degrees F) and 700 degrees C (1,292 degrees F), changes in the flow rate cause relatively insignificant change in the OR. However, at temperatures above 700 degrees C, rapid change occurs over flow rates up to approximately 5 L/min. For flow rates above 5 L/min, the OR increases only gradually.

The above experimental results were further analyzed using a gasification model and studies on various graphites. Figure 4-10 shows the dependence of total gasification flux on oxidation weight loss, as calculated by El-Genk et al. (2012) using oxidation data measured in dry air from Chi and Kim (2008). To understand the gasification phenomenon, El-Genk et al. developed a model to determine the Sherwood number.[5]

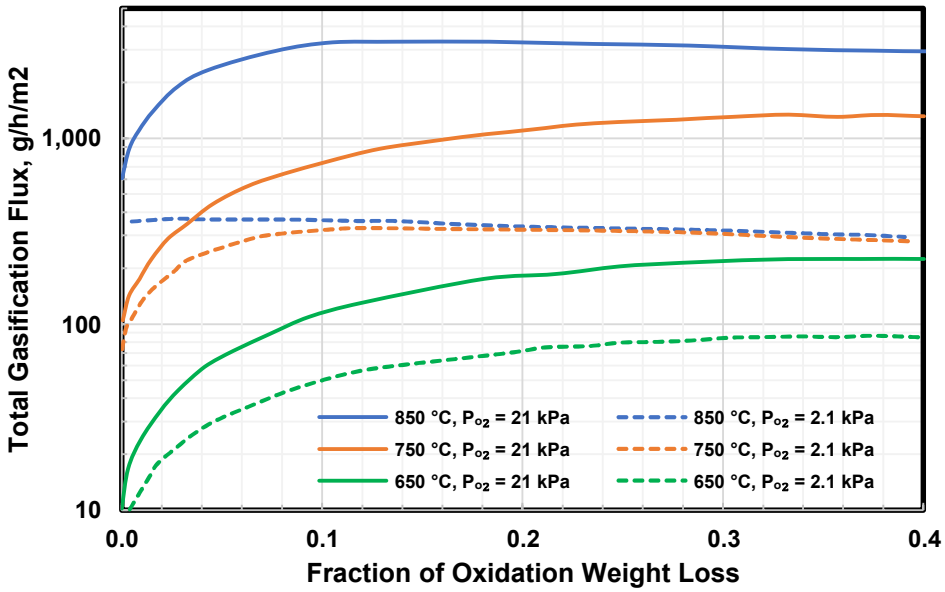

Figure 4-10 Model predictions of gasification rate for NBG-18 test specimens of Chi and Kim (2008) by El-Genk et al. (2012)

In addition to the microstructure and fabrication method of nuclear graphite, gasification rates partially depend on the total porosity, the morphology of the open-volume pores, the type and concentration of impurities that act as catalysts for gasification, and temperature. Below 400 degrees C (752 degrees F), graphite gasification is insignificant. At temperatures up to 677 degrees C (1,251 degrees F), depending on the conditions of the bulk gas mixture and the nuclear graphite grade, gasification is mostly uniform inside the open-volume pores, gradually

---

5 The Nusselt and Sherwood numbers represent the effectiveness of heat and mass convection at the surface. The Sherwood number is to the concentration boundary layer what the Nusselt number is to the thermal boundary layer. The Sherwood number is a dimensionless number that represents the ratio of convective mass transfer to the rate of diffusive mass transport; it is used in the analysis of mass transfer systems such as liquid-liquid extraction. The Sherwood number is defined as

$$Sh = \frac{convective\ mass\ transfer}{mass\ diffusion\ rate} = \frac{k_m}{D/L},$$

where k_m is the convective mass transfer coefficient (m/s), D is the mass diffusivity (m^2/s), and L is a characteristic length (m). As can be seen from the definition, the Sherwood number increases as convective mass transfer or characteristic length increases, and as the mass diffusivity decreases.

For gas systems, an alternative formulation using the gas phase mass transfer coefficient k can be used:

$$Sh = \frac{kRT}{DP},$$

where k is the gas phase mass transfer coefficient (mol./(m^2.s. mole fraction)), R is the gas constant (L/mol.°K), T is the temperature (°K), and P is the pressure.

weakening the structural strength with increased weight loss. At higher temperatures, gasification ceases within the open-volume pores and shifts to corroding the external surface.

The gasification model recently developed by El-Genk and Tournier (2011, 2012) encompasses the chemical kinetics rates and pre-exponential coefficients of four elementary reactions: (1) the chemisorption of oxygen molecules to form oxygen radicals at active sites, (2) the dissociation and adsorption of oxygen radicals to form stable complexes, (3) the desorption of stable complexes to produce CO gas, and (4) the desorption of CO_2 gas.

The model of El-Genk and Tournier used Gaussian-like distributions of the specific activation energies for adsorption of oxygen and desorption of CO gas and the initial surface area of free active sites. A multiparameter optimization algorithm was used to determine these quantities from reported experimental measurements of the transient weight loss and total gasification rate for the different grades of nuclear graphite at different temperatures. The model also accounted for changes in the surface area of free active sites with weight loss. The most active sites are located at the edge positions in the basal planes of the hexagonal graphite crystals. They are abundant in the interior of open-volume pores but relatively sparse at external surfaces. The surface area of the active free sites, which varies across different grades of nuclear graphite, increases with weight loss and was determined to peak at a value of 30–40 percent.

Figure 4-10 shows the calculated results, indicating the effect of temperature on the total gasification rate of the NBG-18 specimens in the experiments of Chi and Kim (2008) in dry air (P_{O2} = 21 kilopascals (kPa) and P_{O2} = 2.1 kPa), as functions of the weight loss fraction X. Below about 777 degrees C (1,430 degrees F), the total gasification rate is governed by the changes in the graphite microstructure and active surface area sites; it is associated with weight loss, which increases exponentially with increasing temperature. At temperatures above 777 degrees C (1,430 degrees F), graphite gasification is diffusion limited; the total gasification rate is almost constant for weight loss fractions greater than 0.10 and is nearly independent of temperature (see Figure 4-10). In this diffusion-limited mode, the total gasification rate is proportional to the oxygen partial pressure in the bulk gas flow, P_{O2}. It is encountered at 750 degrees C (1,382 degrees F) when P_{O2} = 2.1 kPa, and at 850 degrees C (1,562 degrees F) when P_{O2} = 21 kPa. The slight decrease in the total gasification rate in the diffusion-limited mode with increasing weight loss fraction was attributed to the gradual decrease in the external surface area of the NBG-18 test specimen over time.

4.17. Design Strength and Material Reliability Curve Values

Designers must enter the items under this category in the MDS, based on the results of their own testing and analyses and following the requirements in ASME BPVC-III-5, Article HHA-2200. The authors of this report did not attempt to derive these values from the literature and are not providing information on MDS Items 17–27.

4.18. Graphite Oxidation Effects

Oxidation of NBG-18 graphite, like that of other graphites, leads to loss of mass as carbon is oxidized to gaseous products. Because of the relative abundance of oxidation sites at the pore walls and the edges of a graphite specimen, these are the areas most subject to oxidation.

Oxidation generally leads to an increase in pore volume and to changes in pore structure. It is thus expected to change physical properties (density), mechanical properties (elastic modulus and strength), and thermal properties (conductivity) that are affected by pore volume and pore morphology.

4.19. Strength

The compressive strength of NBG-18 graphite decreases with oxidation, because of mass loss, as shown in Figure 4-11. On the macro scale, Matthews et al. (2019), who performed oxidation testing in dry air, observed different types of fracture in the specimens, which they classified into four types:

(1) belt-line fracture: the specimen exhibits a relatively large nominal fracture surface area normal to the direction of applied stress

(2) shear fracture: the specimen exhibits a relatively large nominal fracture surface area, whose plane is approximately 55–65 degrees to the direction of applied stress

(3) cleavage fracture: the specimen exhibits a relatively large nominal fracture surface area, whose plane is parallel to the direction of applied stress

(4) a brittle fracture other than those described in (1)–(3) above

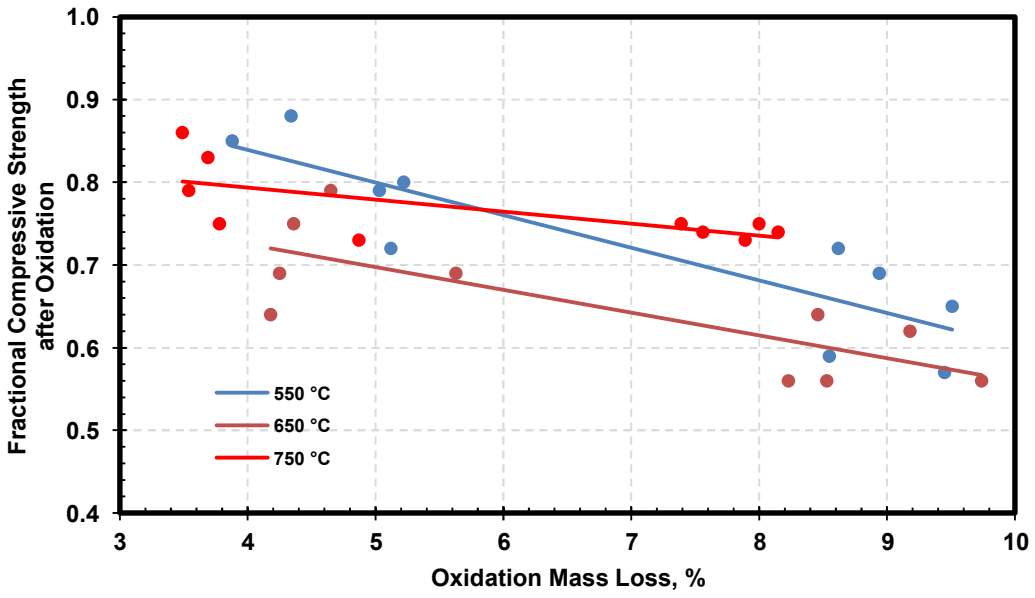

Figure 4-11 Loss in compressive strength due to oxidation of NBG-18 graphite (Matthews et al., 2019)

Variations in the degree of loss of compressive strength due to oxidation may arise from specimen-to-specimen variations in the changes in porosity and pore morphology caused by oxidation. Matthews et al. (2019) also related their test results to the ASME BPVC

requirements, which allow a maximum of 10-percent mass loss, beyond which the component is assumed to have no appreciable or usable mechanical strength. Because oxidation mechanisms differ under different oxidation regimes, Matthews et al. observed that it may be necessary to calculate the structural integrity separately for core components experiencing varying temperatures along and across the core.

4.20. Elastic Modulus

Oxidation leads not only to loss of graphite mass but also to changes in the intrinsic properties of the material; in particular, it affects the porosity and the pore morphology, including the pore size and shape distributions. These microstructural properties govern dependent properties such as the elastic modulus. Olasov et al. (2019) studied the effect of oxidation on the elastic modulus of NBG-18. Olasov et al. oxidized the graphite using dry air in accordance with ASTM D7542-09 to analyze the effects of porosity on elastic modulus, they developed a microstructure-based physics model that included the effects of microcracks on the elastic behavior of graphitized crystallites. They also determined the DYM of NBG-18 and compared experimental data with the results of their analytical model, as shown in Figure 4-12.

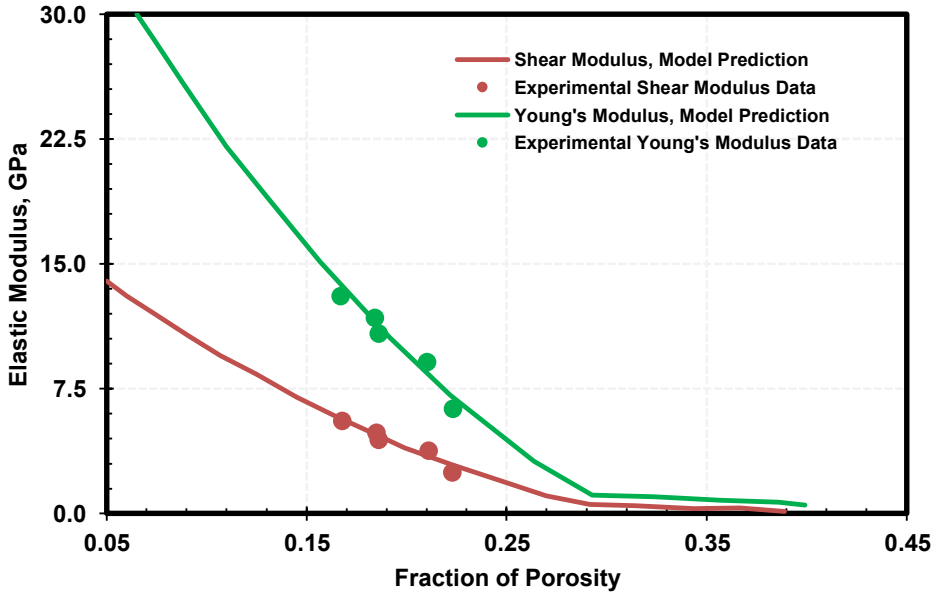

Figure 4-12 Dependence of Young's and shear modulus for NBG-18 as a function of porosity (adapted from Olasov et al., 2019)

The model of Olasov et al. (2019) captures the experimental data, at least within the narrow range of experimentally induced porosity levels, using controlled oxidation at 500 degrees C (932 degrees F) for oxidation times of 238 and 450 hours and at 575 degrees C (1,069 degrees F) for oxidation times of 44 and 80 hours. The weight losses range from approximately 4.3 to 10.9 percent.

4.21. Thermal Conductivity

The authors of this report have not been able to find literature on changes in thermal conductivity resulting from oxidation of NBG-18 graphite.

Irradiated Graphite

4.22. Dimensional Change

Figure 4-13 shows the volume change caused by irradiation of NBG-18 graphite. Heijna et al. (2017) irradiated NBG-18 at the Petten reactor at an irradiation temperature of about 750 degrees C (1,382 degrees F), while Windes et al. (2017a) conducted irradiation experiments in the Advanced Test Reactor at INL at irradiation temperatures of 432–708 degrees C (810–1,306 degrees F). As expected, the experiments of Windes et al. (2017a) show lower volume change than those of Heijna et al. (2017), because of the lower irradiation temperatures.

Figure 4-14 shows the extent of variation in irradiation temperature and dose (Windes, 2012). Thus, scatter is to be expected in the data on volume change versus irradiation dose.

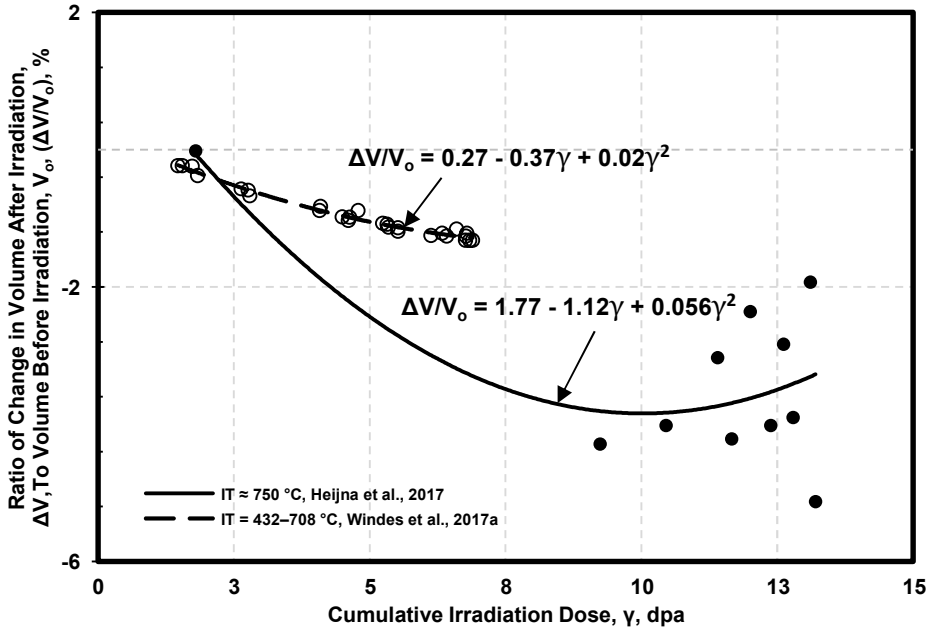

Figure 4-13 Volume change due to irradiation of NBG-18 graphite

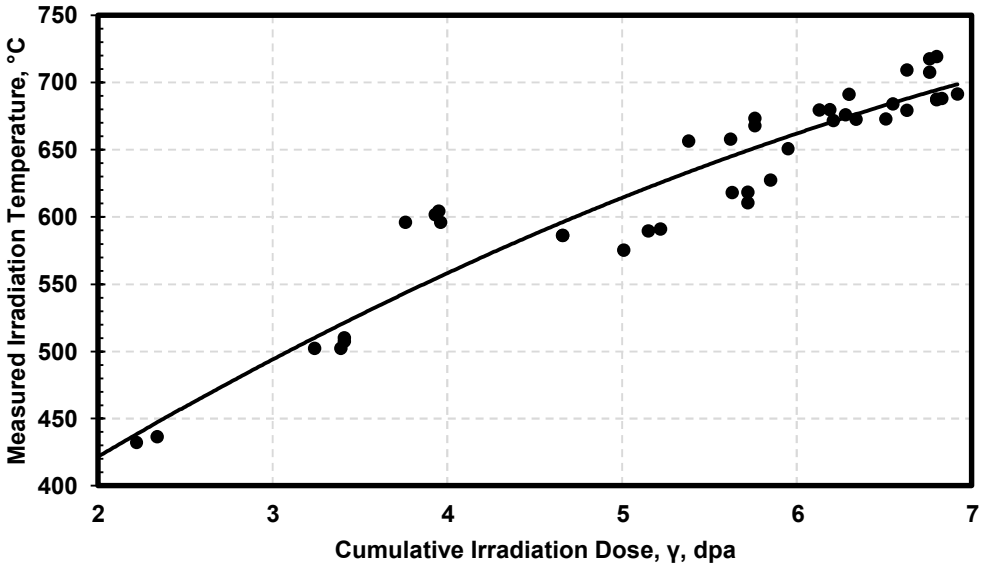

Figure 4-14 Temperature-dose distribution in the NBG-18 irradiation specimens of the experiments conducted by Windes (2012)

NBG-18 graphite also exhibits differences in shrinkage in the WG and AG orientations, as expected. Figure 4-15 shows this behavior.

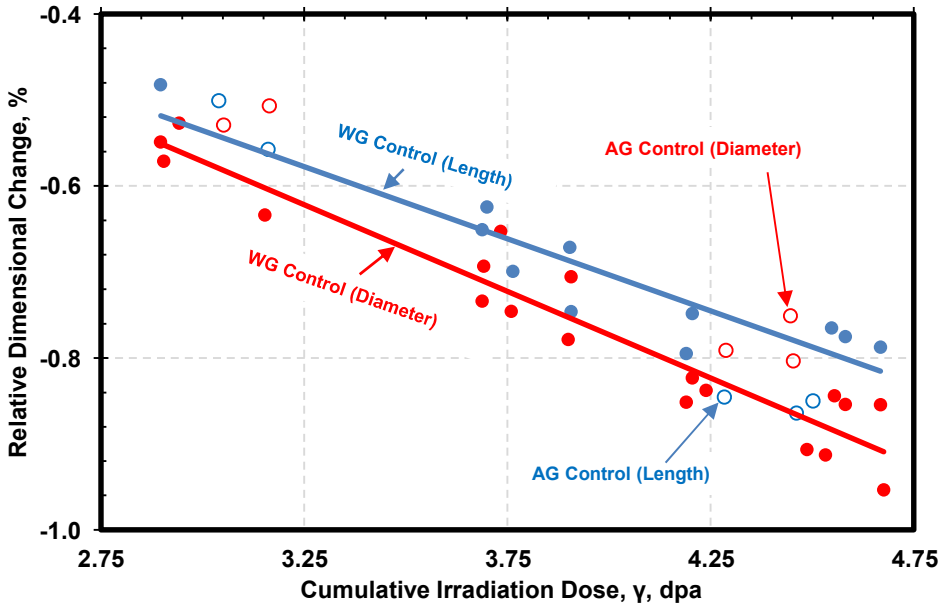

Figure 4-15 Extent of dimensional change in the orthogonal directions of nonstressed NBG-18 control specimens in the creep testing population of experiments conducted at INL (Windes et al., 2016)

Here, the specimens were irradiated at 600 ± 65 degrees C (1,112 ± 149 degrees F). The data scatter precludes any meaningful conclusions; however, at the irradiation doses indicated, it

seems that specimens generally shrink more in the diameter than in the length. That is, AG shrinkage is greater than WG shrinkage.

Windes et al. (2016) provides another set of data, shown in Figure 4-16. Here, the NBG-18 graphite samples studied undergo greater overall dimensional change than those of Figure 4-15. However, it is clear that the creep samples, which were irradiated under stress, again show more shrinkage in the AG direction than in the WG direction.

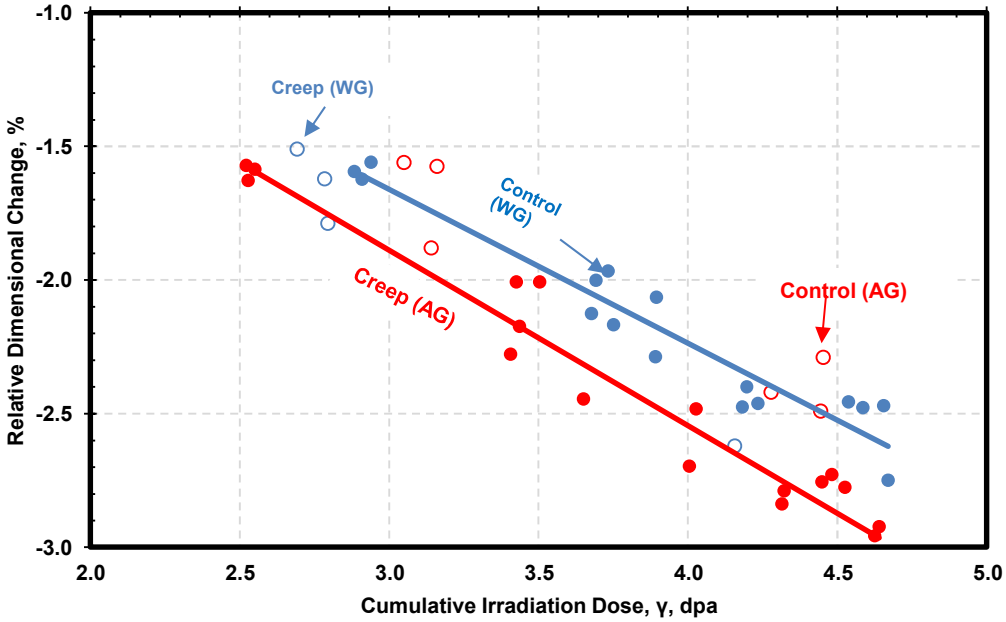

Figure 4-16 Orientation dependence of dimensional change due to irradiation for NBG-18 graphite (Windes et al., 2016)

The applied creep stress only mildly affects the change in volume of NBG-18 graphite, as shown in Figure 4-17.

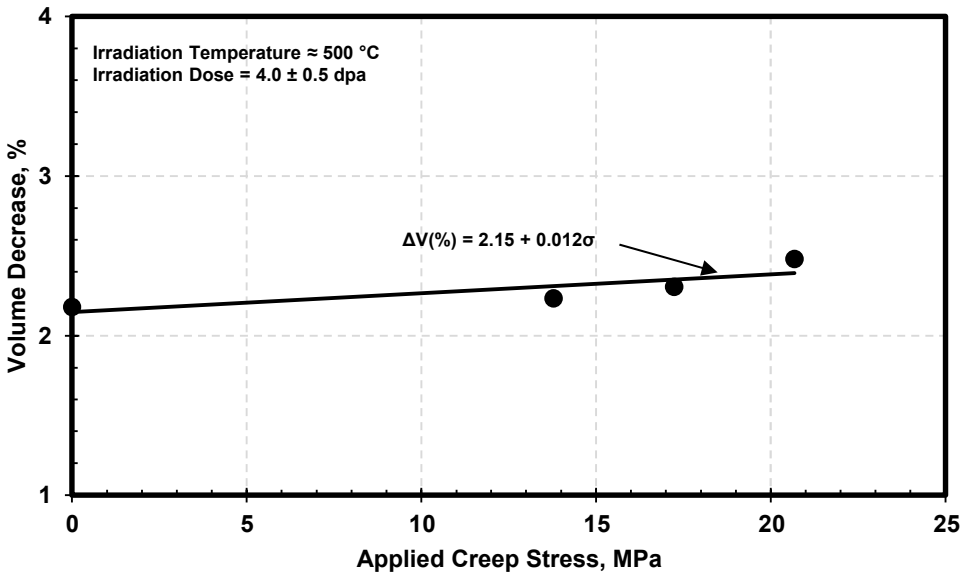

Figure 4-17 Effect of creep stress on volume change during irradiation of NBG-18 graphite (Windes et al., 2015)

The dimensional change measured at room temperature after irradiation of NBG-18 is affected by the stress imposed during irradiation, as shown in Figure 4-18. The total shrinkage, which is due to graphite lattice contraction and the compression caused by creep stress, increases with the amount of applied creep stress. These specimens were irradiated at an average temperature of 350 degrees C (662 degrees F).

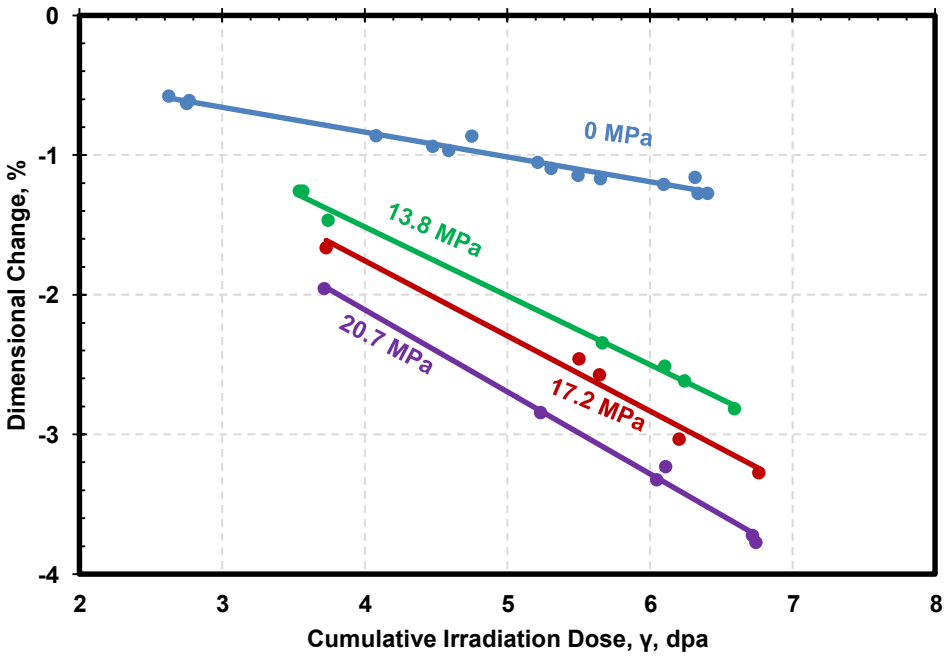

Figure 4-18 Effect of creep stress on dimensional change due to irradiation at 350 degrees C (Windes, 2012)

4.23. Creep Coefficient

Irradiation secondary creep coefficient for NBG-18 has been reported for three temperatures normalized to a stress of 20.7 MPa, as shown in Table 4-4 (Windes et al., 2019).

Table 4-4 Irradiation Secondary Creep Coefficient for NBG-18 Normalized to a Stress of 20.7 MPa (Windes et al., 2019)

Irradiation Temperature, °C (°F)	Creep Coefficient K, (%/MPa-dpa)
600 (1,112)	0.014
625 (1,157)	0.014
820 (1,508)	0.026

Considering the difficulties in attaining and maintaining constant temperature in any materials irradiation program, it may be appropriate to interpret this information as effectively giving the same creep coefficient for an average temperature of about 600 degrees C (1,112 degrees F). Because the data are so limited, not much can be concluded from these values in relation to the overall phenomenon of irradiation creep in NBG-18 graphite other than the creep coefficient increases at 820 degrees C (1,508 degrees F), which is expected.

4.24. Coefficient of Thermal Expansion

Irradiation increases the CTE of NBG-18, with both irradiation dose and irradiation temperature affecting the level of increase. Figure 4-19 shows a comparison of irradiated and nonirradiated CTE, as a function of measurement temperature. The average irradiation temperature for these data was 820 degrees C (1,508 degrees F). The irradiation dose (range) was not reported.

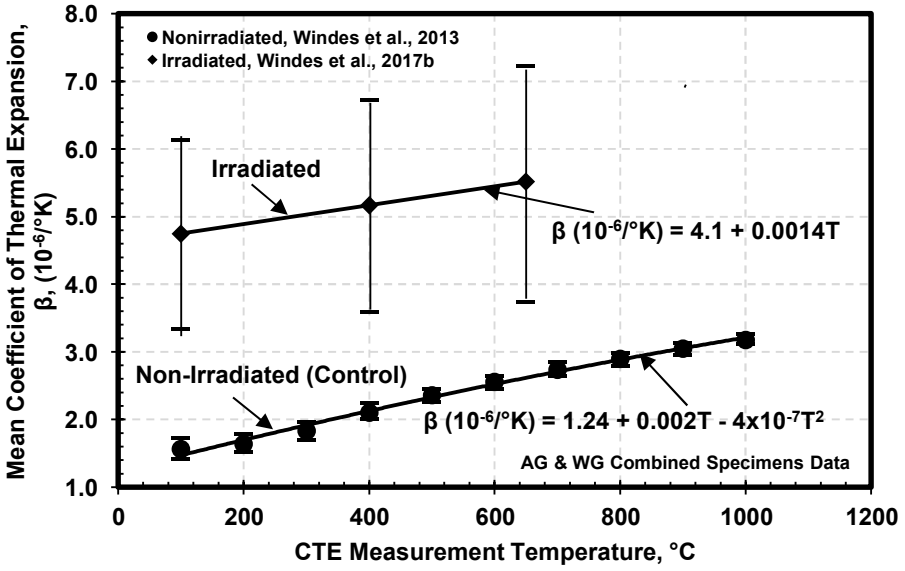

Figure 4-19 Effect of irradiation on CTE as a function of temperature for NBG-18 graphite

Figure 4-20 shows the effect of irradiation temperature on the level of CTE change, for an irradiation dose of 4.0 ± 0.5 dpa. The data scatter makes it impossible to draw any dependable inferences from these data.

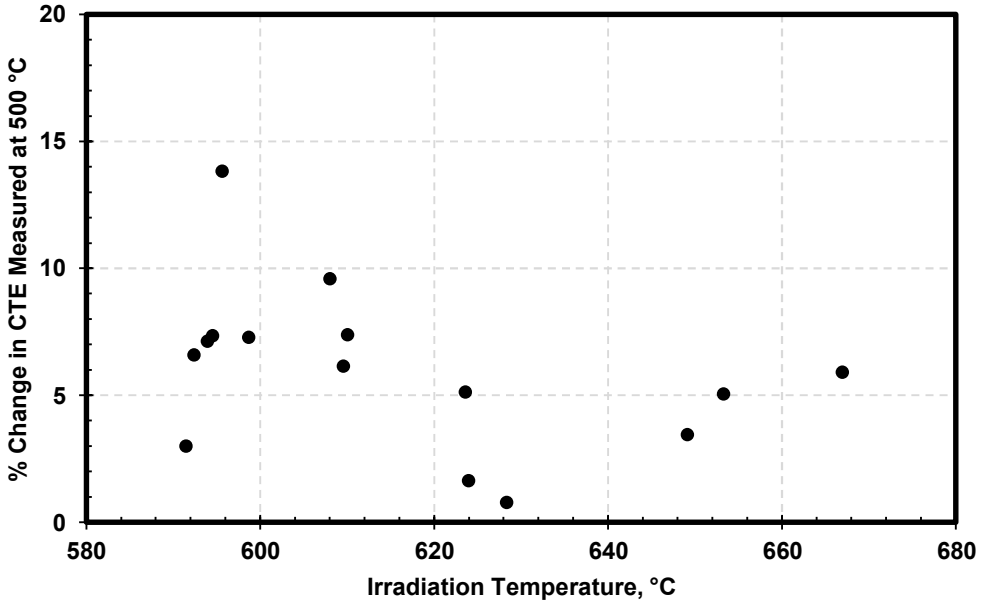

Figure 4-20 Dependence of CTE change on irradiation temperature for NBG-18 graphite (Windes et al., 2017a)

Figure 4-21 shows the irradiation dose dependence of the level of CTE change (with mean CTE measured up to 500 degrees C (932 degrees F)) after irradiation at 2–5 dpa. Again, because of the data scatter, it is impossible to infer any behavioral trends.

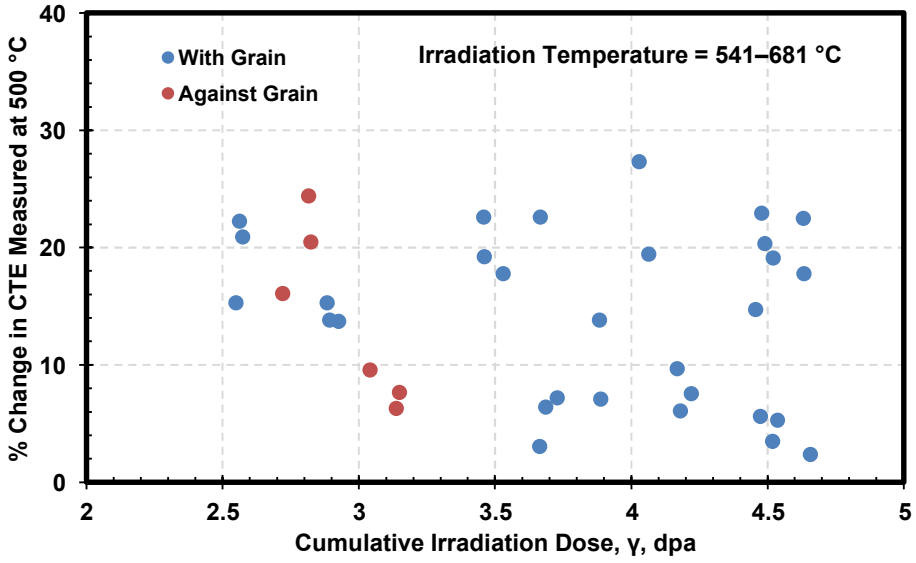

Figure 4-21 Irradiation dose dependence of change in CTE for NBG-18 graphite (Windes et al., 2017a)

Both Euratom and the NGNP research programs have investigated the effect of irradiation dose on CTE. Figure 4-22 shows the results.

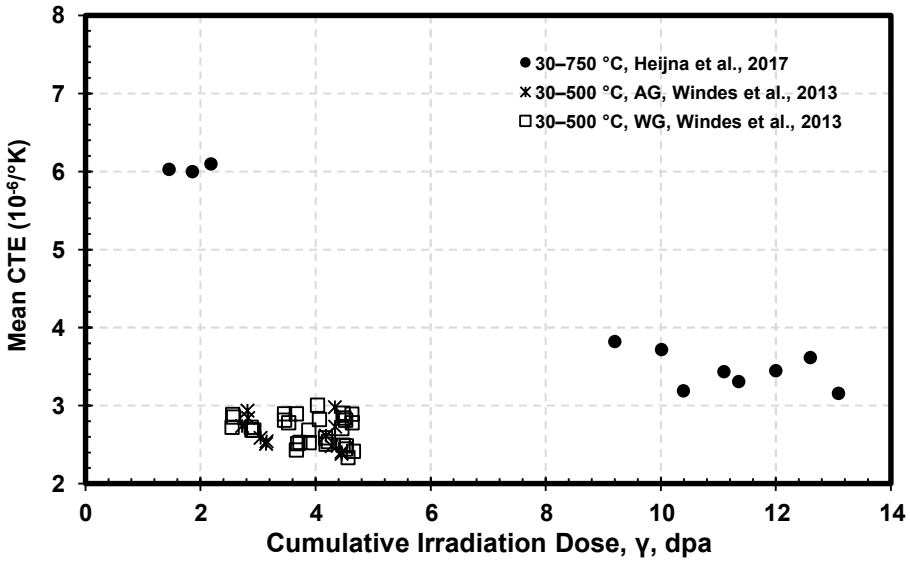

Figure 4-22 Dose dependence of mean CTE after irradiation for NBG-18 graphite

Here, the mean temperature after irradiation represents the range indicated in the figure for each investigation. The Heijna et al. (2017) data are for irradiation conducted at 750 degrees C (1,382 degrees F), whereas the Windes et al. (2013) data are for irradiation conducted at 541–681 degrees C (1,006–1,258 degrees F). The CTE reported by Windes appears to be significantly lower than the CTE reported under the Euratom program, Heijna et al. (2017).

The CTE is also affected by any applied stress during irradiation that results in creep deformation. Figure 4-23 shows this effect, for irradiation temperatures of 541–681 degrees C (1,006–1,258 degrees F).

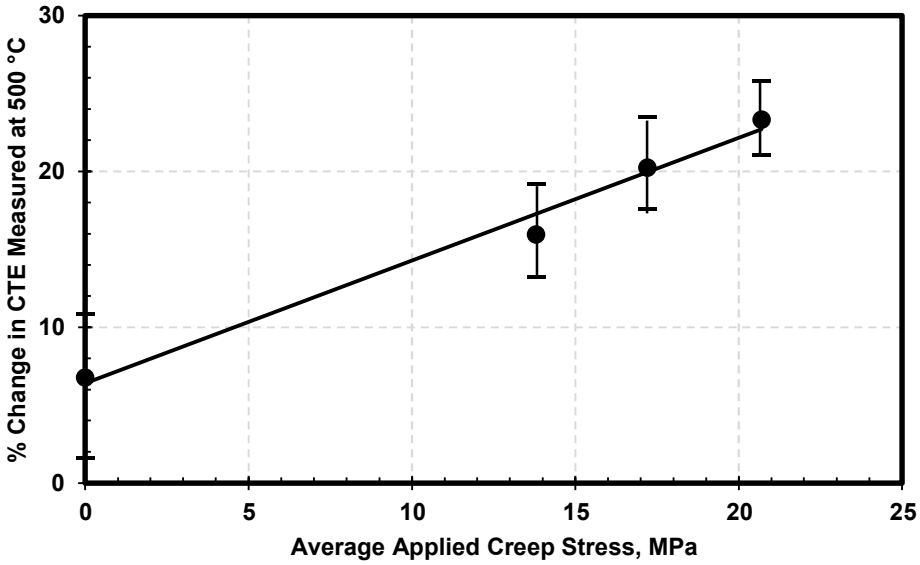

Figure 4-23 Effect of creep stress on relative CTE change for WG and AG orientations of NBG-18 graphite (Windes et al., 2017a)

The schematic in Figure 4-24 shows the overall effect of applied stress on the relative CTE change, based on the observed data for the two grain orientations. The relative change in the mean CTE also exhibits anisotropy, which is shown in Figure 4-24 as a function of CTE measurement temperature (temperature range from room temperature).

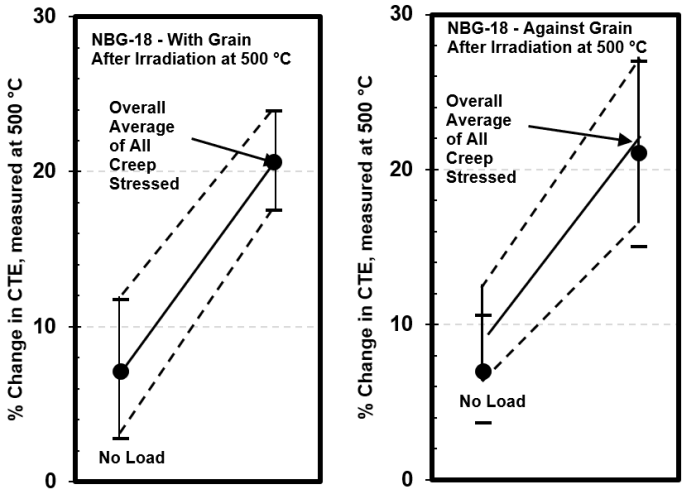

Figure 4-24 Irradiation-enhanced CTE change for NBG-18 graphite (Windes et al., 2017a)

4.25. Strength

Heijna et al. (2017) conducted irradiation testing with discs of NBG-18 graphite, irradiating to 750 degrees C (1,382 degrees F). After irradiation, they conducted diametral compression tests at room temperature and derived the tensile strength from the results, as shown in Figure 4-25. Because of the test specimen geometry and test method, the investigators did not provide

information on strength for WG and AG orientations. However, the trend in the irradiated strength behavior is generally independent of the grain orientation.

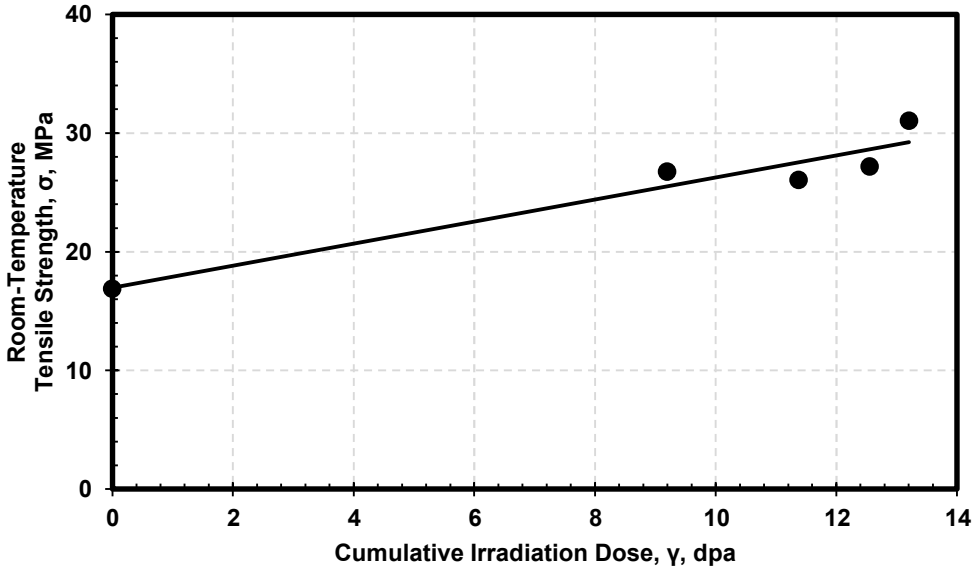

Figure 4-25 Room-temperature tensile (diametral compression) strength of NBG-18 graphite, after irradiation at 750 degrees C (1,382 degrees F) (Heijna et al., 2017)

4.26. Elastic Modulus

One of the fundamental reasons that irradiation changes the properties of graphite is that it causes shrinkage of graphite grains, which changes the density. Figure 4-26 shows the density change behavior of NBG-18 graphite, as studied by Windes (2012). The inset in Figure 4-26, reproduced from Figure 4-14, depicts the temperature variations between specimens experiencing corresponding irradiation doses. Thus, density variations can be related to the differences in the shrinkage levels corresponding to the sample dose and temperature, which are interdependent and interrelated. The data exhibit the generally expected trend of increasing density with dose.

The elastic (Young's) modulus of NBG-18 graphite depends on density and would thus also be expected to increase after irradiation. However, as shown in Figure 4-27, the room-temperature DYM change data after irradiation at 617 ± 85 degrees C (1,143 ± 185 degrees F) have considerable scatter, which precludes recognition of any definite trend.

Windes et al., 2017a calculated the shear modulus using sonic velocity measurements. Figure 4-28 shows the relative change in shear modulus. Here, the irradiation temperature was 541–681 degrees C (1,006–1,258 degrees F). Again, the data scatter may be attributed to the dispersion in the individual temperatures and the inherent inhomogeneity of NBG-18 graphite.

Heijna et al. (2017) characterized the irradiated Young's modulus of NBG-18. Figure 4-29 shows their results, in combination with those of Windes et al. (2017a). The increase in elastic modulus is attributed to the increase in density. Considering the data scatter, the INL (Windes et al.) and Petten (Heijna et al.) irradiation results are in good agreement.

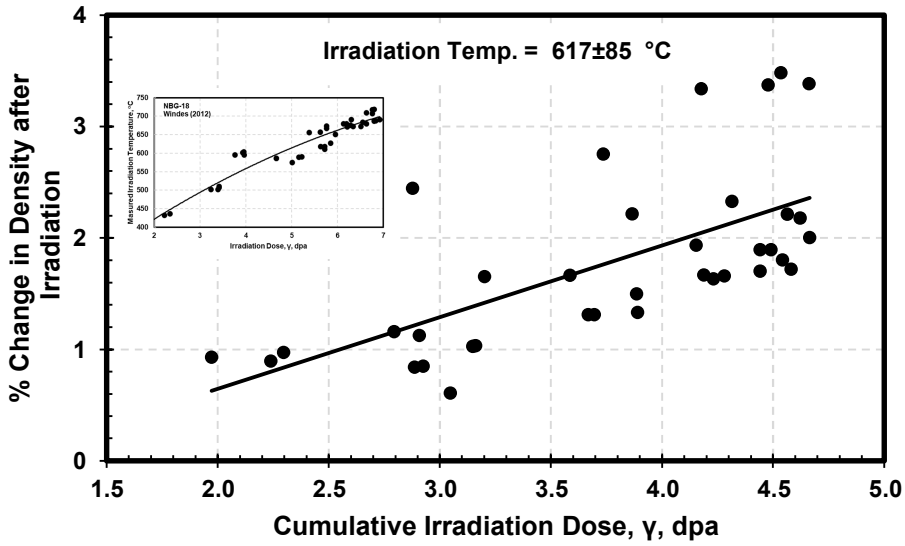

Figure 4-26 Density change due to irradiation for NBG-18 graphite (Windes, 2012)

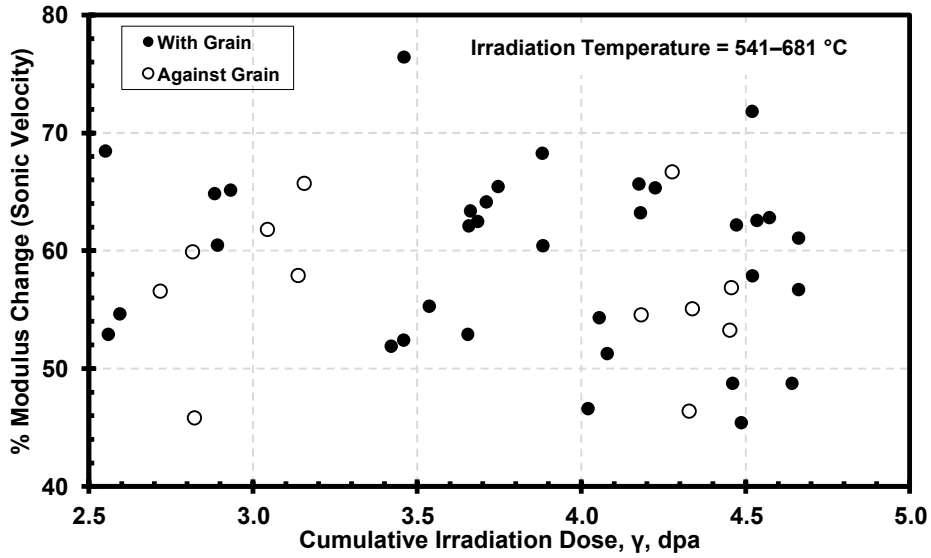

Figure 4-27 Effect of irradiation on the DYM for WG- and AG-oriented NBG-18 specimens (Windes et al., 2017a)

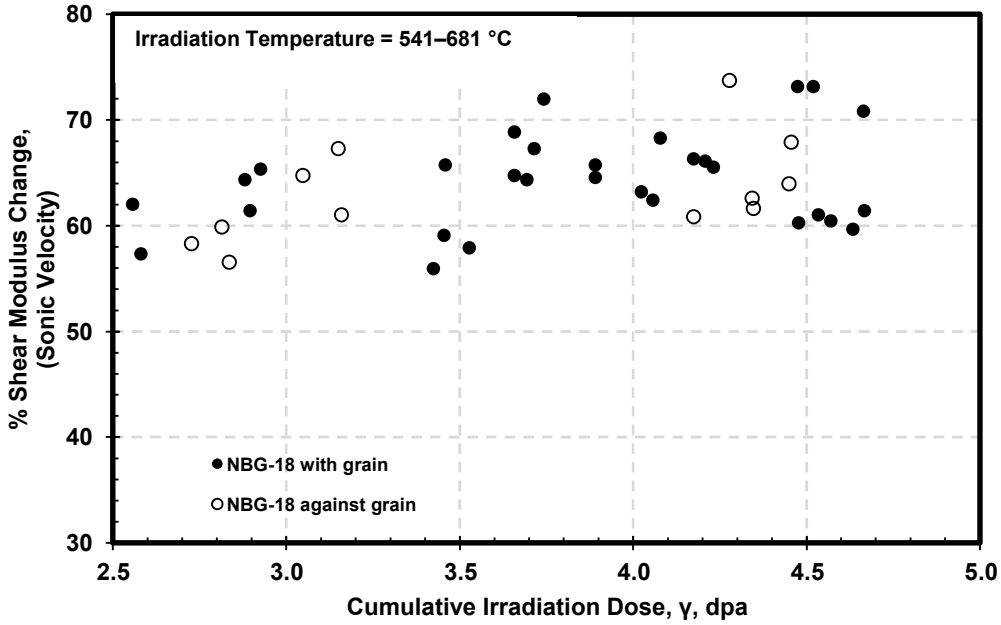

Figure 4-28 Effect of irradiation on shear modulus for WG- and AG-oriented NBG-18 specimens (Windes et al., 2017a)

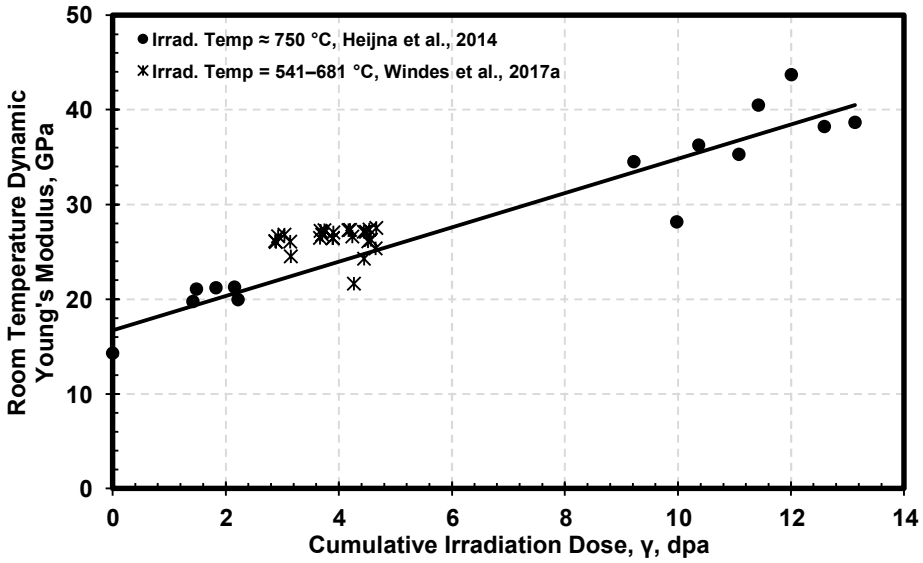

Figure 4-29 Increase in Young's modulus due to irradiation of NBG-18 graphite

As Figure 4-30 shows, the amount by which Young's modulus increases upon irradiation decreases with applied creep stress.

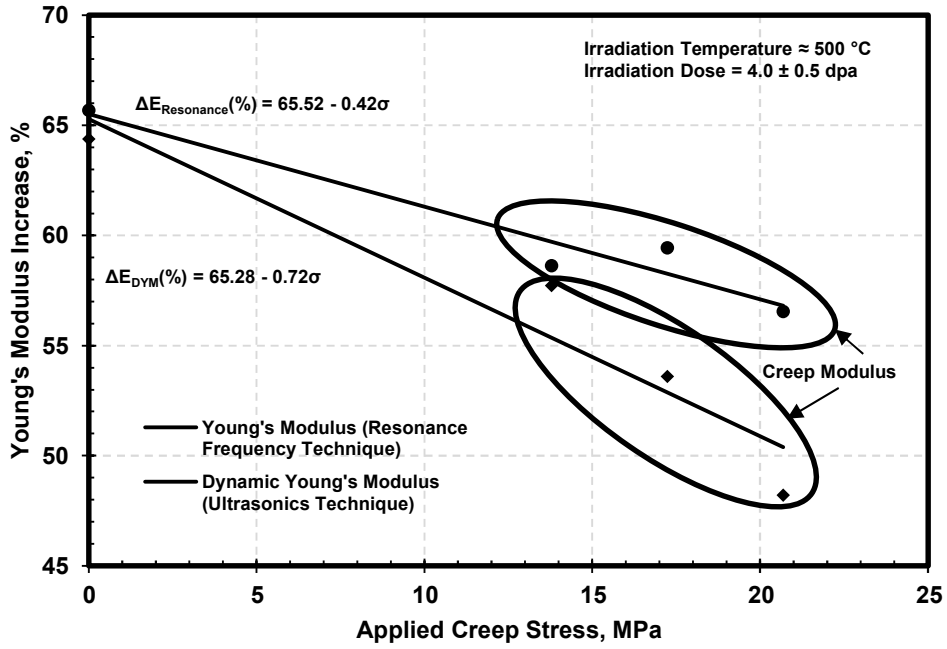

Figure 4-30 The effect of irradiation creep stress on change in Young's modulus of irradiated NBG-18 graphite (Windes et al., 2015)

Irradiation of graphite with no imposed stress generally causes the room-temperature shear modulus to increase relative to that of the nonirradiated graphite. However, applied creep stress reduces the magnitude of this increase, as shown in Figure 4-31 (Windes et al., 2017a). These samples were irradiated to temperatures of 541–681 degrees C (1,006–1,258 degrees F). The creep specimens exhibit varying magnitudes of increase in shear modulus, but generally less than do the control specimens that were not subjected to external creep loading.

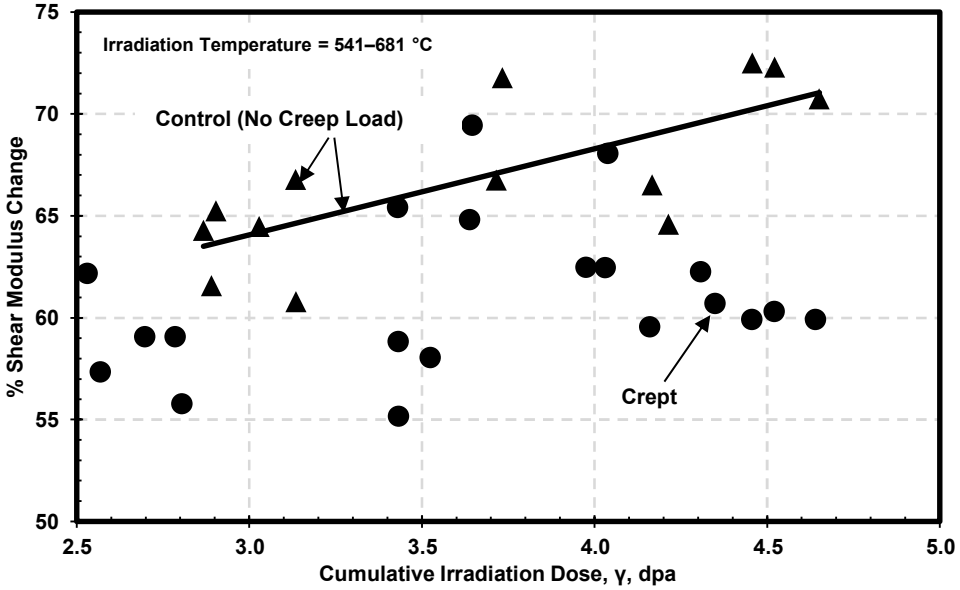

Figure 4-31 The effect of applied creep stress on the relative shear modulus change after irradiation (Windes et al., 2017a)

Using the data of Windes et al. (2017a), Figure 4-32 shows the irradiation temperature dependence of the change in room-temperature Young's modulus of NBG-18 graphite, after irradiation to a dose of 4.0 ± 0.5 dpa.

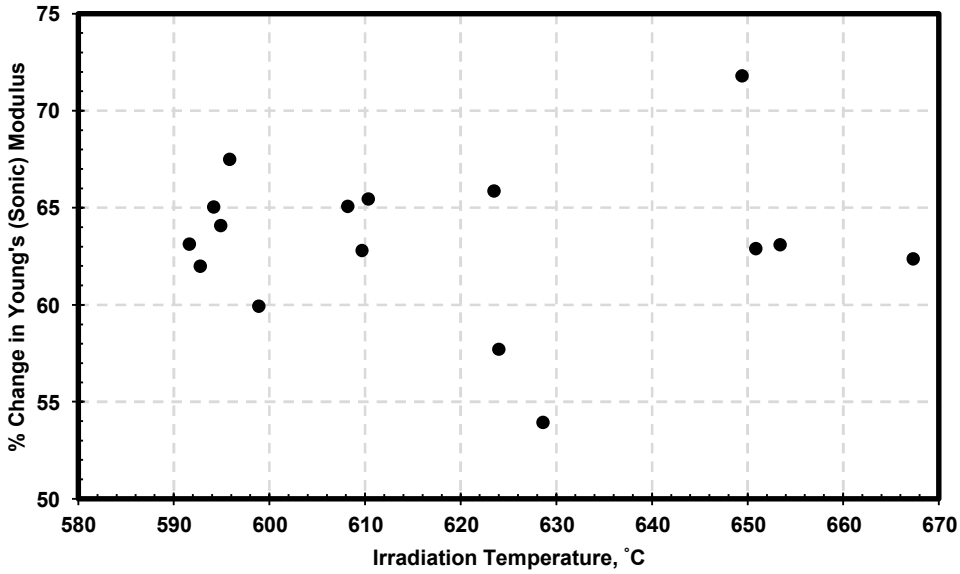

Figure 4-32 Irradiation temperature dependence of change in room-temperature Young's modulus of NBG-18 graphite after irradiation (Windes et al., 2017)

Figure 4-33 shows the irradiation temperature dependence of the change in room-temperature shear modulus of NBG-18 graphite, after irradiation to a dose of 4.0 ± 0.5 dpa, again from the data of Windes et al. (2017a).

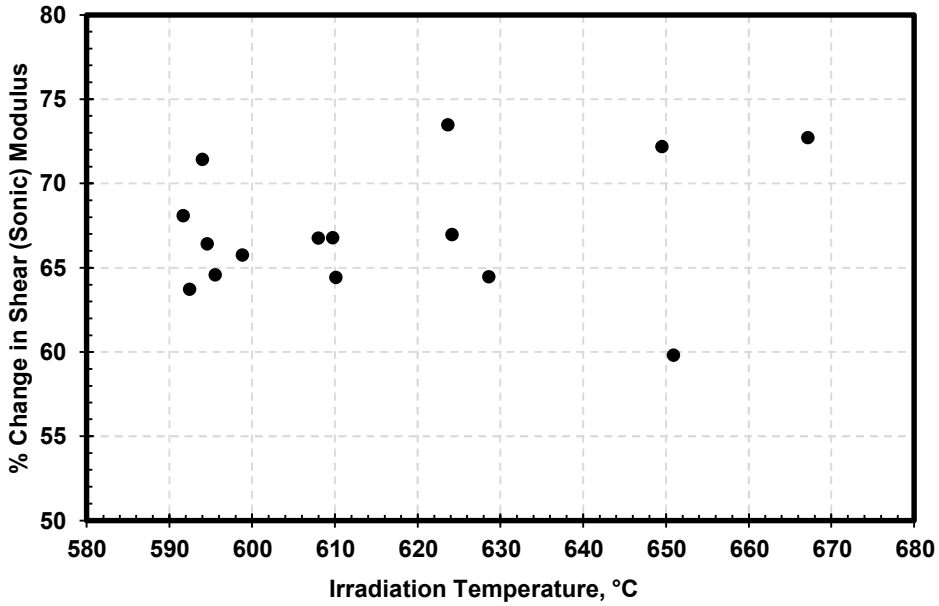

Figure 4-33 Irradiation temperature dependence of change in room-temperature shear modulus of NBG-18 graphite after irradiation (Windes et al., 2017a)

4.27. Thermal Conductivity

Figure 4-34 shows the change in thermal conductivity due to irradiation. For comparison, the figure includes data on nonirradiated NBG-18 graphite, reproduced from Figure 4-5. The limited irradiation data were calculated from thermal diffusivity measurements obtained by Windes et al. (2015), who conducted irradiation at about 500 degrees C (932 degrees F) and at a dose of 4.0 ± 0.5 dpa.

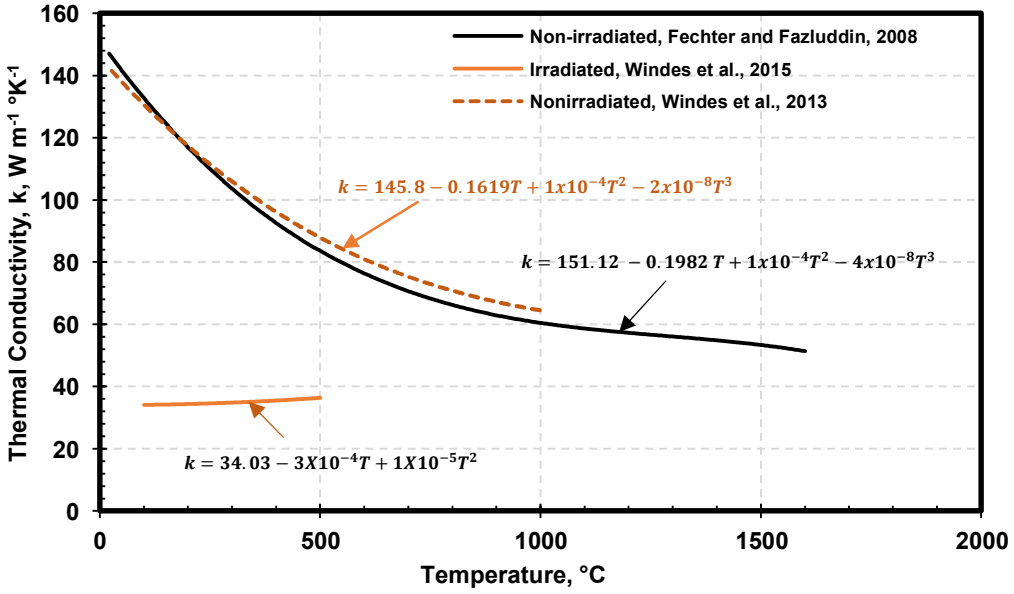

Figure 4-34 Reduction of thermal conductivity of NBG-18 graphite due to irradiation at about 500 degrees C and at a dose of 4.0 ± 0.5 dpa

Figure 4-35 shows the dependence of the room-temperature thermal conductivity on irradiation dose for NBG-18 graphite. Thermal conductivities were calculated from room-temperature thermal diffusivity measurements. Heijna et al. (2017) conducted their irradiation at 750 degrees C (1,382 degrees F) and Windes et al. (2015) at about 500 degrees C (932 degrees F).

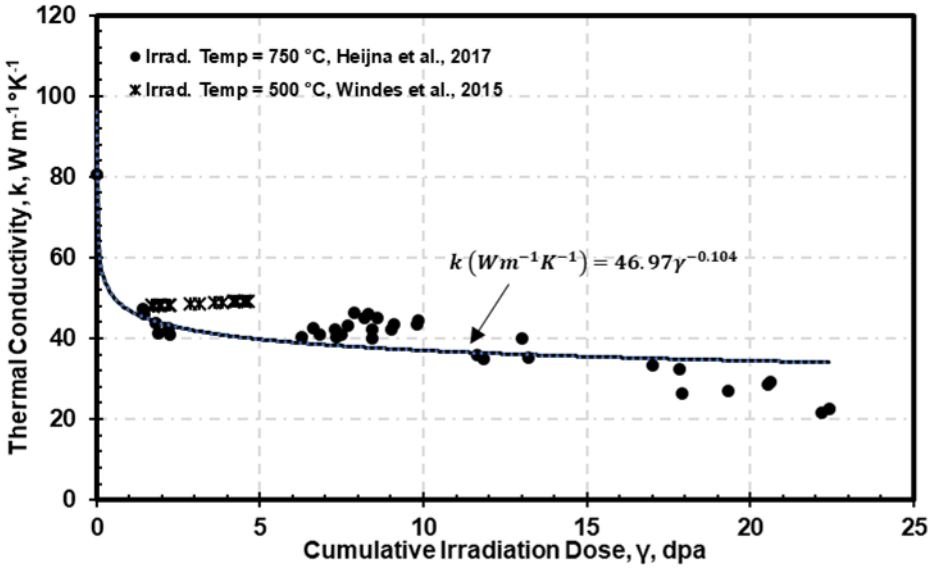

Figure 4-35 Dose dependence of room-temperature irradiated thermal conductivity of NBG-18 graphite

4.28. Chemical Analysis of NBG-18

Table 4-5 provides the elemental analysis of NBG-18, based on the work of Lee et al. (2018), who used GDMS and inductively coupled plasma optical emission spectrometry to detect trace metals. Their results appear to be identical to those reported by Kane (2013) who used inductively coupled plasma mass spectrometry (ICP-MS) and reported the 12 largest impurities as shown in Table 4-6; thus, it is likely that they are from the same source.

Table 4-5 Chemical Analysis of NBG-18 (Lee et al., 2018)

Element	Ash	B	Si	Ca	Fe	Al	Na	V	Cd	Ni	Cr	Co	Gd	Ta	S	Zr
wppm	<10	0.57	38	5.9	4.8	0.24	0.17	0.04	<0.1	<0.1	<0.5	<0.05	<0.05	<5.0	4.8	0.22

Table 4-6 Major Impurities in NBG-18 Samples Investigated by Kane (2013)

Element	ppm	Element	ppm	Element	ppm
Si	38	Fe	4.8	Hg	<0.5
Ca	5.9	F	<1	Mg	<0.5
Ta	<5	B	0.57	Pb	<0.5
S	4.8	Cr	<0.5	Sb	<0.5

Table 4-7 shows the results of an interlaboratory round-robin chemical analysis of NBG-18, which was conducted as input for the development of the ASTM standard specification for elemental analysis of nuclear graphites (Berlioux and Barth, 2008). The participating laboratories used two methods: electrothermal vaporization (ETV), glow discharge mass spectroscopy (GDMS) and inductively coupled plasma optical emission spectrometry. Existing standards were used as a template (ASTM D5600, ISO 14435).

Table 4-7 Results of Round-Robin Chemical Analysis of NBG-18 Graphite

Element	ETV, Lab 1	ETV, Lab 2	ETV, Lab 3	ETV, Lab 5	ICP, Lab 6	ICP, Lab 7	ICP, Lab 8	ICP, Lab 9	GDMS, Lab 4	ICP MS, Lab 4
Al	0.21	0.21	0.32	0.34	0.35	0.22	0.34	0.40	7.0	< 0.5
B	0.27	0.29	0.27	0.28	0.70	0.78			3.0	0.62
Ba	0.75	0.91	0.84	0.95	0.28	0.70	0.60	0.70	0.30	4.1
Ca	6.0	6.6	3.9	3.9	5.9	5.3	5.7	5.0	8.0	
Co	0.15	0.15	0.19	0.19	0.13	0.13	0.14	0.15	0.20	0.16
Cr	1.0	1.5	1.5	1.0	1.7	1.3	1.1	1.2	5.0	2.3
Cu	0.058	0.056	0.066	0.068	0.13	0.066	0.80	0.11	0.15	< 0.5
Fe	21.6	23.5	24.4	28.4	31.1	27.0	33.4	31.0	50.0	28.9
K	1.1	0.92	0.71	1.1	2.5		1.4		0.50	
Li	0.019	0.022	0.022	0.026		0.022			< 0.05	
Mg	0.14	0.15	0.14	0.15	< 0.1	0.11	0.13	0.10	0.25	8.1
Mn	0.084	0.081	0.085	0.10	< 0.1	0.076	0.047	0.080	0.20	< 0.5
Mo	0.17	0.23	0.16	0.15	0.25	0.18	0.13	0.20	0.30	0.59
Na	0.37	0.28	0.25	0.32	7.7	2.1	0.83		1.0	46.2
Ni	5.8	5.2	5.9	5.6	5.9	5.8	5.9	5.5	12.0	6.3
Si	16.1	18.8	17.2	17.4	44.1	14.0	37.5	43.0	100	
Ti	4.9	6.9	9.5	8.8	10.6	3.5	12.2	10.1	7.0	13.3
V	1.3	1.0	2.2	1.4	1.3	1.3	1.2	1.2	1.5	1.2
W	2.3	3.3		3.6	2.9	2.9	2.1		5.5	4.6
Y	0.028	0.072	0.058	0.073		0.036			0.050	
Zn	0.067	0.033	0.040	0.056	0.12	0.081	0.13	0.07	< 0.5	1.7
Zr	0.60	0.84	0.77	0.84	0.89	0.35	0.83		1.5	1.5

5. GrafTech International PCEA Graphite

Table 5-1 provides properties information for PCEA graphite, following the ASME graphite code MDS format. For each property, the table cites the corresponding section of this report, which contains further information extracted from publicly available data.

5.1. Material Grade

The material grade is PCEA.

5.2. Material Specification ID

This identifies the construction specification for the graphite grade applicable to this MDS. The designer enters this value.

5.3. ASTM Specification

This is the Mandatory Appendix HHA-I material specification (ASTM) number that applies to the manufacture of the material. The designer enters this number.

Table 5-1 Example ASME MDS for PCEA Graphite

Appropriate sections of the report are cited for each of the properties, which the reader can access using the hyperlink for more explanations and data.

ASME BPVC-III-5-2017, FORM MDS-1 MATERIAL DATA SHEET (SI UNITS)															
Grade Designation															
Material grade	PCEA			(1) Material grade: The manufacturer's grade designation that complies with the requirements of the Mandatory Appendix HHA-I material specification.											
Material spec. ID	Not applicable			(2) Material spec. ID: The construction specification for the graphite grade applicable to this MDS.											
ASTM spec.	ASTM D7219-08			(3) ASTM spec: The Mandatory Appendix HHA-I material specification (ASTM) number that applies to the manufacture of the material.											
Max. grain size (mm) (Section 5.4)	0.8 (Burchell et al., 2007)			(4) Maximum grain size: The maximum filler particle grain size that is used in the mix formulation. (For isostatically pressed graphite, report mean grain size.)											
Designation				(5) Designation: Material designation as defined in the Mandatory Appendix HHA-I material specification.											
Temperature-Dependent Parameters															
Property	Units														
Bulk density (Section 5.6)	kg/m^3	Mean	Std. Dev						(6) Bulk density: The material bulk density. Mean and standard deviation of material test specimen results.						
		1.83 (Homerin and Miller, 2002)													
Strength—tensile (Section 5.7)	MPa	WG	20 °C	200 °C	400 °C	600 °C	800 °C	1,000 °C (see Note 1 below)							
		Mean	20 (Homerin and Miller, 2002)						(7) Strength, tensile: Mean and standard deviation of material test specimen results. Note that the temperature dependence of only one strength parameter need be determined; the others can be assumed to change by the same relative amount.						
		Std. Dev.													

ASME BPVC-III-5-2017, FORM MDS-1 MATERIAL DATA SHEET (SI UNITS)															
	MPa	AG	20 °C	200 °C	400 °C	600 °C	800 °C	1,000 °C							
		Mean	16 (Homerin and Miller, 2002)												
		Std. Dev.													
Strength—flexural (four-point) (Section 5.8)	MPa	WG	20 °C	200 °C	400 °C	600 °C	800 °C	1,000 °C	(8) Strength, flexural (four-point): Mean and standard deviation of material test specimen results. Note that the temperature dependence of only one strength parameter need be determined; the others can be assumed to change by the same relative amount.						
		Mean	26 (Homerin and Miller, 2002)												
		Std. Dev.													
	MPa	AG	20 °C	200 °C	400 °C	600 °C	800 °C	1,000 °C							
		Mean	23 (Homerin and Miller, 2002)												
		Std. Dev.													
Strength—compressive (Section 5.9)	MPa	WG	20 °C	200 °C	400 °C	600 °C	800 °C	1,000 °C	(9) Strength, compressive: Mean and standard deviation of material test specimen results. Note that the temperature dependence of only one strength parameter need be determined; the others can be assumed to change by the same relative amount.						

ASME BPVC-III-5-2017, FORM MDS-1 MATERIAL DATA SHEET (SI UNITS)															
		Mean	67 (Homerin and Miller, 2002) (only one value available ; not known if this is WG or AG)												
		Std. Dev.													
	MPa	AG	20 °C	200 °C	400 °C	600 °C	800 °C	1,000 °C							
		Mean													
		Std. Dev.													
Elastic modulus (dynamic) (Section 5.10)	GPa	WG	20 °C	200 °C	400 °C	600 °C	800 °C	1,000 °C	(10) Elastic modulus (dynamic): Mean and standard deviation of material test specimen results.						
		Mean	11 (Homerin and Miller, 2002)												
		Std. Dev.													
		AG	20 °C	200 °C	400 °C	600 °C	800 °C	1,000 °C							
		Mean	10 (Homerin and Miller, 2002)												
		Std. Dev.													

ASME BPVC-III-5-2017, FORM MDS-1 MATERIAL DATA SHEET (SI UNITS)																	
Elastic modulus (static) (Section 5.11)	GPa	WG	20 °C	200 °C	400 °C	600 °C	800 °C	1,000 °C	(11) Elastic modulus (static): Mean and standard deviation. Use a measured value of the dynamic elastic modulus (10) scaled by the ratio between static and dynamic. Note that the dynamic and static modulus are related. Only one need be measured; the other can be computed from these measurements and the ratio between the two values.						
		Mean													
		Std. Dev.													
		AG	20 °C	200 °C	400 °C	600 °C	800 °C	1,000 °C							
		Mean													
		Std. Dev.													
Coefficient of thermal expansion, CTE, β (Section 5.12)	/°C	WG	20 °C	200 °C	400 °C	600 °C	800 °C	1,000 °C	(12) Coefficient of thermal expansion: Mean and standard deviation of material test specimen results. This property's temperature dependence shall be determined.						
		Mean	5.1 (Homerin and Miller, 2002)	3.8 (Homerin and Miller, 2002)	3.8 (Homerin and Miller, 2002)	3.8 (Homerin and Miller, 2002)	3.8 (Homerin and Miller, 2002)	3.8 (Homerin and Miller, 2002)							
		Std. Dev.													
		AG	20 °C	200 °C	400 °C	600 °C	800 °C	1,000 °C							
		Mean	5.6 (Homerin and Miller, 2002)	4.3 (Homerin and Miller, 2002)	4.3 (Homerin and Miller, 2002)	4.3 (Homerin and Miller, 2002)	4.3 (Homerin and Miller, 2002)	4.3 (Homerin and Miller, 2002)							
		Std. Dev.													
Thermal conductivity (Section 5.13)	W/m°K	WG	20 °C	200 °C	400 °C	600 °C	800 °C	1,000 °C	(13) Thermal conductivity: Mean and standard deviation of material test specimen results.						

ASME BPVC-III-5-2017, FORM MDS-1 MATERIAL DATA SHEET (SI UNITS)															
		Mean	165 (Homerin and Miller, 2002)												
		Std. Dev.													
		AG	20 °C	200 °C	400 °C	600 °C	800 °C	1,000 °C							
		Mean													
		Std. Dev.													
Temperature-Independent Parameters															
Poisson's ratio (Section 5.14)									(14) Poisson's ratio: Mean and standard deviation of material test specimen results. As an alternative, a published historical value may be used.						
Anisotropy factor (Section 5.15)			1.13 (Homerin and Miller, 2002)						(15) Anisotropy factor: Mean and standard deviation for the charges as described in the graphite specification (Mandatory Appendix HHA-I). The average of the charges is then given in the MDS.						
Critical stress intensity factor, K_{Ic} (Section 5.16)	MPa √ m	0.97 (AG) (Burchell et al., 2016); 1.33 ± 0.06 (WG) and 1.48 ± 0.06 (Burchell et al., 2017)							(16) Critical stress intensity factor (K_{Ic}): The average and standard deviation of the material test specimen results.						
Design Strength and Material Reliability Curve Values															
Ratio of compressive to tensile strength (R_{tc})		Data to be provided by the designer.							(17) Ratio of compressive to tensile strength (R_{tc}): Computed from the mean tensile and mean compressive strengths as published in (7) and (9) above. R_{tc} = Compressive Strength (9) ÷ Tensile Strength (7). This quantity is defined as positive.						

ASME BPVC-III-5-2017, FORM MDS-1 MATERIAL DATA SHEET (SI UNITS)			
Ratio of flexural to tensile strength (R_{tf})		Data to be provided by the designer.	(18) Ratio of flexural to tensile strength (R_{tf}): Computed from the mean tensile and mean flexural strengths as published in (7) and (8) above. R_{tf} = flexural strength (8) ÷ tensile strength (7). This quantity is defined as positive.
$S_{c95\%}$	MPa	Data to be provided by the designer.	(19) $S_{c95\%}$: The computed single-sided 95% confidence interval value for the Weibull characteristic strength that defines the material reliability curve. This is calculated in accordance with HHA-II-3100, based on the tensile strength measurements.
$m_{95\%}$		Data to be provided by the designer.	(20) $m_{95\%}$: The computed single-sided 95% confidence interval value for the Weibull modulus that defines the material reliability curve. This is calculated in accordance with HHA-II-3100, based on the tensile strength measurements.
S_0	MPa	Data to be provided by the designer.	(21) S_0: The computed value for the threshold stress based on the three-parameter distribution that defines the material reliability curve. This is calculated in accordance with HHA-II-3200, based on the tensile strength measurements.
$S_{c095\%}$		Data to be provided by the designer.	(22) $S_{c095\%}$: The computed single-sided 95% confidence interval value for the characteristic stress based on the three-parameter distribution that defines the material reliability curve. This is calculated in accordance with HHA-II-3200, based on the tensile strength measurements.
$m_{095\%}$		Data to be provided by the designer.	(23) $m_{095\%}$: The computed single-sided 95% confidence interval value for the Weibull modulus based on the three-parameter distribution that defines the material reliability curve. This is calculated in accordance with HHA-II-3200, based on the tensile strength measurements.

ASME BPVC-III-5-2017, FORM MDS-1 MATERIAL DATA SHEET (SI UNITS)			
S_g (10^{-4})	MPa	Data to be provided by the designer.	(24) S_g (10^{-4}): The design allowable stress value corresponding to the probability of failure of 10^{-4}, computed in accordance with HHA-II-3300 based on $S_{c95\%}$ and $m_{95\%}$ [(19) and (20) above].
S_g (10^{-3})	MPa	Data to be provided by the designer.	(25) S_g (10^{-3}): The design allowable stress value corresponding to the probability of failure of 10^{-3}, computed in accordance with HHA-II-3300 based on $S_{c95\%}$ and $m_{95\%}$ [(19) and (20) above].
S_g (10^{-2})	MPa	Data to be provided by the designer.	(26) S_g (10^{-2}): The design allowable stress value corresponding to the probability of failure of 10^{-2}, computed in accordance with HHA-II-3300 based on $S_{c95\%}$ and $m_{95\%}$ [(19) and (20) above].
S_g (5×10^{-2})	MPa	Data to be provided by the designer.	(27) S_g(5×10^{-2}): The design allowable stress value corresponding to the probability of failure of 5×10^{-2}, computed in accordance with HHA-II-3300 based on $S_{c95\%}$ and $m_{95\%}$ [(19) and (20) above].

Graphite Oxidation Effects

Property	Units	2%	4%	6%	8%	10%			
Strength [.] (Section 5.19)									(28) Oxidation change in strength: As either a chart or a curve that describes the mean behavior of the relative property change as a function of weight loss. This is expressed as a value normalized to the as-manufactured value and may be based on a strength parameter selected by the designer. The strength parameter used shall be recorded in an attachment to the MDS. The figures in HHA-3141 may be used as an alternative to measurements.
Elastic modulus (dynamic) [.] (Section 5.20)									(29) Oxidation change in elastic modulus (dynamic): As either a chart or a curve that describes the mean behavior of the relative property change as a function of weight loss. This is expressed as a value normalized to the as-manufactured value.

ASME BPVC-III-5-2017, FORM MDS-1 MATERIAL DATA SHEET (SI UNITS)									
Thermal conductivity [.] (Section 5.21)									(30) Oxidation change in thermal conductivity: As either a chart or a curve that describes the mean behavior of the relative property change as a function of weight loss. This is expressed as a value normalized to the as-manufactured value.
Irradiated Graphite									
Property									
Dimensional change [.] (Section 5.22)									(31) Irradiation-induced dimensional change: This is the change in length, normalized to the initial length expressed as a percentage. The data shall be expressed as either a table of data or a mathematical fit, appended to the MDS. Range of applicability to be identified and checked as part of the design assessment.
Creep coefficient [.] (Section 5.23)									(32) Irradiation-induced creep coefficient: Shall be expressed as either a table of data or a mathematical fit, appended to the MDS. Range of applicability to be identified and checked as part of the design assessment. The creep coefficient to be used is the coefficient (or set of coefficients) required for the irradiation creep model proposed for use by the designer. The model shall be recorded in an attachment to the MDS.
Coefficient of thermal expansion [.] (Section 5.24)									(33) Irradiation-induced change in coefficient of thermal expansion: Shall be expressed as either a table of data or a mathematical fit, appended to the MDS. Range of applicability to be identified and checked as part of the design assessment. This is expressed as a value normalized to the as-manufactured value. The temperature dependence of this property shall be determined.

ASME BPVC-III-5-2017, FORM MDS-1 MATERIAL DATA SHEET (SI UNITS)									
Strength [.] (Section 5.25)									(34) Irradiation-induced change in strength: Shall be expressed as either a table of data or a mathematical fit, appended to the MDS. Range of applicability to be identified and checked as part of the design assessment. This is expressed as a value normalized to the as-manufactured value and shall be based on a strength parameter selected by the designer. The strength parameter used shall be recorded in an attachment to the MDS. Note that irradiation-induced change in strength need only be measured should the designer desire to take account of the strength increase at low or intermediate damage doses.
Elastic modulus [.] (Section 5.26)									(35) Irradiation-induced change in elastic modulus: This is expressed as a value normalized to the as-manufactured value.
Thermal conductivity [.] (Section 5.27)									(36) Irradiation-induced change in thermal conductivity: This is expressed as a value normalized to the as-manufactured value. The temperature dependence of this property shall be determined.
GENERAL NOTES:									
(a) WG and AG refer to the with- and against-grain orientations of the material.									
(b) [.] indicates a dimensionless quantity.									
NOTE:									
(1) If the maximum intended use temperature exceeds 1,000 °C, then the temperature-dependent data shall be extended to cover the property values at the maximum intended use temperature.									

5.4. Maximum Grain Size

The maximum particle size of the raw material coke filler for PCEA graphite production is 800 μm. Figure 5-1 shows the microstructure of PCEA graphite, observed at different magnifications (Ubic, 2009). In this figure, Panel (a) shows filler particles with various shapes. Panel (b) depicts a filler with a relatively high degree of crystallite alignment surrounded by the binder matrix. Panel (c) shows a roughly spherical filler particle graphite grain, with regions of shallow shrinkage cracks running along the grain. Panel (d) identifies a relatively small acicular filler particle.

Ubic, 2009 reported the graphitized grains of the filler particle raw material in PCEA graphite were either spherical (about 70 percent) or needle-shaped. The needle-shaped grains had a mean length of 137 ± 12 μm and a mean aspect ratio of 3.2 ± 0.2, while the spherical grains had a mean diameter of 99 ± 21 μm.

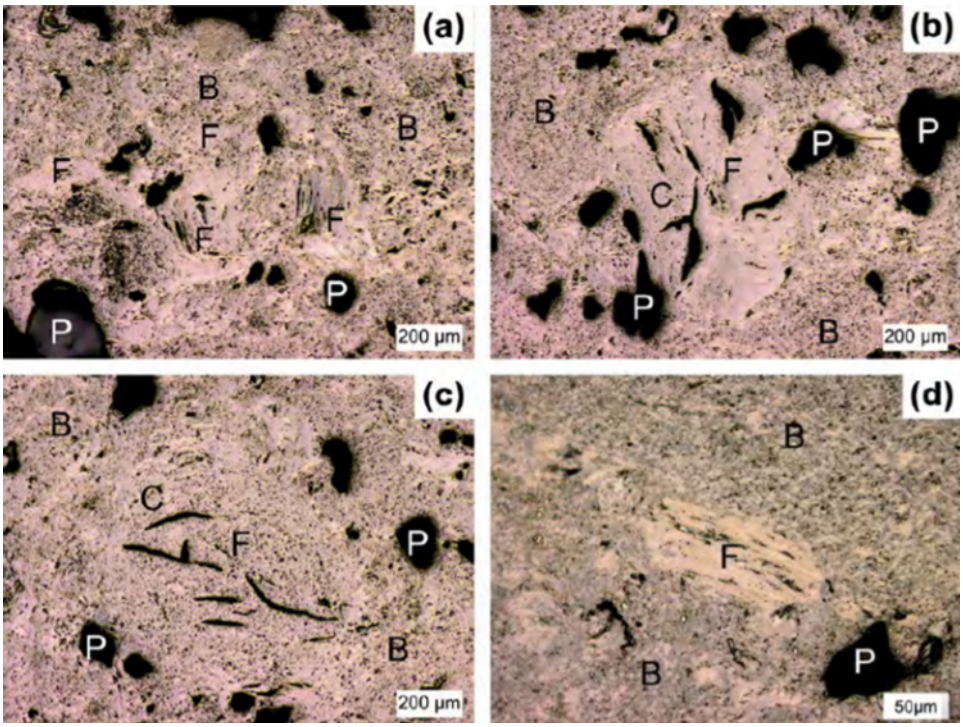

Figure 5-1 Optical micrograph of PCEA graphite, P = Porosity, F = Filler, B = Binder, C = Shrinkage crack (Ubic, 2009)

5.5. Designation

As stated in Article HHA-I-1110, this can be either ASTM D7219-08 or ASTM D7301-08. The designer enters the designation. Since most of the data for this report pertain to ASTM D7219-08, that is the designation entered in Table 5-1.

Temperature-Dependent Parameters

5.6. Bulk Density

As stated in ASTM D7219-08, PCEA belongs to the extruded, near-isotropic, high-purity (ENHP) class of nuclear graphite. The manufacturer's specification (Williams et al., 2002) gives a density of 1.85 Mg/m^3. Calculations using the Weibull statistics data of the densities measured for 1,270 PCEA test specimens, reported by Carroll and Rohrbaugh (2013), yield a (Weibull) mean density of 1.808 ± 0.028 Mg/m^3. Table 5-2 provides more density information for PCEA, obtained from the INL NGNP research.

Table 5-2 Bulk Density of PCEA Graphite

Sample designation	Density, Mg/m^3	Reference
Piggyback Combined Specimens	1.7673 ± 0.0046	Windes et al. (2015)
Piggyback AG Specimens	1.7678 ± 0.0055	
Piggyback WG Specimens	1.7668 ± 0.0036	
Creep Combined Specimens	1.8148 ± 0.02	Windes et al. (2017b)
Creep AG Specimens	1.8164 ± 0.0271	
Creep WG Specimens	1.8142 ± 0.0175	

The ASTM standard requires a minimum bulk density of 1.7 Mg/m^3 for graphites in the ENHP class. PCEA graphite meets this requirement.

5.7. Tensile Strength

Carroll and Rohrbaugh (2013) measured the room-temperature tensile strength of PCEA graphite using the ASTM C749-08 standard. However, they did not report the mean strength or the standard deviation for the results, providing only information on the Weibull statistical analysis of the strength data, obtained on a sample population of 484. An evaluation of their data yields a (Weibull) mean tensile strength of 16.83 ± 5.07 MPa.

5.8. Flexural Strength (Four-Point)

Carroll and Rohrbaugh (2013) measured the room-temperature flexural strength of PCEA graphite using the ASTM C651-10 four-point bend test standard. However, they did not report the mean strength or the standard deviation for the results, providing only information on the Weibull statistical analysis of the strength data, obtained on a sample population of 515. An evaluation of their data yields a (Weibull) mean flexural strength of 27.74 ± 5.28 MPa.

5.9. Compressive Strength

Carroll and Rohrbaugh (2013) measured the room-temperature compressive strength of PCEA graphite using the ASTM C695-91 test standard. However, they did not report the mean strength or the standard deviation for the results, providing only information on the Weibull statistical analysis of the strength data, obtained on a sample population of 528. An evaluation of their data yields a (Weibull) mean flexural strength of 63.83 ± 10.40 MPa.

5.10. Elastic Modulus (Dynamic)

The NGNP research program at INL has determined the room-temperature DYM for PCEA graphite, as shown in Table 5-3.

Table 5-3 Room-Temperature Young's Modulus Data for PCEA Graphite from NGNP Research (Windes et al., 2013b)

Measurement Method	Against-Grain, GPa	With-Grain, GPa	Anisotropy Ratio (AG/WG)
DYM	11.76 ± 0.08	12.47 ± 0.11	0.94
Resonance	8.73 ± 0.27	9.92 ± 0.24	0.88

5.11. Elastic Modulus (Static)

Carroll and Rohrbaugh (2013) reported the static elastic modulus of PCEA graphite, obtained from tensile tests, in the form of Weibull statistics. From their data, a (Weibull) mean static elastic modulus of 9.03 ± 0.65 GPa can be calculated. It is not clear from the report which grain direction these data represent.

5.12. Coefficient of Thermal Expansion

The mean CTE of PCEA depends on temperature, as shown in Figure 5-2. Burchell and Strizak (2014) made measurements along the grain direction. They measured the CTE up to 900 degrees C (1,652 degrees F), whereas Windes et al. (2013) measured the CTE up to 1,000 degrees C (1,832 degrees F). Windes et al. obtained CTE values substantially lower than those of Burchell and Strizak.

The CTE of PCEA graphite also depends on the grain orientation. Windes et al. (2013) found the anisotropy ratio of the CTE to vary mildly (by less than 2 percent) with temperature, as shown in Figure 5-3.

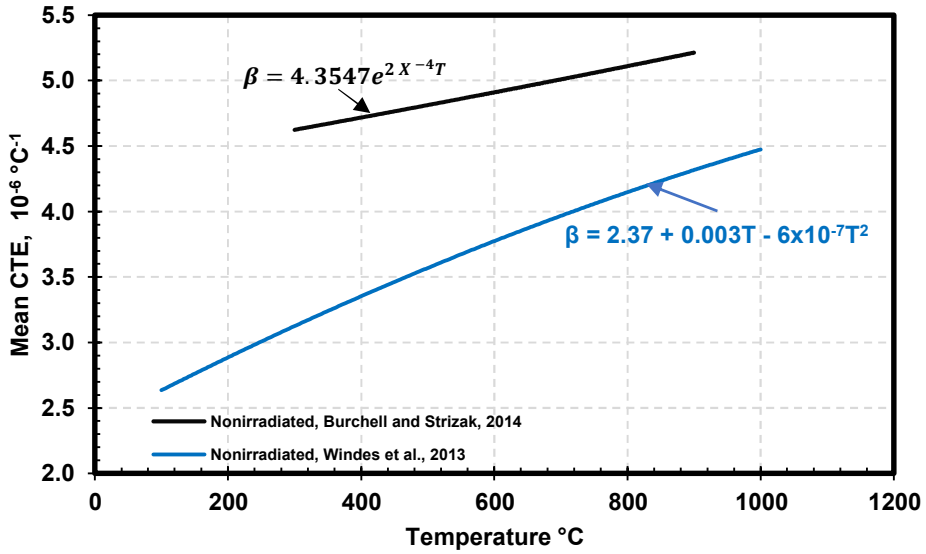

Figure 5-2 Temperature dependence of CTE for PCEA graphite

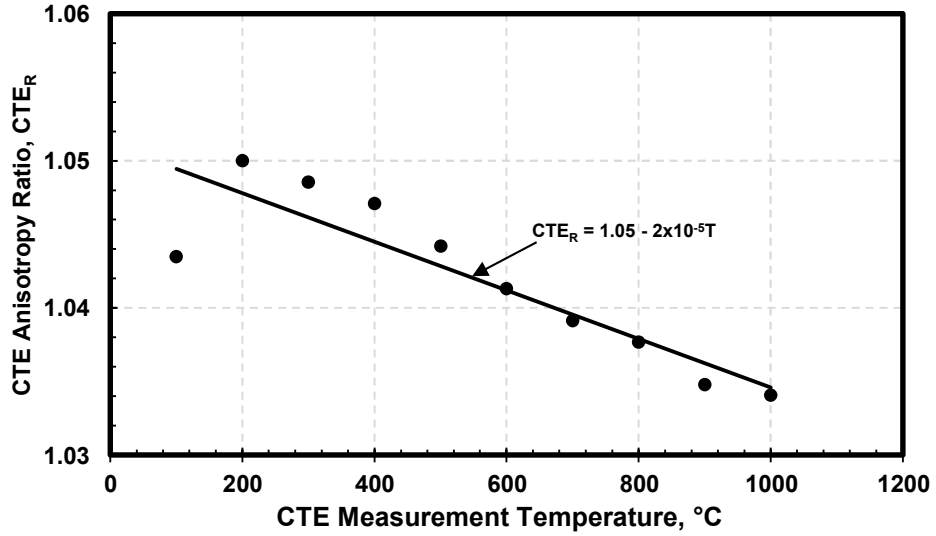

Figure 5-3 Temperature dependence of CTE anisotropy ratio for PCEA graphite (Windes et al., 2013)

5.13. Thermal Conductivity

Swank et al. (2018) measured the thermal diffusivity of nonirradiated PCEA graphite as a function of temperature. Figure 5-4 shows their results. They did not report specimen grain orientation. Their data show that the diffusivity decreases gradually over relatively low temperatures, then trends to about 20.7×10^{-6} m^2/s at 1,000 degrees C (1,832 degrees F).

Figure 5-5 shows thermal conductivity values, calculated from the data in Figure 5-4 using a nonirradiated density of 1.78 Mg/m^3 for PCEA graphite and the previously described relationship between specific heat and temperature. As expected, the thermal conductivity decreases with temperature.

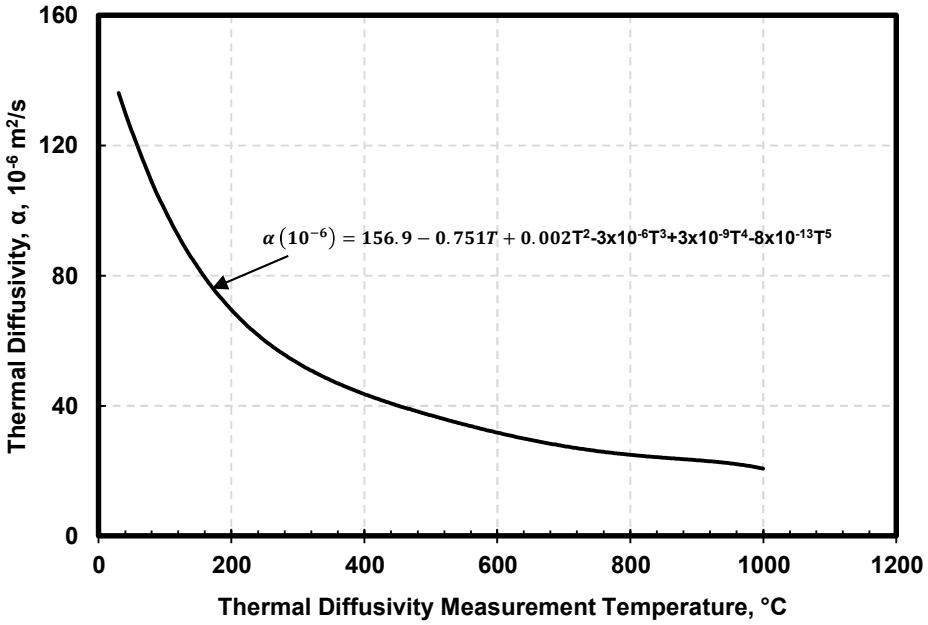

Figure 5-4 Laser flash thermal diffusivity as a function of temperature for PCEA graphite (Swank et al., 2018)

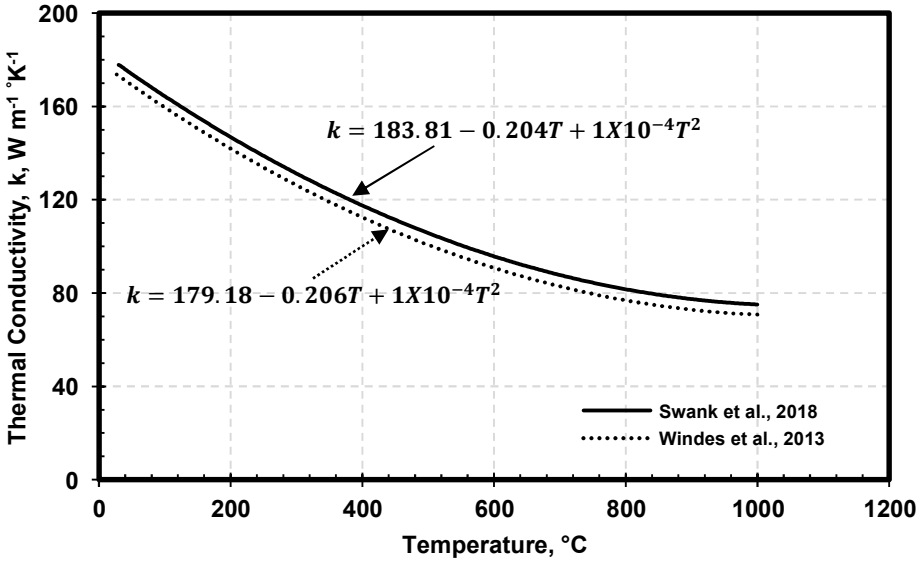

Figure 5-5 Thermal conductivity of nonirradiated PCEA graphite

Temperature-Independent Parameters

5.14. Poisson's Ratio

Carroll (2014) calculated a room-temperature Poisson's ratio (μ) value of 0.178 for PCEA graphite from the Weibull scale parameters for the modulus measurements in flexural and torsional modes.

5.15. Anisotropy Factor

PCEA graphite belongs to the ENHP class in the ASTM D7219-08 material specification. For this class, the room-temperature anisotropy factor is required to be between 1.10 and 1.15. However, as shown in Figure 5-6, the anisotropy factor of PCEA does decrease very slightly with temperature. Over the temperature range shown, the average is 1.042 ± 0.005.

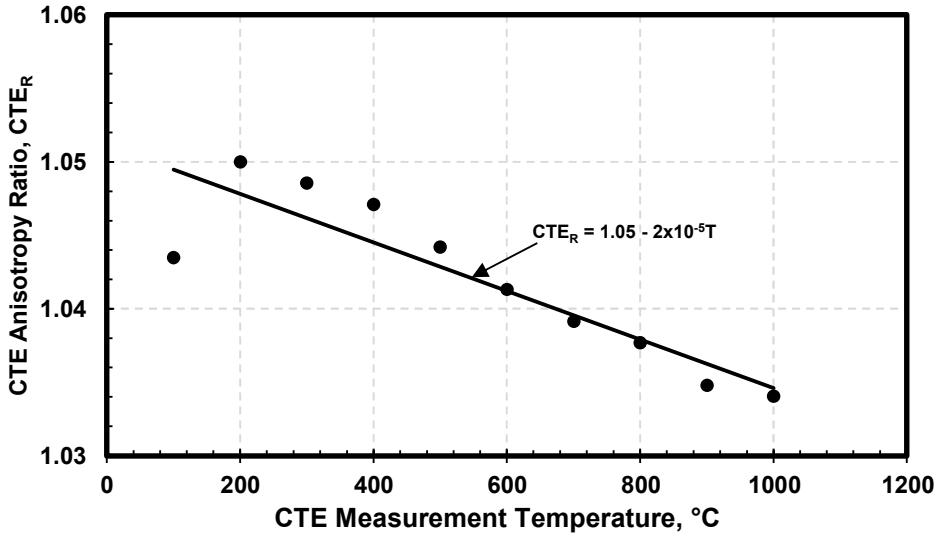

Figure 5-6 Temperature dependence of the CTE anisotropy factor for PCEA graphite (Windes et al., 2013)

5.16. Critical Stress Intensity Factor, K_{Ic}

Burchell and Strizak (2014) conducted room-temperature fracture mechanics tests for PCEA graphite using the SENB method in a three-point bend configuration. For specimens with the WG orientation perpendicular to the stressing direction and with crack propagation in the AG orientation, they reported an average K_{Ic} value of 0.971 MPa √m. The K_{Ic} value increased to 1.44 MPa √m after irradiation to 6.6 dpa and to 1.65 MPa √m after irradiation to 10.2 dpa.

For specimens with the WG orientation parallel to the stressing direction and with crack propagation in the WG orientation, Burchell and Strizak (2014) reported an average K_{Ic} value of 0.941 MPa √m. Chi (2016) obtained an average value of 0.88–1.15 MPa √m for specimens of two different thicknesses at room temperature, again using SENB specimens with three-point bending.

Graphite Oxidation Effects

5.17. Chronic Oxidation

The oxidation of graphite under HTGR operating conditions involves several potential reactions. As the coolant gas composition is controlled, the accumulation of CO and H_2 in the reactor is expected to be small. The real concern is that chronic oxidation of graphite may slowly corrode the fuel elements and other structural components in the core, weakening their mechanical strength and jeopardizing reactor integrity.

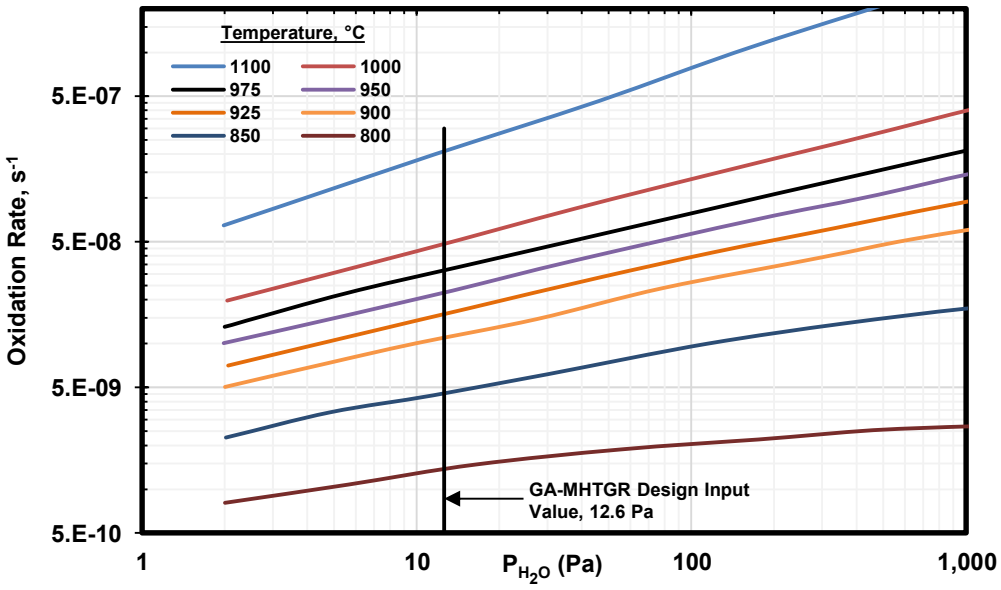

Figure 5-7 Oxidation rate of PCEA graphite by moisture with no hydrogen (P_{H2} = 0) at various temperatures, as a function of partial pressure of moisture (Contescu and Mee, 2016); rate = (1/original mass) × (Δmass/Δtime)

Contescu and Mee (2016) developed a Boltzmann-enhanced Langmuir–Hinshelwood model using 10 parameters to obtain a mathematical fit ("predicted" rate) for their oxidation kinetics data. Figure 5-7 shows their results for PCEA graphite oxidation at various temperatures. As expected, the OR increases with increasing temperature for a given partial pressure of moisture. The isothermal plots of curve fit rates separate well at high P_{H2O} and congregate closely toward low P_{H2O}.

5.18. Design Strength and Material Reliability Curve Values

Designers must enter the items under this category in the MDS, based on the results of their own testing and analyses and following the requirements in ASME BPVC-III-5, Article HHA-2200. The authors of this report did not attempt to derive these values from the literature and are not providing information on MDS Items 17–27.

5.19. Strength

Oxidation was found to decrease the compressive strength of PCEA graphite, as stated in Chi (2009) and as shown in Figure 5-8. However, Chi (2009) did not specify any oxidation conditions.

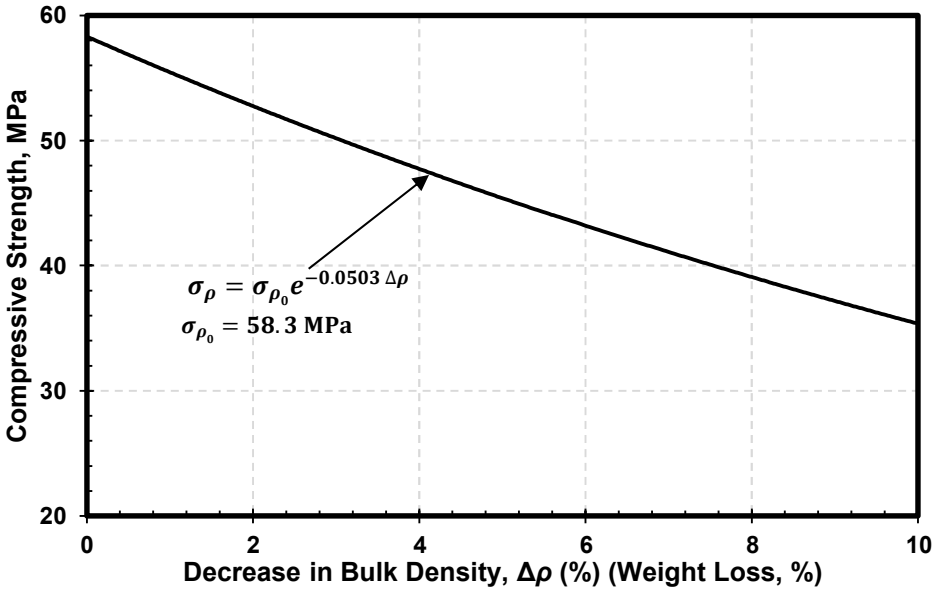

Figure 5-8 Decrease in compressive strength of PCEA graphite due to oxidation mass loss (Chi, 2009)

5.20. Elastic Modulus

Thus far, the authors have found no published data on the effect of oxidation on the elastic modulus of PCEA graphite.

5.21. Thermal Conductivity

Thus far, the authors have found no published data on the effect of oxidation on the thermal conductivity of PCEA graphite.

Irradiated Graphite

5.22. Dimensional Change

Various investigators have studied the dimensional change of PCEA due to irradiation, but most of the work on this topic seems to have been performed in the NGNP research program at ORNL and INL.

Irradiation causes different levels of dimensional change along the WG and AG orientations of PCEA graphite. Figure 5-9 shows this phenomenon in the results of irradiation tests conducted at ORNL and INL. The ORNL tests were conducted after irradiation at 896 degrees C (1,645 degrees F) at doses of 6.61 and 10.6 dpa, while the INL tests involved irradiation temperatures of 541–681 degrees C (1,006–1,258 degrees F).

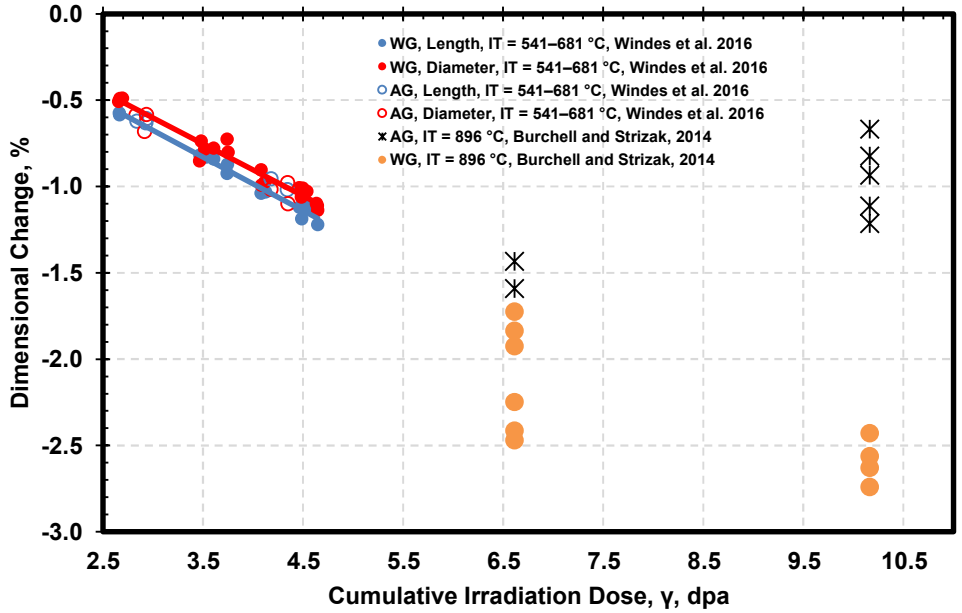

Figure 5-9 Anisotropy in irradiation-induced dimensional change in PCEA graphite

Heijna et al. (2017) also noted such anisotropy, which they defined as the difference between the relative dimensional change in the AG and WG directions. Figure 5-10 shows their data, as well as data from two other investigations. Anisotropy values were calculated from the data of Burchell and Strizak (2014), using the average values of the data shown in Figure 5-9 for the two doses. Regression analysis was performed on the data of Windes et al. (2016) for WG orientations.

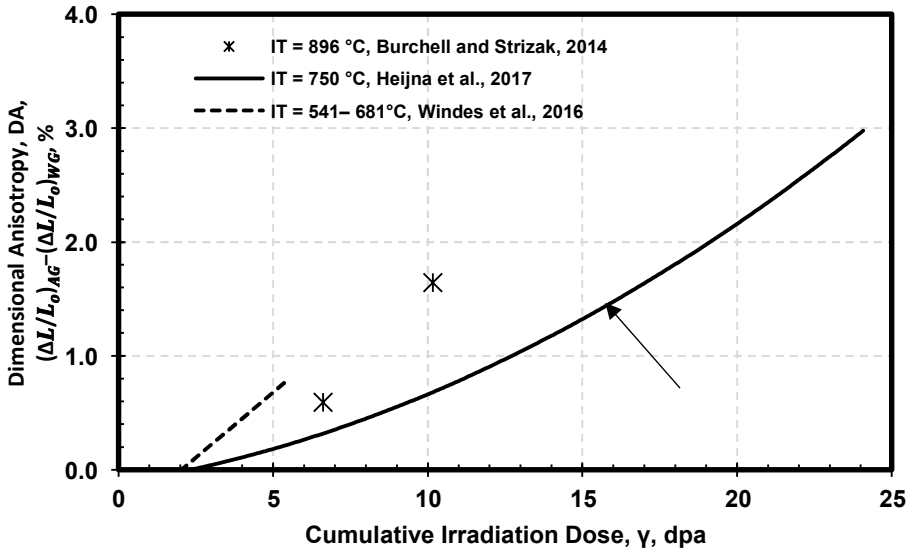

Figure 5-10 Dependence of dimensional anisotropy on dose for PCEA graphite

Creep stress also affects dimensional change, as illustrated in Figure 5-11, which shows results obtained at an irradiation temperature of 350 degrees C (662 degrees F) and with different applied stresses, as a function of irradiation dose (Windes, 2012). The grain orientation with respect to the direction of stressing is not known.

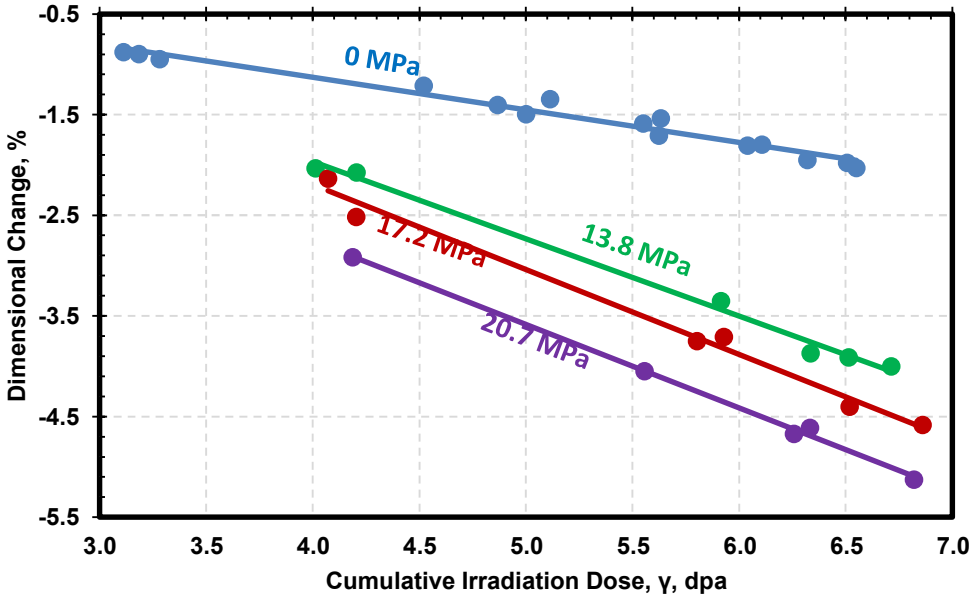

Figure 5-11 Effect of creep stress on irradiation-induced dimensional change for PCEA graphite (Windes, 2012)

Figure 5-12 shows the relative volume change for PCEA graphite, after irradiation at various temperatures, as a function of dose. Despite expected data scatter due to the dispersion in material and experimental condition variables, the data obtained by different investigations show reasonable agreement.

While Figure 5-12 shows only data for nonstressed specimens, creep stress also affects the relative change in volume. Figure 5-13 shows the effect of creep stress for irradiated and crept PCEA graphite. The effect of creep is similar in both grain orientations, as would be expected.

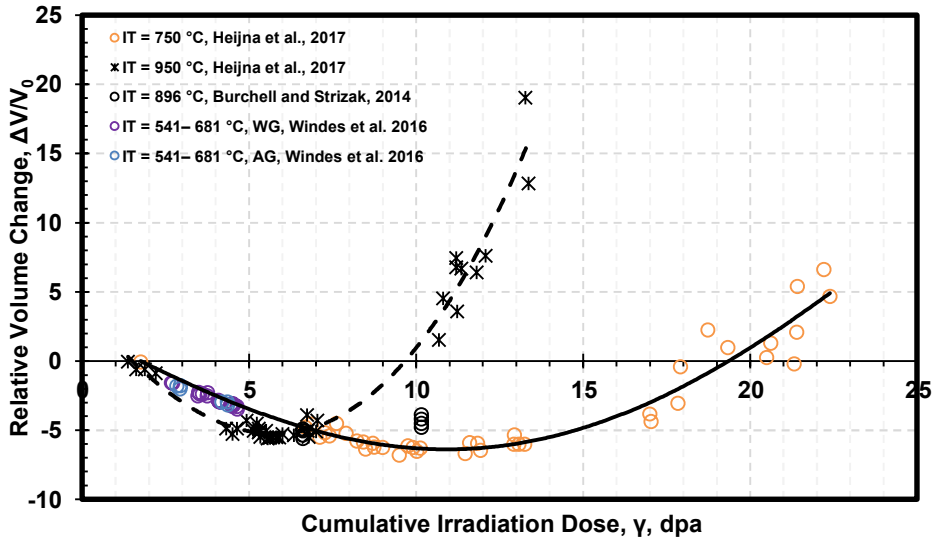

Figure 5-12 Relative volume change as a function of irradiation dose for PCEA graphite

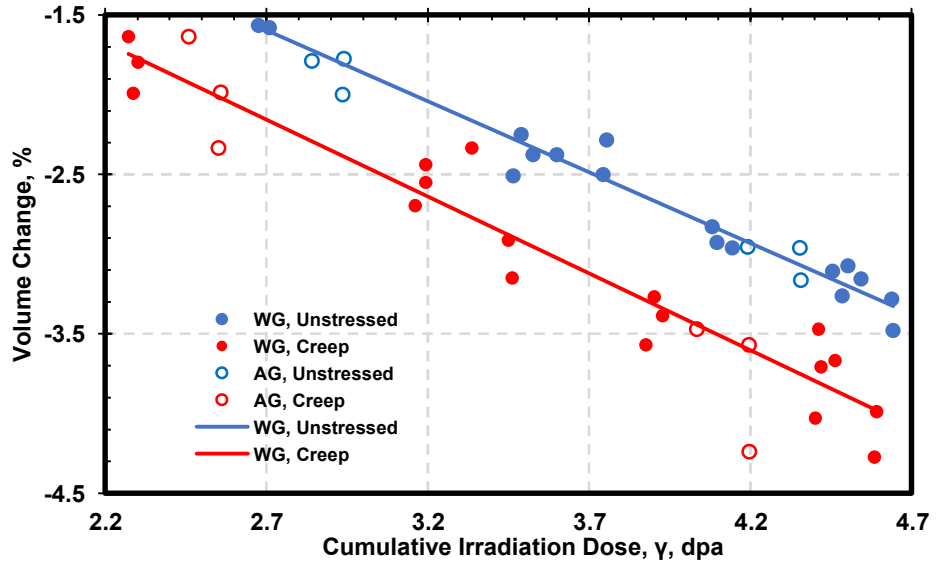

Figure 5-13 Relative volume change as a function of irradiation dose for unstressed and stressed PCEA graphite (Windes et al., 2016)

5.23. Creep Coefficient

The irradiation secondary creep coefficient for PCEA has been reported for three temperatures normalized to a stress of 20.7 MPa, as shown in Table 5-4 (Windes et al., 2019).

Table 5-4 Irradiation Secondary Creep Coefficient for PCEA Normalized to a Stress of 20.7 MPa (Windes et al., 2019)

Irradiation Temperature, °C (°F)	Creep Coefficient K, (%/MPa-dpa)
600 (1,112)	0.018
625 (1,157)	0.019
820 (1,508)	0.032

Considering the difficulties in attaining and maintaining constant temperature in any materials irradiation program, it may be appropriate to interpret this information as effectively giving the same creep coefficient for an average temperature of about 600 degrees C (1,112 degrees F). Because the data are so limited, not much can be concluded from these values in relation to the overall phenomenon of irradiation creep in PCEA graphite other than the creep coefficient increases at 820 degrees C (1,508 degrees F), which is expected.

5.24. Coefficient of Thermal Expansion

Both irradiation temperature and dose affect the CTE. Drawing from several investigations, Figure 5-14 shows the functional dependence of CTE on irradiation dose.

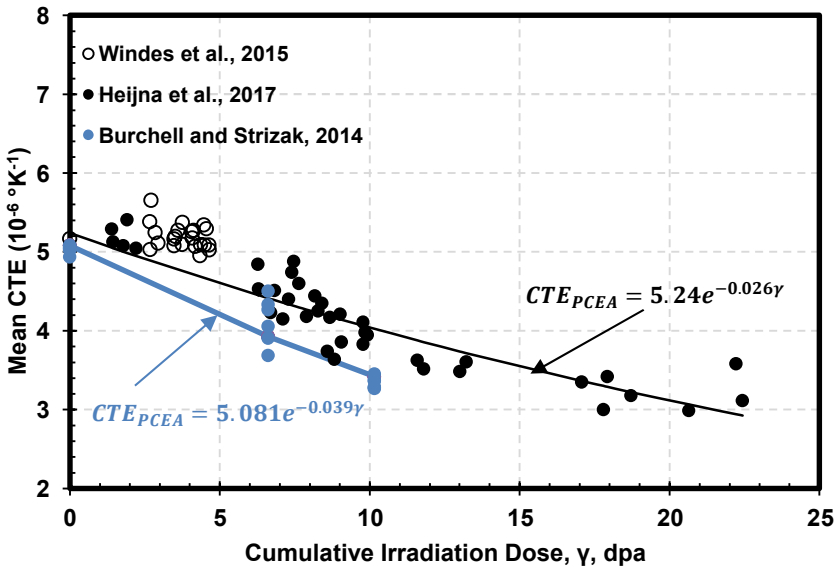

Figure 5-14 Dose dependence of mean CTE for PCEA graphite

The mean CTE values shown in Figure 5-14 were measured by the indicated investigators after irradiation to different temperatures. The scatter within each dataset may be due to temperature variation within the irradiation capsule and thus between different specimens. Heijna et al. (2017) irradiated PCEA samples at the Petten irradiation facility at an irradiation temperature of 750 degrees C (1,382 degrees F). Their mean CTE values represent data over a range of 30–750 degrees C (86–1,382 degrees F). Heijna et al. also stated that CTE is independent of specimen orientation; that is, it is the same in the WG and AG orientations.

Burchell and Strizak (2014) irradiated PCEA specimens at the ORNL High Flux Reactor facility at an irradiation temperature of 896 degrees C (1,645 degrees F). Their mean CTE values represent data over a range of 20–800 degrees C (68–1,472 degrees F), for the WG orientation.

Windes et al. (2017a) irradiated PCEA specimens at the INL's Advanced Test Reactor facility over an irradiation temperature range of 541–681 degrees C (1,006–1,240 degrees F). Their report does not give details on the grain orientation of the specimens.

The CTE can also be expected to change with irradiation temperature for a given irradiation dose; however, the data obtained by Windes et al. (2017b) exhibit too much scatter to indicate a definite trend. Figure 5-15 shows these data as the percent change in mean CTE (over a range of 100–500 degrees C (212–932 degrees F)), plotted against the irradiation temperature. The specimens were subjected to an irradiation dose of 4.0 ± 0.5 dpa.

Figure 5-16 shows how irradiation affects CTE behavior of PCEA graphite. For a constant temperature, mean CTE decreases as irradiation dose increases. Also, for all three dose levels shown, the data follow the general trend of increasing mean CTE with temperature. Figure 5-16 also reproduces the nonirradiated data previously shown in Figure 5-2, to enable comparison of the CTE behavior before and after irradiation. The CTE values obtained by Windes et al. (2013) for nonirradiated creep specimens seem unusually high compared to those of the other data sets. The irradiated CTE values measured for these specimens, with irradiation at 820 degrees C (1,472 degrees F) to a dose range of 2–4 dpa, are higher than the nonirradiated CTE values, which is contrary to the behavior observed by Burchell and Strizak (2014).

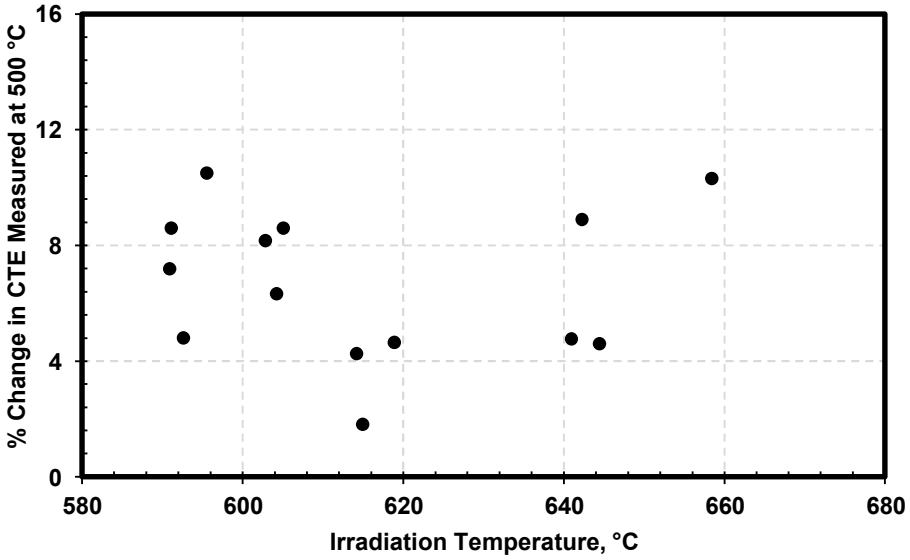

Figure 5-15 Relative change in CTE for PCEA graphite, measured at 500 degrees C (932 degrees F), as a function of irradiation temperature (Windes et al., 2017a)

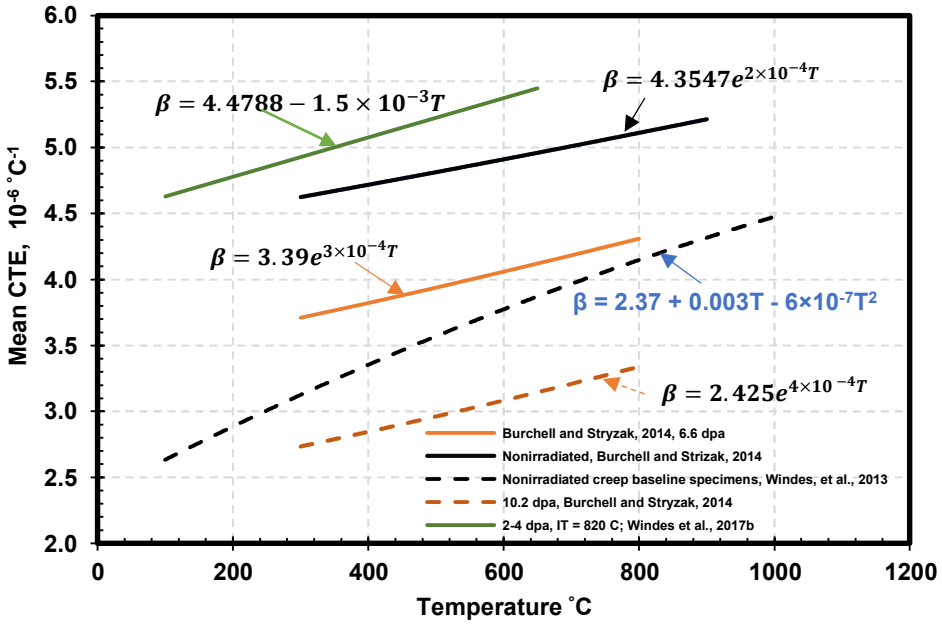

Figure 5-16 Dependence of CTE on temperature, before and after irradiation, for PCEA graphite

Creep stresses can also influence the CTE. Figure 5-17 shows this effect. For these data, the samples were irradiated to 4.0 ± 0.5 dpa, at temperatures of 541–681 degrees C (1,006–1,258 degrees F). Error bars represent ±1 standard deviation from the mean. The percent increase in CTE is directly proportional to the applied stress.

The irradiated CTE under creep stress also depends on the CTE measurement temperature. Figure 5-18 shows the average percent CTE change at measurement temperatures of 100–500 degrees C (212–932 degrees F), for both creep and control specimens. The samples were irradiated to 4.0 ± 0.5 dpa. Error bars represent ±1 standard deviation from the mean. At 500 degrees C (932 degrees F), differences of more than a factor of 4 can be observed.

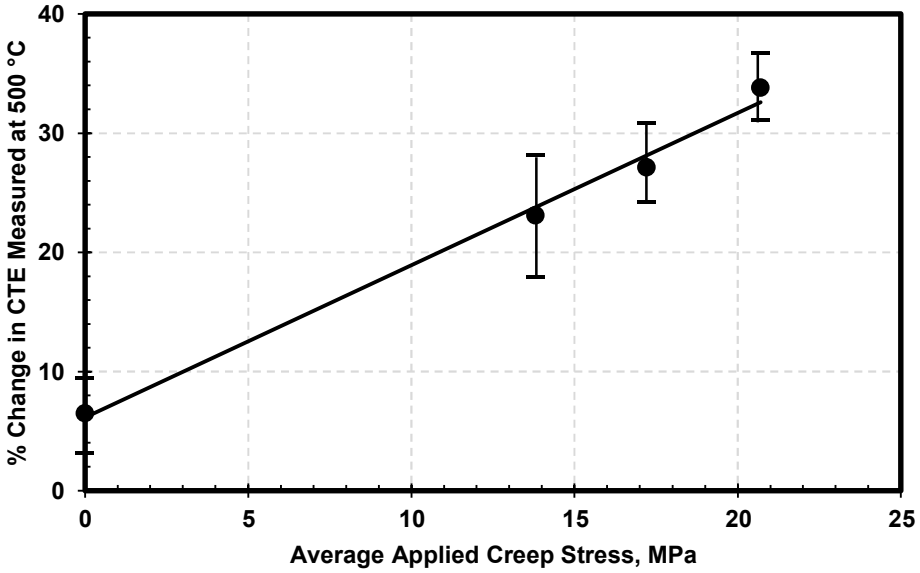

Figure 5-17 Influence of creep stress on CTE change after irradiation for PCEA graphite (Windes et al., 2017a)

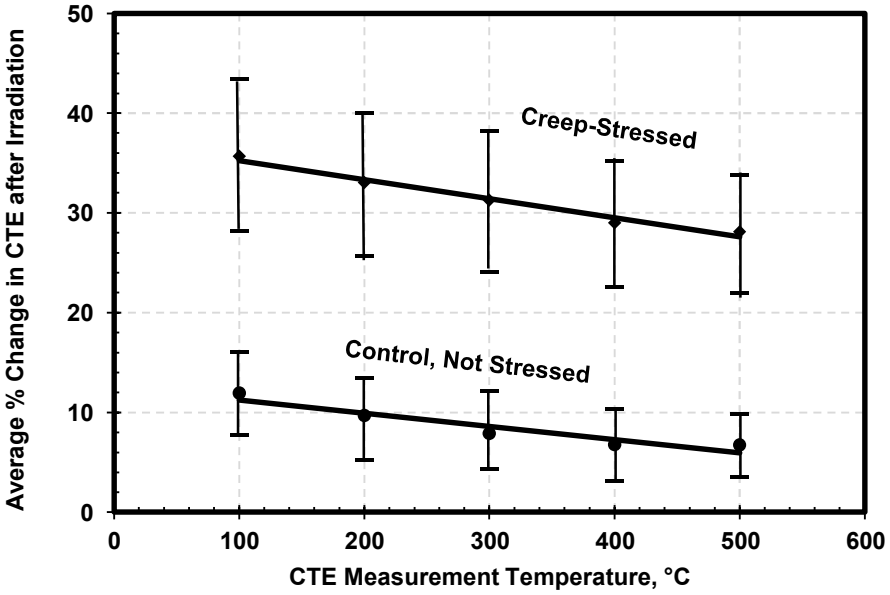

Figure 5-18 Influence of temperature on CTE change after irradiation for creep-stressed specimens of PCEA graphite (Windes et al., 2017a)

Windes et al. (2015a) also studied how applied creep stress affects the dependence of the CTE change on irradiation dose. Figure 5-19 shows their results. Because the data exhibit considerable scatter, it is impossible to infer any trends. However, the CTE change appears to saturate with increasing dose and irradiation temperature; also, creep stress increases the CTE values significantly, as already documented in Figure 5-17.

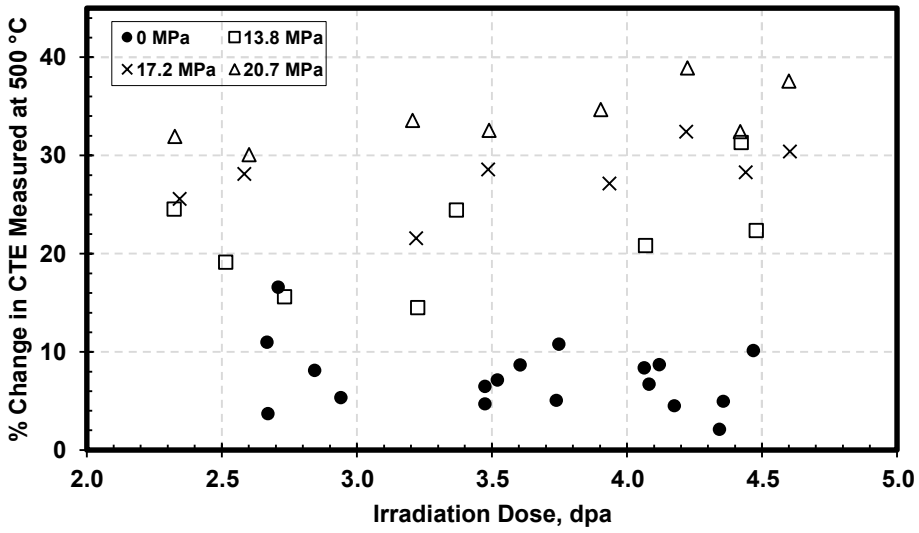

Figure 5-19 Irradiation dose dependence of change in CTE for PCEA graphite under applied creep stress (Windes et al., 2015)

5.25. Strength

Irradiation increases the density and (equivalently) decreases the porosity of PCEA graphite. Figure 5-20 illustrates this with data from Windes (2012), for a range of irradiation temperatures as shown in the inset. The reported average and standard deviation of the irradiation temperatures is 627 ± 78 degrees C (1,161 ± 172 degrees F). As mentioned previously, the scatter in the data is due to multiple factors, including temperature variations and the inherent microstructural inhomogeneity of the tested sample populations. Despite the scatter, however, the PCEA graphite data follow the usual trend: density increases with irradiation.

The irradiation dose will influence any property that depends, as the strength does, on the density or overall porosity of graphite. Heijna et al. (2017) conducted irradiation testing with discs of PCEA graphite, irradiating them to 750 degrees C (1,382 degrees F). After irradiation, they conducted diametral compression tests at room temperature and derived the tensile strength from the results, as shown in Figure 5-21. Because of the test specimen geometry and test method, the investigators did not provide information on strength for WG and AG orientations. However, the trend in the irradiated strength behavior is generally independent of the grain orientation.

The initial increase in strength for up to approximately 14 dpa is due to the expected increase in irradiation-induced dimensional shrinkage and thus the increase in overall density.

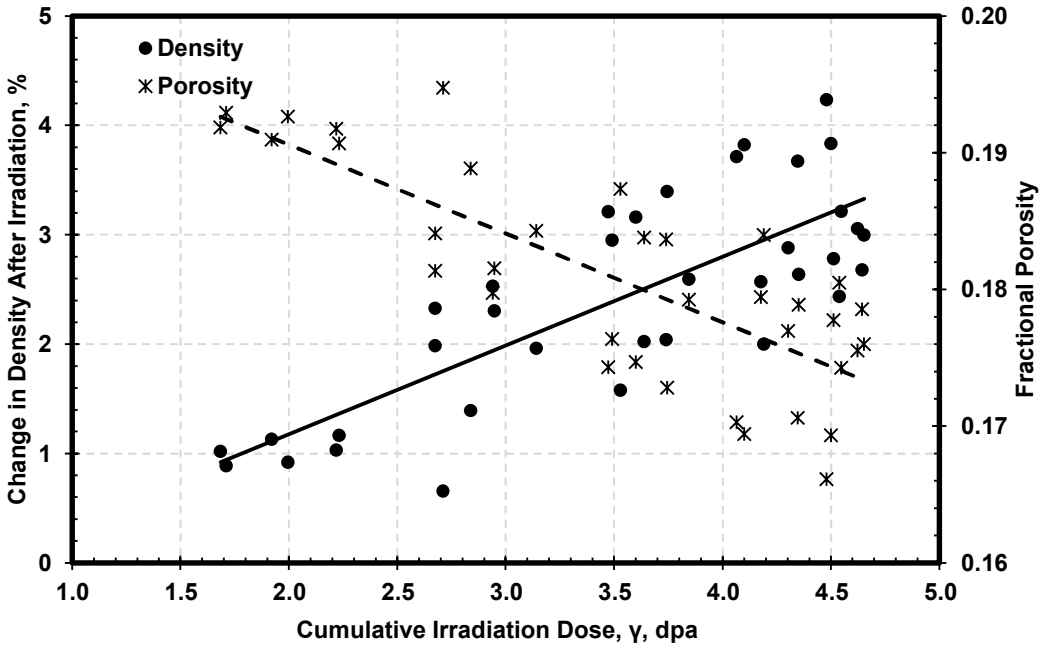

Figure 5-20 Irradiation-induced change in density (porosity) for PCEA graphite (Windes, 2012)

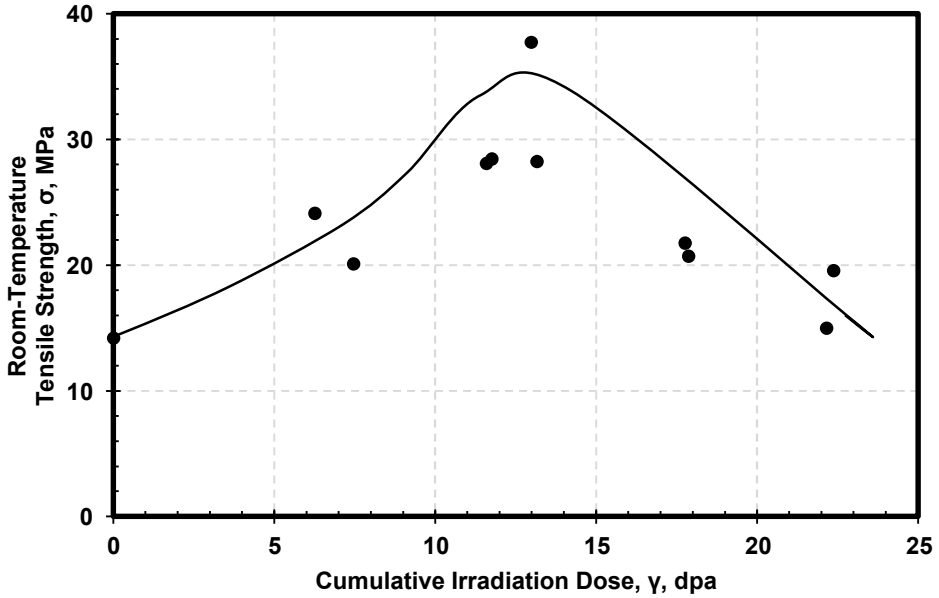

Figure 5-21 Room-temperature tensile (diametral compression) strength of PCEA graphite, after irradiation at 750 degrees C (Heijna et al., 2017)

Burchell and Strizak (2014) measured the fracture toughness, K_{Ic}, defined as the critical stress intensity factor in Mode I (opening) fracture, at room temperature using SENB specimens in a three-point bend configuration for both irradiated and nonirradiated PCEA graphite. Figure 5-22 shows their results. The trend in fracture toughness increase mirrors the trend in strength increase, even though these are separate investigations, and no correlation has yet been

established between the tensile strength measured by diametral compression testing and true uniaxial tensile strength.

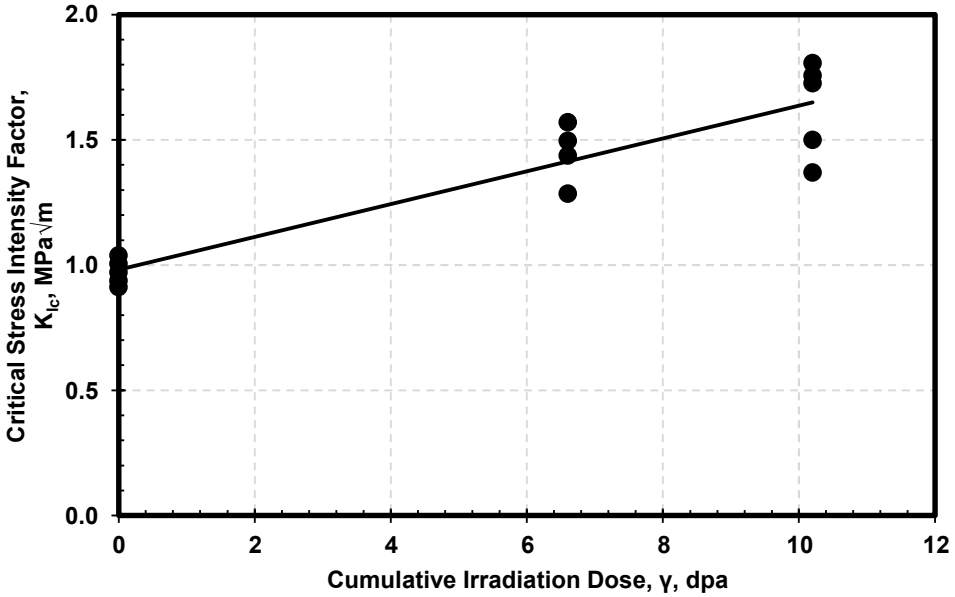

Figure 5-22 Effect of irradiation on fracture toughness of PCEA graphite (Burchell and Strizak, 2014)

5.26. Elastic Modulus

Dimensional shrinkage (partial or complete closure of microcracks and micropores over lower irradiation dose ranges) increases the density of PCEA graphite. This increased density or, equivalently, decreased porosity contributes to many of the irradiation-induced changes in mechanical properties that depend on density.

The nonirradiated average Young's modulus of PCEA graphite is 12.5 GPa. Irradiation increases the Young's modulus, as shown in Figure 5-23 (Windes et al., 2017a). The exact orientation of the specimens represented is unknown here. The data scatter is due to the inherent inhomogeneity of the tested specimens and to variations in the temperatures experienced by different specimens. Windes et al. (2017a) report the irradiation temperature as 541–681 degrees C (1,006–1,258 degrees F). In terms of actual values, the Young's modulus for irradiated PCEA graphite varies between 20.4 GPa and 24.4 GPa.

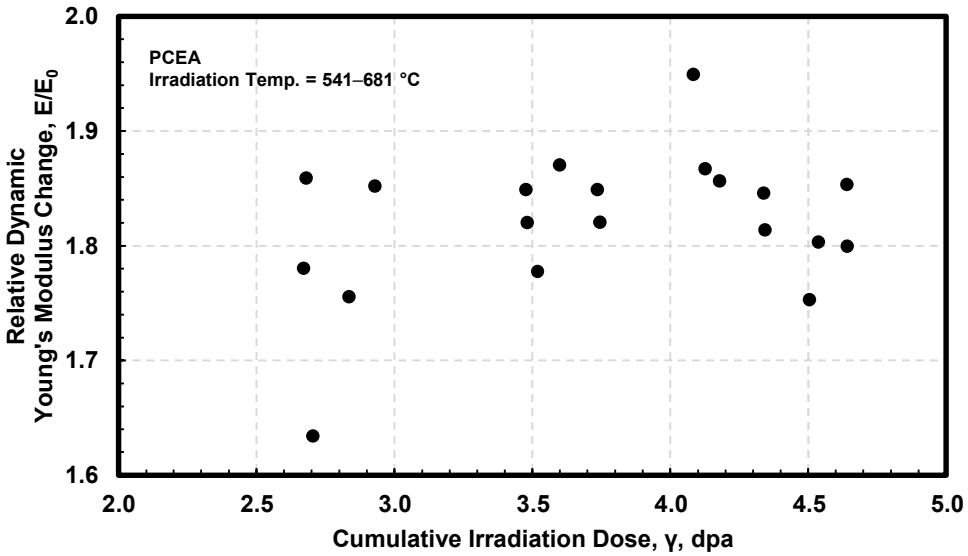

Figure 5-23 Dependence of the increase in Young's modulus of PCEA graphite on irradiation dose (Windes et al., 2017a)

Windes et al. (2017a) also report data on the orientation dependence of DYM change due to irradiation, as shown in Figure 5-24. Here, grain orientation appears to make no difference in the percent change in modulus for any given irradiation dose.

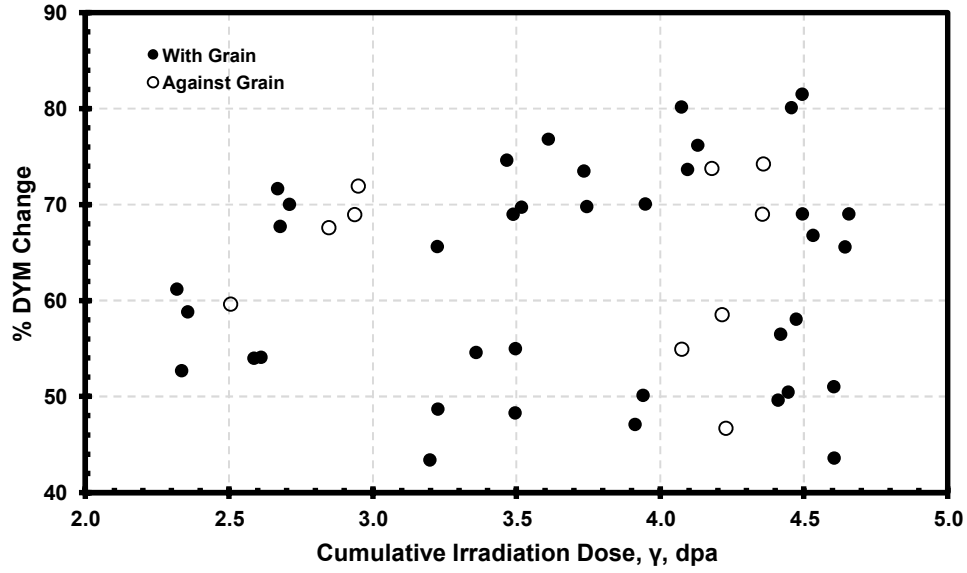

Figure 5-24 DYM change for WG and AG samples as a function of dose (Windes, 2017a)

Figure 5-25 shows the dependence of the relative change in Young's modulus on the irradiation temperature. Here, the irradiation dose was 4.0 ± 0.5 dpa.

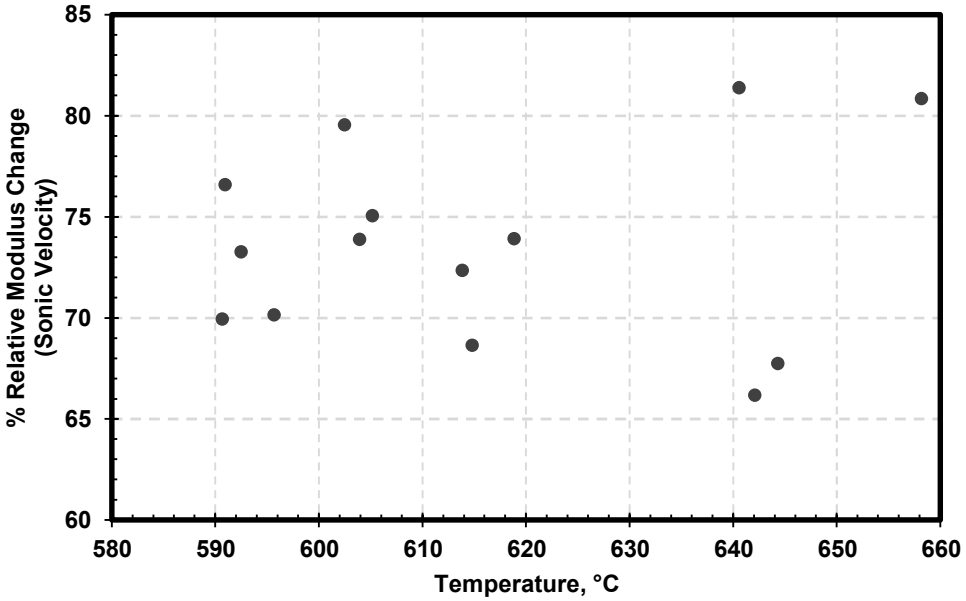

Figure 5-25 Dependence of the increase in DYM of PCEA graphite on irradiation temperature (Windes et al., 2017a)

The nonirradiated average shear modulus of PCEA graphite is 4.5 GPa. However, because irradiation shrinkage increases density, irradiation increases the shear modulus. Figure 5-26 shows how this increase depends on irradiation temperature. The data scatter is due to the inherent inhomogeneity of the tested specimens and to variations in the doses received by different specimens. The dose range reported was 4.0 ± 0.5 dpa. In terms of actual values, the shear modulus varied between 6.09 and 8.29 GPa for the irradiated PCEA graphite.

For PCEA graphite specimens that have undergone applied creep stress, irradiation increases the shear modulus less than it does for specimens that have not. Figure 5-27 shows this effect. Here, the irradiation temperatures were 541–681 degrees C (1,006–1,258 degrees F). Because of the wide data scatter, a trend cannot be discerned for this behavior.

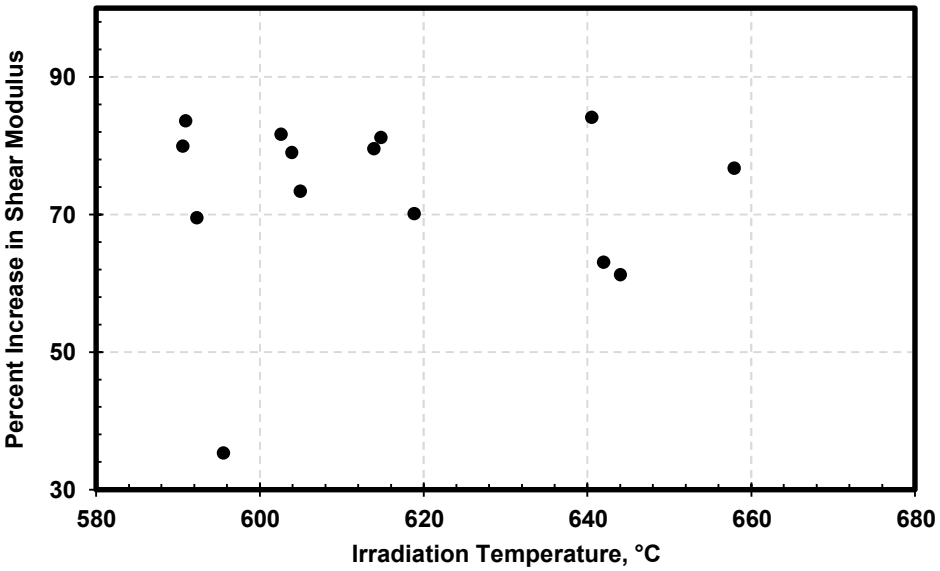

Figure 5-26 Dependence of increase in shear modulus of PCEA graphite on irradiation temperature (Windes et al., 2017a)

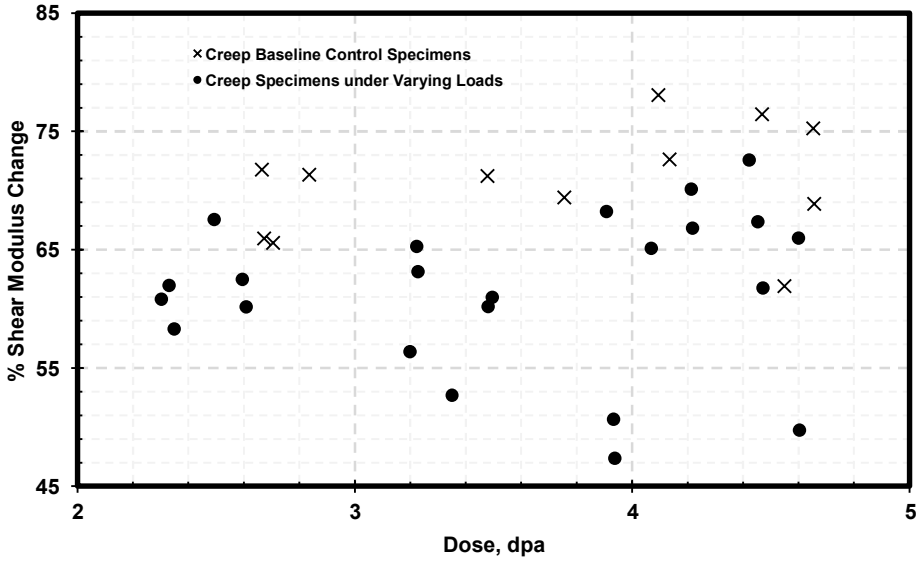

Figure 5-27 Effect of creep stress on irradiation-induced change in shear modulus of PCEA graphite (Windes et al., 2017a)

The irradiation-induced increase of Young's modulus also decreases with applied creep stress, as shown in Figure 5-28 (Windes et al., 2015). That is, irradiation of graphite with no imposed stress generally results in an increase in the room-temperature Young's modulus; any applied creep stress reduces the magnitude of such increase. In the experiments of Windes et al. (2015), samples were irradiated to temperatures of 541–681 degrees C (1,006–1,258 degrees F). The creep specimens exhibited varying magnitudes of increase in Young's modulus but less than the control specimens not subjected to external creep loading.

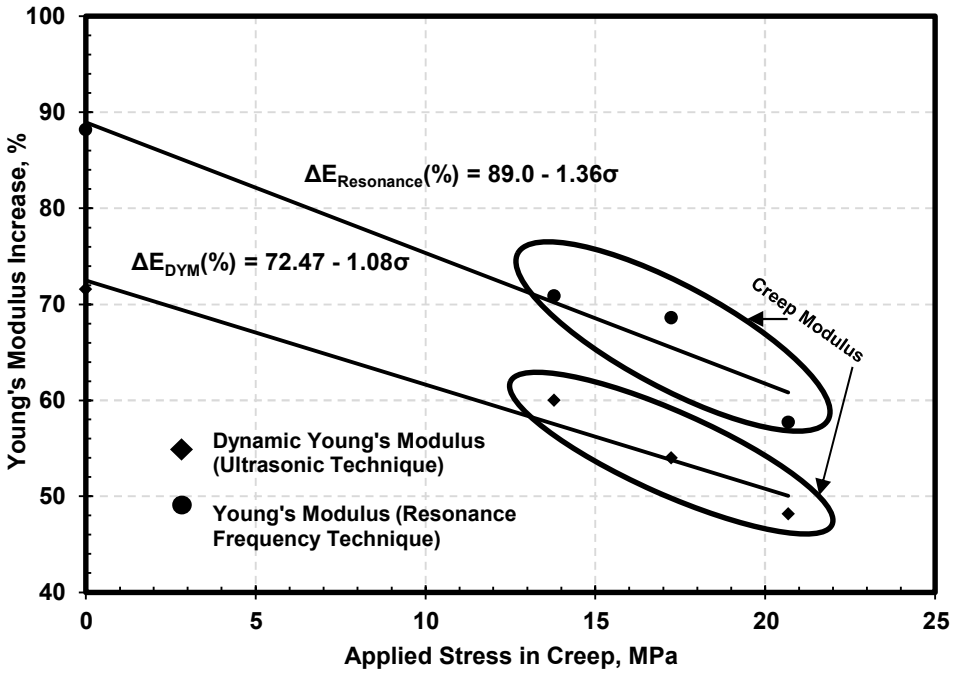

Figure 5-28 Effect of creep stress on irradiation-induced increase in Young's modulus for PCEA graphite (Windes et al., 2015)

5.27. Thermal Conductivity

Swank et al. (2018) measured the thermal diffusivity of irradiated PCEA graphite as a function of temperature. They did not report specimen orientation information. Figure 5-29 shows their results. For comparison, Figure 5-29 also includes the data for nonirradiated graphite, previously shown in Figure 5-4.

Figure 5-30 shows thermal conductivity values for irradiated PCEA graphite, calculated from the irradiated thermal diffusivity data shown in Figure 5-29, using an irradiated density of 1.823 Mg/m^3 and the previously described relationship between specific heat and temperature. Also shown are data from Windes et al. (2015) obtained on baseline specimens intended for irradiation creep study. Here, the irradiation was conducted at about 500 degrees C (932 degrees F) and at a dose of 4.0 ± 0.5 dpa. For this PCEA graphite, irradiated thermal conductivity is observed to increase slightly with temperature.

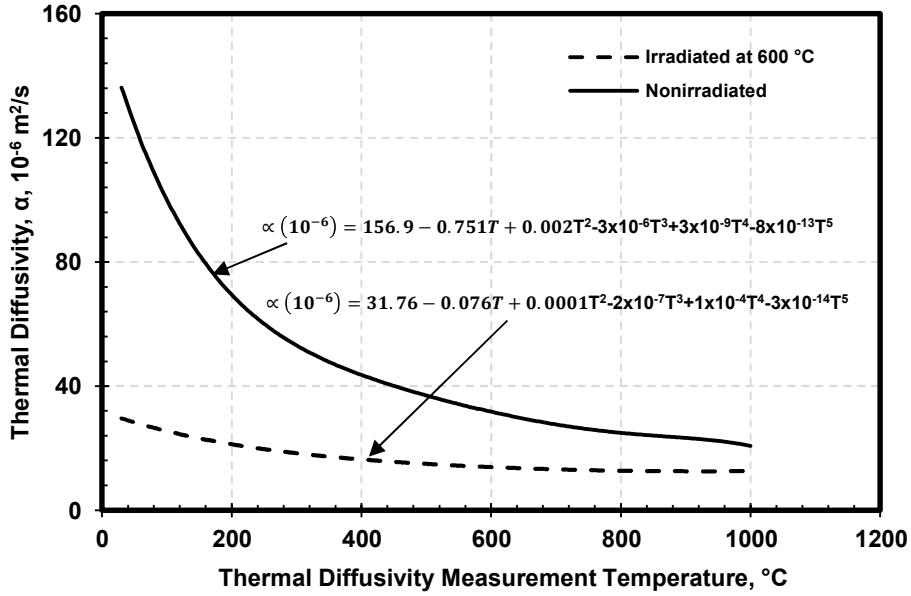

Figure 5-29 Temperature dependence of nonirradiated and irradiated (4.0 ± 0.5 dpa) thermal diffusivity of PCEA graphite (Swank et al., 2018)

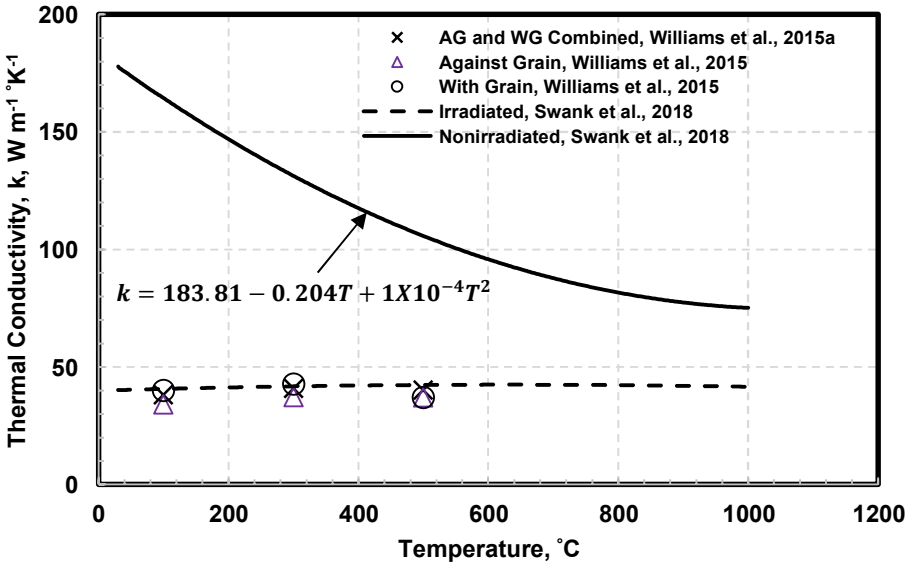

Figure 5-30 Temperature dependence of nonirradiated and irradiated (4.0 ± 0.5 dpa) thermal conductivity for PCEA graphite, calculated from thermal diffusivity data

Thermal conductivity of PCEA graphite also depends on the irradiation dose. Figure 5-31 shows this effect based on the data of Heijna et al. (2017), together with calculations made for the present report from multiple sources of interdependent density, dose, and diffusivity data from the NGNP research reports (Windes et al., 2015, 2017; Swank et al., 2018).

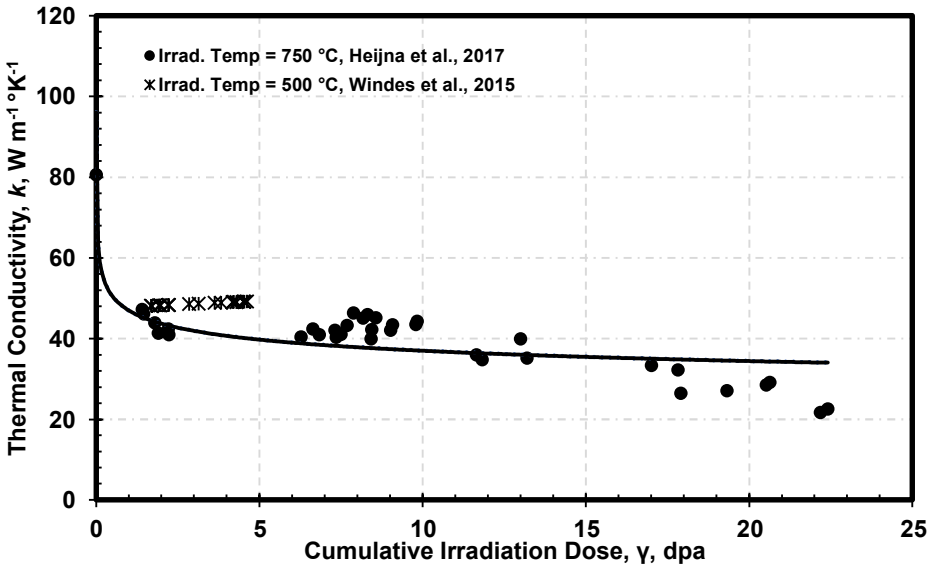

Figure 5-31 Dose dependence of thermal conductivity of PCEA graphite

In Figure 5-31, the data of Heijna et al. (2017) represent irradiation conducted at 750 degrees C (1,382 for degrees C). The NGNP research data, on the other hand, represent irradiation conducted at 500 degrees C (932 degrees F) and thus correspond to higher values of thermal conductivity in Figure 5-31.

5.28. Chemical Analysis of PCEA

Table 5-5 presents the chemical analysis data for PCEA graphite. All analysis was performed using GDMS.

Table 5-5 Chemical Analysis of PCEA Graphite (Strizak et al., 2006)

Element	ppm (wt%)	Element	ppm (wt%)	Element	ppm (wt%)	Element	ppm (wt%)
Li	<0.01	Ca	0.19	Br	<0.1	Te	<0.1
Be	<0.01	Sc	<0.05	Rb	<0.05	I	<0.1
B	0.71	Ti	0.04	Sr	<0.05	Cs	<0.1
C	Matrix	V	0.28	Y	<0.05	Ba	<0.1
N	-	Cr	<0.5	Zr	<0.05	La	<0.5
O	-	Mn	<0.05	Nb	<0.1	Ce	<0.05
F	<1	Fe	0.06	Mo	0.35	Pr	<0.05
Na	0.08	Co	<0.05	Ru	<0.1	Nd	<0.05
Mg	<0.5	Ni	<0.1	Rh	<0.1	Sm	<0.05
Al	0.06	Cu	<0.1	Pd	<0.1	Eu	<0.05
Si	1.5	Zn	<0.1	Ag	<0.1	Gd	<0.05
P	0.22	Ga	<0.1	Cd	<0.1	Tb	<0.05
S	4.6	Ge	<0.1	In	<0.1	Dy	<0.05
Cl	0.19	As	<0.1	Sn	<0.5	Ho	<0.05
K	0.1	Se	<0.1	Sb	<0.5		

6. References

American Society of Mechanical Engineers (ASME), “Quality Assurance Requirements for Nuclear Facility Applications,” ASME Nuclear Quality Assurance (NQA)-1-2008, New York, NY.

ASME, “Quality Assurance Requirements for Nuclear Facility Applications,” ASME NQA-1a-2009, New York, NY.

ASME, *Boiler and Pressure Vessel Code*, Section III, “Rules for Construction of Nuclear Facility Components,” Division 5, “High Temperature Reactors,” New York, NY, 2017 Edition.

Arai, T., Ugachi, H., Oku, T., Kodaira, T., and Eto, M., “Evaluation of Fracture Toughness and Resistance of High Strength Graphite,” *Proceedings of the International Symposium on Carbon*, pp. 162–65, 1990.

Arai, T., Ioka, I., and Ishihara, M., “Statistical Assessment of Uniaxial Strengths of a Fine-Grained Isotropic Graphite for Nuclear Applications,” *Japan Society of Mechanical Engineers International Journal, Series 1*, 34(4):470–476, 1991a.

Arai, T., Sato, S., Oku, T., Schiffers, H., and Delle, W., “Assessment of Heterogeneity and Anisotropy of IG-110 Graphite for Nuclear Components,” *Journal of Nuclear Science and Technology*, 28(8):713–720, 1991b.

AREVA NP Inc., “NGNP Conceptual Design DDN/PIRT Reconciliation,” Document No. 12-9102279-001, September 2008.

AREVA NP Inc., “NGNP with Hydrogen Production Preconceptual Design Studies Report,” Document No. 12-9051191-001, AREVA-16-03616, November 2016.

ASTM International, “Standard Test Method for Bulk Density by Physical Measurements of Manufactured Carbon and Graphite Articles,” ASTM C559-90, West Conshohocken, PA.

ASTM International, “Standard Test Method for Flexural Strength of Manufactured Carbon and Graphite Articles Using Four-Point Loading at Room Temperature,” ASTM C651-11, West Conshohocken, PA.

ASTM International, “Standard Test Method for Compressive Strength of Carbon and Graphite,” ASTM C695-91, West Conshohocken, PA.

ASTM International, “Standard Test Method for Moduli of Elasticity and Fundamental Frequencies of Carbon and Graphite Materials by Sonic Resonance,” ASTM C747-93, West Conshohocken, PA.

ASTM International, “Standard Test Method for Tensile Stress-Strain of Carbon and Graphite,” ASTM C749-08, West Conshohocken, PA.

ASTM International, “Standard Practice for Testing Graphite and Boronated Graphite Materials for High-Temperature Gas-Cooled Nuclear Reactor Components,” ASTM C781-08, West Conshohocken, PA.

ASTM International, “Standard Test Method for Dynamic Young’s Modulus, Shear Modulus, and Poisson’s Ratio for Advanced Ceramics by Impulse Excitation of Vibration,” ASTM C1259-08, West Conshohocken, PA.

ASTM International, “Standard Specification for Isotropic and Near-Isotropic Nuclear Graphites,” ASTM D7219-08, West Conshohocken, PA.

ASTM International, “Standard Specification for Nuclear Graphite Suitable for Components Subjected to Low Neutron Irradiation Dose,” ASTM D7301-08, West Conshohocken, PA.

ASTM International, “Standard Test Method for Oxidation Rate and Threshold Oxidation Temperature for Manufactured Carbon and Graphite in Air,” ASTM D7542-09, West Conshohocken, PA.

Béghein, P., Berlioux, G., Mesnildot, B., Hiltmann, F., and Melin, M., “NBG-17—An Improved Graphite Grade for HTRs and VHTRs,” *Nuclear Engineering and Design*, 251:146–149, 2012.

Berlioux, G., and Barth, P., “Interlaboratory Study on Determination of Trace Elements in Graphite Materials,” ASTM D02.F0 Subcommittee Meeting, Tampa, FL, December 9–11, 2008.

Boer, B., “Optimized Core Design and Fuel Management of a Pebble-Bed Type Nuclear Reactor,” International Atomic Energy Agency (IAEA) Publication Collection, 2008. Available from https://inis.iaea.org/collection/NCLCollectionStore/_Public/43/066/43066439.pdf (accessed August 29, 2019).

Burchell, T.D., Oku, T., and Eto, M., “A Comparison of Fracture Toughness Measurement Techniques as Applied to Nuclear Graphite,” Extended Abstracts and Program, International Carbon Conference, Paris, France, pp. 278–279, July 1990.

Burchell, T., Bratton, R., and Windes, W., “NGNP Graphite Selection and Acquisition Strategy,” ORNL/TM-2007/153, Oak Ridge National Laboratory, September 2007.

Burchell, T., “HTGR Technology Course for the Nuclear Regulatory Commission, Module 9: Graphite,” Oak Ridge National Laboratory, May 24–27, 2010.

Burchell, T.D., and Strizak, J.P., “The Effect of Neutron Irradiation on the Fracture Toughness of Graphite,” *Nuclear Engineering and Design*, 271:262–269, 2014.

Burchell, T., Erdmann, D., III, Lowden, R.R., Hunter, J., and Hannel, C., “The Fracture Toughness of Nuclear Graphite Grades,” ORNL/TM-2016/678, Oak Ridge National Laboratory, April 2017.

Burchell, T., “Graphite: Properties and Behavior,” Presentation to U.S. Nuclear Regulatory Commission and U.S. Department of Energy, January 12, 2011.

Campbell, A.A., and Katoh, Y., “Report on Effects of Irradiation on Material IG-110—Prepared for Toyo Tanso Co., Ltd.,” ORNL/TM-2017/705, Oak Ridge National Laboratory, November 2017.

Campbell, A.A., and Katoh, Y., “Summary Report on Effects of Irradiation on Material IG-110—Prepared for Toyo Tanso Co., Ltd.,” ORNL/TM-2018/1040, Oak Ridge National Laboratory, November 2018.

Carré, F., Yvon, P., and Chaix, P., “Innovative Reactor Systems and Requirements for Structural Materials,” *Proceedings of the OECD NEA NSC Workshop on Structural Materials for Innovative Nuclear Systems (SMINS)*, FZK, Karlsruhe, June 4–6, 2007, July 2008.

Carroll, M., Lord, J., and Rohrbaugh, D., “Baseline Graphite Characterization: First Billet,” INL/EXT-10-19910, Idaho National Laboratory, September 2010.

Carroll, M.C., “Initial Comparison of Baseline Physical and Mechanical Properties for the VHTR Candidate Graphite Grades,” INL/EXT-14-33120, Idaho National Laboratory, September 2014.

Carroll, M.C., and Rohrbaugh, D.T., “Statistical Comparison of the Baseline Mechanical Properties of NBG-18 and PCEA Graphite,” INL/EXT-13-30011, Idaho National Laboratory, August 2013.

Chi, S.-H., and Kim, G.-C., “Comparison of the Oxidation Rate and Degree of Graphitization of Selected IG and NBG Nuclear Graphite Grades,” *Journal of Nuclear Materials*, 381:9–14, 2008.

Chi, S.-H., “Graphite for High Temperature Gas-Cooled Reactor (HTGR),” presentation at ASME Code Week, San Diego, CA, May 10, 2009.

Chi, S.-H., “Comparison of Fracture Toughness (K_{Ic}) and Strain Energy Release Rate (G) of Selected Nuclear Graphites,” *Journal of Nuclear Materials*, 476:188–197, 2016.

Chi, S.-H., and Kim, G.-C., “Effects of Air Flow Rate on the Oxidation of NBG-18 and NBG-25 Nuclear Graphite,” *Journal of Nuclear Materials*, 491:37-42, 2017.

Choi, Q.-K., Kim, N.-J., Kim, E.-S., Chi, S.-H., and Park, S.-J., “Oxidation Behavior of IG and NBG Nuclear Graphites,” *Nuclear Engineering and Design*, 241:82−87, 2011.

Collishaw, P.G., and Evans, J.R.G., “An Assessment of Expressions for the Apparent Thermal Conductivity of Cellular Materials,” *Journal of Materials Science*, 29:2261–2273, 1994.

Contescu, C.I., and Mee, R.W., “Status of Chronic Oxidation Studies of Graphite,” ORNL/TM-2016/195, Oak Ridge National Laboratory, May 2016.

Contescu, C.I., Mee, R.W., Lee, Y., Arregui-Mena, J.D., Gallego, N.C., Burchell, T.D., Kane, J.J., and Windes, W.E., “Beyond the Classical Kinetic Model for Chronic Graphite Oxidation by Moisture in High Temperature Gas-Cooled Reactors,” *Carbon*, 127:158–169, 2018.

Davies, M.A., and Bradford, M., “A Revised Description of Graphite Irradiation Induced Creep,” *Journal of Nuclear Materials*, 381:39–45, 2008.

Eason, E.D., Hall, G., and Marsden, B.J., “Development of a Model for Dimensional Change in AGR Graphite Irradiated in Inert Environments,” in *Management of Ageing Processes in*

Graphite Reactor Cores, G.B. Neighbour, ed., Royal Society of Chemistry, Cambridge, United Kingdom, pp. 43–50, 2007.

El-Genk, M.S., and Tournier, J.-M., "Development and Validation of a Graphite Oxidation Model," *Journal of Nuclear Materials*, 411:193–207, 2011.

El-Genk, M.S., Tournier, J.-M., and Travis, B., "Graphite Oxidation Simulation in HTR Accident Conditions—3rd Year and Final Technical Report," Technical Report ISNPS-UNM-1-2012, U.S. Department of Energy, October 2012.

Eto, M., Ishiyama, S., Nishiyama, Y., Oku, T., and Burchell, T.D., "Fracture Toughness of Fine-Grained Nuclear Graphite by Means of Various Methods," *Proceedings of the International Symposium on Carbon*, pp. 170–173, 1990.

Eto, M., and Growcock, F.B., "Effect of Oxidizing Environment on the Strength of H451, PGX and IG-11 Graphites," *Carbon*, 21:135–147, 1983.

Eto, M., Kurosawa, T., Imai, H., Nomura, S., and Oku, T., "Estimation of Graphite Materials Corrosion with Water-Vapor in Coolant of the VHTR and Oxidation Effect on the Materials Properties," *IAEA Specialists' Meeting on Graphite Component Structural Design*, JAERI-M 86-192, Japan Atomic Energy Research Institute, Tokai, Japan, 1987.

Eto, M., Oku, T., and Konishi, T., "High Temperature Young's Modulus of a Fine-Grained Nuclear Graphite Oxidized or Prestressed to Various Levels," *Carbon* 29(1):11–21, 1991.

Favre-Marinet, M., and Tardu, S., *Convective Heat Transfer: Solved Problems*, John Wiley & Sons, Hoboken, NJ, 2009.

Fazio, C., Alamo, A., Almazouzi, A., De Grandis, S., Gomez-Briceno, D., Henry, J., Malerba, L., and Rieth, M., "European Cross-cutting Research on Structural Materials for Generation IV and Transmutation Systems," *Journal of Nuclear Materials*, 392:316–323, 2009.

Fechter, M., "PBMR Progress Report," Gen. IV Graphite Working Group (GWG), INTEC, Korea Atomic Energy Research Institute, Daejeon, Korea, March 29–30, 2010.

Fechter, M., and Fazluddin, S., "Characterisation of NBG-18 Graphite for the PBMR Demonstration Power Plant," 9th International Nuclear Graphite Specialists Meeting (INGSM-9), Egmond aan Zee, the Netherlands, September 15–17, 2008.

Fuller, E., and Okoh, J.M., "Kinetics and Mechanisms of the Reaction of Air with Nuclear Grade Graphites: IG-110," *Journal of Nuclear Materials*, 240:241–250, 1997.

Gallego, N.C., and Burchell, T.D., "A Review of Stored Energy Release of Irradiated Graphite," ORNL/TM-2011/378, Oak Ridge National Laboratory, September 2011.

Gao, J., Yao, W., and Ma, Y., "Analytical and Numerical Study of Graphite IG110 Parts in Advanced Reactor under High Temperature and Irradiation," *Nuclear Engineering and Design*, 305:421–432, 2016.

General Atomics, “Graphite Design Handbook,” DOE-HTGR-88111/Rev. 0, 1988a.

General Atomics, “Review of Oxidation of Graphite,” DOE-HTGR-8810, 1988b.

Heijna, M.C.R., de Groot, S., and Vreeling, J.A., “Comparison of Irradiation Behaviour of HTR Graphite Grades,” *Journal of Nuclear Materials*, 492:148–156, 2017.

Hindley, M., “Observations in the Statistical Analysis of NBG-18 Nuclear Graphite Strength Tests,” *Journal of Nuclear Materials*, 420:110–115, 2012.

Hodgkins, A., Marrow, T.J., Mummery, P., Marsden, B., and Fok, A., “X-Ray Tomography Observation of Crack Propagation in Nuclear Graphite,” *Materials Science and Technology*, 22:1045–1051, 2006.

Homerin, P., and Miller, D., “UCAR Nuclear Grade Graphites,” presentation at the HTR-M1 Committee Meeting, University of Notre Dame, Notre Dame, IN, March 2002.

Huang, W-H., Tsai, S-C., Yang, C-W., and Kai, J-J., “The Relationship between Microstructure and Oxidation Effects of Selected IG- and NBG-Grade Nuclear Graphites,” *Journal of Nuclear Materials*, 454:149–158, 2014.

Idaho National Engineering and Environmental Laboratory, “Next Generation Nuclear Plant Research and Development Program Plan,” INEEL/EXT-05-02581, Idaho Falls, ID, January 2005.

International Atomic Energy Agency, “Considerations in the Development of Safety Requirements for Innovative Reactors: Application to Modular High Temperature Gas Cooled Reactors,” IAEA-TECDOC-1366, August 2003.

Ishihara, M., Mogi, H., Ioka, I., Arai, T., and Oku, T., “Statistical Considerations of Graphite Strength for Assessing Design Allowable Stresses,” *IAEA Specialists Meeting on Graphite Component Structural Design*, JAERI-M 86-192, Japan Atomic Energy Research Institute, Tokai, Japan, 1987.

Ishihara, M., Shiozawa, S., and Oku, T., “Evaluation of Structural Integrity of Core Support Post and Seat Component under Air or Water Ingress Accident in HTTR,” *Nuclear Safety*, 38(1):51–59, 1997.

Ishihara, M., Sumita, J., Shibata, T., Iyoku, T., and Oku, T., “Principle design and data of graphite components,” *Nuclear Engineering and Design*, 233:251–260, 2004.

Ishiyama, S., Eto, M., and Oku, T., “Fatigue Behavior of Fine-Grained Isotropic Graphite for HTGRs,” *IAEA Specialists Meeting on Graphite Component Structural Design*, JAERI-M 86-192, Japan Atomic Energy Research Institute, Tokai, Japan, 1987.

Ishiyama, S., Oku., T., and Eto, “Fatigue Failure and Fracture Mechanics of Graphites for High Temperature Engineering Testing Reactor,” *Journal of Nuclear Science and Technology*, 28(5):472-483, 1991.

Kane, J., Karthik, C., Butt, D.P., Windes, W.E., and Ubic, R., "Microstructural Characterization and Pore Structure Analysis of Nuclear Graphite," *Journal of Nuclear Materials*, 415:189–197, 2011.

Kane, J., "An Intrinsic Model for Graphite Oxidation and the Effects of Microstructural Features on Apparent Rate," Ph.D. thesis, Boise State University, 2013. Available from https://scholarworks.boisestate.edu/cgi/viewcontent.cgi?article=1584&context=td (accessed November 29, 2019).

Kelley, B.T., and Brocklehurst, J.E., "UKAEA Reactor Group Studies of Irradiation-Induced Creep in Graphite," *Journal of Nuclear Materials*, 65:79–85, 1977.

Kikuchi, K., and Futakawa, M., "Structural Strength of Core Graphite Bars," *IAEA Specialists Meeting on Graphite Component Structural Design*, JAERI-M 86-192, Japan Atomic Energy Research Institute, Tokai, Japan, 1987.

Kim, E.S., Oh, C.H., No, H.C., and Kim, B.J., "Estimation of Graphite Density and Mechanical Strength of VHTR During Air-Ingress Accident," INL/CON-07-12640, 12th International Topical Meeting on Nuclear Reactor Thermal Hydraulics (NURETH-12), Pittsburgh, PA, September 30–October 4, 2007.

Kim, E.S., Hong, S.-D., and Kim, Y.-W., "Fracture Behavior of Nuclear Grade Graphite under Mixed Mode I-II," *Journal of Ceramic Processing Research*, 14(2):251–254, 2013.

Kim, B.J., Kim, D., Jang, C., and Chi, S.-H., "Oxidation and Temperature Effects on the Fracture Toughness of Nuclear Graphite at VHTR," *Transactions of the Korean Nuclear Society Spring Meeting*, Gyeongju, Korea, May 29–30, 2008.

Kim, J., Lee, Y., Kim, J., Yoon, Y., Kang, Y., Choo, K., and Cho, M., "High Temperature Compressive Test of Nuclear Graphite IG-110," *Transactions of the Korean Nuclear Society Autumn Meeting*, Jeju, Korea, October 21–22, 2010.

Kunimoto, E., Shibata, T., Shimazaki, Y., Eto, M., Shiozawa, S., Sawa, K., Maruyama, T., and Oku, T., "Expansion of Irradiation Data by Interpolation and Extrapolation for Design of Graphite Components in High Temperature Gas-Cooled Reactor—Evaluation on IG-110 Graphite Irradiation Data for Component Design," JAEA-Research 2009-008, Japan Atomic Energy Agency, June 2009.

Kunimoto, E., Yamaji, M., Konishi, T., Katoh, Y., Snead, M., Campbell, A.A., Sumita, J., and Shibata, T., "Irradiation Program for IG-110 and IG-430 Graphite for Evaluation of High Fluence Behavior," 15th International Nuclear Graphite Specialists Meeting (INGSM-15), Hangzhou, China, September 15–18, 2014.

Lee, J.J., "Oxidation of Nuclear- and Matrix-Grade Graphite for VHTR Air Ingress Accident Scenarios," Ph.D. thesis, University of Missouri-Columbia, 2016.

Lee, J.J., Ghosh, T.K., and Loyalka, S.K., “Oxidation Rate of Nuclear-Grade Graphite IG-110 in the Kinetic Regime for VHTR Air Ingress Accident Scenarios,” *Journal of Nuclear Materials*, 446:38–48, 2014.

Lee, J.J., Ghosh, T.K., and Loyalka, S.K., “Comparison of NBG-18, NBG-17, IG-110 and IG-11 Oxidation Kinetics in Air,” *Journal of Nuclear Materials*, 500:64-71, 2018.

Marsden, B.J., Haverty, M., Bodel, W., Hall, G.N., Jones, A.N., Mummery, P.M., and Treifi, M., “Dimensional Change, Irradiation Creep and Thermal/Mechanical Property Changes in Nuclear Graphite,” *International Materials Reviews*, 61(3):155–182, 2016.

Maruyama, T., Kaito, T., Onose, S., and Shibahara, I., “Change in Physical Properties of High Density Isotropic Graphites Irradiated in the ‘JOYO’ Fast Reactor,” *Journal of Nuclear Materials*, 225:267–272, 1995.

Matsuo, H., Nomura, S., Imai, H., Oku, T., and Eto, M., “Effects of High Temperature Neutron Irradiation on the Physical, Chemical and Mechanical Properties of Fine-Grained Isotropic Graphite,” *IAEA Specialists Meeting on Graphite Component Structural Design*, JAERI-M 86-192, Japan Atomic Energy Research Institute, Tokai, Japan, 1987.

Matthews, A.C., Kane, J.J., Swank, W.D., and Windes, W.E., “The Degradation of Strength under Varying Oxidizing Conditions for Nuclear Graphite,” INL/EXT-19-53723, Revision 0, Idaho National Laboratory, April 2019.

McEligot, D.M., Swank, W.D., Cottle, D.L., and Valentin, F.I., “Thermal Properties of G-348 Graphite,” INL/EXT-16-38241, Revision 0, Idaho National Laboratory, May 2016.

McEnaney, B., “Relating Measurements of Mechanical Properties of Nuclear Graphites to Reactor Conditions: A Review of the Effects of Temperature and Pressure,” in *Management of Ageing Processes in Graphite Reactor Cores*, G.B. Neighbour, ed., Royal Society of Chemistry, Cambridge, United Kingdom, pp. 51–58, 2007.

Munk, M., “An Analysis of Radiation-Induced Stresses of a Graphite Central Reflector in a Pebble Bed Fluoride Salt-Cooled Reactor Core,” M.S. thesis, University of California, Berkeley, 2013.

Nomura, S., Kurosawa, T., Imai, H., Eto, M., and Oku, T., “A Graphite Corrosion Rate Equation under High-Concentration Water-Vapor in Helium and an Estimation of the VHTR Support Post Corrosion and Strength,” *IAEA Specialists Meeting on Graphite Component Structural Design*, JAERI-M 86-192, Japan Atomic Energy Research Institute, Tokai, Japan, 1987.

Oh, C.-H., Kim, E.-S., No, H.-C., and Cho, N.-Z., “Final Report on Experimental Validation of Stratified Flow Phenomena, Graphite Oxidation, and Mitigation Strategies of Air Ingress Accidents,” INL/EXT-10-20759, Idaho National Laboratory, January 2011.

Oku, T., Ishiyama, S., Eto, M., Goto, U., Urashima, K., and Inagaki, M.J., “Effects of Notch Sharpness and Size of Specimen on the Fracture Toughness of Nuclear Graphites,” *Journal of the Ceramic Society of Japan*, 96:773–777, 1988.

Oku, T., Eto, M., and Ishiyama, S., “Irradiation Creep Properties and Strength of a Fine-Grained Isotropic Graphite,” *Journal of Nuclear Materials*, 172:77–84, 1990.

Olasov, L.R., Zenga, F.W., Spicer, J.B., Gallego, N.C., and Contescu, C.I., “Modeling the Effects of Oxidation-Induced Porosity on the Elastic Moduli of Nuclear Graphites,” *Carbon*, 141:304–315, 2019.

Park, B., and No, H., “Strength Degradation of Oxidized Graphite Support Column in VHTR,” *Journal of Nuclear Science and Technology*, 47:998–1004, 2010.

Price, R.J., “Statistical Study of the Strength of Near-Isotropic Graphite,” GA-A-13955, General Atomic Company, 1976. .

Romanoski, G.R., and Burchell, T.D., “The Effects of Specimen Geometry and Size on the Fracture Toughness of Nuclear Graphites,” CONF-9109266-1, Oak Ridge National Laboratory, 1991.

Shibata, T., “Nuclear Graphite,” in *Handbook of Advanced Ceramics*, S. Somiya, ed., Academic Press, Waltham, MA, Chapter 2.5, pp. 113–123, 2013.

Shibata, T., “R&D progress in JAEA,” Generation IV International Forum Very High Temperature Reactor System Graphite Working Group, Materials Project Management Board, Jeju, Korea, September 26–27, 2011.

Shibata, T., Eto, M., Kunimoto, E., Shiozawa, S., Sawa, K., Oku, T., and Maruyama, T., “Draft of Standard for Graphite Core Components in High Temperature Gas-Cooled Reactor,” JAEA-Research 2009-042, Japan Atomic Energy Agency, January 2010.

Shibata, T., Kunimoto, E., Sumita, J., Yamaji, M., Konishi, T., and Sawa, K., “R&Ds for Application of IG-110 Graphite to VHTR In-Core Components,” 9th International Nuclear Graphite Specialists Meeting (INGSM-9), Egmond aan Zee, the Netherlands, September 15–17, 2008.

Smith, D.S., Alzina, A., Bourret, J., Nait-Ali, B., Pennec, F., Tessier-Doyen, N., Otsu, K., Matsubara, H., Elser, P., and Gonzenbach, U.T., “Thermal Conductivity of Porous Materials,” *Journal of Materials Research*, 28(17):2260–2272, 2013.

Snead, L., Contescu, C.I., Byun, T.S., and Porter, W.D., “Thermophysical Property and Pore Structure Evolution in Stressed and Non-stressed Neutron Irradiated IG-110 Nuclear Graphite,” *Journal of Nuclear Materials*, 476:102–109, 2016.

Srinivasan, M., “Effect of Specimen Size on Fracture Mechanics Properties of Coarse-Grained Graphite,” 18th International Nuclear Graphite Specialists Meeting (INGSM-18), Baltimore, MD, September 17–21, 2017.

Srinivasan, M., “Optimizing Fracture Mechanics Specimen Design for Fine Grain Graphite and Analysis,” 19th International Nuclear Graphite Specialists Meeting (INGSM-19), Shanghai, China, September 2–6, 2018a.

Srinivasan, M., “Fracture Mechanics and Crack Growth Rates in Graphites,” 19th International Nuclear Graphite Specialists Meeting (INGSM-19), Shanghai, China, September 2–6, 2018b.

Srinivasan, M., “Microscopy of Fracture of Graphite,” 19th International Nuclear Graphite Specialists Meeting (INGSM-19), Shanghai, China, September 2–6, 2018c.

Strizak, P., Burchell, T.D., and Windes, W.E., “Status of Initial Assessment of Physical and Mechanical Properties of Graphite Grades for NGNP Applications,” ORNL-GEN4/LTR-06-023, Oak Ridge National Laboratory, September 2006.

Sumita, J., Shibata, T., Hanawa, S., Ishihara, M., Iyoku, T., and Sawa, K., “Characteristics of First Loaded IG-110 Graphite in HTTR Core,” JAEA-Technology 2006-048, Japan Atomic Energy Agency, October 2006.

Swank, W.D., Lord, J., Rohrbaugh, D.T., and Windes, W.E., “AGC-2 Graphite Preirradiation Data Package,” INL/EXT-10-19588, Idaho National Laboratory, August 2010.

Swank, W.D., Rohrbaugh, D.T., Cottle, D.L., and Windes, W.E., “High Temperature Annealing of Irradiated Graphite,” INL/CON-18-45742, Revision 0, Idaho National Laboratory, October 2018.

Takahashi, T., Ishihara, M., Baba, S., Arai, T., Hayashi, K., and Konishi, T., “Effect of Coarse-Grain Contents on Strength and Fracture Toughness of Fine-Grained Graphite,” JAERI-Research 2001-005, Japan Atomic Energy Research Institute, 2001.

Toyo Tanso Co., Ltd., “Carbon Graphite Products” (product brochure), AE-01-01, 2013. Available from https://www.ttu.com/carbon_graphite_product_catalog_eg.pdf (accessed August 20, 2019).

Travis, B.W., and El-Genk, M.S., “Numerical Simulation and Turbulent Convection Heat Transfer Correlation for Coolant Channels in a VHTR,” *Heat Transfer Engineering*, 34(1):1–14, 2013.

Tzelepi, A., Carroll, M. "Graphite Testing for Nuclear Applications: The Significance of Test Specimen Volume and Geometry and the Statistical Significance of Test Specimen Population," ASTM STP-1578, 2014

Ubic, R., “Irradiation Creep in Graphite,” Final Report of Nuclear Energy University Program (NEUP) Project 09-794, Idaho National Laboratory, 2009.

Ugachi, H., Arai, T., and Isozaki, T., “Bending Deformation and Fracture Behavior of Unirradiated and Irradiated Fine-Grain Isotropic Fine Grain Graphite Specimens,” *Proceedings of the International Symposium on Carbon*, pp. 538–541, 1990.

U.S. Code of Federal Regulations, “Domestic Licensing of Production and Utilization Facilities,” Part 50, Chapter I, Title 10, “Energy.”

Vasudevamurthy, G., Byun, T.S., Pappano, P., Snead, L.L., and Burchell, T.D., “Effect of Specimen Size and Grain Orientation on the Mechanical and Physical Properties of NBG-18 Nuclear Graphite,” *Journal of Nuclear Materials*, 462:1–7, 2015.

Williams, P., Ferry, F., Miller, D., and Pichot, P., “UCAR Graphites,” presentation to the HTR-M1 Committee, Notre Dame, France, March 2002.

Windes, W.E., “Data Report on Post-irradiation Dimensional Change in AGC-1 Samples,” INL/EXT-12-26255, Idaho National Laboratory, June 2012.

Windes, W.E., Swank, W.D., Rohrbaugh, D.T., and Lord, J., “AGC-3 Graphite Preirradiation Data Analysis Report,” INL/EXT-13-30297, Revision 0, Idaho National Laboratory, September 2013a.

Windes, W.E., Rohrbaugh, D.T, Swank, W.D., and Lord, J., “AGC-2 Graphite Preirradiation Data Analysis Report,” INL/EXT-13-28612, Revision 1, Idaho National Laboratory, August 2013b.

Windes, W.E., Swank, D., Rohrbaugh, D.T., and Cottle, D.L., “AGC-2 Specimen Post-irradiation Data Package Report,” INL/EXT-15-36244, Revision 0, Idaho National Laboratory, August 2015.

Windes, W.E., Rohrbaugh, D.T., and Swank, W.D., “AGC-2 Irradiation Creep Strain Data Analysis,” INL/EXT-16-39682, Revision 0, Idaho National Laboratory, August 2016.

Windes, W.E., Rohrbaugh, D.T., and Swank, W.D., “AGC-2 Irradiated Material Properties Analysis,” INL/EXT-17-41165, Revision 0, Idaho National Laboratory, May 2017a.

Windes, W.E., Rohrbaugh, D.T., Swank, W.D., and Cottle, D.L., “AGC-3 Specimen Post-irradiation Examination Data Package Report,” INL/EXT-17-43823, Revision 0, Idaho National Laboratory, December 2017b.

Windes, W.E., Rohrbaugh, D.T., Swank, W.D., and Cottle, D.L., “AGC-3 Irradiation Creep Strain Data Analysis,” INL/EXT-19-54725, Revision 0, Idaho National Laboratory, July 2019.

Wu, H., Carotti, F., Gakhar, R., Patel, N., and Scarlat, R., “Fluorination of Nuclear Graphite IG-110 in Molten 2LiF-BeF_2 (FLiBe) Salt at 700 ºC,” *Journal of Fluorine Chemistry*, 211:159–170, 2018.

Yu, S., and Sun, L., “The Design of HTR-PM Graphite Internals,” presentation at Nuclear Science and Engineering Institute, University of Missouri-Columbia, July 12, 2010.

Yvon, P., and Carré, F., “Structural Materials Challenges for Advanced Reactor Systems,” *Journal of Nuclear Materials*, 385(2):217–222, 2009.

Zheng, G., Xu, P., Sridharan, K., and Allen, T., “Characterization of Structural Defects in Nuclear Graphite IG-110 and NBG-18,” *Journal of Nuclear Materials*, 446:193–199, 2014.

Zhou, Y., Yujie, D., Yin, H., Li, Z., Yan, R., Li, D., Gu, Z., Sun, X., Shi, L., and Zhang, Z., “Characterizing Thermal-Oxidation Behaviors of Nuclear Graphite by Combining O_2 Supply and Micro Surface Area of Graphite,” *Scientific Reports*, 8:13400, 2018. Available from https://www.nature.com/articles/s41598-018-31493-4.pdf (accessed August 16, 2019).

Zhou, X., Wang, H., and Yu, S., “Anisotropy of Coefficient of Thermal Expansion of Nuclear Graphite under Compressive Stresses,” *Nuclear Engineering and Design*, 241:752–754, 2011.

Appendix B

List of Gas-Cooled and Liquid-Cooled Experimental, Prototype Demonstration, and Commercial High-Temperature Reactors with Graphite Components

Table B-1 High-Temperature Reactors (HTRs)—Research, Prototype, and Demonstration Power Reactors

Reactor	Purpose	Country	Criticality	Shutdown	Type	MW(t)	Graphite
Dragon	Research	OECD	1962	1976	Prism	20	Various, including extruded Gilsocarbon
Peach Bottom	Research	US	1966	1974	Prism	115	
Fort St. Vrain	Power	US	1977	1992	Prism	842	H-451
AVR	Research	Germany	1967	1988	Pebble	49	ARS/AMT
THTR	Power	Germany	1983	1989	Pebble	750	Gilsocarbon, PXA_2N
HTTR	Research	Japan	2003	Operating	Prism	30	IG110, PGX reflector
HTR-10	Research	China	2003	Operating	Pebble	10	IG-11
HTR-PM	Prototype	China	Under construction		Pebble	two 250, MWt units each	IG-110
PBMR	Power	South Africa	On hold		Pebble	240	NBG-18
GT-MHR	Power	International	Design concept		Prism	600	Not decided
Advanced Atomic Cogenerator for Industrial Applications (ACACIA)	Power	NRG	Design concept		Pebble	40	Not decided
NGNP	Research	US	Design in progress		Pebble or Prism	600	Not decided

Table B-2 Advanced Gas-Cooled Reactors (AGRs) in the United Kingdom

Station	MW(t) per Reactor	Channels	Gas Inlet Temp., T1 °C	Gas Outlet Temp., T2 °C	Criticality	Graphite	Designer/Builder
Windscale Advanced Gas-Cooled Reactor (WAGR)	100	253	250–325	500–575	1962	PGA	UKAEA—decommissioned
Hinkley Point B	1,493	308	292	645	1967	Gilsocarbon AGL	The Nuclear Power Group
Hunterston B	1,496	308	318	649	1977	Gilsocarbon AGL	The Nuclear Power Group
Dungeness B	1,485	465	320	675	1984	Gilsocarbon AGL	Atomic Power Construction Ltd.
Heysham 1	1,500	324	287	651	1984	Gilsocarbon BAEL	Babcock, English Electric Nuclear
Hartlepool	1,500	324	286	675	1985	Gilsocarbon BAEL	Babcock, English Electric Nuclear
Heysham 2	1,650	332	292	635	1988	Gilsocarbon UCAR	National Nuclear Company
Torness	1,650	332	298	635	1989	Gilsocarbon UCAR	National Nuclear Company

Table B-3 Magnox Reactors

Station	Number of Reactors	Thermal Power	Number of Fuel Channels	Pressure Containment	Gas Pressure, MN/m^2	Inlet Temp., °C	Outlet Temp., °C	Graphite
Windscale Piles	2	180MW	3,444	Concrete steel-lined	atmosphere	20	180	Various grades AGX, AGXP, chosen by purity
Calder Hall and Chapelcross	8	270	1,696	Steel cylindrical	0.69	145	340	
Berkeley	2	556	3,265	Steel cylindrical	0.96	160	345	PGA core, PGB reflector
Bradwell	2	531	2,624	Steel spherical	1.01	180	390	PGA core, PGB reflector
Hinkley Point A	2	954	4,500	Steel spherical	1.38	181	378	PGA core, PGB reflector
Hunterston A (fueled from underneath, sleeved fuel)	2	535	3,288	Steel spherical	0.98	204	395	PGA core, PGB reflector
Trawsfynydd	2	870	3,740	Steel spherical	1.76	202	392	PGA core, PGB reflector
Dungeness A	2	835	3,932	Steel spherical	1.97	250	410	PGA core, PGB reflector
Sizewell A	2	948	3,784	Steel spherical	1.93	214	401	PGA core, PGB reflector
Oldbury	2	892	3,308	Concrete cylindrical	2.52	250	411	PGA core, PGB reflector
Wylfa	2	1,875	6,156	Concrete spherical	2.75	247	414	PGA core, PGB reflector
Latina (Italy)	1	650	2,930	Steel spherical	1.32	180	390	PGA core, PGB reflector
Tokai (Japan)	1	585	2,052	Steel spherical	1.37	203	293	Pechiney, made from Texas Lockport coke (grade Q1 moderator and Q2 reflector)

Table B-1 Magnox Reactors in France (All Shut Down)

Location	Reactor	Type	Thermal Power, MW(t)	Graphite in Reactor, Metric Tons	Commissioned	Graphite
Marcoule	G1	Air-cooled	50	1,200	1956	
Marcoule	G2	Magnox	255	1,207	1959	
Marcoule	G3	Magnox	255	1,207	1960	
Loyettes	Bugey 1	Magnox	2000	2039	1972	P_3AN grade, made of LIMA petroleum coke
Avoine	Chinon A1	Magnox	300	1,050	1963	
Avoine	Chinon A2	Magnox	800	2,200	1965	
Avoine	Chinon A3	Magnox	1,300	2,530	1966	
Orléans	St. Laurent A1	Magnox	1,570	2,572	1969	P_3AN grade, made of LIMA petroleum coke
Orléans	St. Laurent A2	Magnox	1,690	2,440	1971	P_3AN grade, made of LIMA petroleum coke
Hospitalet de l'Infant (Spain)	Vandellós	Magnox	1,750	2,440	1972	P_3AN grade, made of LIMA petroleum coke

Table B-5 Other Graphite-Moderated Reactors

Reactor Name	Location	Number of Reactors	Startup Date	Shutdown Date	Initial Power, MWt	Final Power, MWt	Graphite
B-Reactor	Hanford, WA, USA	1	Sep-44	Feb-68	250	2,210	
D-Reactor	Hanford, WA, USA	1	Dec-44	Jun-67	250	2,165	
F-Reactor	Hanford, WA, USA	1	Feb-45	Jun-65	250	2040	
H-Reactor	Hanford, WA, USA	1	Oct-49	Apr-65	400	2,140	
DR-Reactor	Hanford, WA, USA	1	Oct-50	Dec-64	250	2015	
C-Reactor	Hanford, WA, USA	1	Nov-52	Apr-69	650	2,500	
KW-Reactor	Hanford, WA, USA	1	Jan-55	Feb-70	1,800	4,400	
KE-Reactor	Hanford, WA, USA	1	Apr-55	Jan-71	1,800	4,400	
N-Reactor	Hanford, WA, USA	1	Dec-63	Jan-87	4,000	4,000	
Jiuquan	China (Russian design)	1	1958	Operating	450		
Guangyuan	China (Chinese design)	1	1973	Operating	1,000		
A-Anotchka	Mayak, Russia	1	1948	1987	100	500	
AV-1	Mayak, Russia	1	1951	1987	65	500	
AV-2	Mayak, Russia	1	1951	1989	250	2000	
AV-3	Mayak, Russia	1	1952	1990	250	2,090	
I-1 Ivan-1	Seversk, Russia	1	1955	1990	250	1,500	
I-2 Ivan-2	Seversk, Russia	1	1958	1990	286	2000	
ADE-3	Seversk, Russia	1	1961	1990	286	2000	
ADE-4	Seversk, Russia	1	1962	2008	286	2,500	
ADE-5	Seversk, Russia	1	1963	Operating	286	2,500	
AD	Zheleznogorsk, Russia	1	1958	1992	286	2,500	
ADE-1	Zheleznogorsk, Russia	1	1961	1992	286	2,500	
ADE-2	Zheleznogorsk, Russia	1	1961	2009	286	2,500	
Kursk	Russia	4	1976–1985	Operating	3,200 (1000 MW(e))		GR-280 moderator, GRP2-125 location rings
Kursk-5	Russia	1	Under construction				GR-280 moderator, GRP2-125 location rings
Leningrad	Russia	4	1973–1980	Reactor 1 shut down, others operating	3,200 (1000 MW(e))		GR-280 moderator, GRP2-125 location rings

Reactor Name	Location	Number of Reactors	Startup Date	Shutdown Date	Initial Power, MWt	Final Power, MWt	Graphite
Smolensk	Russia	3	1982–1989	Operating	3,200 (1000 MW(e))		GR-280 moderator, GRP2-125 location rings
Chernobyl	Ukraine	4	1977–1983	Shut down	3,200 (1000 MW(e))		GR-280 moderator, GRP2-125 location rings
Ignalina	Lithuania	2	1983–1986	Shut down	4,200 (1500 MW(e))		GR-280 moderator, GRP2-125 location rings
APS-1	Obninsk	1	1954	2002	30 (5 MW(e))		
AMB-100	Beloyarsk	1	1964	1983	286 (108 MW(e))		
AMB-200	Beloyarsk	1	1967	1989	530 (160 MW(e))		
EPG-6	Bilabino	4	1973–1976	Operating	62 (12 MW(e))		

Appendix C

Regression Analysis of Irradiation Dimensional and Volume Change Data

Considerable scatter is common in data on dimensional and volume change due to irradiation, for many reasons, including inherent heterogeneity in graphite microstructure and variations in irradiation conditions. The analysis reported in these appendices used DigitizeIt digitization software (Version 2.2.2, 2016) to extract data from referenced publications. The digitized data were exported individually as Microsoft Excel spreadsheet files (*.csv format), from which they were analyzed. The reported fluence values were converted to displacements per atom (dpa) using the generally accepted conversion factors, which were appropriate to the reported high-energy neutron threshold. Where applicable, the data were fitted to a polynomial regression equation, and the associated curves were analyzed and evaluated for significance of irradiation behavior.

This analysis produced several derived data. For the dimensional change data, the regression-fitted polynomial was of the general form

$$\frac{\Delta L}{L_0} = a + \sum_{i=2}^{n} \gamma^n,$$

where *a* is the intercept of the plot of relative dimensional change, ($\Delta L/L_0$), versus cumulative irradiation dose, γ. Typically, no more than a fourth-degree polynomial was required to obtain a good fit ($R^2 > 0.9$). In many instances, the use of higher degree polynomials was considered unnecessary because the experimental data scatter precluded meaningful mathematical analysis. The "averaged" curve fit using a lower-degree polynomial, with marginal fit ($0.8 \leq R^2 \geq 0.7$), was considered adequate, representing the behavior more holistically than $R^2 > 0.9$ fit, which tended to connect all experimental data, swamping the effects of natural data scatter common for inhomogeneous materials.

The data-fit equation was then differentiated to obtain an equation of the form

$$\frac{d\left(\frac{\Delta L}{L_0}\right)}{d\gamma} = c + \sum_{i=2}^{n} \gamma^n.$$

From this regression analysis, several graphite behavior parameters critical to reactor design and operation were derived. Using the Solver feature in Excel software, the value of $d(\Delta L/L_0)/d\gamma$ at which the function $d(\Delta L/L_0)/d\gamma$ is zero was set as the estimated turnaround dose (ETAD). The ETAD was used in the primary equation to obtain the estimated turnaround shrinkage (ETAS). Using the curve fit equation and the Solver feature, the estimated crossover dose (ECOD) (i.e., the dose at which the original porosity level is approximately restored) was calculated. Beyond the ECOD, dimensional shrinkage stops completely, and dimensional expansion begins.

Similar parameters were derived for the data on volume change. Here, the value of $d(\Delta V/V_0)/d\gamma$ at which the function $d(\Delta V/V_0)/d\gamma$ is zero is set as the ETAD. This value is used in the primary equation to obtain the estimated turnaround volume (ETAV) shrinkage. Using the curve fit equation and the Solver feature, the ECOD (i.e., the dose at which the original porosity level is approximately restored) was calculated. Beyond the ECOD, volume shrinkage stops completely, and the volume begins to increase.

This report refers to ETAD, ETAS, ETAV, and ECOD as “derived parameters,” because they are derived from a regression analysis of the estimated general dimensional and volume change behaviors. It is understood that these derived values are estimated from the curve-fitted general pattern of behavior of the irradiated test population and are not direct measurements of the corresponding properties. Even dimension and volume are not inherent properties of graphite; rather, they are properties of the tested specimen. The fundamental “variables” governing the contraction and expansion of graphite under irradiation are related to the graphite crystal lattice dimensions and the characteristics of the pores (namely, the size, shape, and orientation distributions).

Appendix D

Dynamic Coefficient of Friction

The dynamic coefficient of friction (μ_d) of graphite-on-graphite contact is the most relevant mechanical property parameter, directly influencing erosion and abrasion resistance of graphite in a high-temperature reactor. Luo et al. (2010) provide an excellent review of the coefficients (both static and dynamic) for various graphites, under different environmental conditions. As an important historical note, the choice of design values for μ_d has previously had significant impact. The designers of the Arbeitsgemeinschaft Versuchsreaktor (AVR) were not aware that μ_d changes significantly as a function of temperature and environment; they incorrectly assumed that experiments measuring the motion of fuel pebbles in air would provide appropriate data for operational use. The actual abrasion resistance of the fuel pebbles in AVR operation was orders of magnitude lower than anticipated, resulting in excessive dust generation and contributing to fuel damage (Moormann, 2008).

Given the current state of knowledge, it would not be appropriate to attempt to quantitatively predict the influence of coke source and processing methods on the value of μ_d and the consequent abrasion resistance of the resulting graphite. For the purposes of this report, however, a brief discussion on environmental conditions influencing μ_d is warranted.

The coefficient of friction of graphite is highest in a vacuum. Because graphite has a layered hexagonal crystallographic structure, impurities in the environment can be absorbed between the atomic planes of the structure, essentially acting as a lubricant and decreasing friction. For example, Kikuchi et al. (1984) reported a μ_d of 0.3 for PGX graphite in helium at 1,000 degrees Celsius (C) (1,832 degrees Fahrenheit (F)), which decreased to 0.2 when 1,000 parts per million of O_2 was added to the helium gas. In helium, μ_d decreases with temperature, owing to the absorption of oxygen and the reduction of force between atomic planes. The resulting change in μ_d can be seen in several studies reviewed by Luo et al. (2010). Citing their own work on IG-11 graphite in helium, Luo et al. reported a decrease of μ_d from 0.40 to 0.22 as the temperature was increased from 25 degrees C (77 degrees F) to 400 degrees C (752 degrees F).

Luo et al. (2010) documented what limited impact irradiation has upon the dynamic coefficient of friction of graphite, citing Nightingale (1962), who tested 50 irradiated samples of TSGBF graphite. Nightingale's study showed an approximately 20-percent drop in the room-temperature static coefficient of friction following irradiation at 400–500 degrees C (752–932 degrees F), but this change was chiefly attributed to oxidation of the graphite during irradiation. No measurements reporting the dynamic coefficient of friction or reported. Summarizing Nightingale's work, Luo et al. (2010) simply stated, "Radiation has hardly any effect on the friction property of graphite."

References

Luo, X., Li, X., and Yu, S., “Nuclear Graphite Friction Properties and the Influence of Friction Properties on the Pebble Bed,” *Nuclear Engineering and Design*, 240:2674–2681, 2010.

Kikuchi, K., Kaburaki, H., and Sanokawa, K., “Impurity Gas Effects on Friction and Wear of High-Temperature Materials for VHTRs,” *Nuclear Technology*, 66:491–502, 1984.

Moormann, R., “Fission Product Transport and Source Terms in HTRs: Experience from AVR Pebble Bed Reactor,” *Science and Technology of Nuclear Installations*, 2008:597491, 2008.

Nightingale, R.E., *Nuclear Graphite*, Academic Press, New York, NY, 1962.